A PRECISE 3D BEAM DYNAMICS MODEL OF THE PSI INJECTOR II

By
Anna Maria Kolano

A THESIS SUBMITTED TO THE UNIVERSITY OF HUDDERSFIELD
IN PARTIAL FULFILMENT OF THE REQUIREMENTS FOR
THE DEGREE OF DOCTOR OF PHILOSOPHY

THE UNIVERSITY OF HUDDERSFIELD IN COLLABORATION WITH
PAUL SCHERRER INSTITUT

March 2017

Contents

Declaration **15**

Abstract **16**

Acknowledgements **17**

1 Introduction **18**
1.1 Motivation for the research 18
1.2 Injector II and PSI High Intensity Proton Accelerator facility 21
1.3 Research literature review 24
1.4 Chapter summary 27

2 Theoretical background **28**
2.1 Cyclotron beam dynamics 28
2.2 Separate-sector isochronous cyclotrons 32
2.3 Tune diagrams & Accelerated and Static Equilibrium Orbit 35
2.4 Space charge effects 37
2.5 Stationary distribution 40
2.6 Halo quantification 41

3 Methods **43**
3.1 OPAL code - Cyclotron mode 43
3.2 Optimisation 45
3.2.1 Orbit finder 45
3.2.2 Radial intensity peak matching 46
3.2.3 Visualization 47
3.3 Post-processing 47
3.4 Approach 48

3.5 Chapter summary 51

4 3D models of Injector II **52**
4.1 Stationary distribution and the closed orbit 53
4.2 Production configuration 55
4.2.1 Applying the continuous 4σ cut model to the production configuration 56
4.2.2 Applying the 6-turn 4σ model to the production configuration 61
4.3 Upgraded set-up 68
4.3.1 Applying continuous 4σ cut model to the upgraded configuration 69
4.3.2 Applying 6-turn 4σ cut model to the upgraded configuration . 74
4.4 Chapter summary 80

5 Physical collimator model **81**
5.1 Applying the physical collimation model to the production configuration 81
5.1.1 Probe environment 83
5.1.2 The collimators 86
5.1.3 Currents on collimators 87
5.1.4 Peak matching 91
5.2 Applying the physical collimation model to the upgraded configuration 95
5.3 Chapter summary 96

6 Comparison and validation of 3D models **97**
6.1 Continuous and 6-turn cut 4σ models before and after the upgrade . . 97
6.2 Physical collimator model comparison 99
6.3 Comparison of the physical collimator model based on statistics (particle number) 110
6.3.1 Longitudinal tail correction with KIP4 collimator 113
6.3.2 Flat-top mode check 118
6.4 Validation with measurements 121
6.4.1 Scaling laws 123
6.4.2 Uncertainties on the Injector II parameters and our predictions 130
6.5 Chapter summary 131

7 Summary **133**
7.1 Summary 133
7.2 Possible improvements 136

Bibliography **137**

A Additional data **142**

A.1 Production configuration models 143

A.1.1 Continuous 4σ cut 143

A.1.2 6-turn 4σ cut 147

A.2 Physical collimator model 154

A.2.1 KIP4 collimator adjustment 165

A.2.2 Current on collimators 165

Word count: 21396

List of Tables

1.1 Injector II parameters [1]. 23

3.1 Simulation parameters. 45

5.1 Currents read on the selected collimators from EPICS system (See Figure 5.6 for graphical representation. The currents are shown in μA.) . 88

5.2 Last peak positions (mm) of the measured Injector II beam with the RIE1 probe for currents from 0.05 to 2.5 mA (Figure 5.9 in grey). . . 91

List of Figures

1.1 High Intensity Proton Accelerator Facility. Starting from the left: Cockcroft-Walton generator, the Acceleration Tube, Injector II, transfer line and Ring cyclotron [2]. 19
1.2 PSI Injector II [2]. 21
1.3 Overview of the High Intensity Proton Accelerator Facility [3]. 22
1.4 Central region of Injector II with collimators. Starting from the centre KIL, KIS, KIP2, KIG3, KIV, KIP3, KIR1, KIG1, KIR3 and KIP4 [1]. 24

2.1 Principle of a classic cyclotron acceleration. 30
2.2 Principle of weak focusing for field index $n < 0$, $n = 0$ and $n > 0$. . . 31
2.3 Equilibrium orbit of an isochronous AVF cyclotron, where v is the velocity of the particle with its radial (v_r) and azimuthal (v_θ) components. 32
2.4 Axial focusing forces created at the edges of the hill. 33
2.5 ν_r and $2\nu_z$ tunes of Injector II with marked $\nu_r + 4 = 2\nu_z$ resonance at around 2 MeV. 36
2.6 AEO of Injector II. 37
2.7 Coulomb repulsion and magnetic attraction between two particles of equal charge, at rest and travelling. 38

3.1 Flow chart of the steps taken in the model development. 49

4.1 Coordinate system used in the thesis. 52
4.2 Emittance convergence study for considered intensities. Selected for 2 mA initial energy. 53
4.3 Closed 2 MeV orbit of the production set-up at 2 mA current. The distribution is not matched for Injector II field map, hence the initial "blow-up". Requires about 10 -20 turns to "match" itself. 54
4.4 2 mA distribution in x-y after injecting (a) and after 100 turns of "coasting" (b) at 2 MeV orbit. 55

4.5 Schematic of the Injector II production configuration. The cyclotron has four sector magnets operating at 2 T (green), two double-gap resonators (grey) and two 3rd harmonic cavities (maroon). 56
4.6 Production set-up 2.2 mA case applied to continuous 4σ cut (2.5 mA $5 \cdot 10^4$ macroparticles injected). 58
4.7 Production set-up 3.5 mA case applied to continuous 4σ with 10^6 macroparticles. 59
4.8 Production set-up 3.9 mA case applied to continuous 4σ cut (4 mA $5 \cdot 10^4$ particles injected) spatial. Even at continuous cut, beam size is too big to pass through the septum. 60
4.9 Production set-up 2.3 mA case. 6-turn 4σ cut with injected 2.5.mA ($5 \cdot 10^4$ macroparticles). Radial and longitudinal planes are well matched with very smooth vertical plane. However longitudinal halo is generated that after 40 turns couples to radial plane. 62
4.10 Production set-up 2.9 mA case applied to 6-turn 4σ cut (injected 3 mA $5 \cdot 10^4$ macroparticles). X and y planes are well matched with very smooth vertical plane. Longitudinal halo couples to the radial plane after about 40 turns. 63
4.11 Production set-up for 1.9 mA case. 6-turn 4σ cut with injected 2 mA $5 \cdot 10^4$ macroparticles. Last turn in 360°. 65
4.12 Production set-up 3.8 mA case applied to 6-turn 4σ cut with injected 4 mA $5 \cdot 10^4$ macroparticles. 66
4.13 Comparison of production set-up for 1.9-5.7 mA cases applied to 6-turn 4σ cut with injected $5 \cdot 10^4$ macroparticles. RMS beam size remains constant throughout acceleration while physical extent of the beam (halo) increases. 67
4.14 Current outside 5σ . The 2.9 mA beam carries 0.005 mA outside the selected boundary for 3.8 mA it already reaches 0.008 mA. 67
4.15 Schematic of the Injector II upgraded configuration. The cyclotron has four sector magnets operating at 2 T (green), two double-gap resonators and two single-gap resonators (grey). 68
4.16 Upgraded set-up 1.8 mA case applied to continuous 4σ cut with injected 2 mA 10^6 macroparticles. 70
4.17 Upgraded set-up 3.5 mA case applied to continuous 4σ cut with injected 4 mA 10^6 particles. Very well matched case. 71

4.18 Upgraded set-up 5.3 mA case applied to continuous 4σ cut with injected 6 mA 10^6 particles. 72
4.19 Comparison of 2, 4, 6 mA injected currents with continuous 4σ cut in the upgraded configuration leaving net 1.8, 3.5 and 5.3 mA currents respectively. Modelled with10^6 macroparticles. 73
4.20 Upgraded set-up 1.9 mA case applied to 6-turn 4σ cut with injected 2 mA $5 \cdot 10^4$ particles. X , y and z planes are exceptionally well matched. 75
4.21 Upgraded set-up 2.9 mA case applied to 6-turn 4σ cut with injected 3 mA $5 \cdot 10^4$ particles. X , y and z planes are exceptionally well matched leading to near-gaussian distribution as profile parameter in all planes is close to unity. 76
4.22 Upgraded set-up 3.8 mA case applied to 6-turn 4σ cut with injected 4 mA $5 \cdot 10^4$ particles. X , y and z planes are exceptionally well matched. Near-gaussian distribution as profile parameter in all planes is close to unity. 77
4.23 Upgraded set-up 5.0 mA case. 6-turn 4σ cut with $5 \cdot 10^4$ macro-particles. 78
4.24 Upgraded set-up 5.8 mA case applied to 6-turn 4σ cut with injected 6 mA $5 \cdot 10^4$ particles. 79

5.1 Top view on the modelled collimators in the central region. Green colour marks horizontal and yellow vertical collimators. 82
5.2 Diagnostic devices in Injector II with marked predicted last turn orbit and corresponding energies and radii [1]. 84
5.3 Horizontal halo parameter for 10^5 and 10^6 particle distributions. We observe steady growth of this parameter which is consistent with the configuration space plots. 85
5.4 An example of progression of the distribution in the configuration space passed through collimators and accelerated to 72 MeV. Despite significant distribution deformations due to large cuts, the tails “wrap” around the spiralling centre of the distribution leading to formation of a stable core with halo around. 85
5.5 Central region of Injector II with highlighted collimators. Vertical ones are marked in yellow and horizontal in orange [1]. 87

5.6 Current measured on the collimator leaves in Injector II. These readings vary with each commissioning. Up to 5% discrepancy in measurement can be observed due to equipment limitations and secondary electron emission (SEE). 89
5.7 Current measured on the collimator leaves in Injector II compared to a simulated 2 mA current. Measured current (grey) shown with variation over a whole day with 5% discrepancy. Main limitation in better matching is the small number of macroparticles. Up to 5% discrepancy in measurement can be be observed, due to equipment limitations and secondary electron emission (SEE) [4]. 89
5.8 Simulated current scanned from 1.8 to 4 mA. 90
5.9 Positions of measured and simulated radial intensity peaks of Injector II. The range of measured peak locations is marked in grey, the simulated peaks matched to the lower bound are shown in red and those matched to the higher bound in blue. 92
5.10 Positions of measured and simulated radial intensity peaks of Injector II in the production configuration. The range of measured peak locations is marked in grey, the simulated peaks matched to the lower bound are shown in red and those matched to the higher bound. The peak positions of multi particle space charge run are in green. 92
5.11 Visualisation of good solutions of the peak matching python script. *Phi*, *pr*, *volt*, *r* and *ekin* correspond respectively to RF phase, radial momentum, voltage offset, start radius and kinetic energy. $Pk1-7$ refer to deviation of peak positions from measured values and *ssqr* is the least squared value. Blue lines indicate possible good solutions with minimum *ssqr*, the remaining solutions are marked in green. 93
5.12 Positions of radial intensity peaks measured and simulated in Injector II in the upgraded configuration. The range of peak locations measured is marked in grey, the simulated peaks matched to the lower bound are shown in red and those matched to the higher bound in blue. This is more an exercise, the goal is to match only the last turn. 96

6.1 Upgraded set-up (bold) compared to production set-up at 2 mA current. Continuous 4σ cut model with 10^6 particles. 98
6.2 Upgraded set-up (bold) compared to production set-up at 2 mA case. 6-turn 4σ cut with $5 \cdot 10^4$ particles. 99

6.3 Production set-up with collimators at 1.8, 2.2, 3.2, 4.0 and 4.7 mA modelled with $5 \cdot 10^4$ macroparticles over 82 turns comparison. 100
6.4 Mid-plane of 2.2 mA bunch at 71.9 MeV, showing a large tail. 100
6.5 Production set-up with collimators at 2.2 mA modelled with $5 \cdot 10^4$ macroparticles over 82 turns. 102
6.6 Halo particles outside 5σ 2.2 mA and $5 \cdot 10^4$ macroparticles. The current outside the region reaches 0.025 mA. Particles outside 5σ are tagged in the last step, traced back to the beginning (red) and then compared to the total halo outside the cut (grey). 103
6.7 Production set-up with collimators at 3.2 mA and $5 \cdot 10^4$ macroparticles modelled over 82 turns. The longitudinal tail is specially visible in (e) in the last 20 turns where it eventually couples to the radial plane increasing the RMSx thus full beam extent (f). 104
6.8 Production set-up with collimators at 2.3 mA and 10^5 macroparticles modelled over 82 turns. RMSx, y and z (a) remain steady despite the long tail. 105
6.9 Halo particles outside 5σ at 2.3 mA current modelled with 10^5 macroparticles (physical collimator model). The amount of charge in this region is of order of 10^{-3}. 106
6.10 Production set-up with collimators at 3.1 mA modelled with 10^5 macroparticles over 82 turns. For all intensities RMSx and y remains comparable (a). Large longitudinal tail is formed in (d) and later coupled to form radial halo (e). 107
6.11 Halo particles outside 5σ region at 3.1 mA current modelled with 10^5 macroparticles. 108
6.12 Production set-up with collimators. The current outside 5σ in x and y planes at 3.1 mA with 10^5 macroparticles over the last turn. 108
6.13 Production set-up with collimators at 3.1 mA with 10^5 macroparticles over the last turn. 109
6.14 Beam size of the production set-up with collimators at 0.5, 2.3 and 3.1 mA modelled with 10^5 macroparticles over 82 turns. 109
6.15 Comparison between the models with additional 6-turn cut simulation. 111

6.16 Beam extent horizontal x and longitudinal y. Collimator model comparison of the number of macroparticles for around 2 mA. This variation is due to the need to readjust collimators every time the number of macroparticles changes, here only KIP2 has been moved. 111
6.17 RMS x and y. Collimator model comparison of the number of macroparticles at 2 mA beam current. This variation is due to the need to readjust collimators every time the number of macroparticles changes. Here only KIP2 is moved. 112
6.18 Comparison between approximated 6-turn 4σ cut models and the physical collimator model at 2 mA intensity. 112
6.19 Current outside 5σ per degree over first 7 turns where the collimators are present. Each step is a degree. We can see that final halo is never fully visible as these are phase tails. 114
6.20 Current outside 5σ in x and y. First 7 turns where the collimators cut. Significantly improved results of simulations with shifted KIP4 are shown in bold. 115
6.21 Comparison of halo outside 5σ over the full acceleration with halo after the KIP4 shift. The halo is 5 times smaller. Modelled with $5 \cdot 10^4$ macroparticles. 115
6.22 Profile parameter h for original set-up and after shifting KIP4 (bold). . 116
6.23 Parameters after fixing the KIP4 collimator (in bold) compared to original KIP4 position. Improved model is marked in bold. The major change is observed in the longitudinal direction with significantly decreased RMSy, the extent remains similar, due to a few particles that were not cleaned. 116
6.24 Mid-plane of the distribution at different energies simulated with $5 \cdot 10^4$ (first two columns). The tail that is seen in (e) and after removing (f). In the first case it remains stationary. 117
6.25 Comparison of RMS beam size in 3 planes in accelerating (bold) and decelerating operation. 118
6.26 Comparison of emittance in 3 planes in accelerating (bold) and decelerating operation. 119
6.27 Comparison of profile parameter h in 3 planes in accelerating (bold) and decelerating operation. 119

6.28 Comparison of radial and longitudinal full beam extent with energy spread of accelerating (bold) and decelerating operation. 120
6.29 Bunch mid-plane after 61 turns. Blue colour marks 3rd harmonic cavity set to accelerating mode, red is the original decelerating operation. 120
6.30 Orbit patterns of Injector II at various intensities. We observe "clustering" of orbits at higher intensities, where trim coils are used to manipulate final orbits. 122
6.31 RIZ1 probe real-space measurement for 0.5 mA current. The top histogram shows 1D longitudinal projection and bottom right plot, the 1D radial projection of the bunch. Halo is large, however the measuring equipment is not sensitive enough to adequately quantify it. 123
6.32 Variation of 1σ RMS beam size in the last turn for simulated 2-4.5 mA measured by RIZ1 probe (dash line). Beam is extracted after SM3. Spikes in 4.5 mA beam size indicate the field fringe having an imbalancing effect at higher intensities. 124
6.33 Measurements compared to 3rd and 4th power scaling. 125
6.34 Log plot of measurements compared to 3rd power scaling law and new suggested scaling. 125
6.35 6-turn sigma and physical collimator model simulation results compared to measurements and new suggested scaling. 126
6.36 6-turn 4σ beamsize and both 3rd and 4th power fits that appear to be equivalent. 127
6.37 Beam size evolution with intensity of production configuration of 6-turn 4σ and physical collimator models compared to measurements. Added uncertainties on the simulated beam size based statistical fluctuations of multivariate random distribution. 128
6.38 Plot of beam size evolution with intensity of the upgraded 6-turn 4σ model with its fits. 129

A.1 Production set-up 2 mA case. Continuous 4σ cut with 10^6 macro-particles. 143
A.2 Production set-up 4 mA case. Continuous 4σ with 10^6 macro-particles. 144
A.3 Production set-up 6mA case. Continuous 4σ with 10^6 macro-particles. 145
A.4 Production set-up 6 mA case. Continuous 4σ cut with $5 \cdot 10^4$ macro-particles. 146
A.5 Production set-up 1.0 mA case. 6-turn 4σ cut with $5 \cdot 10^4$ macro-particles. 147

A.6 Production set-up 2.0 mA case. 6-turn 4σ cut with $5 \cdot 10^4$ macro-particles. 148
A.7 Production set-up 3.5 mA case. 6-turn 4σ cut with $5 \cdot 10^4$ macro-particles. 149
A.8 Production set-up 4.5 mA case. 6-turn 4σ cut with $5 \cdot 10^4$ macro-particles. 150
A.9 Production set-up 5.0 mA case. 6-turn 4σ cut with $5 \cdot 10^4$ macro-particles. 151
A.10 Production set-up 6.0 mA case. 6-turn 4σ cut with $5 \cdot 10^4$ macro-particles. 152
A.11 Production set-up 10.0 mA case. 6-turn 4σ cut with $5 \cdot 10^4$ macro-particles. 153
A.12 Production set-up with collimators 1.8 mA and $5 \cdot 10^4$ macro particles over 82 turns. 154
A.13 Halo particles outside 5σ at 1.8 mA modelled with $5 \cdot 10^4$ macroparticles. 155
A.14 Production set-up with collimators 4.0 mA and $5 \cdot 10^4$ macro particles over 82 turns. 156
A.15 Halo particles outside 5σ at 4.0 mA modelled with $5 \cdot 10^4$ macroparticles. 157
A.16 Production set-up with collimators 4.66 mA and $5 \cdot 10^4$ macro particles over 82 turns. 158
A.17 Halo particles outside 5σ at 4.66 mA modelled with $5 \cdot 10^4$ macroparticles. 159
A.18 Production set-up with physical collimators 0.5 mA case with and 10^5 macro-particles 160
A.19 Current outside 5σ in x and y for 0.5 mA with 10^5 macro-particles. . 161
A.20 Production set-up with collimators 2.3 mA with 10^5 macro-particles. . 162
A.21 Current outside 5σ in x and y at 2.3 mA with 10^5 macro-particles. . . 163
A.22 Production set-up with collimators at 2.3 mA with 10^6 macro-particles. 164
A.23 Current outside 5σ in x and y at 2.3 mA with 10^6 macro-particles. . . 165
A.24 Halo particles outside 5σ at 3.2 mA modelled with $5 \cdot 10^4$. The amount of halo found in the last step traced back through turns remains unchanged. 165
A.25 Halo particles outside 5σ at 0.5 mA with minimal 0.005 mA outside 5σ region modelled with 10^5 macroparticles. 166
A.26 Mid-plane of the distribution at different energies of the KIP4 collimator correction (FIX) simulated with $5 \cdot 10^4$ (first two columns) and 10^5particles (last two columns). The tail that appears at (i) and after removing (j). In the first case it remains stationary. 167
A.27 Selection of extracted collimator currents in Injector II. 168

A.28 Simulated current read on collimators for 10^5 macro-particles. 168
A.29 Simulated current read on collimators for $5 \cdot 10^4$, 10^5 and 10^6macro-particles at 2mA. Only KIP2 has been moved, discrepancies noticeable in the last collimators. 169
A.30 Simulated current on collimators for selected intensities. 169

Declaration

i The author of this thesis (including any appendices and/or schedules to this thesis) owns any copyright in it (the "Copyright") and s/he has given The University of Huddersfield the right to use such Copyright for any administrative, promotional, educational and/or teaching purposes.

ii Copies of this thesis, either in full or in extracts, may be made only in accordance with the regulations of the University Library. Details of these regulations may be obtained from the Librarian. This page must form part of any such copies made.

iii The ownership of any patents, designs, trade marks and any and all other intellectual property rights except for the Copyright (the "Intellectual Property Rights") and any reproductions of copyright works, for example graphs and tables ("Reproductions"), which may be described in this thesis, may not be owned by the author and may be owned by third parties. Such Intellectual Property Rights and Reproductions cannot and must not be made available for use without the prior written permission of the owner(s) of the relevant Intellectual Property Rights and/or Reproductions.

Abstract

We have developed a precise beam dynamics model of the PSI Injector II, a high intensity separate-sector isochronous cyclotron operating at 2.2 mA current. A particle distribution with an intensity of 9.5 mA (DC) is injected into the central region and shaped by a sophisticated collimator system. This defines the initial condition for the subsequent formation of a round stationary bunch. The intensity limits are estimated based on the developed models, additionally supported by fitted scaling laws and measurements. In this research we consider two configurations: *production* and *upgraded* (adding two new cavities). The model is based on the OPAL (Object Oriented Parallel Accelerator Library) simulation code, a tool for charged-particle optics calculations in large accelerator structures and beam lines, including 3D space charge.

Even though Injector II has been successfully operating for years, we do not know if the current production configuration is the best possible. Since we would like to extract as much current as possible with minimal losses, detailed simulations are needed to estimate those limits. This gives us possibility to look into the operation after the upgrade.

This is the first attempt to model Injector II using powerful computing, allowing multi-particle space charge simulations. We have been able to perform more detailed analysis of the bunch parameters and halo development than any previous study. Also optimisation techniques enable better matching of the simulation set-up with Injector II parameters and measurements.

We have found that the production configuration current scales to the power of four with the beam size, setting the limit to approximately 3 mA. Further analysis of the upgraded configuration suggests that intensities up to 5 mA could be produced with an adjusted collimation scheme.

Acknowledgements

First of all, I would like to express my special appreciation and thanks to my advisor, Prof Roger Barlow, for being such an amazing mentor for me. Thank you for all the motivation, continuous support and immense knowledge and time that you always were happy to share during all stages of my PhD. At the same time, I would like to thank my PSI co-supervisor, Dr Andreas Adelmann, for expertly guiding me during my PhD. Your enthusiasm, not only for accelerator physics, tremendously helped me keep engaged with my research. I would like to thank you both for encouraging my research and allowing me to grow as a research scientist. Thank you for your invaluable advice on research, support and patience throughout the years.

Many thanks to Dr Christian Baumgarten for your advice and expertise during our weekly meetings.

Many thanks to all my dearest friends I have met during my PhD studies. Thank you Naomi, Simon, Louise, Vasim, Jenny, Ishkhan, Cigdem, Belen and Zeina for always being there for me! I would also like to thank my colleagues and officemates from Huddersfield and PSI for being so welcoming and making those study years enjoyable.

A special thanks to my closest family for their forever unconditional support. I will be always grateful to my mother and father for all the sacrifices that you have made to help me succeed. Thanks to your encouragement and prayers I have managed to come this far.

I would like to express my gratitude to EPSRC and Paul Scherrer Institut as this research would not have been possible without their financial assistance.

Chapter 1

Introduction

In recent years we have observed a growing demand for high intensity beams in both scientific and industrial fields. Here cyclotrons play the leading role, despite being limited by space charge induced losses, and provide the most space and cost-efficient solution. This highlights the need for better understanding of space charge effects in high intensity isochronous cyclotrons, such as the Injector II at PSI. This separate-sector machine exhibits a special feature, where due to space charge forces combined with radial and longitudinal coupled motion, a stationary compact beam is developed within the first several turns of the injector and remains quasi-stationary until extraction. There is currently no self-consistent theory to match bunched beams with non-linear space charge in cyclotrons. Therefore, to model these effects we rely on numerical methods.

For this study we use a precise beam dynamics model based on the OPAL (Object oriented Parallel Accelerator Library) simulation code. OPAL is a tool for charged-particle optics calculations in large accelerator structures and beam lines, including 3D space charge [5].

Many attempts at theoretical estimations and validations with measurements have been made. However, to test the true limits of the operating machines, it is only in the recent years that computing power allows more detailed simulations, opening new possibilities for further research in this field.

1.1 Motivation for the research

The High Intensity Proton Accelerator complex, HIPA, is located in Switzerland at the Paul Scherrer Institut (PSI). Its Ring cyclotron is one of the most powerful high intensity cyclotrons in the world producing a 1.3 MW beam. Throughout the years

efforts have been made to improve the efficiency and intensity of the beam delivered to a number of experimental halls. The plan to upgrade the facility to produce a 3 mA beam will make it an attractive option to industrial and scientific applications of high intensity proton beams.

HIPA consists of a chain of pre-accelerators and the main accelerator, called the Ring cyclotron. Figure 1.1 shows the overview of the HIPA accelerators. The beam leaving a proton ion source is pre-accelerated to 870 keV by a Ckockroft-Walton and further accelerated to 590 MeV by two isochronous accelerators: Injector II and the Ring cyclotron. The beam is produced at 50.6 MHz in continuous wave (CW) mode and delivered to targets to produce pions, muons, and neutrons by spallation reactions. Top research areas at the PSI accelerator facility include neutron scattering, particle physics experiments and muon spectroscopy.

Figure 1.1: High Intensity Proton Accelerator Facility. Starting from the left: Cockcroft-Walton generator, the Acceleration Tube, Injector II, transfer line and Ring cyclotron [2].

Activation in the accelerator is induced by lost particles interacting with the beam line and machine components. Generated radiation can be dangerous to personnel especially during shutdown periods, therefore keeping these doses at absolute minimum is important. Currently HIPA losses are minimal and of order 10^{-4}. Highest beam loss is observed at the extraction beam line, where the dose can reach 10 mSv/h, with average doses around the Ring cyclotron of 1 mSv/h [3].

The facility is equipped with a very fast interlock system, connected to hundreds of ionisation chambers, collimators and aperture foils controlling correct loss pattern in the accelerators. The rapid system response is of the order of 100 μs, to counter the effects of a miss-steered full beam that could melt components in 10 ms.

Both accelerators are separate-sector type machines, with constant revolution frequency and varying azimuthal field. This is used to compensate for the loss of vertical focusing, that would occur in a homogenous bending field. Additionally, the Ring cyclotron has spiral-shaped magnets.

A single sector or module consists of a magnet and an RF accelerating cavity. The

combination of such modules in a ring enables construction of larger accelerators, thus allowing cleaner low-loss extraction.

The beam is extracted by an electrostatic septum that deflects the last orbit towards the extraction line. Some of the highly energetic beam halo particles can scatter off the electrode material, thus causing the extraction procedure to be a major loss contributor. It is therefore vital to keep a large orbit separation to allow clean extraction, however, radius increment per turn typically decreases with increasing energy making it a rather difficult task.

A better understanding of space charge effects in high-intensity low-energy machines such as Injector II is now of great interest. Understanding space charge effects and halo formation through detailed numerical modelling could give clues on how one could maximise the extracted current in alternative ways.

Some efforts have been made in predicting such losses with simplified models, such as the "sector model" developed at PSI by W. Joho [6]. The model predicts losses scaling with third power of the turn number in a cyclotron. Based on this finding an obvious approach to minimise losses is to increase the acceleration gap voltage or injection energy. This way the number of turns required to accelerate the beam to desired energies can be decreased [3].

Injector II, shown in Figure 1.2, is a pre-accelerator delivering a high intensity 72 MeV proton beam into the 590 MeV Ring cyclotron. The cyclotron is composed of four sector magnets and four cavities with an injection energy of 870 keV, normalised emittance of 2π mm$\times$mrad and DC current of 11 mA [3].

Isochronous cyclotrons lack longitudinal focusing. This allows space charge forces to contribute to the generation of longitudinal energy spread that is eventually transformed into transverse beam tails counteracting achieved turn separation. However, in Injector II a round beam that is strongly coupled in radial-longitudinal planes is developed and remains stable until extraction [7]. Numerical methods are required to model these effects. The prediction of the performance of a high power accelerator is a difficult task since the relevant factors are not accessible by usual beam dynamics calculations. The current limit is given by the losses due to tails and halo that are several orders of magnitude smaller than the beam itself. A reliable beam simulation requires tracking of millions of particles, a good knowledge of the initial conditions, the consideration of higher order effects, and detailed beam diagnostics for comparison and validation of the calculations.

In the presented study we estimate true intensity limits of Injector II and predict

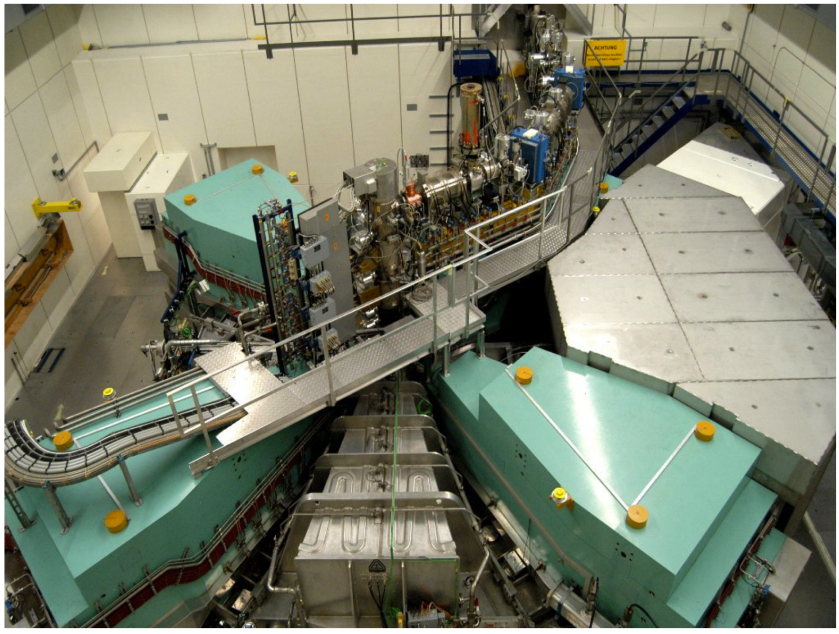

Figure 1.2: PSI Injector II [2].

operation of the cyclotron after the upgrade based on our 3D model and measurements.

1.2 Injector II and PSI High Intensity Proton Accelerator facility

Injector II is one of the accelerators in HIPA chain (Figure 1.3) delivering a 590 MeV (1.3 MW) beam to the muon-, pion- and neutron production facilities SINQ (Swiss Spallation Neutron Source), UCN (Ultra Cold Neutron Source) and isotope production (IP2).

Protons are produced in a microwave powered 60 keV ion source that is placed on the dome raising the energy to 810 keV. The beam is then pre-accelerated to 870 keV in the Cockcroft-Walton generator and transported through a conventional beam line were the beam quality deteriorates due to space charge forces. A double-gap harmonic buncher has been installed in the 870 keV transfer line drastically improving the capture efficiency of Injector II [8].

To inject the beam into the central region of the cyclotron, the beam has to be bent down from the top with one 90° magnet (See Figure 1.2). Second 90° magnet places the beam into the horizontal plane at 360 mm radius that it is further accelerated to

reach energies of approximately 72 MeV. Following the extraction, the beam is debunched in the IW2 transfer line and accelerated to its final energy of 590 MeV at the Ring cyclotron.

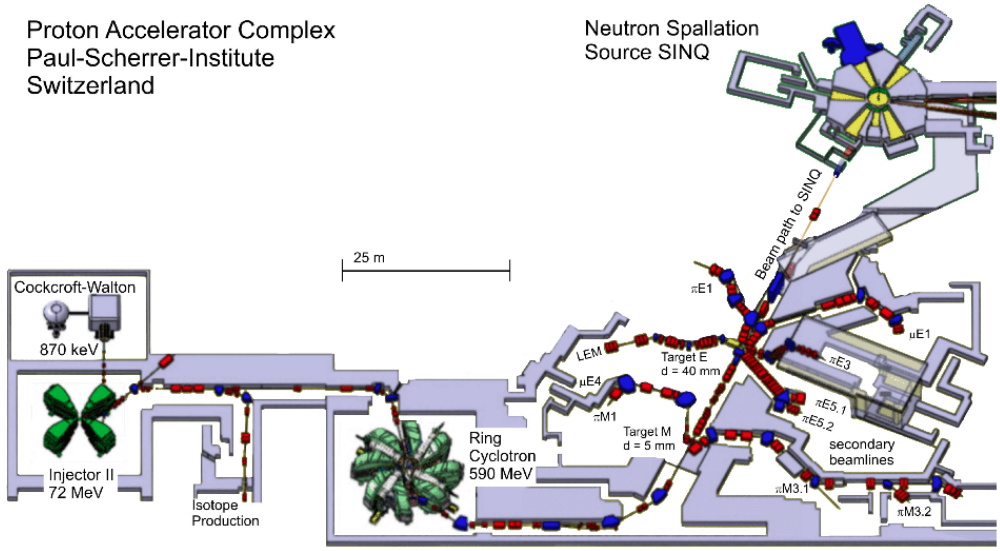

Figure 1.3: Overview of the High Intensity Proton Accelerator Facility [3].

Injector II (Figure 1.2) located in the intermediate accelerating stage is a four-sector isochronous cyclotron operating at 10th harmonic with frequency of 50.63 MHz. It operates with the same RF-frequency as the Ring cyclotron, however at a higher harmonic mode. A lower magnetic field has been introduced to increase the turn separation, reaching 20 mm at extraction corresponding to about 6σ of the beam profile. Table 1.1 shows some basic parameters of Injector II.

The machine accelerates and extracts up to 2.2 mA with minimal losses in approximately 81 turns. The RF system consists of two double-gap acceleration cavities at 50 MHz and two single-gap 3rd harmonic cavities at 150 MHz, originally used as flat-topping cavities. The idea of a 3rd harmonic flat-top cavity is to have the accelerating field peak located in such way that particles which are too far ahead are slowed down and those too slow get an accelerating kick. In other words, the net accelerating peak is flattened allowing longer bunch acceptance. However, the bunches in Injector II are short enough length allowing operation in the acceleration mode. This feature of very short bunches allows exchange of the flat-top cavities for single-gap resonators at 400 kVp (peak voltage) as a part of a planned upgrade to achieve 3 mA beam current. Injector II is expected to accelerate in 60 turns, significantly increasing final turn separation, and therefore extracted current.

Table 1.1: Injector II parameters [1].

Cyclotron parameters		
Sector magnets	4	
Angle of sector magnets	28°	
Flux densty	10	kG
Gap width	35	mm
Injection radius (between magnets)	360	mm
Extraction radius (between magnets)	3000	mm
Extraction radius (inside magnets)	3750	mm
Betatron frequency horizontal	1.2-1.35	ν_r
Betatron frequency vertical	1.25-1.6	ν_z
Cyclotron frequency	5.063	MHz
Harmonic number	10	

A 12 mA DC proton beam is delivered from the ion source followed by over 1 mA loss on the collimators along the 870 keV injection beam line. The beam is bunched before being coupled to the central region of Injector II shown in Figure 1.4. The phase selection is done on the 1st turn by KIP1 and KIP2 collimators, cutting away 2.4 and 4.8 mA respectively for 2.2 mA standard operation. Vertical and radial cleaning is done with several collimators within the first 5 turns at energies from 870 KeV to 3.7 MeV respectively leading to excellent beam properties. Only about 50% of the beam is accepted through the collimation system in the 1st turn [9].

As Injector II is a low-energy high-intensity machine, space charge effects are dominate, particularly in the central region. Generally, this adds to the beam quality deterioration, however, Injector II exhibits a special feature. It was discovered that an initially elongated bunch becomes round in the mid-plane (radial-longitudinal) and remains stationary until extraction. Strong transverse and longitudinal coupling creates a“vortex” inside the bunch with spiralling tails that wrap around the compact core. These tails are removed with collimators in the first turns. This effect is inversely proportional to the momentum [10].

Extrapolating the V^3 scaling law [6] for Injector II, an energy gain of about 1.2 MeV per turn is needed to accelerate a 3 mA beam in 60 turns. Replacement of two 3rd harmonic cavities for two single-gap 400 kVp cavities as a part of planned upgrade of the HIPA facility will enable production of higher intensity beams [11]. However, the question remains whether that is the true intensity limit of Injector II.

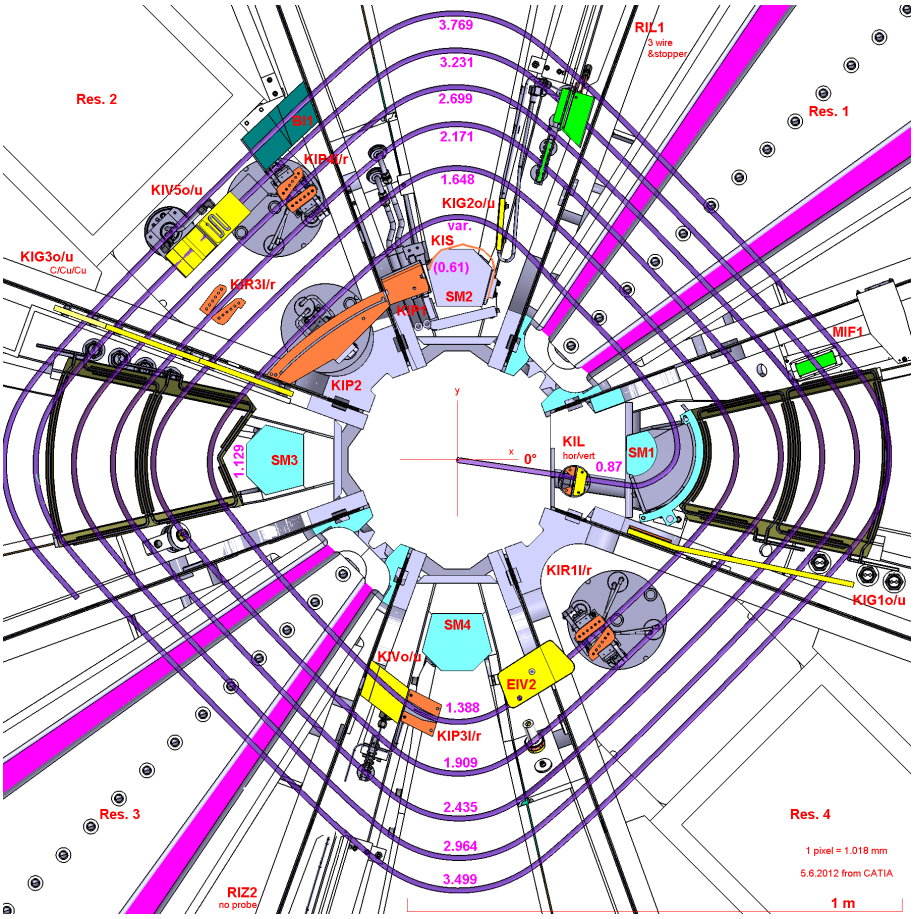

Figure 1.4: Central region of Injector II with collimators. Starting from the centre KIL, KIS, KIP2, KIG3, KIV, KIP3, KIR1, KIG1, KIR3 and KIP4 [1].

1.3 Research literature review

This section summarises the scientific efforts made over several decades to better understand space charge effects in isochronous accelerators. The absence of longitudinal focusing in isochronous machines enables space charge to contribute to additional energy spread. M.M. Gordon conducted detailed analysis of this important effect in 1969 [12]. His analytical model, taking into the account continuous radial beam intensities (non-separated turns), predicted space charge induced energy spread. Separate turns were taken into the account in work by W. Joho in the early 1980's, in his "sector model", that was an extension of Gordon's work. Joho treats circulating protons as a filled "piece of cake"-like shape with azimuthal extensions $\Delta\theta$, describing induced energy spread. Both Gordon's and Joho's models failed, when the "vortex effect" was seen in PSI Injector II that can keep the distribution stationary. Nonetheless, Joho found

that the space charge induced energy spread was proportional to the beam current and to the square of the number of turns, N, thus predicting that the intensity limit from longitudinal space charge scales with cubed accelerating voltage [6]. In 1983 Chasman and Baltz [13] studied space charge in heavy ion cyclotron using their simplified numerical model showing that "the maximum radial displacement due to space charge and the period of oscillation are independent of the radius of the orbit".

Simulations performed by S. Adams as early as 1985, show longitudinal space charge effects contributing to the rotation of space charge induced halo formation [14]. His particle-in-cell code simulations of Injector II based on the "disks" model from 1981, showed that the "spiralling instabilities" in isochronous cyclotrons are especially important at low energies [15]. However, the approximations made in this early model left significant uncertainty in those results.

Separate-sector cyclotrons are strongly coupled in the transverse-longitudinal plane. Longitudinal energy spread transfers to the radial plane having an effect of increasing radial beam size, thus limiting the extracted current. In the PhD study of Kleeven from 1988 [16] it was concluded that if a bunch charge distribution is symmetric it will remain stationary for any given intensity, moreover, a non-symmetric distribution would keep evolving until it reaches its equilibrium state in the form of a symmetric stationary bunch. For this to happen the bunches have to be short enough. If this is not the case, recent studies show so called "beam break-up" occurring under the space charge forces [17]. Another interesting attempt to model such effects is the use of fluid dynamics on the behaviour of isolated vortices as found in isochronous cyclotrons. This work carried out by A.J. Cerfon [18] was also able to reproduce the beam breakdown presented in Pozdeyev's study.

Computing technology has been developing rapidly in recent years. New codes and methods have been introduced allowing precise simulations of physics in isochronous machines. Detailed analysis of space charge effects, such as halo, bunch-bunch effects etc require significant computing power/CPU and sophisticated numerical methods. At PSI itself, years after work done by Joho and Adam *et al* [14, 6], a new code, OPAL, has been developed by A. Adelmann *et al* [5]. This full 6D parallel PIC (Particle-in-cell) code, also used in this thesis, was already successfully implemented in modelling of the PSI Ring cyclotron trim coil influence and DIC (DAEδALUS Injector Cyclotron) injector cyclotron for the DAEδALUS project (Decay-at-Rest Experiment for δcp studies At the Laboratory for Underground Science) [19, 20, 21]. Trim coils improving the radial intensity profile for cleaner extraction were modelled and matched

the measured data well, the influence of neighbouring bunches was also investigated. The findings suggest a positive influence of these effects, where bunches in fact repel each other, improving turn separation. In this work, beside a full 6D space charge modelling of Injector II, we also present optimising capabilities of this code combined with PSI-developed *optPilot* [22].

Another important topic is analytical estimation of intensity limits in such machines. Here I refer to R. Baartman's (TRIUMF) proceedings of Cyclotrons 2013 conference, where he estimates intensity limits for the Ring cyclotron and Injector II based on Kleeven's work. The model of a 3D charge distribution under space charge is based on the work of Bertrand and Ricaud [23]. This analytical model applies to short bunches that undergo the vortex effect. Kleeven, based on Sacherers technique [24], simplifies 21 first order envelope equations into two second order envelope equations coupled only by space charge force influence on the beam size [16].The intensity limits estimated by this model are underestimated as here zero emittance is assumed and other factors such as tuning of betatron oscillations to increase the final turn separation are not included. However, it is a good indication for scaling of parameters and confirmation of the cubic scaling law derived by Joho. To generate strongly coupled distributions for cyclotron modelling C. Baumgarten [25, 26] uses a symplectic approach. His model generating matched beams was originally developed for higher energies in Ring cyclotron and has been optimised by the author for lower energy high intensity beams. This model, based on linear space charge, will be discussed in more detail in the following sections.

When talking about intensity limits, another important aspect of high intensity machines is detailed halo analysis. Most common practice is the use of kurtosis-like parameter h, measuring 1D spacial projections of the distribution proposed by Wangler and Crandall [27]. This basic approach gives a good insight into the observable halo formation in real space. However, to have an idea of its development in phase-space, C.K. Allen *et al* [28, 29] proposes introduction of a 2D parameter based on the kinematic invariants that vary only if nonlinearities are present. Both parameters are equal in case of elliptically symmetric beam, which is observed in Injector II, hence 1D projections are considered to be sufficient during the initial analysis. We shall see if this is the case in the later chapters.

1.4 Chapter summary

In this thesis we introduce a beam dynamics model including 3D space charge model used to estimate the intensity limits of a high current separate-sector cyclotron, Injector II. Injector II is a part of the HIPA facility and has been working exceptionally well for over 40 years, beating its design limits on many occasions. Previously studied numerical models predict a limit of approx. 2 mA, however we already know that a successful extraction of 2.7 mA was achieved. These detailed simulations will allow the study of intensities that have not been possible up to this point.

Chapter 2

Theoretical background

This chapter covers theoretical background to the relevant beam dynamics physics in relation to separate-sector cyclotrons, looking into space charge effects and how it is possible that appropriate self-fields combined with strong radial and longitudinal coupling can lead to round matched beam formation. This makes selecting starting conditions such as radius, RF phase and azimuth together with charged particle distribution a non-trivial task that requires some optimisation. There are no self-consistent models for generating stationary matched beams such as those observed e.g. in Injector II. We will briefly describe a theoretical model developed by C. Baumgarten (PSI) [25] that was used to generate a distribution.

2.1 Cyclotron beam dynamics

Cyclotrons, among other circular accelerators, have become a basis for groundbreaking discoveries across just over 80 years of circular accelerator history. Starting with the palm-size Lawrence and Livingston cyclotron accelerator and ranging up to 27 km circumference Large Hadron Collider (LHC) [30]. Cyclotrons serve as an effective source of high-intensity beams. Maximum attainable energy in cyclotrons is limited to about 1 GeV, due to relativistic effects that technology cannot currently address. Cyclotrons are one of the most used accelerators for industrial purposes, such as ion implantation, medical application or isotope production. Thanks to their compactness and efficiency this technology has been taken outside of the research laboratories.

The bottom line of this technology is the electro-magnetic forces acting upon charged ions. The electric force is used to accelerate particles. The magnetic fields guide the beam. Starting with simple uniform magnetic field, B_z, a charged particle q

with mass m and azimuthal velocity v will travel on a circular trajectory of a radius r. When the inward magnetic Lorentz force $F = q(v \times B_z)$ is balanced by the opposite centrifugal force, its trajectory is in equilibrium tracing a so called static equilibrium orbit (SEO):

$$\frac{mv^2}{r} = qvB_z. \tag{2.1}$$

From this a magnetic rigidity is derived, which is a useful design parameter to describe the bending strength

$$B\rho = \frac{mv}{q} = \frac{p}{q}, \tag{2.2}$$

where p is the momentum and ρ is the bending radius. The revolution frequency of the ions, $\omega = \frac{v}{r} = \frac{qB_z}{m}$ (Larmor frequency), depends only on the charge to mass ratio of the particle $(\frac{q}{m})$ and the magnetic field for non-relativistic energies [31, 32]. This is valid for all circular accelerators in non-relativistic regime such as cyclotrons, storage rings, synchrotrons and FFAGs.

If there is an accelerating gap every half a turn; every time a particle crosses the gap it will receive an accelerating kick. Higher momentum ions deflect less under the magnetic field and spiral outwards, gaining energy with every gap crossing as seen in Figure 2.1.

There are two types of electric fields used for acceleration: the DC acceleration column used in low energy accelerators such as the Cockcroft-Walton or Van de Graaff, and the RF cavity providing longitudinal electric field at a chosen frequency from a few hundreds kHz to GHz.

For a particle with charge q, the energy gain/loss per passage through a cavity gap is:

$$\Delta E = q\Delta V, \tag{2.3}$$

where $\Delta V = V_0 sin(\omega_{rf} t + \phi)$ is the effective gap voltage, ω_{rf} is the RF frequency, V_0 is the effective peak accelerating voltage, and ϕ is the phase angle. Low frequency RF cavities are usually used to accelerate hadron beams, and high frequency ones to accelerate electron beams [32].

Acceleration of charged particles via resonators and flat-topping cavities to high energies requires synchronisation and phase focusing. The synchronisation is achieved by matching the cavity frequency with particle velocity, and the phase focusing is

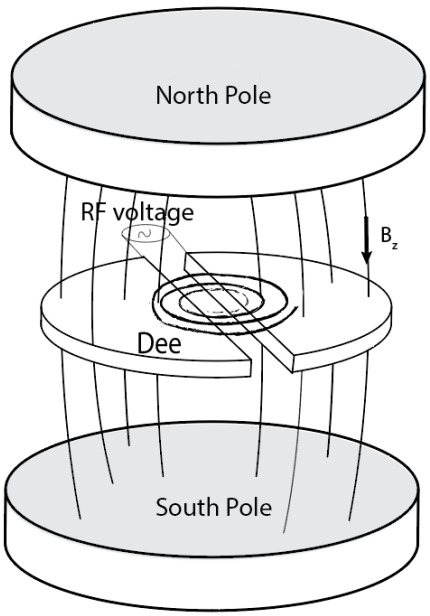

Figure 2.1: Principle of a classic cyclotron acceleration.

achieved by choosing a proper phase angle between the RF wave and the beam bunch.

The ion gets an energy gain equal to the number of individual passages through the gap crossing. The kinetic energy E_k can be calculated from the equation:

$$E_k = \frac{q^2 B^2 r^2}{2m} = \frac{m\omega^2 r^2}{2}. \tag{2.4}$$

Here, we can see that maximum kinetic energy does not depend on the accelerating voltage but is determined by the type of ion, maximum radius R of the cyclotron and the magnetic field. With a higher electric field the particle simply takes fewer turns to accelerate still reaching its maximum energy at the extraction radius R.

Accelerated particles approaching the speed of light, as dictated by special relativity, not only gain energy but also appear to gain mass, in fact this is the increasing relativistic factor γ . In a classic cyclotron with a homogenous magnetic field the relativistic mass increase limits the maximum attainable energy and in Injector II is of order of 1.07.

Up to this point angular momentum was considered independent of the energy of the particle, but with relativistic effects this is no longer the case. Angular velocity decreases with increasing mass so that the particle arrives later at the gap with each turn. It reaches the point where it arrives at the decelerating potential of the dee, the point where the physical energy limit is reached.

An obvious solution to this would be to increase the magnetic field with the radius to compensate for the mass increase, however, in a classic cyclotron, this would lead to orbit instabilities (lack of vertical focusing).

Accelerated particle beams tend to "disperse" in all directions due to self-fields, machine component errors and interactions with residual gas. Therefore, to keep the beam in a stable orbit appropriate focusing in both the horizontal and vertical planes is required. This is an important task in all kinds of accelerators. In cyclotrons, we can set the stability condition using the field index n defined as:

$$\left(\frac{dB_0}{B_0}\right) = -n\left(\frac{dr}{r}\right). \tag{2.5}$$

Field index is determined by adjusting the opening between the magnet poles outwardly to produce a horizontal field that varies with vertical displacement. This *weak focusing*, for a classic cyclotron, has to fall between $0 \leq n \leq 1$ and the following, inspired by thorough discussion in [33], explains why. Lets consider all three cases for $n < 0$, $n = 0$ and $n > 0$, as shown in Figure 2.2.

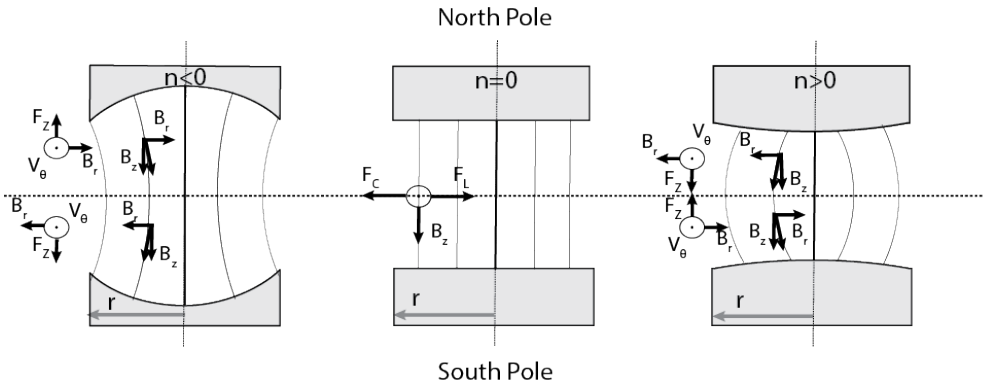

Figure 2.2: Principle of weak focusing for field index $n < 0$, $n = 0$ and $n > 0$.

When the vertical magnetic field is perpendicular to the orbit plane ($n = 0$), forces are balanced as long as we do not observe relativistic mass increase. This is also true for any field index in the mid-plane. As the magnetic field lines are bent, a radial magnetic component appears, yielding a vertical force, below and above the mid-plane. And so for a positive n, this force will be directed towards the stable orbit plane while the force for the negative n directed outwards will lead to vertical instabilities.

Radial stability is achieved for $n < 1$. To compensate for the relativistic mass increase, a negative field index has to be applied, to ensure increase of the magnetic field, and as we saw earlier, this cannot be achieved in the classic cyclotron.

2.2 Separate-sector isochronous cyclotrons

The increasing relativistic mass issue is overcome by the idea of an isochronous cyclotron, where magnetic field increases with radius. The isochronous condition means constant revolution time independent of energy, where RF frequency remains constant during acceleration. To satisfy this condition an average B field has to increase proportionally to the relativistic factor γ:

$$B_z(R) \sim \gamma(R). \tag{2.6}$$

As n has to be kept below zero, this inevitably leads to vertical instabilities for an azimuthally symmetric field. However, azimuthally varying magnetic fields can add stabilising vertical focusing. This property was discovered by Thomas in 1938 and gave rise to AVF (Azimuthally Varying Field) cyclotrons. Removing fragments from the magnet poles creates "hills" with a stronger magnetic field, and "valleys" where poles are further apart producing a weaker magnetic field. The beam is first defocused in the valley to then be focused in the hill, resembling the FODO cell principle. The Field $B_z(R)$ is averaged over the full orbit, which is no longer a circle as shown in Figure 2.3. Its shape will depend on the number of sectors in the cyclotron. A sector in a cyclotron consists of both a hill and a valley.

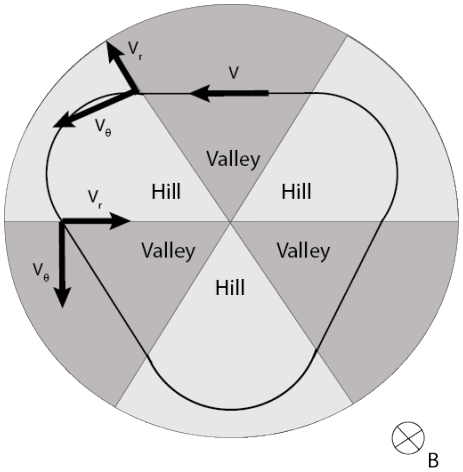

Figure 2.3: Equilibrium orbit of an isochronous AVF cyclotron, where v is the velocity of the particle with its radial (v_r) and azimuthal (v_θ) components.

The minimum required number of sectors is 3, as using 2 leads to resonance of horizontal focusing frequency [34]. Also too narrow sectors can lead to vertical overfocusing. When a beam is moving between the hill and valley, it will experience a

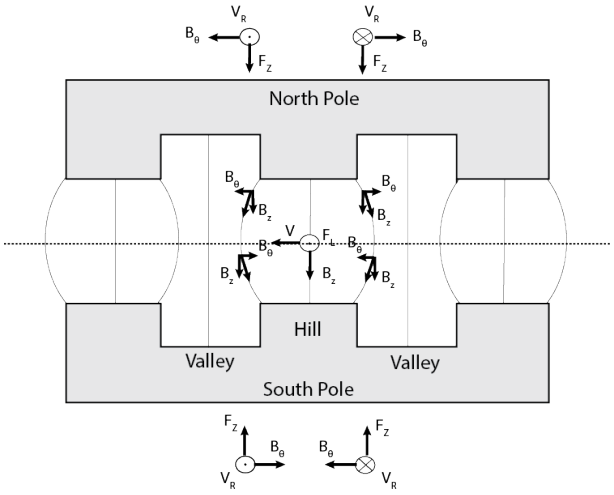

Figure 2.4: Axial focusing forces created at the edges of the hill.

vertical restoring force directed towards the mid-plane (Figure 2.3 and 2.4).

The next and most recent addition to the cyclotron family was the idea of separate magnetic sectors proposed by Willax in 1963 [31, 32]. It relays on the same principles used in the AVF design but with completely removed magnet iron in the valley, leading to almost zero magnetic field regions. It was first tested at PSI in the design of the Ring cyclotron commissioned in 1974 with the goal of 100 μA at 590 MeV and currently operating at 2.2 mA [10].

Now with relativistic considerations, we can write magnetic rigidity in the form of

$$B\rho = \frac{p}{e} = \beta\gamma\frac{m_0 c}{e}. \tag{2.7}$$

Orbit radius becomes

$$R = \frac{c}{\omega_c}\beta, \tag{2.8}$$

due to the isochronous condition, where $\omega_c = \frac{eB}{\gamma m_0}$. From this relation some useful scaling can be derived, and so:

$$R \propto \beta \rightarrow B\rho \propto p \propto \beta\gamma, \tag{2.9}$$

thus the magnetic field in an isochronous cyclotron scales with γ [35]. Radius increment per turn decreases with increasing energy as the revolution time $\tau = \frac{2\pi r}{\beta c}$ must stay constant. This makes the extraction more difficult at higher energies, however separate turn design combined with higher accelerating voltage can solve this issue to some

extent. Number of turns n_t needed to accelerate to kinetic energy E_k, can be found by

$$n_t = \frac{E_k}{E_{gain}} = \frac{E_0}{E_{gain}}(\gamma - 1), \tag{2.10}$$

and field index n is equal to $\gamma^2 - 1$, to satisfy the isochronicity condition [35]. E_0 is the rest energy and E_{gain} is the energy increase per turn.

If we want to accelerate particles continuously in harmonic operation, the RF cavity angular frequency ω_{rf} has to be equal to the revolution frequency of the injected particles, ω_c, times a number of bunches in one turn at an instance, called harmonic number h. This is expressed by

$$\omega_{rf} = \omega_c h. \tag{2.11}$$

The variation of magnetic field between the valleys and hills, called Thomas focusing, is described by flutter factor F:

$$F = \frac{\langle {B_z}^2 \rangle - \langle B_z \rangle^2}{\langle B_z \rangle^2}. \tag{2.12}$$

The major factor limiting the intensity in separate-sector machines are losses on the extraction electrode that is placed between last two turns. Accordingly, radial turn separation should be kept to a maximum. It can be found from the radius and turn number (Equations 2.10 and 2.8):

$$\frac{\mathrm{d}r}{\mathrm{d}n_t} = \frac{\gamma}{\gamma^2 - 1}\frac{r}{n+1}\frac{E_{gain}}{m_0 c^2} \tag{2.13}$$

or expressed with radial tune, ν_r:

$$\frac{\mathrm{d}r}{\mathrm{d}n_t} = \frac{\gamma}{\gamma - 1}\frac{rE_{gain}}{E_k/e}\frac{1}{\nu_r^2}\ [35]. \tag{2.14}$$

Therefore, to increase turn separation we either have to increase the radius of the accelerator or the energy gain. Also manipulation of the betatron oscillations can be used to increase the extraction turn separation, by simply shaping the field around the last turns. As an example, in Injector II the radial betatron oscillation (tune) ν_r is kept at 1.3 over the last several turns and in the Ring cyclotron it is decreased to maximise the turn separation. This also can be done to some extent by off-center injection.

The separate-sector design brings several additional advantages to the AVF cyclotron including the possibility of installing multiple resonators in-between the sectors

increasing the turn separation thus extracted intensity. Modular layout makes component production and installation much easier. However, this requires external injection i.e. pre-accelerator and detailed field shaping for focusing and isochronicity. These machines can accelerate in the continuous (CW) mode up to 1 GeV with high extraction efficiency up to 99.98 % as in PSI Ring cyclotron [35].

2.3 Tune diagrams & Accelerated and Static Equilibrium Orbit

In isochronous cyclotrons, for each energy, a closed orbit called Static Equilibrium Orbit (SEO) can be found with a circumference of $L = 2\pi R$ and a constant revolution frequency

$$\omega_c = \frac{q}{m}\frac{B_0(R)}{\gamma(R)}, \tag{2.15}$$

with

$$B_0(R) \equiv \frac{\int_L^0 B_z(s)ds}{L} \text{ [34]}. \tag{2.16}$$

The tune is the betatron oscillation frequency ν_r (radial) and ν_z (vertical) for different energies that is used to evaluate the focusing characteristics for a given magnetic field. Its value represents the number of particle oscillations in one turn. To determine the cyclotron tune in a model two particles are tracked; one on axis of a closed orbit and the other off-centred. In OPAL, the simulation tool of choice in this work, the tune values are obtained using spectral methods such as fast Fourier transform (FFT). The ν_r and ν_z tunes of Injector II are shown in Figure 2.5. In this calculation we have used measured mid-plane fields.

In a classical cyclotron we can obtain the betatron oscillation frequencies from equations of motion and first order expansion of the magnetic field, expressed with the previously discussed field index n [35]:

$$\nu_r = \frac{\omega_r}{\omega_c} = \sqrt{1-n} \tag{2.17}$$

$$\nu_z = \frac{\omega_z}{\omega_c} = \sqrt{n}, \tag{2.18}$$

and $\nu_r^2 + \nu_z^2 = 1$, where for stable focusing $0 < n < 1$.

Separate-sector cyclotron has vertical betatron frequency increased by the Thomas

focusing (Equation 2.12) to satisfy the isochrnonicity condition of $n < 0$:

$$\nu_z = \sqrt{n+F}, \tag{2.19}$$

and for spiral sector magnets with additional angle δ of the bending field it becomes:

$$\nu_z = -\sqrt{n+F(1+2\cdot tan^2\delta)}. \tag{2.20}$$

Sometimes, due to lattice imperfections or superimposition of oscillations, radial and vertical tunes couple causing resonant tunes e.g. $\nu_r = 2\nu_z$. In such cases betatron amplitude can be transferred into the vertical oscillations deteriorating the beam. In general, all integer values and other coupling resonances ($\nu_r + \nu_z = 2$, $\nu_r = \nu_z$ etc.) also must be avoided as they lead to beam perturbations. However, these resonant points can be passed quickly with fast acceleration. In the case of the Ring cyclotron coupling resonance $\nu_r = 2\nu_z$ was passed twice until correcting trim coils were introduced [3].

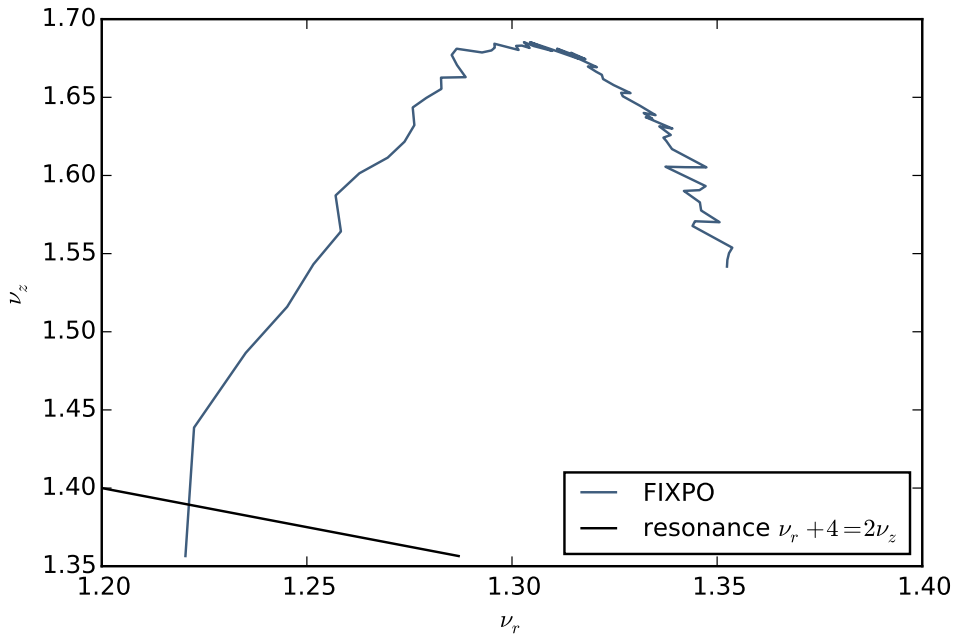

Figure 2.5: ν_r and $2\nu_z$ tunes of Injector II with marked $\nu_r + 4 = 2\nu_z$ resonance at around 2 MeV.

Accelerated Equilibrium Orbit (AEO) is shown in Figure 2.6. It can be described as the "ideal" path for an accelerated charged particle, where all the focusing forces are perfectly balanced. The AEO is used at the preliminary design phase of the cyclotron

and gives information about the fields of the cyclotron.

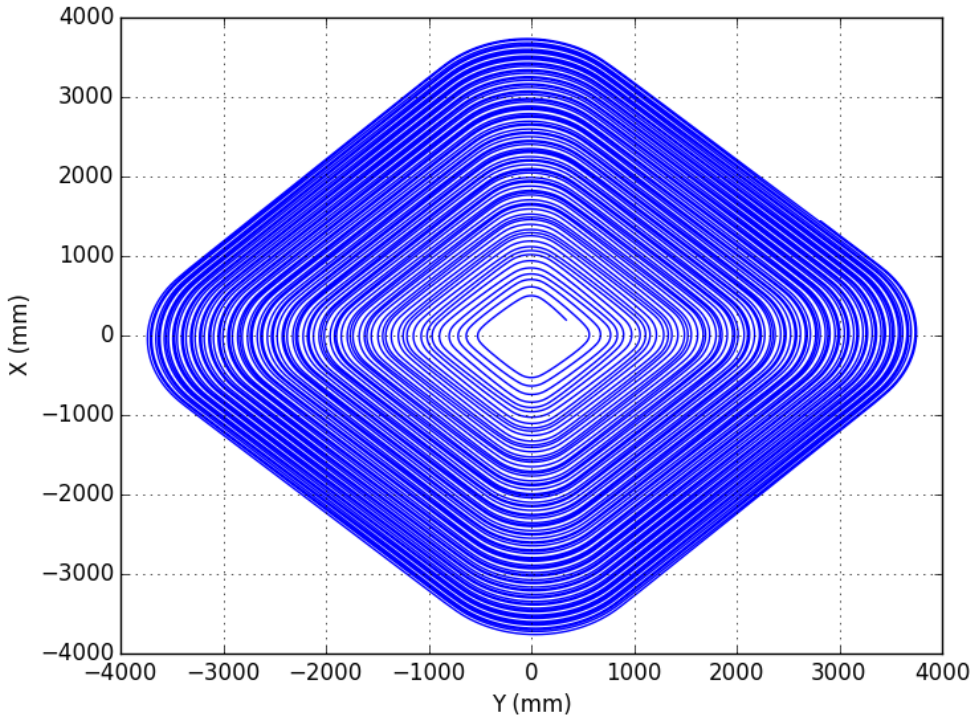

Figure 2.6: AEO of Injector II.

2.4 Space charge effects

One of the most basic properties of charged particles is the interaction via Coulomb forces. This simple collective effect of multiple equally charged particles comes under the name of the space charge. In multi-particle beams this effect is proportional to the intensity affecting not only single particle dynamics but also dynamics of the whole distribution. Is especially prominent at low energies of high currents. The direct space charge defocuses the beam in each plane (x, y, z), therefore lowering of the betatron tunes is expected.

Particles moving with speed v are equivalent to two current wires, $I = qv$. The magnetic force between two current wires is attractive and electrostatic forces are repulsive (Equation 2.31). The overall effect is still repulsive but decreases with particle speed (Figure 2.7). Special relativity implies that the forces become equal at the speed of light and thus cancel out [36].

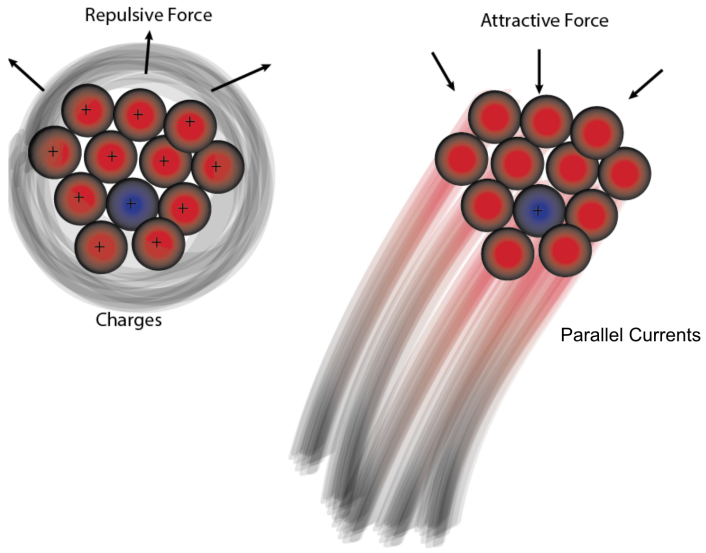

Figure 2.7: Coulomb repulsion and magnetic attraction between two particles of equal charge, at rest and travelling.

Now lets consider many charged particles travelling in an unbunched beam with circular cross section. The Coulomb repulsion pushes a test particle, located at a distance a from the beam centre of a radius r. The force F_r acting on it is:

$$F_r = e(E_r - v_s B_\phi), \tag{2.21}$$

where electric field E_r is:

$$E_r = \frac{I}{2\pi\varepsilon_0 \beta c} \frac{r}{a^2}, \tag{2.22}$$

where $I = \beta c \pi a^2 \eta$ is the total current and η being a uniform charge density. Magnetic field B_ϕ is then:

$$B_\phi = \frac{I}{2\pi\varepsilon_0 c^2} \frac{r}{a^2}. \tag{2.23}$$

The overall force is zero in the beam centre and increases towards the edge. This behaviour applies also to the test particle in a travelling beam, represented by parallel currents, except that the magnetic force vector is directed towards the beam centre.

Generally, the magnetic attractive force acting on a bunch in a local frame will be close to zero, and at Injector II energies space charge dominates, therefore can be neglected in the simulation code (electrostatic approximation). The force acting upon

a particle becomes:

$$F_r = \frac{eI}{2\pi\varepsilon_0\beta c}\frac{r}{a^2}. \tag{2.24}$$

Another way to describe space charge is through its equivalence to a defocussing quadrupole with strength

$$K(s) = \frac{2Nr_0}{a^2\gamma^3\beta^2} = \frac{K_{SC}}{a^2}. \tag{2.25}$$

K_{SC} is the normalised space charge perveance parameter [32]:

$$K_{SC} = \frac{2Nr_0}{\gamma^3\beta^2}. \tag{2.26}$$

The root mean square (RMS) beam radius is $a^2 = \frac{\langle\beta_y\rangle\varepsilon_N}{\gamma\beta}$, where $\langle\beta_y\rangle$ the average betatron amplitude function and ε_N is the RMS normalised emittance, r_0 is the classical radius of particle and N is the number of particles per unit length.

The definition of normalised emittance as e.g. used for calculations in the computer codes can be expressed by

$$\varepsilon_{n,rms} = \frac{1}{m_0 c}\sqrt{\langle x^2\rangle\langle p_x^2\rangle - \langle xp_x\rangle^2}. \tag{2.27}$$

$\varepsilon_{n,rms}$ is proportional to the area of the phase space ellipse. It is a quantity defining beam quality.

The betatron (Laslett) tune shift induced by the space charge force is given :

$$\Delta\nu_{sc} = \frac{F_B N_B r_0}{2\pi\varepsilon_N\beta\gamma^2} = \frac{2\pi R K_{SC}}{4\pi\varepsilon} \tag{2.28}$$

and $F_B = \frac{2\pi R}{\sqrt{2\pi}\sigma_l}$ is the bunching factor and $\varepsilon = \frac{\varepsilon_N}{\beta\gamma}$.

In estimating the space charge tune shift for actual accelerators, the formula (2.28) should be adjusted by a beam distribution form factor F_{dist}:

$$\Delta\nu_{sc} = \frac{F_{dist}F_B N_B r_0}{2\pi\varepsilon_N\beta\gamma^2}, \tag{2.29}$$

where N_B is the particle number per bunch.

Longitudinal space charge produces unwanted energy spread ΔE_{SC}, derived based on the non-relativistic "sector model" [35] can be expressed as:

$$\Delta E_{SC} = \frac{16}{3}\frac{eg_{1c}Z_0}{\beta_{max}}\frac{I_{avg}}{D_f}{n_t}^2 \approx 2800(\Omega)\frac{eI_{avg}{n_t}^2}{\beta_{max}D_f}, \tag{2.30}$$

where g_{1c}, is the form factor coming from the influence of the bunch geometry and calculated with elliptical integrals. Z_0 is the impedance of free space of 377Ω. D_f is fraction of the circumference covered by the beam. This relation shows the energy spread dependence on the turn number. Accumulated energy spread will couple to the transverse plane broadening the beam width proportionally to ${n_t}^2$.

Transverse, space charge induced tune shift $\Delta\nu_z$:

$$\Delta\nu_z = -\sqrt{2\pi}\frac{r_p R}{e\beta c\nu_{z0}\sigma_z}\frac{E_0 I_{avg}}{E_{gain}}, \tag{2.31}$$

where r_p is the average radius of a proton and σ_z is the vertical RMS beam size.

Space charge effects generally contribute to beam deterioration, however in isochronous machines under special conditions favourable vortex motion is induced producing a round beam. This was first observed in Injector II. The conditions required for the existence of this phenomenon include short bunches and well separated turns. All models predicting space charge effects on the beam quality are based on either overlapping turn model, or continuous beam. The model presented by Baartman [37] takes into account separate turns and round bunches, however overall it underestimates the intensity limits, therefore a 6D non-linear numerical model of Injector II can give us a closer answer to the question of the intensity limits.

2.5 Stationary distribution

Injected, initially uncoupled, bunches of particles undergo linear deformations/transformations under the influence of fields generated by the beam optics and space charge as they travel through an accelerator. Particle-in-cell (PIC) simulations require generation of such multivariate particle distributions. To adequately model such beams, we should begin simulations at the ion source or the buncher, however that would require additional modelling that is not of interest and outside of the content of this thesis. Attempts have been made to address this topic allowing simulations with more realistic distributions, however no self-consistent model/theory have been developed yet. In this research we use theoretical model by C. Baumgarten [25], in which covariance matrix of a Gaussian distribution is generated via symplectic transformations [38].

In Injector II, after initial matching in the first several turns, a round stationary distribution is generated. We search for a σ matrix of the distribution second moments, that after one turn in the accelerator will remain the same:

$$\sigma_t = M\sigma_0 M^T, \tag{2.32}$$

where σ is the symmetric matrix of second moments at time t, M is the transfer matrix and σ_0 is the matrix of the initial distribution.

This is a linear space charge model, based on the idea of the inverse of the Real Dirac Matrices (RDM) decoupling [39]. RDM transformations allow decoupling of the variables in transport, force and σ matrices. Here, we need the opposite: a transformation of a set of independent variables e.g. position and momentum, into a distribution that will yield a covariance matrix of interest with coupled variables.

Producing the σ-matrix of matched distribution requires input of initial emittances in x, y and z planes with the beam current of interest. The program begins with an initial guess of the beam size in x, y and z. Based on that guess, driving space charge forces are computed and a one-turn transfer matrix for all azimuthal angles is generated. Next, eigenvectors of this matrix are calculated by diagonalisation. The beam emittances provided at the start are then used to calculate the eigenellipsoid from which the beam sizes are calculated again and compared to previous ones. If they change significantly, subsequent iterations are performed until convergence is reached.

This theoretical model, based on a simplified azimuthally symmetric cyclotron with linear space charge, is the best available approach to generate multivariate matched distributions for isochronous cyclotrons. This theoretical model was already successfully used for the high-intensity injector cyclotron in DAEδALUS project [21]. The work presented in this thesis is based on tracking these "matched" distributions in a nonlinear model of Injector II.

2.6 Halo quantification

Another important aspect of high intensity machines is detailed halo analysis. We have chosen a basic approach and used a kurtosis-like parameter h, measuring 1D spatial projections of the distribution [27]. This basic approach gives a good insight into the observable halo formation in real space.

The so-called profile parameter, h, chosen to quantify halo is showing 1D spacial

projections of the distribution. We normalise h-parameter to unity for Gauss-like distributions, where for h =1. It can be written as:

$$h = \frac{\langle x^4 \rangle}{\langle x^2 \rangle^2} - 2. \tag{2.33}$$

The profile parameter is based on the second and fourth moments is an indication of the "tailedness" of the distribution. It tells us how the distribution deviates away from Gaussian. If the distribution is leptokurtic and h$<$1, we get a sharp peak in the core of the distribution and long tails. If h$>$1, the platykurtic distribution is closer to flat. The h parameter does not necessarily change with intensity. The beam size changes (σ) but not the ratios between the moments. It may be necessary to consider other ways of quantifying halo such as halo parameter H that describes presence of halo in 2D phase-space [29, 28]. However, using profile parameter together with beam size data may be sufficient.

Chapter 3

Methods

This chapter covers the description of the steps taken to develop the full 6D beam dynamics model of Injector II. Starting with the simulation code used and why it was chosen to be the best tool, simulation resolution and HPC (High-Performance Computing) resources. We also briefly mention post-processing tools and the optimisation scripts used to select the best initial conditions.

3.1 OPAL code - Cyclotron mode

The interest in precise accelerator beam dynamics modelling has grown in recent years enabled by rapidly increasing computer technology capabilities. Most lattice codes are based on a set of ordinary differential equations for the second-order moments of a particle distribution that evolves with time. However for quantitive studies of space charge effects this becomes insufficient.

Accurate modelling of complex beam dynamics in cyclotrons can be done using a Vlasov-Poisson description of phase-space [40]. It includes external fields and self-fields induced by Coulomb interactions, and, if required, other effects such as wake-fields.

The precise beam dynamics model is developed using the OPAL (Object Oriented Parallel Accelerator Library) C++ based simulation code [5]. It is a tool for charged-particle optics calculations in large accelerator structures and beam lines including 3D space charge. Successor of MAD9P (Methodical Accelerator Design version 9 - parallel) [41], OPAL is based on the MAD (Methodical Accelerator Design) code [42]. It is a parallel application making the most out of the available HPC (High Performance Computing) resources. OPAL-CYCL and OPAL-T are the two main ”flavours” that

the code offers. OPAL-CYCL, relevant in this research, allows 3D tracking with space charge in cyclotrons and the OPAL-T can model injectors, guns (components producing narrow collimated beam of particles), and X-ray Free Electron Lasers (XFEL).

The time evolution of the function representing the particle distribution density $f(x, c\beta, t)$ in phase space, at position x with velocity βc at time t, in OPAL [43] is expressed by:

$$\frac{\mathrm{d}f}{\mathrm{d}t} = \partial_t f + \beta c \cdot \bigtriangledown_x f + q(E + \beta c \times B)) \cdot \bigtriangledown_{\beta c} f = 0, \tag{3.1}$$

which is the collisionless Vlassov-Poisson equation. In this equation q denotes charge. Magnetic, B, and electric, E, fields both include external and internal space charge fields:

$$E = E_{ext} + E_{sc}, \tag{3.2}$$

$$B = B_{ext} + B_{sc}. \tag{3.3}$$

Knowing E and B, each charged (macro)particle can be propagated by the following equation of motion:

$$\frac{\mathrm{d}p(t)}{\mathrm{d}t} = q(\beta c \times B + E). \tag{3.4}$$

External magnetic fields of the Injector II used in the simulations are read from the field maps based on the measurements with excited trim coils. Particle-in-cell FFT (Fast Fourier Transform) method is used to solve space charge fields that are approximated. Relative motion of the particles in a bunch is non-relativistic in the beam rest frame, so the self-induced magnetic field is practically null and can be ignored, whereas the electric field is computed using Poisson‘s equation.

OPAL is based on the PIC (Particle-in-Cell) technique that allows solving certain type of partial differential equations. In this method, individual particles are put in a Lagrangian frame and tracked continuously in the phase-space. Currents and densities (moments of the distribution), on the other hand, are calculated using Eulerian stationary mesh points. Particle bunch properties can be represented by joining the particles into collections, so called *macroparticles*, that will carry the cumulative charge. Extensive parallel capabilities of OPAL are based on IPPL (Independent Parallel Particle Layer) framework. Sophisticated numerical models and algorithms accompanied by

the evolution of HPC have become an essential connection between theory and experiment.

All simulations were performed on the Merlin4 HPC cluster at PSI. This machine has 30 compute nodes (total of 360 cores) and 2 login nodes (24 cores) for common resources. It consists of HP BL460c G7 blades, two Intel Xeon X5670 2.93GHz CPUs (12 cores per node),16 nodes with 24 GB RAM per node and 16 nodes with 48 GB RAM per node (extendable to 96 GB per node) and Infiniband interconnect [44].

The time needed to complete the simulations depends on the number of turns and particles used in the selected runs the mesh size and the number of processing cores. The parameters shown in Table 3.1 have been found to be optimal depending on the size of the simulation. A parallel FFT solver was used in all planes. For statistically valuable results of space charge simulations, the number of particles used in a simulation should be 10^5 and the mesh cube should contain less than 20 particles.

Table 3.1: Simulation parameters.

Number of particles	Mesh size	Cores
1	N/A	1
$5 \cdot 10^4$	8	8
10^5	16	32
10^6	32	64

3.2 Optimisation

In this section we briefly describe the optimisation techniques and reasoning behind the use of optimisation algorithms. To obtain a final precise model, three-step optimisation has been used including *OptPilot* [22] based on Genetic Algorithms (GA), minimising python script and expertise/observation. To visualise these multivariate results, a parallel coordinates technique is implemented.

3.2.1 Orbit finder

The *OrbitFinder.py* developed at PSI (A. Foster) was created to find cyclotron accelerated orbits satisfying various requirements. The script combines selected bi-objective functions and variables within the *OptPilot* framework. *OptPilot* is a general-purpose framework for simulation-based multi-objective optimisation methods, to generate a

set of candidate solutions. It is based on Genetic Algorithms (GA), which generate solutions to optimisation problems using techniques inspired by natural evolution, such as inheritance, mutation, selection, and crossover.

The *OrbitFinder.py* script produces an input file for *OptPilot* with the supplied additional data, that can be used by the *OptPilot*. In *run.sge*, job submitting file, we specify additional GA parameters, such as number of generations and population size.

This is a bi-objective optimisation with multiple variables. The first objective, counts the number of turns, and compares it to the specified maximum number of turns the simulation should track, this counted total is then subtracted from a constant and minimized.

The second objective ensures that the candidate solution has more than a constant (currently set to 20 turns) number of successive radius measurements, the script fits a power law to the radii with the turn index as the independent variable using Pythons's SciPy *optimize.leastsq()* function. The script then returns the sum of squared errors for the fit as the second objective value. In case there is not enough turns the function evaluation halts.

In the frame of this project, the initial input parameters to be optimised are radial momentum (PR), initial azimuth position of the particle (PHI01), RF phase (PHIRF) and radius (R) of the particle. The optimisation is done for a single particle case at a chosen energy orbit within set boundries. Results are obtained in separate folders with beam dynamics data files as in OPAL, allowing simple data analysis. It is necessary to check for AO (Accelerated Orbit) and maximum energy requirement of 72 MeV because not all solutions found by the optimiser reach this energy and some of the orbits may have patterns of clustered or cross-over orbits.

3.2.2 Radial intensity peak matching

One of the ways to validate the model is to compare radial intensity peaks of the simulations and measurements. To find initial conditions satisfying the requirement of accurate radial position of simulated intensity peaks, a Python optimising script *opt.py* was developed based on a *spicy.optimize()* minimising function with an *L-BFGS-B* algorithm for bound constrained optimisation. Function chosen to be minimised is the least squared method between measured and simulated radial intensity peak positions or radial position of the test particle at given azimuth when the single particle optimisation is used.

This is a single-objective optimisation with two or three parameters to vary. Available parameters include radius, radial momentum, azimuth and RF cavity voltage offset. Once the varied parameters' boundaries are set and initial parameter estimated, the script automatically submits jobs, and *Optim.C* Root script is run with each solution chosen by the optimiser. *Optim.C* reads phase-space data saved in *h*5 data format and produces *sim_xpeaks.dat* file containing radial positions of intensity peaks. This is then compared to the measured peak positions saved in *mes_xpeaks.dat*. The iteration of variables continues until the minimum distance between simulated and measured peaks is found or chosen maximum number of iterations reached.

Among initial parameters, R and RF offset is found to be the most effective as it varies both radial and longitudinal positions of the beam and as we can see in Equation 2.13 these are the main parameters defining the turn spacing. Even though, this method indeed shows good results, the best match is found with additional scans based on the observations and experience with data.

3.2.3 Visualization

Both methods require some expertise and intuition in selecting boundaries and variables and also choosing the best solution, where visualisation comes in very helpful. To visualise multi-objective optimisation solutions that require trade-off decisions, script *parallelcoord.C* based on Root's *TParallelCoord* function have been used. Parallel coordinates are a common way of visualising high-dimensional geometry and analysing multivariate data.

3.3 Post-processing

Several post-processing tools have been developed during this research to aid the analysis and interpretation of findings. Initial analysis is made using Gnuplot and H5root, Root based tools processing h5-type files containing phase-space data. More detailed analysis requires development of more specific scripts. They have been written based on the fastest and most flexible way of processing simulated and measured data. Post processing tools include Python, Root, Gnuplot [45] and Shell scripts.

Root is a data analysis framework, based on C++, that provides all the functionalities needed to deal with big data processing, statistical analysis, visualisation and storage [46]. It is a complex, yet very powerful, tool enabling processing of any data

sets. Python, used as a part of Anaconda framework, is a straightforward tool to optimise and visualise already generated data [47], allowing communication between other platforms. Shell scripting, run in the Unix shell, is a very efficient way to process and manipulate ascii data files, often used as a pilot script combining Root and Python post-processing tools.

A number of Root scripts have been developed for analysing and extracting data from large *.h*5 and *.root* (multidimensional data files), and *ascii* files, of the order of several GB. Some post processing scripts include beam halo analysis: 1D profile parameter quantification (kurtosis), visualisations of beam passage through the cyclotron and *TSpectrum* peak finder used for radial intensity probe analysis. In addition, many shell scripts processing ascii files were produced, submitting simulations and searching for desired data in large output files, amongst other things.

The main post-processing tools developed and/or extended within the frame of this study include:

- Transverse and longitudinal RMS beam size and emittance (Root Gnuplot)
- Accelerated and static orbits (Gnuplot and Python)
- Collimator positions on the accelerated orbit (Python)
- Mid-plane and phase-space plots (Root)
- Peak finder comparing measured and simulated data (Root)
- Parallel coordinates visualisation tool (Root)
- Halo parameter (kurtosis) (Root)
- Halo particle tagging (Root)
- RF phase slip, turn separation etc (Shell scripting and Gnuplot).

3.4 Approach

In this section we describe the general approach in developing the precise model. A summary can be found in Figure 3.1.

The aim of this research is to develop a numerical model of Injector II, a separate-sector cyclotron that has been operating perfectly for over 40 years, to then estimate its

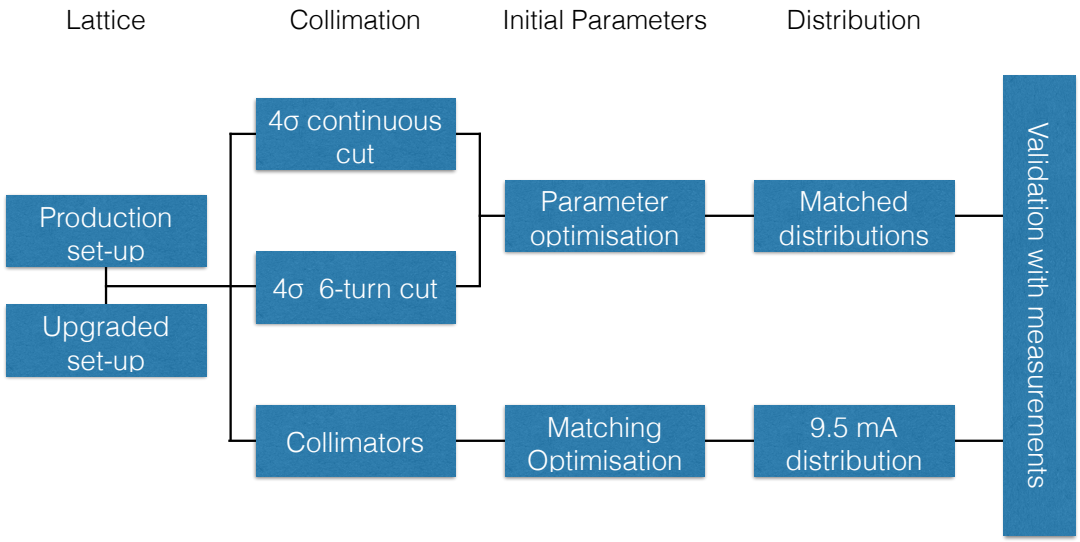

Figure 3.1: Flow chart of the steps taken in the model development.

intensity limits. In this machine phase, collimator positions, intensity, and particle distribution are strongly however, non-linearly, correlated. Excellent machine optimisation is carried out by experienced operators and accelerator division staff. It would have been too difficult to design a model with all parameters included from the beginning and expect positive results, therefore a step-by-step method has been implemented. Magnetic field map, based on the magnetic field measurements with the influence of trim coils, is believed to be a good representation of the fields in Injector II. RF voltage on the cavities is also based on the measurements and re-calculated in OPAL for the peak voltage and integrated profile.

Injector II operates with two double-gap resonators and two 3rd harmonic flat-top cavities currently operating in acceleration mode due to sufficiently narrow beam phase width, here referred to as *production set-up*. *Upgraded set-up* refers to the 3 mA upgrade of HIPA that also involves exchanging 3rd harmonic cavities in the injector for single-gap resonators. During upcoming upgrade of Injector II, flat-topping cavities will be exchanged for single-gap resonators, enabling extraction of higher intensities. We consider both configurations and the following methodology applies to each case.

Injector II is equipped with a number of radial intensity and time structure measuring probes and a complex system of collimators in the central region used for phase

selection and cleaning. As simulations from the injection radius require the introduction of collimators, a simpler scheme was chosen to start up the model. A 2 MeV start radius has been chosen to avoid the region with most rigorous collimator cutting. the first step is to find closed Static Equilibrium Ofrbit (SEO) at selected energy and verify the tunes for energies from 2 to 72 MeV. Starting a simulation in OPAL requires a number of initial conditions of the particle/distribution including radius R, starting azimuth PHI01, radial momentum PR and RF phase PHIRF. As they are strongly correlated, searching for SEO requires manual optimisation based on measured Injector II parameters. Also the charged particle distribution, that is strongly correlated in Injector II, has to be generated using a linear space charge model coupled to the injector lattice.

The next step is to add the accelerating resonators. This needs additional optimisation, as the SEO starting conditions are not fully valid in case of accelerated orbit. For example, PR is nonzero as the particle trajectory is no longer perpendicular to the radial direction in the valley region where the simulation begins. As the starting parameters are extremely sensitive, manual optimisation becomes no longer time-efficient and an optimising script *Orbitfinder.py* connected with *OptPilot* has been introduced to search for the ideal accelerated orbit. Once the starting parameters are selected, a particle distribution is then injected for the intensity of interest and a continuous 4σ x-y cut is applied, as the beam would still pass through several collimators. However, to have a better insight into the halo formation, a 4σ cut should be introduced only in the first several turns to more adequately mimic the collimation system. At this point the model can be initially validated with the measurements by comparing last turn RMS beam size at the position of the time structure probe RIZ1. Subsequently, collimators have been introduced starting from 870 keV injection orbit. Again to find starting conditions, an *OptPilot* optimisation had to be performed and finally a 9.5 mA distribution passed through the central region collimators can be tracked.

Injector II orbit pattern is very specific and the radial positions of the last two turns are dictated by the extraction electrode position. Another way to validate the model is to match the modelled radial profile with the measured one at a chosen location of radial probe RIE1. For this purpose a peak-matching optimising script has been successfully applied allowing further validation of the model. Considering time and computing resource constrains, first scans were performed using 50000 macroparticle distributions. However, for statistics of order of 5-6σ, 10^5 and 10^6 particle bunches have also been simulated.

3.5 Chapter summary

A number of steps have been used to estimate the limits in the most efficient way. This involves development of simulation and analysis tools together with *OptPilot* and Python optimisation routines. These tools have allowed in-depth study of the models and their validation with Injector II measurements. We have gradually expanded the models to eventually include all important components such as collimators and probes.

Chapter 4

3D models of Injector II

In this chapter we begin with a description of matching the generated distributions without acceleration. We then describe the three collimation models of Injector II:

1. Continuous 4σ cut,
2. 6-turn 4σ cut,
3. Physical collimator.

These models are considered under two configurations: production and upgraded. The production refers to the currently operating 2.2 mA mode of Injector II and the upgraded refers to planned exchange of flat-top cavities for new resonators. The physical collimator model will be described separately in detail in Chapter 5. All simulations presented in the thesis use multivariate Gaussian distributions generated based on the model described in Section 2.5.

The coordinate system used in the models and analysis is shown in Figure 4.1, where longitudinal direction is y, radial x and vertical z.

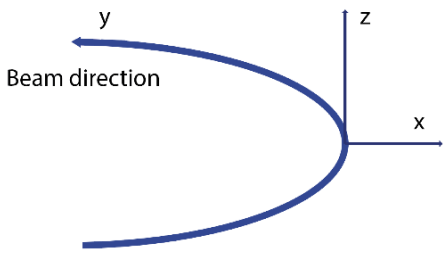

Figure 4.1: Coordinate system used in the thesis.

4.1 Stationary distribution and the closed orbit

Injector II is characterised with relatively small 2π mm$\times$mrad normalised emittance at extraction. Generating a particle distribution requires estimating the input emittance for each studied intensity. The chosen approach is to search for the minimum value that is required for the numerical model generating the distribution to converge (see Section 2.5). In Figure 4.2 we can find values selected for currents from 0.5 to 10 mA.

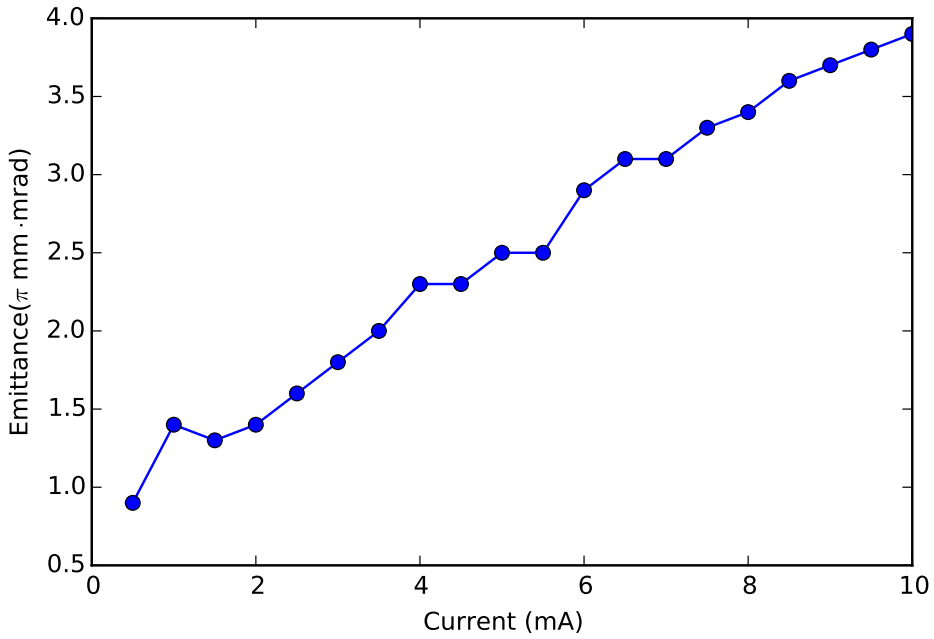

Figure 4.2: Emittance convergence study for considered intensities. Selected for 2 mA initial energy.

We can test how well the distribution is matched by passing it through the cyclotron without RF for a number turns at a constant energy. Simulations are performed with matched initial distribution at 2 MeV. The beam current is set to 2.0 mA with 1.4 mm$\times$mrad input beam emittance. The bunch is then left circulating for 100 turns to investigate the bunch size, emittance and halo evolution.

The RMS beam size and emittance shown in Figure 4.3 are slightly growing due to space charge forces and non-linearities present in the machine lattice. Looking at halo development (h parameter), however, we observe that in the first 10 turns the bunch size undergoes rapid changes to then eventually smooth out. It is important to remember that, the distribution is generated using a linear space charge model and

is then run through a non-linear lattice. Some "mismatch" is therefore expected, and as observed in isochronous separate-sector machines, a "self-matching" occurs after several turns and is then kept over 100 turns, which is an excellent result.

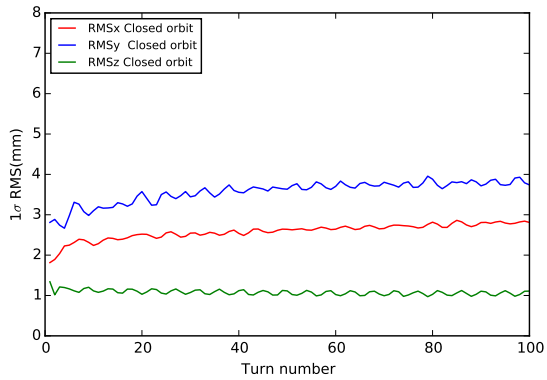

(a) RMS x y z

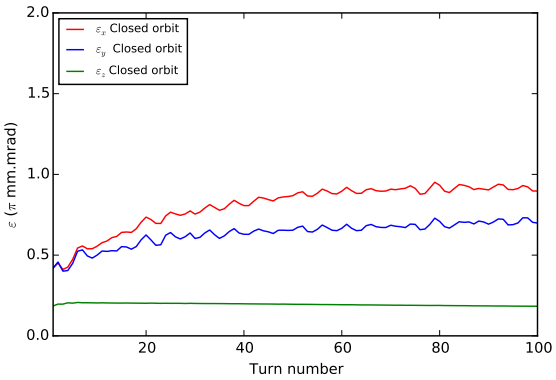

(b) Emittance x y z

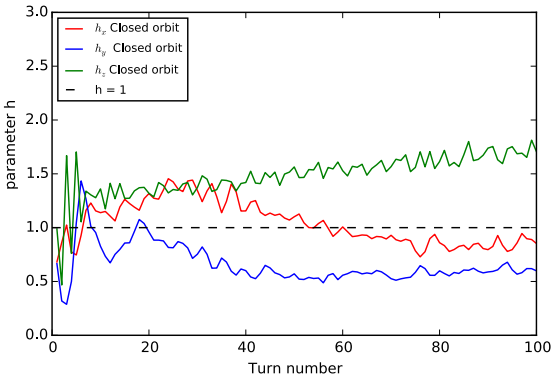

(c) Parameter h in x, y, z

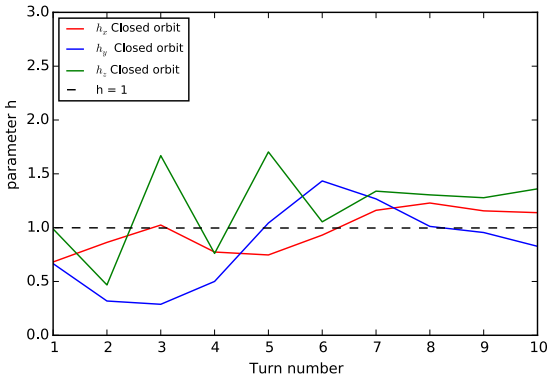

(d) Profile parameter zoomed to first 10 turns.

Figure 4.3: Closed 2 MeV orbit of the production set-up at 2 mA current. The distribution is not matched for Injector II field map, hence the initial "blow-up". Requires about 10 -20 turns to "match" itself.

A "dilution" of the bunch core is observed in Figure 4.4, nonetheless the beam stays round. These results are satisfactory providing that we have used a linear space charge model to generate the initial distribution, whereas subsequent tracking with OPAL includes the non-linear effects. Other studies [37, 17, 20] show these effects in more detail, together with the bunch length: width ratio required to sustain round bunch.

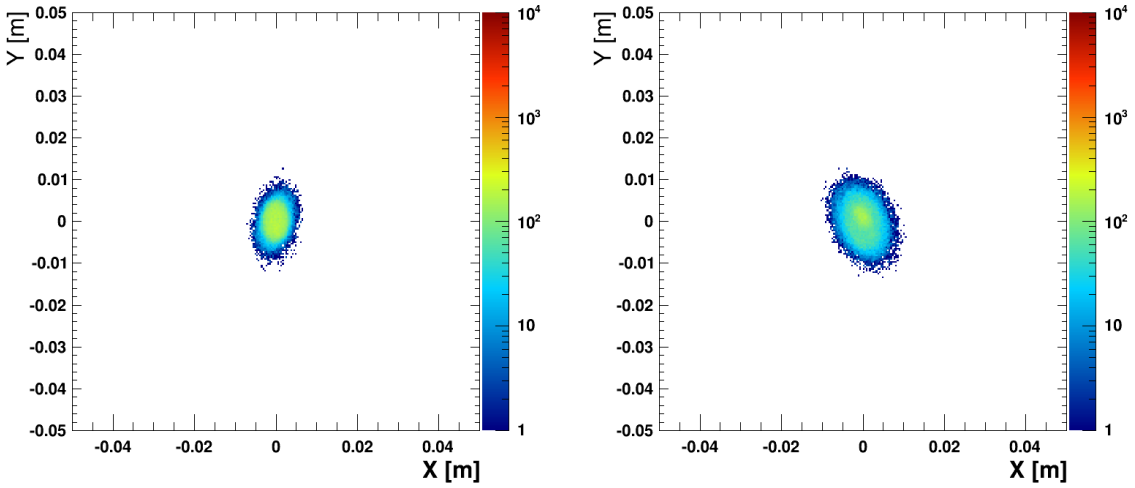

(a) (b)

Figure 4.4: 2 mA distribution in x-y after injecting (a) and after 100 turns of "coasting" (b) at 2 MeV orbit.

4.2 Production configuration

The Injector II operates with two double-gap resonators located 180° apart and two single-gap 3rd harmonic flat-top cavities used as additional accelerating cavities (Figure 4.5). The machine accelerates from 870 keV to 72 MeV in 83 $\pm$1 turns. More details about Injector II can be found in Chapter 1.2. The following parameters change with each commissioning after shutdowns and as for 2015 the voltages on the cavities are:

- Resonator 1 (gaps RF0 and RF1) 431.357 kVp,
- Resonator 2 (gaps RF2 and RF3) 400.374 kVp,
- Flat-top 3 (RF4) 31.698 kVp,
- Flat-top 4 (RF5) 31.382 kVp.

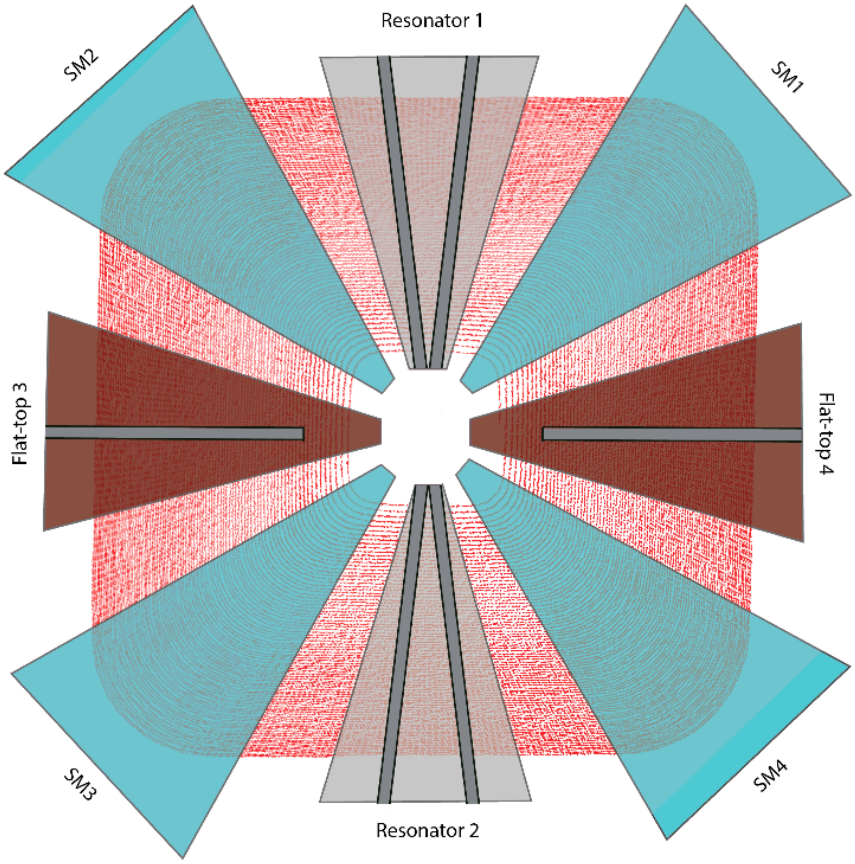

Figure 4.5: Schematic of the Injector II production configuration. The cyclotron has four sector magnets operating at 2 T (green), two double-gap resonators (grey) and two 3rd harmonic cavities (maroon).

In the following section we apply both continuos 4σ and 6-turn 4σ cut models to the production set-up. The physical collimation model will be discussed in Chapter 5.

4.2.1 Applying the continuous 4σ cut model to the production configuration

Developing a beam dynamics model of Injector II should begin with simplified cases. Therefore, we apply the first simplified model to the production set-up. This idealised model of Injector II does not include lumped collimators, but instead a 4σ continuous cut around all planes. This model can give an estimate of RMS (Root Mean Square) beam sizes and emittance, however information about halo is invalid in this case since we cut the distribution outer regions at each step. Nonetheless, the results show an

impressively matched beam accelerated up to 72 MeV as shown in Figure 4.6. Full beam extent is around 20 mm close to that measured in Injector II.

There are several approaches to investigate what is happening in the model. The information that can give useful insight into the beam dynamics, as shown in subfigures of e.g. Figure 4.6, include RMS beam size (a), emittance (b) and profile parameter h (e). All these parameters describe the size of the beam from different perspectives. For instance, beam halo can be increasing, but not the beam σ. This can give hints on the source of beam quality deterioration. Emittance tells us about dynamics within the bunch (as it is in the x-px space). Combining several parameters in one plot can provide valuable indication about the model and beam behaviour at the same time showing how well the distribution and initial conditions are matched. In Figure 4.6 we compare combined 1σ RMS beam size, emittance and profile parameter in the horizontal (c) and longitudinal (d) planes. All parameters appear stable after the first several turns where the bunch matching occurs. In the last subfigure (f) we take a look at beam extent, meaning the furthest point where we can still find scattered particles in the mid-plane. This gives an information about physical beam size of the full distribution and whether it can fit through apertures, septum or simply whether neighbouring bunch effect should be a worry. This is combined with the δE increased with energy of the accelerated bunch. This approach to data analysis will be followed through all considered models and intensities.

If we analyse this idealised model of Injector II, 3.5 mA (Figure 4.7) is already not feasible with 1σ of 4 mm (6σ of 24 mm). This is dictated by the physical radial aperture of the extraction devices of approximately 20 mm. Therefore, a beam with 6σ of 3.3 mm is considered as the safe limit. It is a rough model, but as we will see in further sections, the horizontal (radial) RMS beam size will be valid for all considered models but detailed longitudinal information is lost. It is, in fact, the radial beam extent combined with turn separation that dictates how much intensity we can pass through the machine. Longitudinal tails can couple to the radial plane, as we will see in the following sections, therefore it is crucial to minimise these effects. In Figure 4.8 we model 4 mA beam continuously cutting all the particles outside 4σ region. Even in such ideal case, 1σ RMS (a) is over 3 mm implying that space charge is too strong to keep the beam compact at higher intensities with full radial beam extent also over 20 mm (f).

Based on continuous 4σ cut we can conclude that intensities above approximately

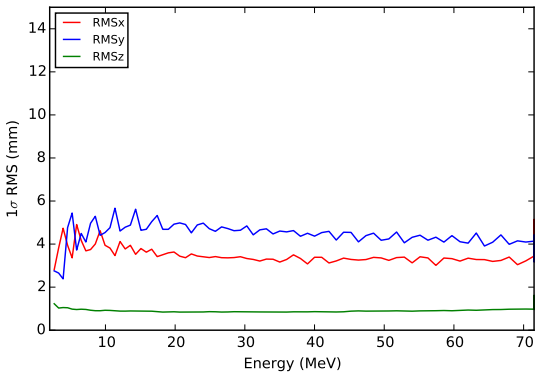

(a) RMS beam size

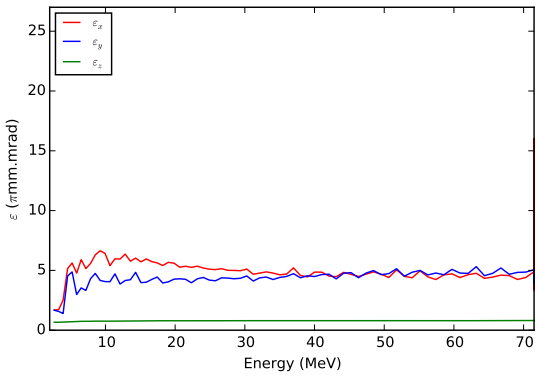

(b) Emittance

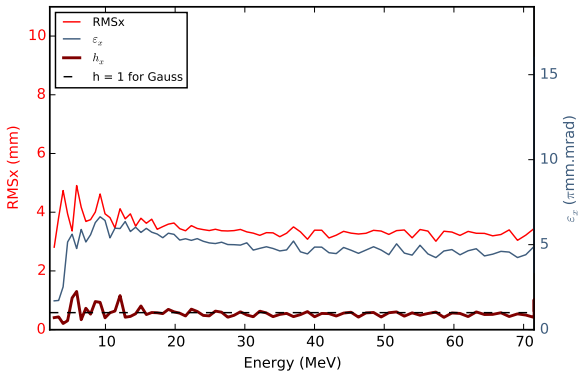

(c) Horizontal RMS, Emit, h

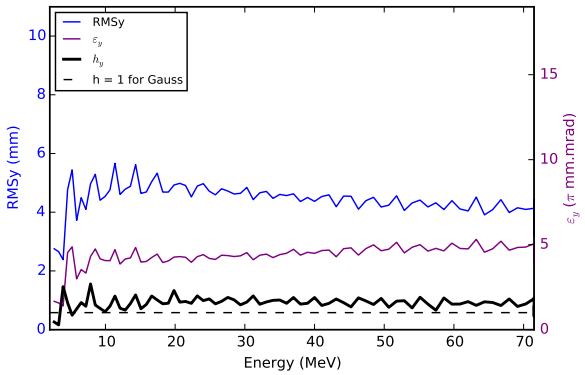

(d) Longitudinal RMS, Emit, h

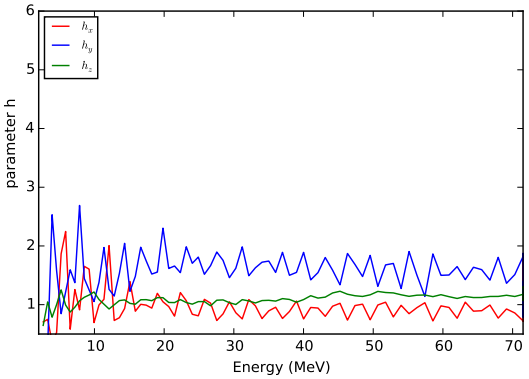

(e) Profile parameter h

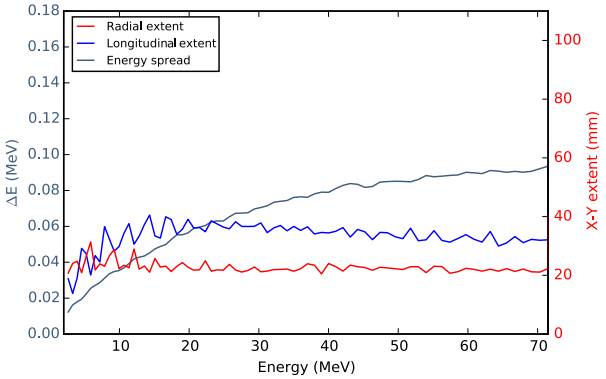

(f) Full extent of the bunch with energy spread

Figure 4.6: Production set-up 2.2 mA case applied to continuous 4σ cut (2.5 mA $5 \cdot 10^4$ macroparticles injected).

3.5 mA are not feasible. More currents with varied statistics are shown in the Appendix A.1.

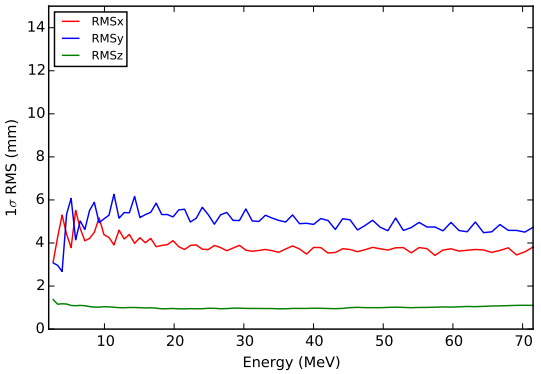

(a) RMS beam size

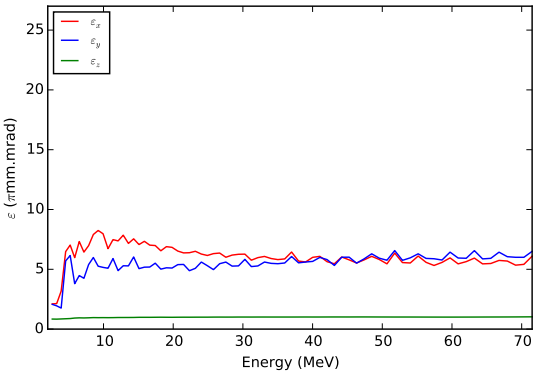

(b) Emittance

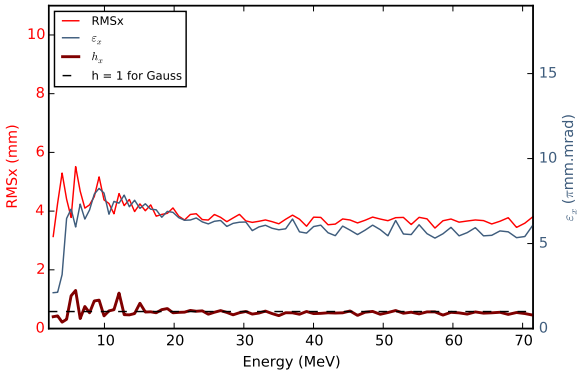

(c) Horizontal RMS, Emit, h

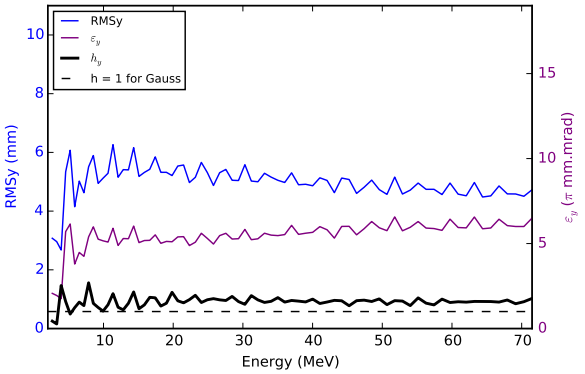

(d) Longitudinal RMS, Emit, h

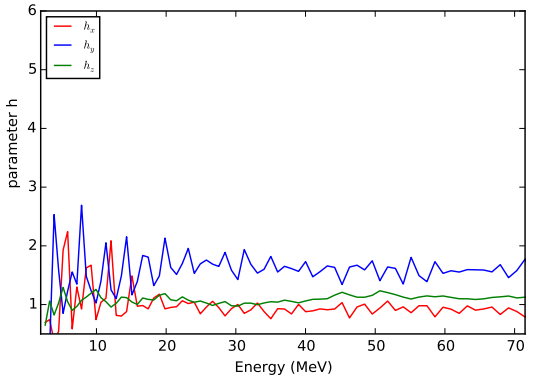

(e) Profile parameter h

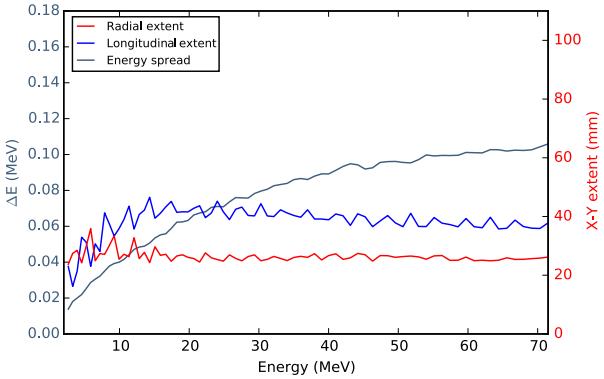

(f) Full extent of the bunch with energy spread

Figure 4.7: Production set-up 3.5 mA case applied to continuous 4σ with 10^6 macroparticles.

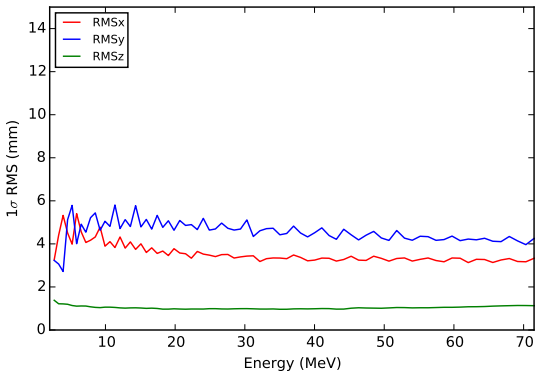

(a) RMS beam size

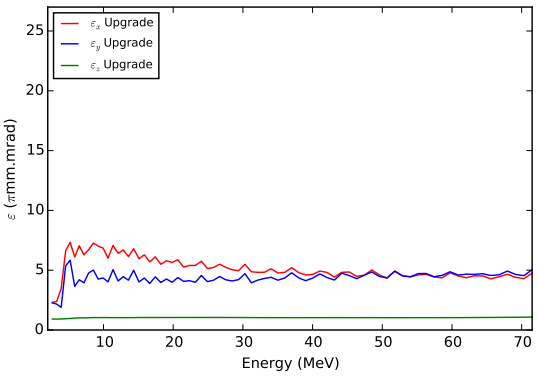

(b) Emittance

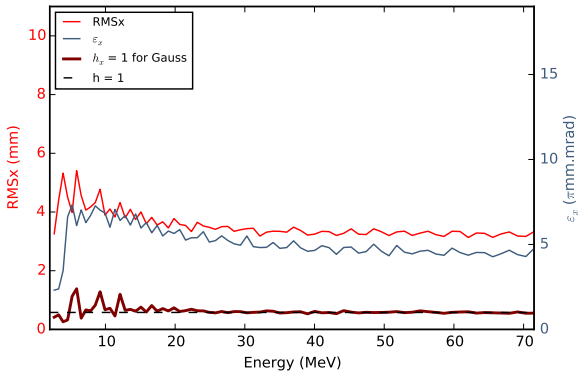

(c) Horizontal RMS, Emit, h

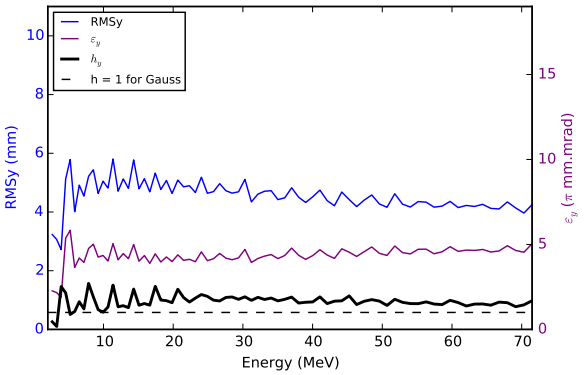

(d) Longitudinal RMS, Emit, h

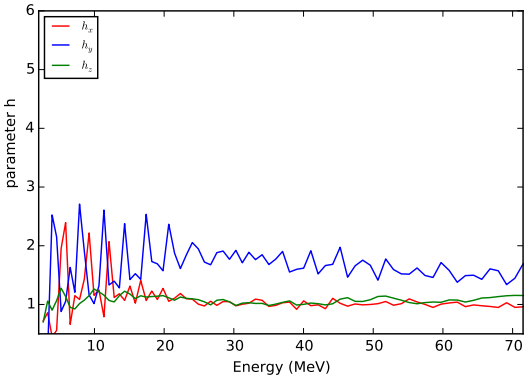

(e) Profile parameter h

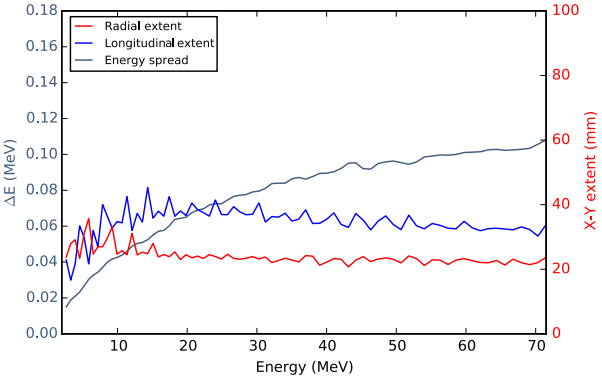

(f) Full extent of the bunch with energy spread

Figure 4.8: Production set-up 3.9 mA case applied to continuous 4σ cut (4 mA $5 \cdot 10^4$ particles injected) spatial. Even at continuous cut, beam size is too big to pass through the septum.

4.2.2 Applying the 6-turn 4σ model to the production configuration

Beam cleaning is performed in the low energy regions to minimize activation. The previously studied continuous cut via collimation is not feasible in cyclotrons. Additionally, removing particles outside the 4σ region throughout the acceleration will not give a full picture of the halo formation. As one of the ongoing questions is whether halo is re-formed after the collimators, some simulations have been performed with the beam being cut with 4σ only for the first 6 turns (later referred to as 6-turn cut). Presented simulations were performed using $5 \cdot 10^4$,10^5 and 10^6 macroparticle bunches with 4σ cut in x, y and z planes in the first 6 turns. This mimics the collimation system located within the first 6-7 turns of the Injector II. It is thought to be a reasonable approximation for initial modelling. The starting orbit was chosen to be 2 MeV where most of collimation is already completed and a stationary distribution is being formed. We could attempt to estimate the losses, defined as particles being lost outside of the 5σ region, however no firm conclusions can be drawn based on such approximation. It was noticed that these "losses" strongly depend on the selected initial conditions. It is nothing more than an indication of a possible field of improvement in the real set-up.

We should expect more accurate result compared to the previous model. Interestingly enough, even though the halo is cleaned in the first turns, it begins to re-form again after several turns. With full 4σ cleaning we should remove phase and energy tails. This indicates that no collimation in the first turns can fully get rid of the halo, as part of it may come from lattice non-linearities and phase mixing due to space charge forces acting upon the bunch. This could also be consistent with particle core model suggestions [48]. One should not forget about likely mismatch of the initial distribution or not large enough cut at specific steps.

As we can see in Figure 4.9 (e), the profile parameter remains close to 1 in the horizontal plane until about the 40th turn and then sharply increases. This is the point where steadily growing longitudinal tails couple to the radial plane nearly tripling the longitudinal, and doubling horizontal beam extent. What is more, in case of 2.9 mA the full beam extent is 40×50 mm with less than 0.004 mA charge outside of the 5σ region. RMSx is here around 3.2 mm fitting closely to the 20 mm turn separation and thus the septum acceptance (Figure 4.10).

Next is to investigate how the beam changes within one turn. In Figure 4.11 we show 360° beam evolution along the extraction orbit for a 1.8 mA distribution. Interestingly enough the profile parameter does not behave symmetrically showing 2-fold

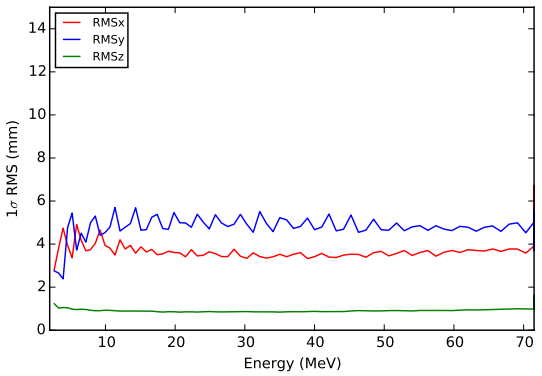

(a) RMS beam size

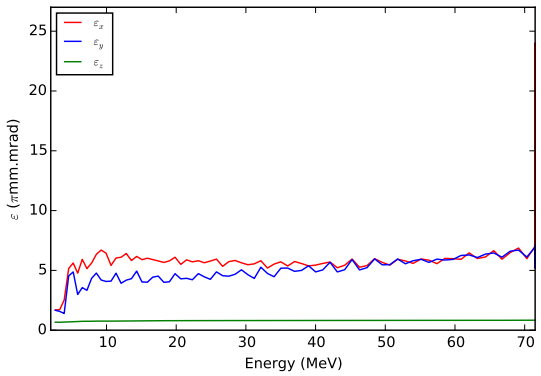

(b) Emittance

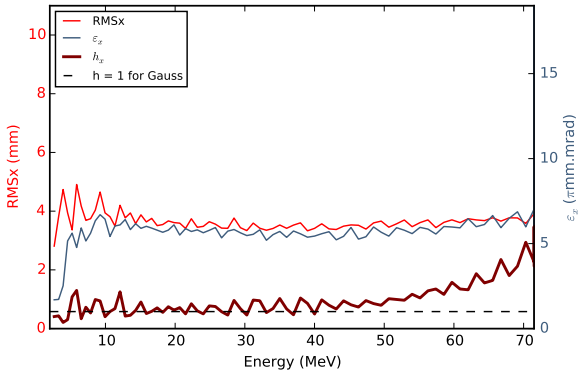

(c) Horizontal RMS, Emit, h

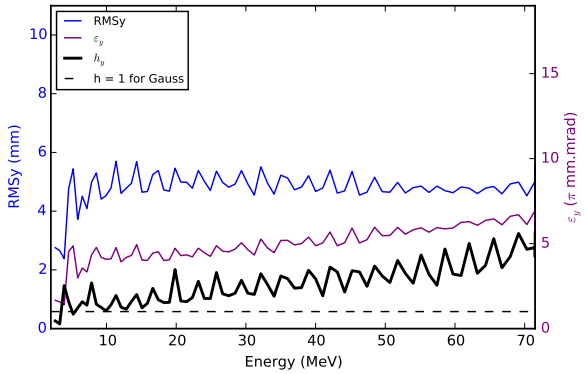

(d) Longitudinal RMS, Emit, h

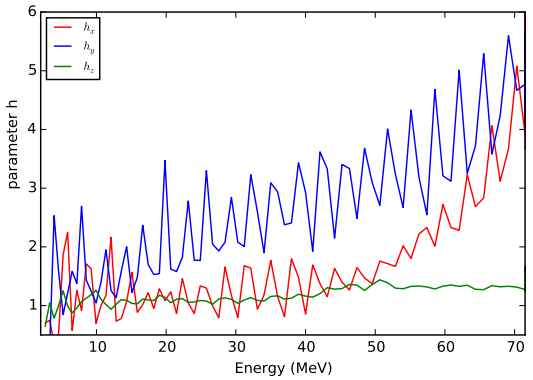

(e) Profile parameter h

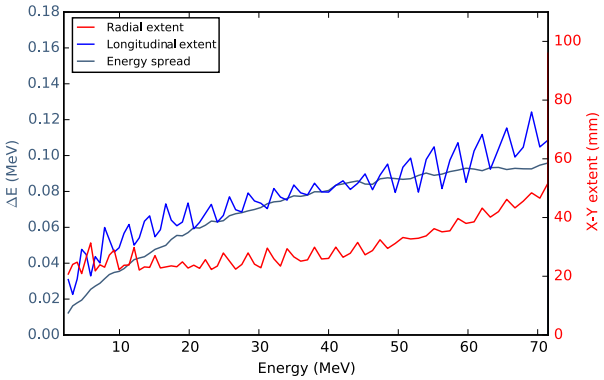

(f) Full extent of the bunch with energy spread

Figure 4.9: Production set-up 2.3 mA case. 6-turn 4σ cut with injected 2.5.mA ($5 \cdot 10^4$ macroparticles). Radial and longitudinal planes are well matched with very smooth vertical plane. However longitudinal halo is generated that after 40 turns couples to radial plane.

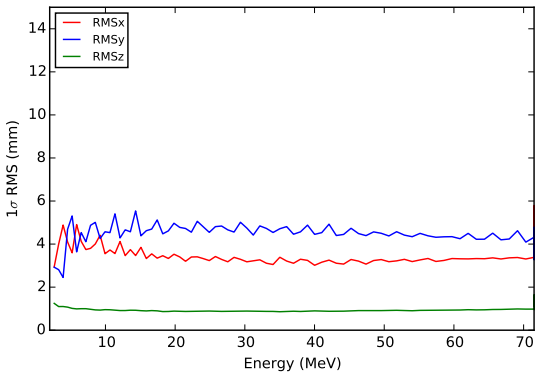

(a) RMS beam size

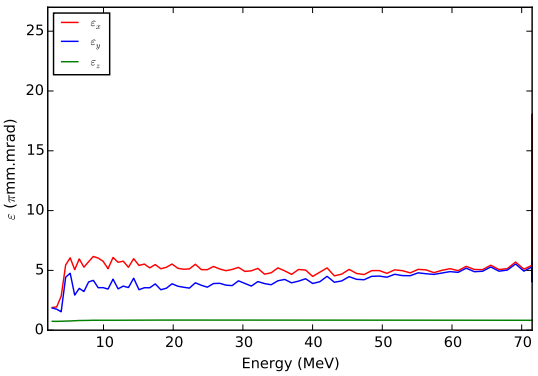

(b) Emittance

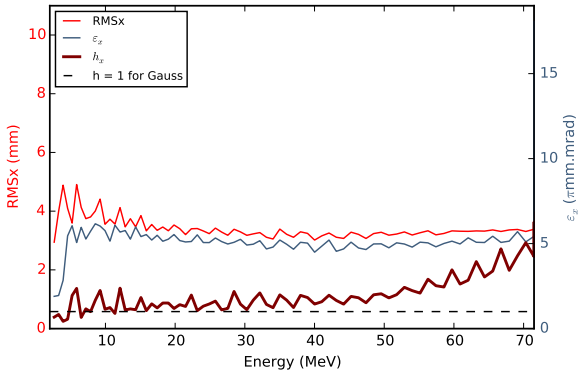

(c) Horizontal RMS, Emit, h

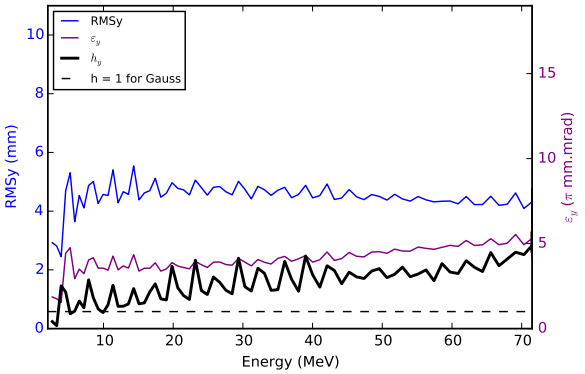

(d) Longitudinal RMS, Emit, h

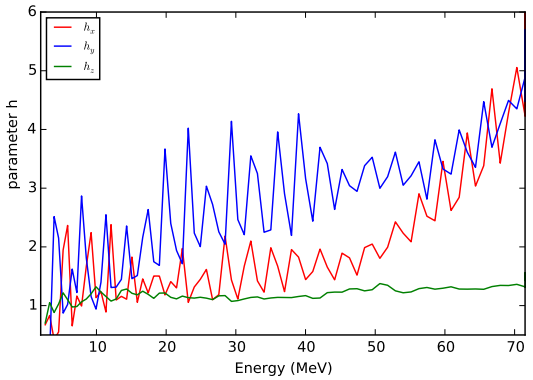

(e) Profile parameter h

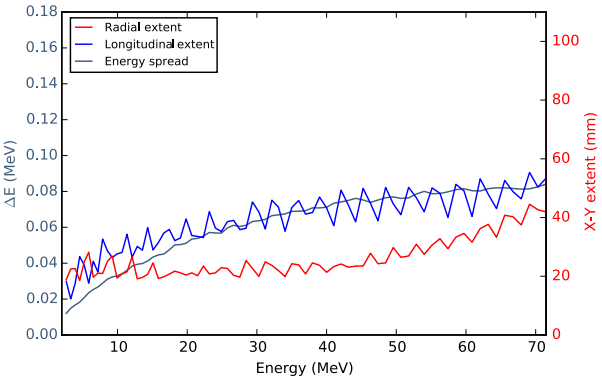

(f) Full extent of the bunch with energy spread

Figure 4.10: Production set-up 2.9 mA case applied to 6-turn 4σ cut (injected 3 mA $5 \cdot 10^4$ macroparticles). X and y planes are well matched with very smooth vertical plane. Longitudinal halo couples to the radial plane after about 40 turns.

symmetry, and not 4 as Injector II lattice suggests. It could be influenced, however, by the two 3rd harmonic or two resonator cavities. Looking at this 360° view, the behaviour of the beam waist resembles the focusing-defocusing FODO cell [32].

Now we take a look at the same parameters as described in previous analysis but in the extraction radius from 360° perspective (Figure 4.11). In subfigure (a) we can clearly see how the RMS x, y, z beam size changes while being propagated through the lattice, resembling a FODO cell. The radial emittance blows up, however y and z emittance stays stable (b). This corresponds to the location of magnets, where the beam undergoes external forces. This is consistent with large variations of RMS beam size in (c).

In Figure 4.12 x and y are well matched with smooth vertical plane, however this exceeds the horizontal physical acceptance. Halo is partly induced by space charge in Injector II and possibly mismatch in stationary distribution, therefore complete halo removal may not be possible without the aid of fast acceleration.

Comparison of beam sizes for currents from 1.9 to 5.7 mA is shown in Figure 4.13. We can see that in all cases the RMS beamsize increases from around 30 MeV what corresponds to increasing longitudinal beam extent. This suggests that the tail couples to the radial plane increasing its radial size. In Figure 4.14 we can see the total charge carried by halo outside of the 5σ.Up to 3 mA beam, around 0.004mA (1%) is found, what is within typical cyclotron operational losses.

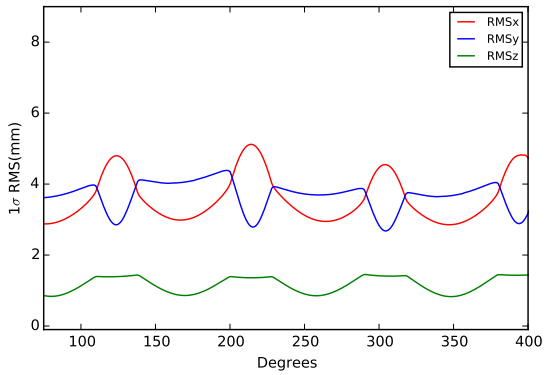

(a) RMS beam size

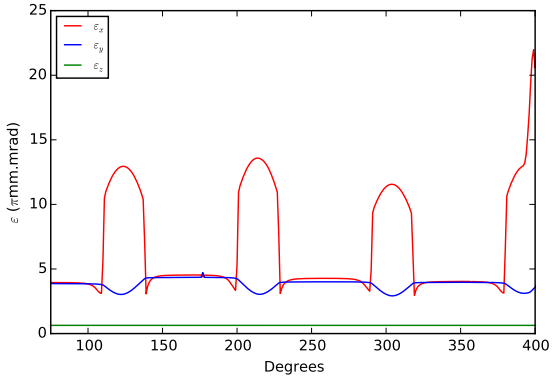

(b) Emittance

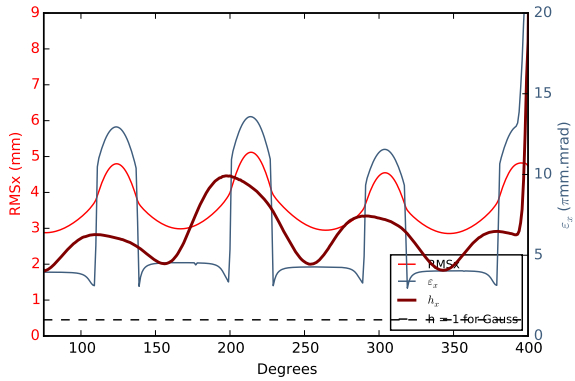

(c) Horizontal RMS, emittance and h parameter.

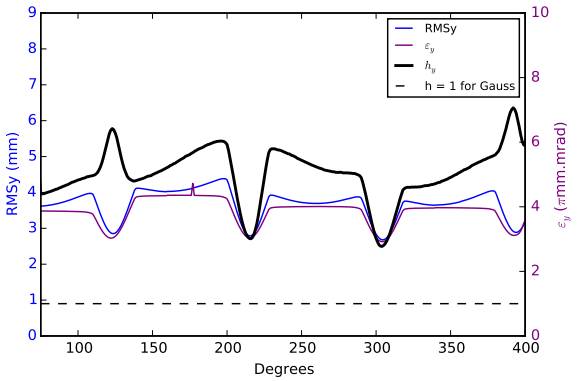

(d) Longitudinal RMS, emittance and h parameter.

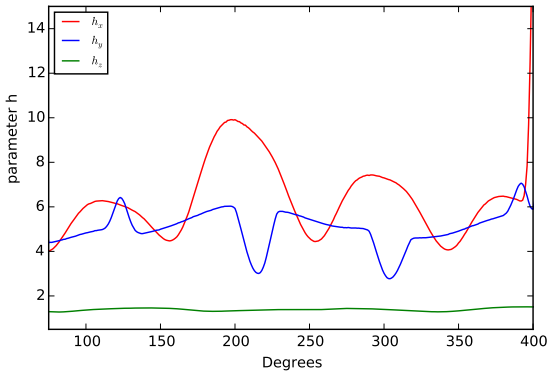

(e) Profile parameter h

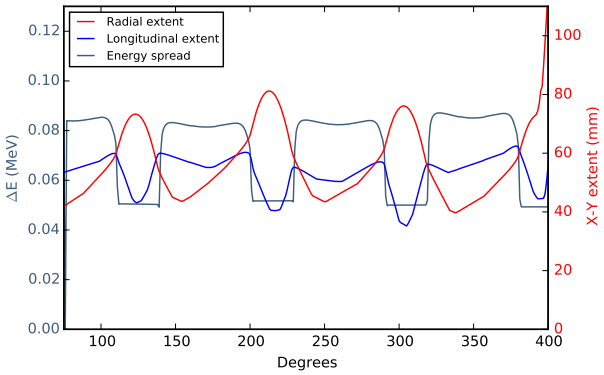

(f) Full extent of the bunch with energy spread

Figure 4.11: Production set-up for 1.9 mA case. 6-turn 4σ cut with injected 2 mA $5 \cdot 10^4$ macroparticles. Last turn in 360°.

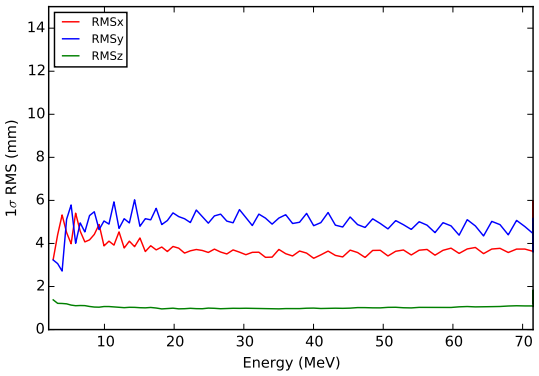

(a) RMS beam size

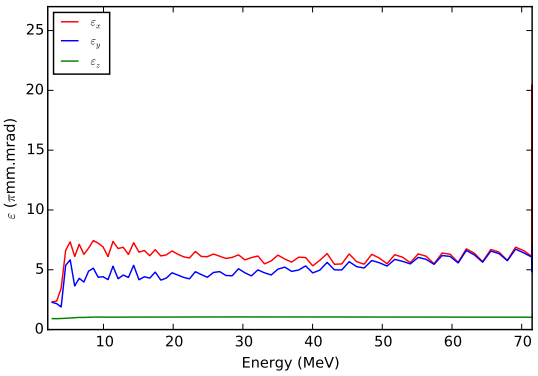

(b) Emittance

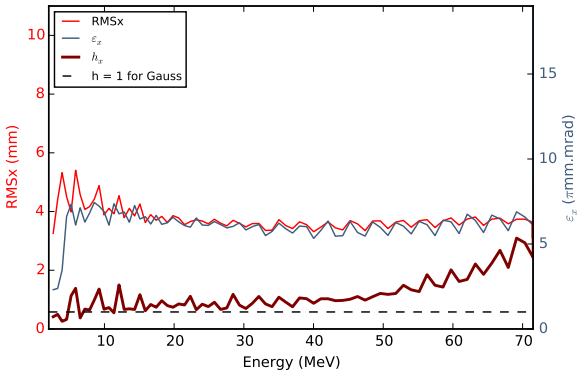

(c) Horizontal RMS, Emit, h

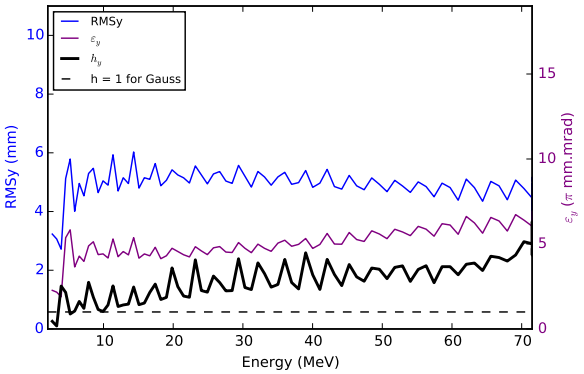

(d) Longitudinal RMS, Emit, h

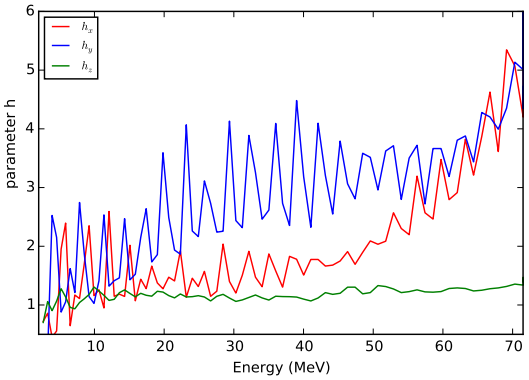

(e) Profile parameter h

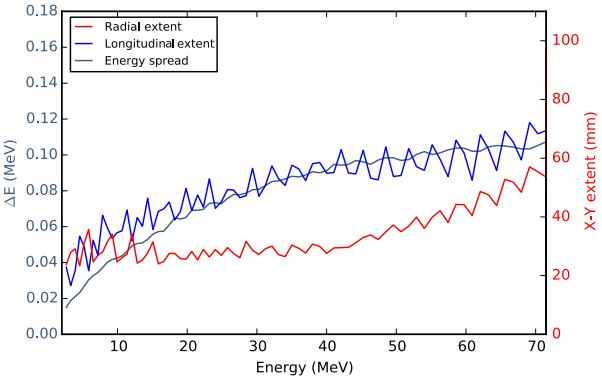

(f) Full extent of the bunch with energy spread

Figure 4.12: Production set-up 3.8 mA case applied to 6-turn 4σ cut with injected 4 mA $5 \cdot 10^4$ macroparticles.

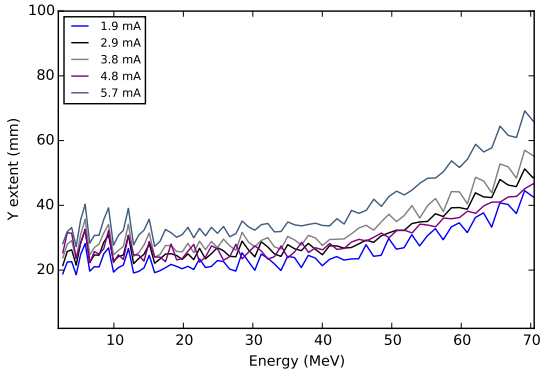

(a) Horizontal extent of the beam

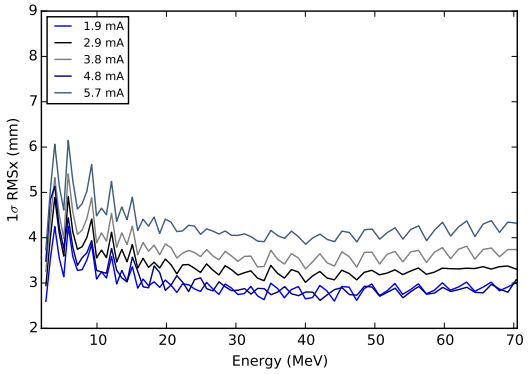

(b) Horizontal RMS beamsize

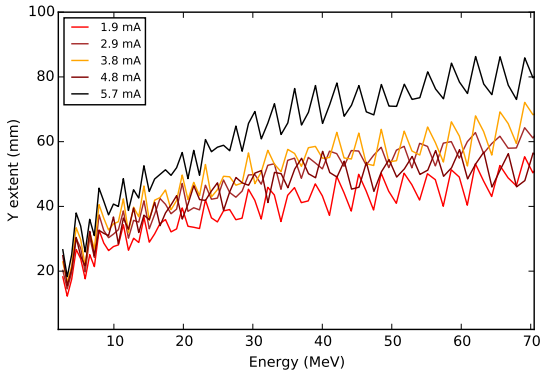

(c) Longitudinal extent of the beam

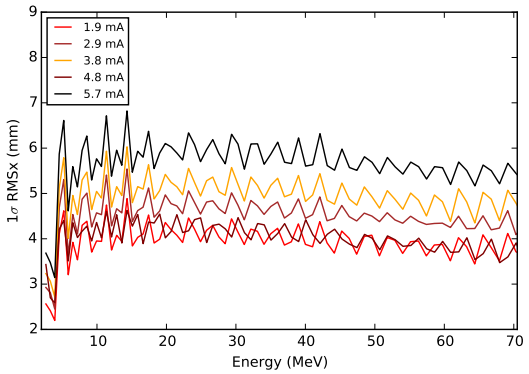

(d) Longitudinal RMS beamsize

Figure 4.13: Comparison of production set-up for 1.9-5.7 mA cases applied to 6-turn 4σ cut with injected $5 \cdot 10^4$ macroparticles. RMS beam size remains constant throughout acceleration while physical extent of the beam (halo) increases.

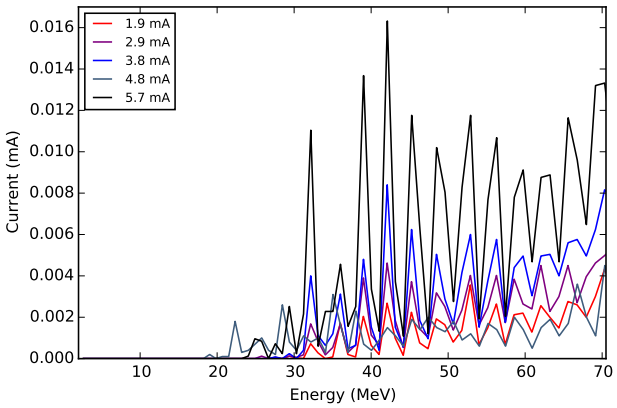

Figure 4.14: Current outside 5σ . The 2.9 mA beam carries 0.005 mA outside the selected boundary for 3.8 mA it already reaches 0.008 mA.

4.3 Upgraded set-up

In this section we apply two 4σ models (continuous 4σ cut and 6-turn 4σ cut) to the upgraded configuration of Injector II. The physical collimator model will be described in the following chapter.

PSI is planning an upgrade of the HIPA facility taking up the extracted beam current up to 3 mA. The upgrade will also include the Injector II and will involve replacing the 3rd harmonic cavities with single-gap resonators, similar to those already installed, allowing faster acceleration (Figure 4.15). In this set-up new cavities operate at peak voltage of 0.425 MV. Unlike the double-gap resonators they begin to accelerate after the collimation region, therefore no significant changes will have to be introduced in the central region. Injector II is expected to accelerate to 72 MeV in 60 turns.

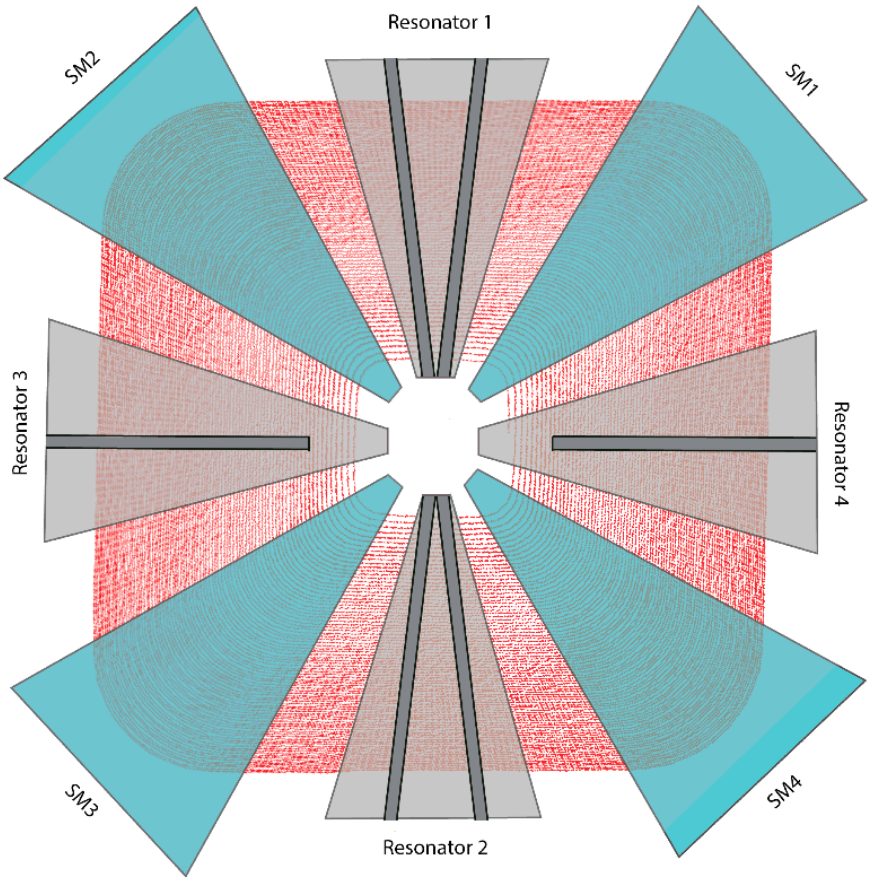

Figure 4.15: Schematic of the Injector II upgraded configuration. The cyclotron has four sector magnets operating at 2 T (green), two double-gap resonators and two single-gap resonators (grey).

.

4.3.1 Applying continuous 4σ cut model to the upgraded configuration

Using the same constant 4σ cut principle, we can test the intensity limits of Injector II after the planned upgrade. Figure 4.16 shows 2 mA distribution accelerated and cut continuously to give final 1.8 mA. Beam size is not changing significantly, but the turn width is, hence higher intensities can be passed. Numerical simulations suggest that in this ideal case, exchanging cavities would allow delivering much higher intensities with total beam extent of 30×40 mm. Turn separation in this configuration is expected to double (up to 40 mm).

Modelled data in Figures 4.16 to 4.19 shows that RMS beam size (a), emittance (b) are very well matched after around 20 turns with minimal halo growth for all considered cases. The profile parameter (e) does not exceed 1.5, meaning the beam profile is close to Gaussian. RMS beam size grows from 3 mm to 4 mm at 5.3 mA with full beam extent reaching 30 x 40 mm in the mid plane. They appear elevated as we show results modelled with 10^6 macroparticles. This should still be sufficiently small to extract from Injector II with the new turn separation, however with the present acceptance of 6σ the RMS radial width is 24 mm, which may exceed the extraction septum acceptance. As shown in Figure 4.17 for 3.5 mA and Figure 4.18, not even 3.5 mA but intensities close to 5 mA could be passed through. In Figure 4.19 a comparison of RMS beam size and beam extent is shown. We will take a look at the scaling of the beam size with intensity in Chapter 6.

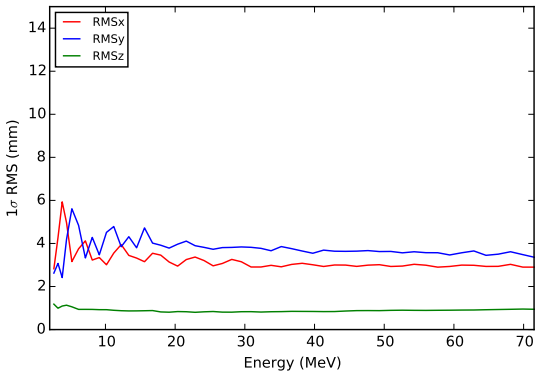

(a) RMS beam size

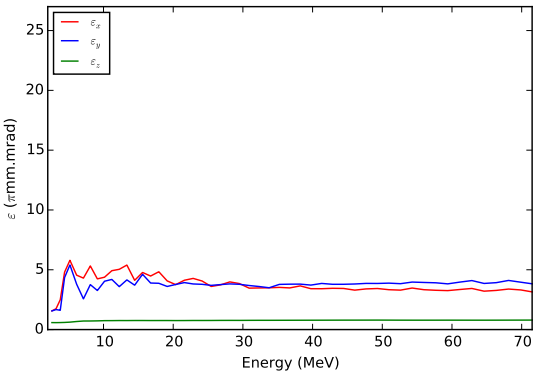

(b) Emittance

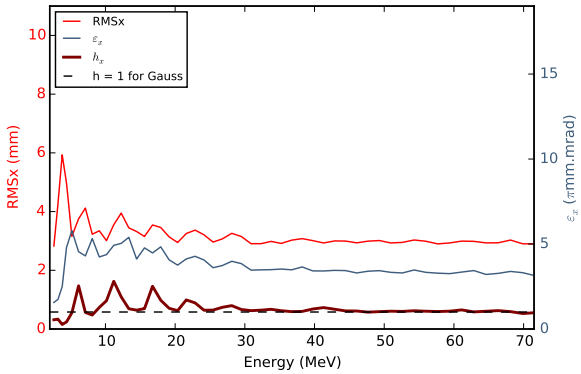

(c) Horizontal RMS, Emit, h

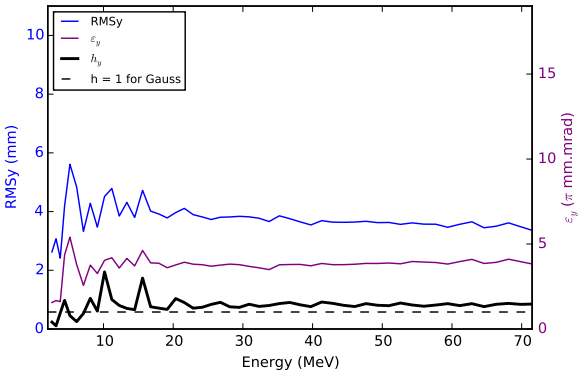

(d) Longitudinal RMS, Emit, h

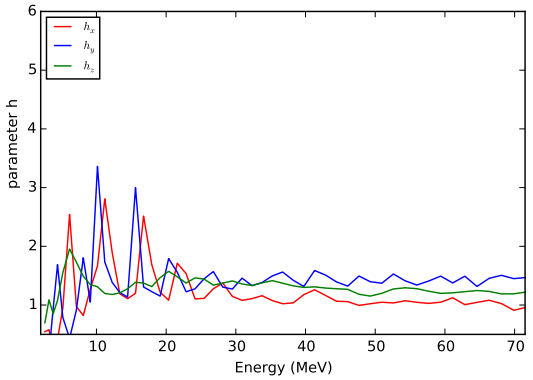

(e) Profile parameter x y z

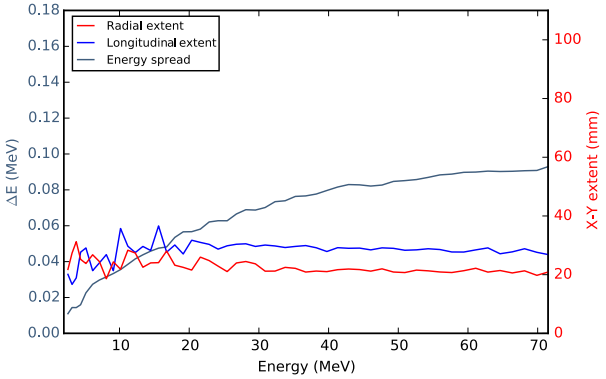

(f) Full extent of the bunch with energy spread

Figure 4.16: Upgraded set-up 1.8 mA case applied to continuous 4σ cut with injected 2 mA 10^6 macroparticles.

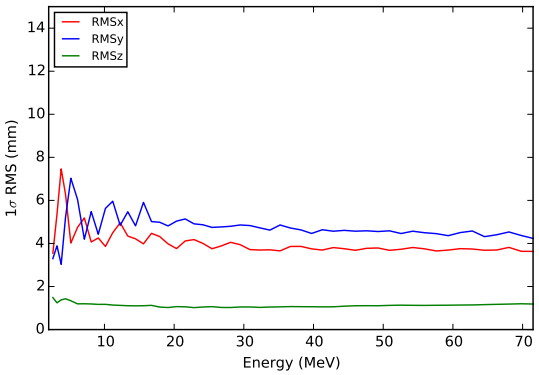

(a) RMS beam size

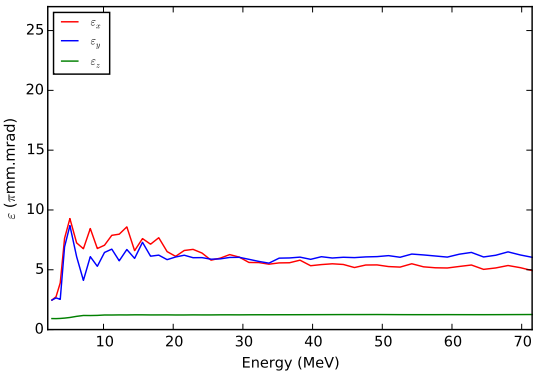

(b) Emittance

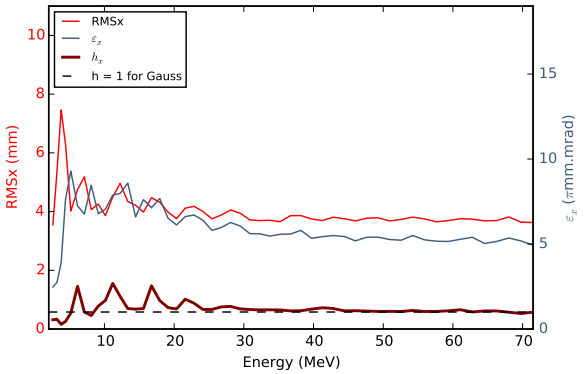

(c) Horizontal RMS, Emit, h

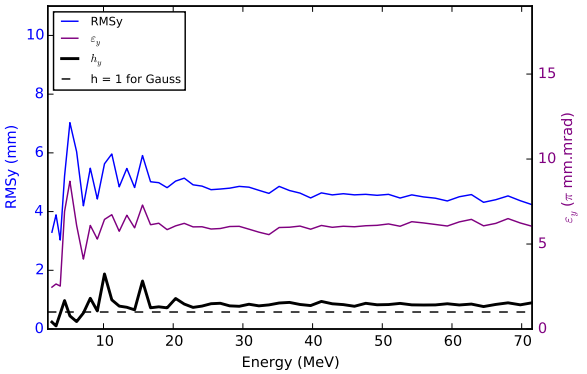

(d) Longitudinal RMS, Emit, h

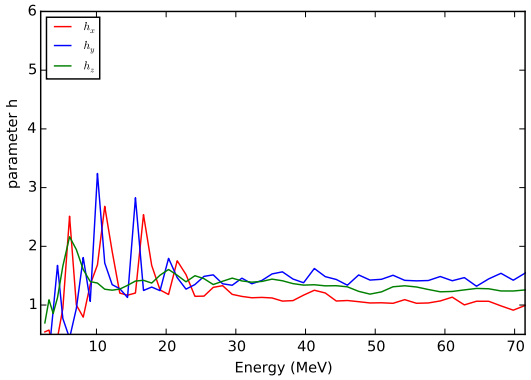

(e) Profile parameter x y z

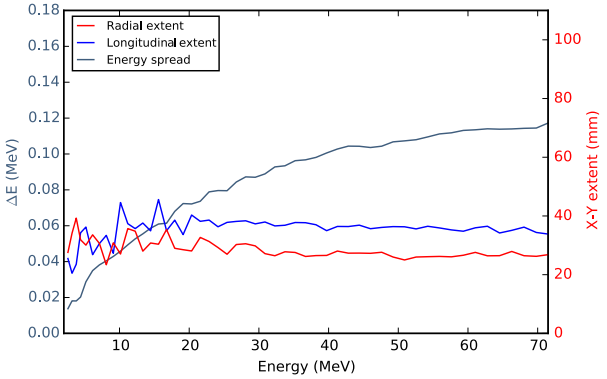

(f) Full extent of the bunch with marked energy spread

Figure 4.17: Upgraded set-up 3.5 mA case applied to continuous 4σ cut with injected 4 mA 10^6 particles. Very well matched case.

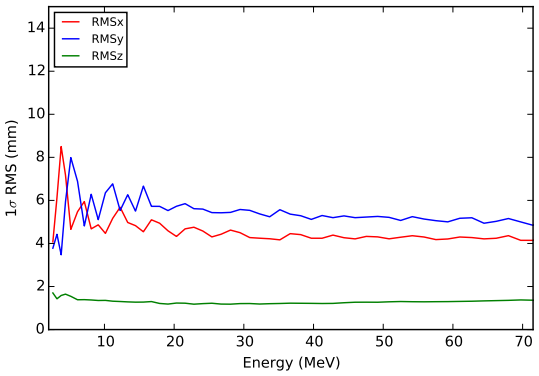

(a) RMS beam size

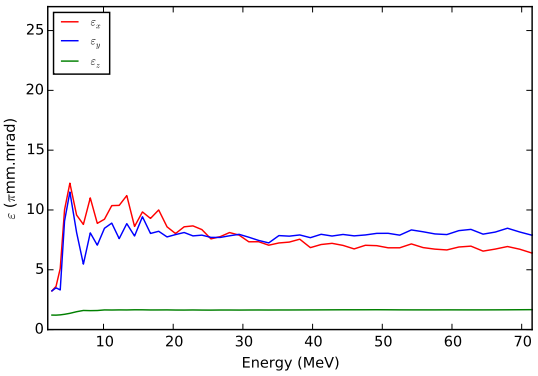

(b) Emittance

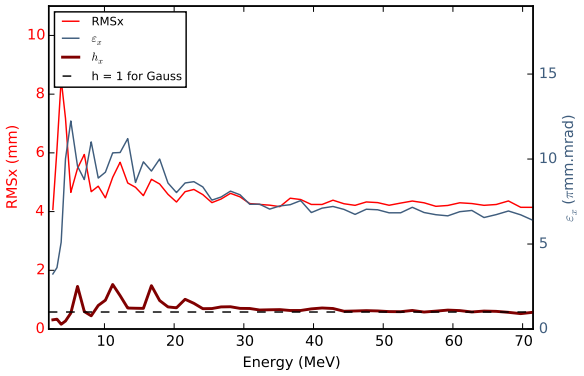

(c) Horizontal RMS, Emit, h

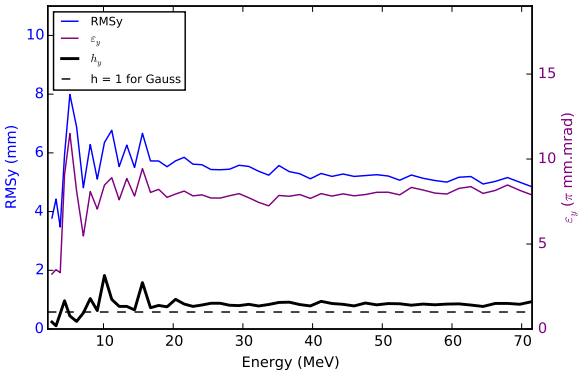

(d) Longitudinal RMS, Emit, h

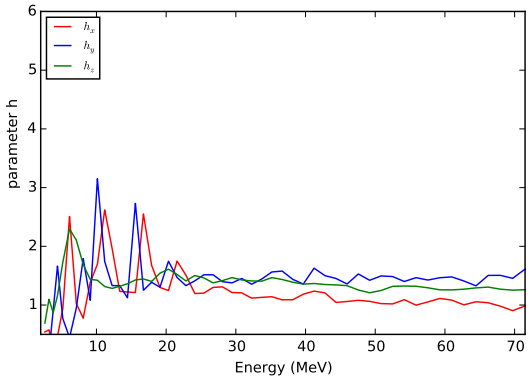

(e) Profile parameter x y z

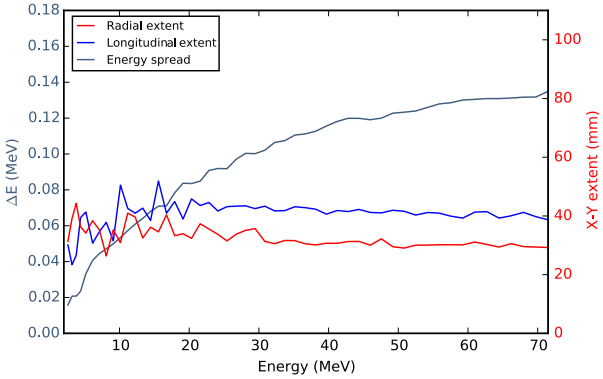

(f) Full extent of the bunch with energy spread

Figure 4.18: Upgraded set-up 5.3 mA case applied to continuous 4σ cut with injected 6 mA 10^6 particles.

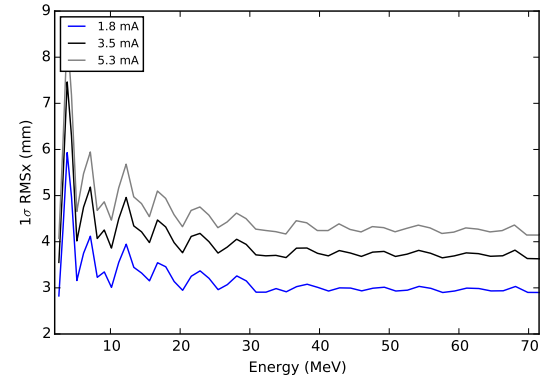

(a) RMSx beam size

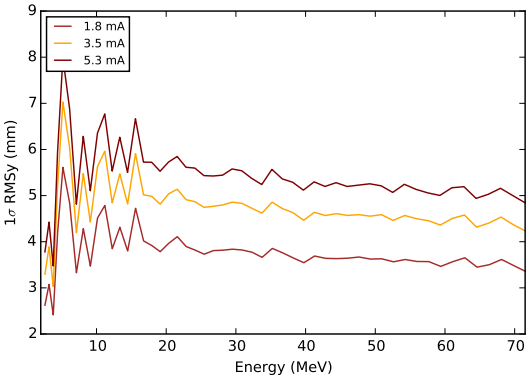

(b) RMSy beam size

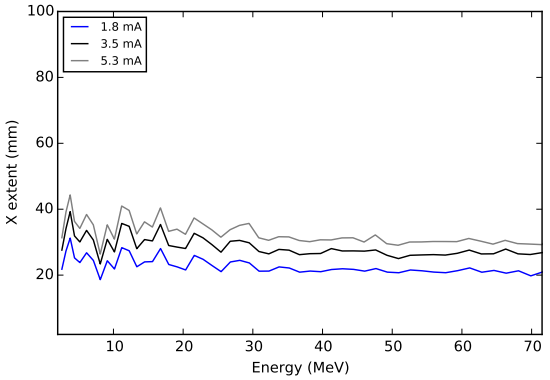

(c) Horizontal beam extent

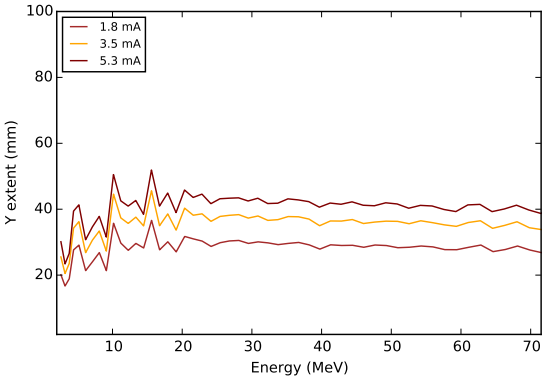

(d) Vertical beam extent

Figure 4.19: Comparison of 2, 4, 6 mA injected currents with continuous 4σ cut in the upgraded configuration leaving net 1.8, 3.5 and 5.3 mA currents respectively. Modelled with10^6 macroparticles.

4.3.2 Applying 6-turn 4σ cut model to the upgraded configuration

We have extended the approach of the 6-turn 4σ cut also to the upgraded configuration of Injector II. It becomes apparent that replacing the 3rd harmonic cavity makes significant improvement in beam quality. The number of turns required to accelerate to 72 MeV will decrease to 60 turns, and final turn separation is expected to increase up to 4 cm. It is important to note that the multi particle distributions used for these simulations are the same. For example some parameters of accelerated 2 mA distribution ($5 \cdot 10^4$ particles) are shown in Figure 4.20. Currents from 1.9 to 5 mA have been investigated (Figures 4.20- 4.23). Looking through (a)-(f) it is remarkable how well matched the beam is with uniform RMS and emittance. Even though we stop cutting after the 6th turn, halo formation is also minimal with h-parameter not exceeding 2 (e) and full beam extent (f) of 20 x 30 mm for currents of 2 mA in the mid-plane.

Even after the cut is removed full beam extent does not exceed 20 mm horizontally. RMSx of 2 mm, gives 5σ of only 10 mm. In Figure 4.22, the RMSx of 3 mm, gives 5σ of 15 mm only, full horizontal beam extent is less than 30 mm. Such parameters are within the physical apertures of extraction devices. These results suggest that with such set-up even at 4 mA (3.8 mA) losses will be significantly decreased.

6 mA beam with RMSx close to 4 mm is may be too large to pass through the extraction septum (Figure 4.24). The current limit based on this model is set at 5 mA with RMSx of approx 3.2 mm as shown in Figure 4.23.

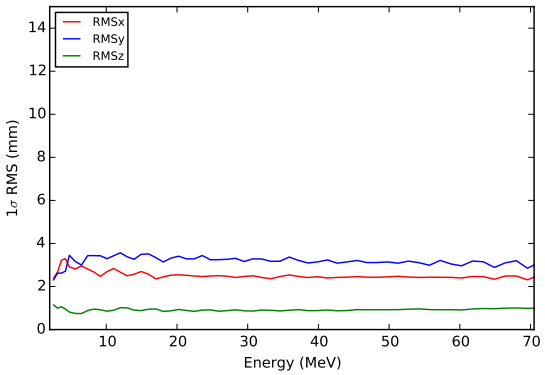

(a) RMS beam size

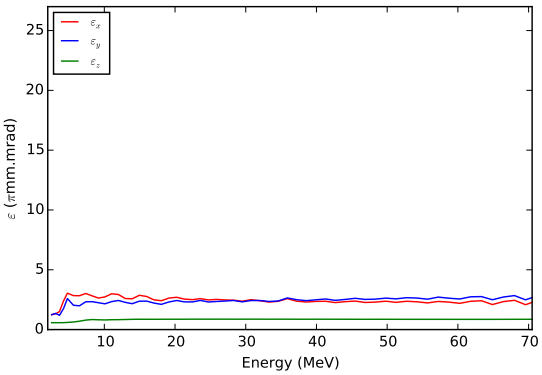

(b) Emittance

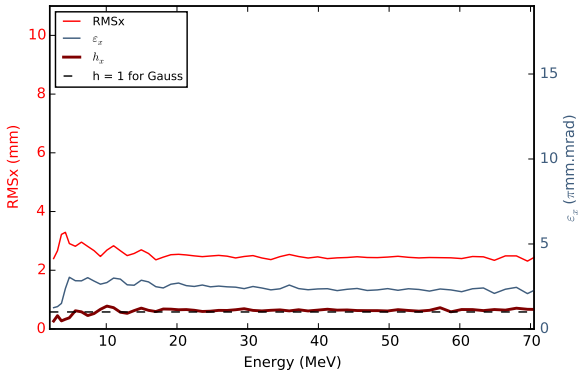

(c) Horizontal RMS, Emit, h

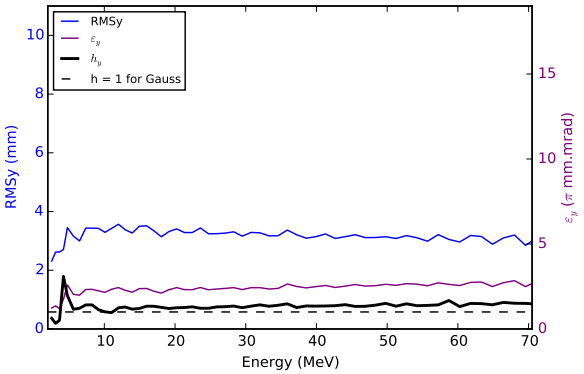

(d) Longitudinal RMS, Emit, h

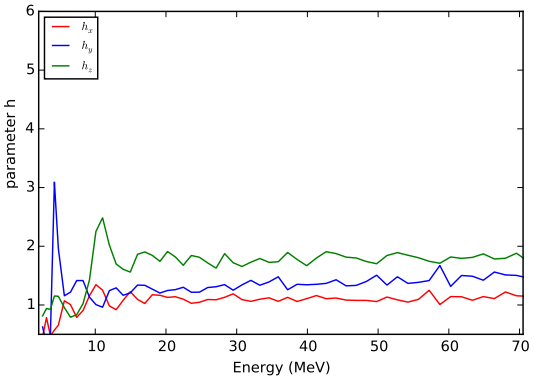

(e) Profile parameter h

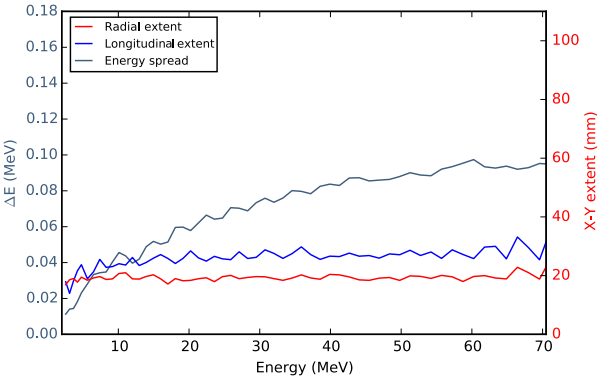

(f) Full extent of the bunch with energy spread

Figure 4.20: Upgraded set-up 1.9 mA case applied to 6-turn 4σ cut with injected 2 mA $5 \cdot 10^4$ particles. X , y and z planes are exceptionally well matched.

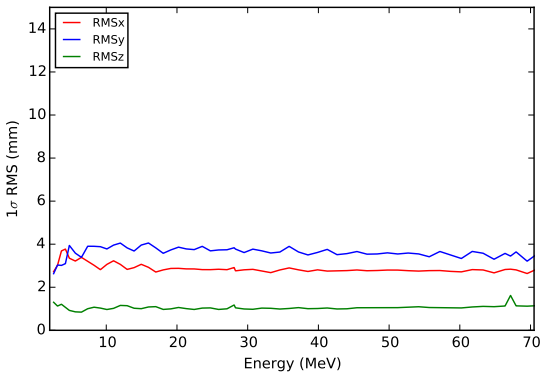

(a) RMS beam size

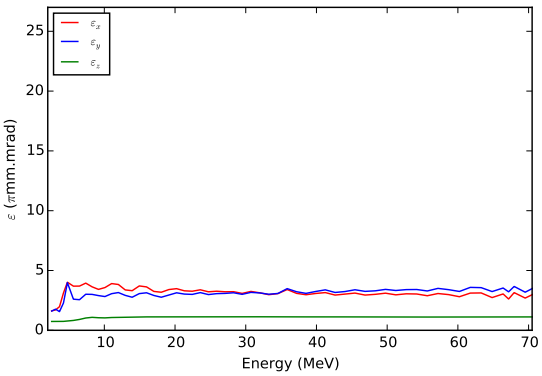

(b) Emittance

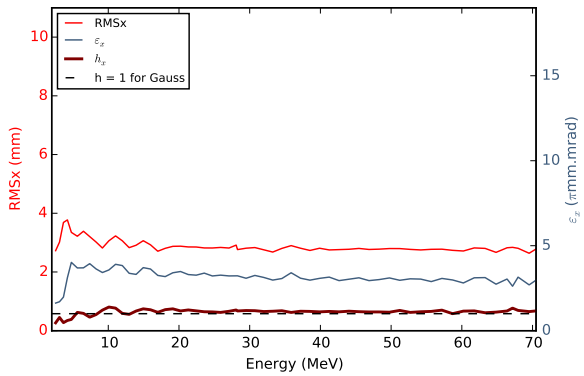

(c) Horizontal RMS, Emit, h

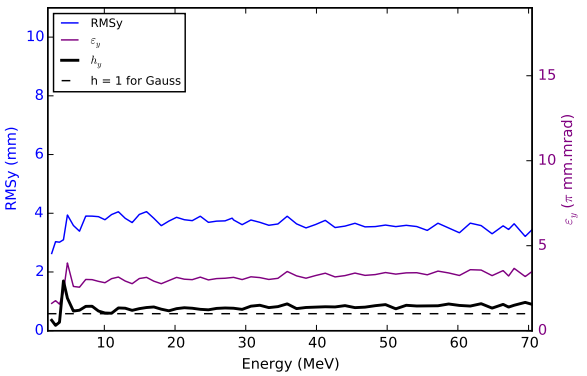

(d) Longitudinal RMS, Emit, h

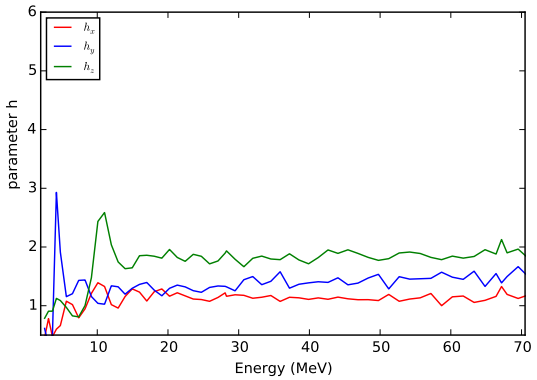

(e) Profile parameter h

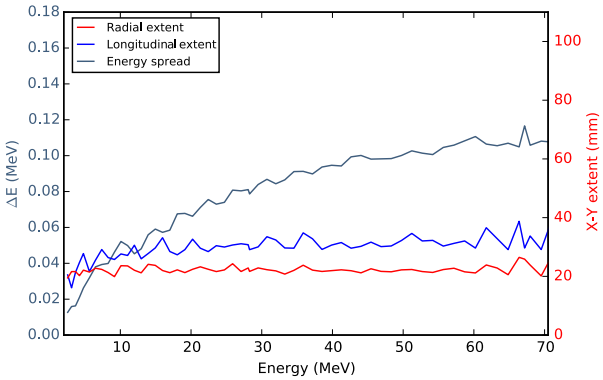

(f) Full extent of the bunch with energy spread

Figure 4.21: Upgraded set-up 2.9 mA case applied to 6-turn 4σ cut with injected 3 mA $5 \cdot 10^4$ particles. X , y and z planes are exceptionally well matched leading to near-gaussian distribution as profile parameter in all planes is close to unity.

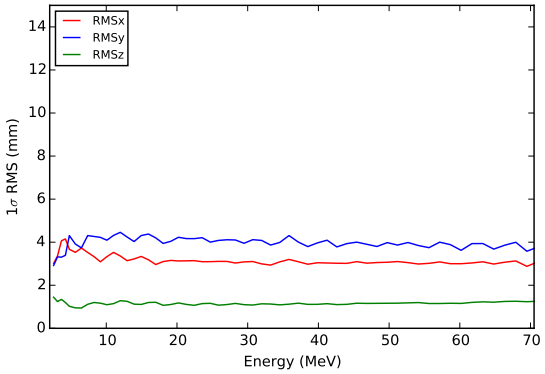

(a) RMS beam size

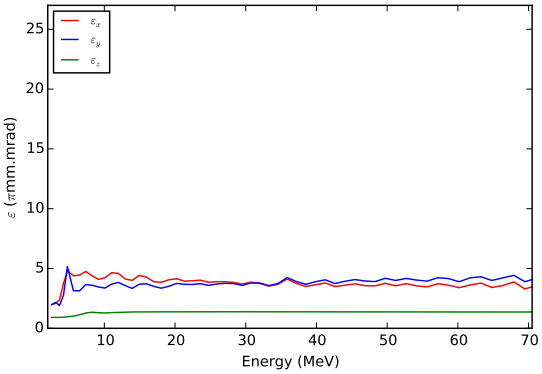

(b) Emittance

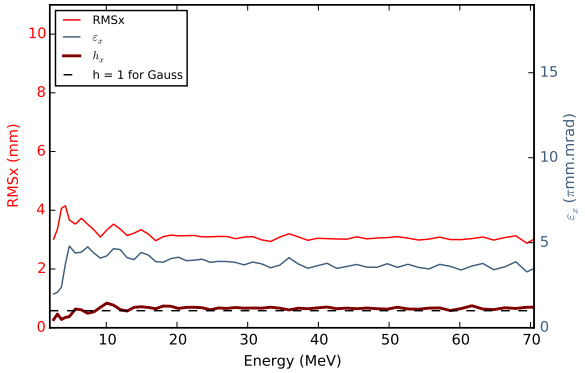

(c) Horizontal RMS, Emit, h

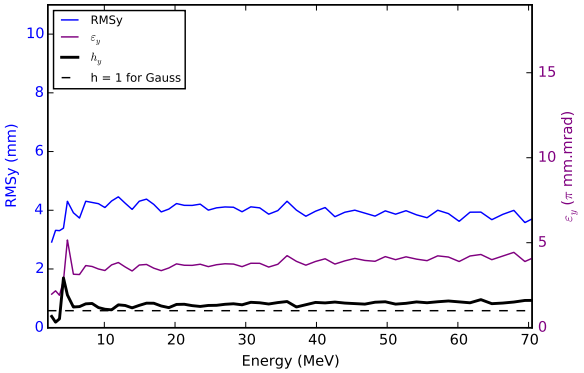

(d) Longitudinal RMS, Emit, h

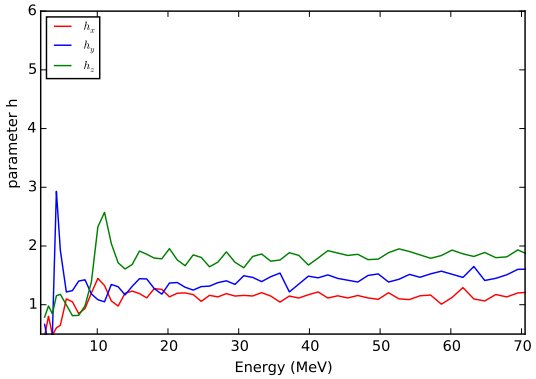

(e) Profile parameter h

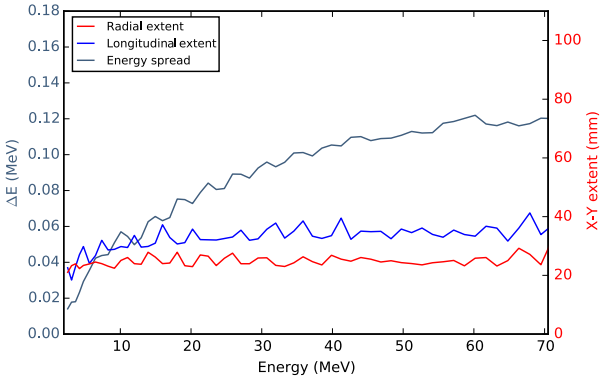

(f) Full extent of the bunch with energy spread

Figure 4.22: Upgraded set-up 3.8 mA case applied to 6-turn 4σ cut with injected 4 mA $5 \cdot 10^4$ particles. X , y and z planes are exceptionally well matched. Near-gaussian distribution as profile parameter in all planes is close to unity.

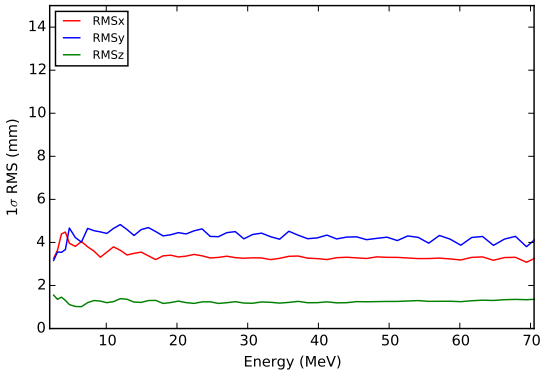

(a) RMS beam size

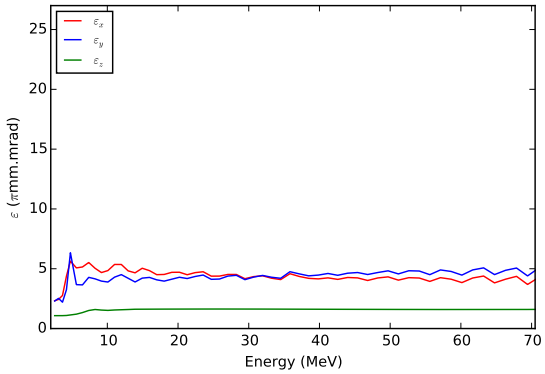

(b) Emittance

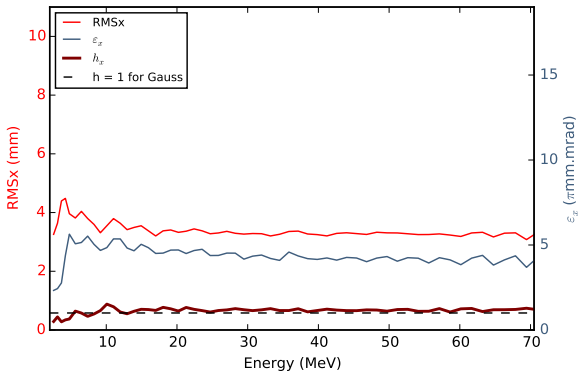

(c) Horizontal RMS, Emit, h

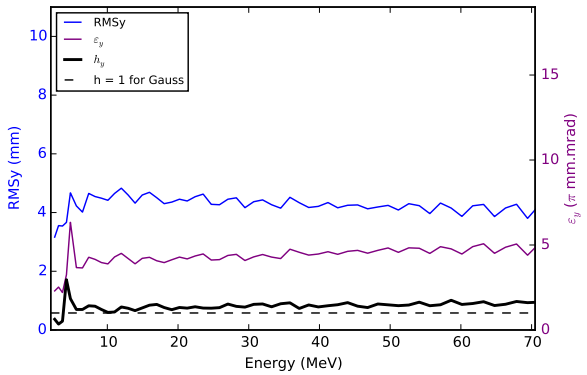

(d) Longitudinal RMS, Emit, h

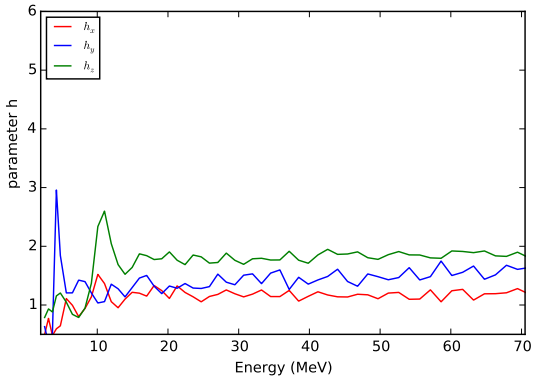

(e) Profile parameter h

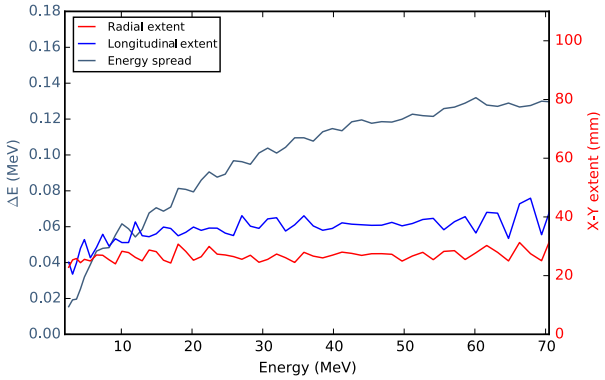

(f) Full extent of the bunch with energy spread

Figure 4.23: Upgraded set-up 5.0 mA case. 6-turn 4σ cut with $5 \cdot 10^4$ macro-particles.

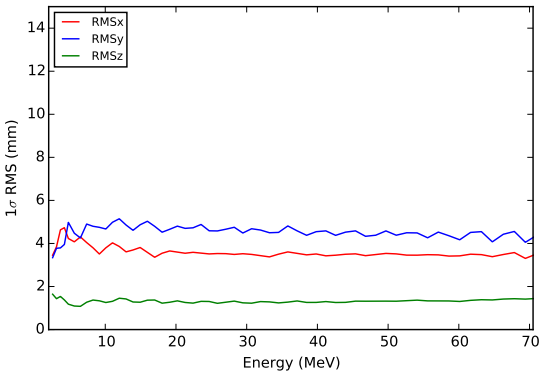

(a) RMS beam size

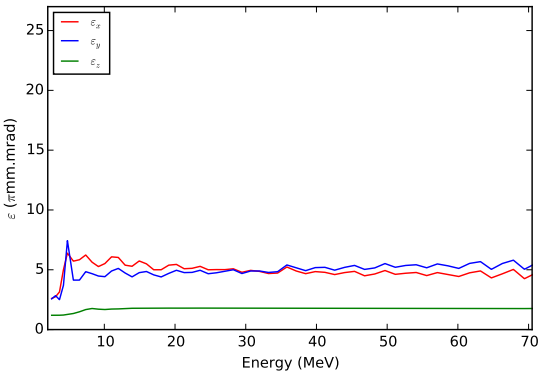

(b) Emittance

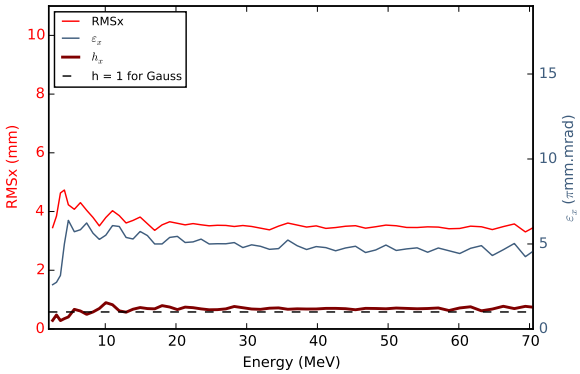

(c) Horizontal RMS, Emit, h

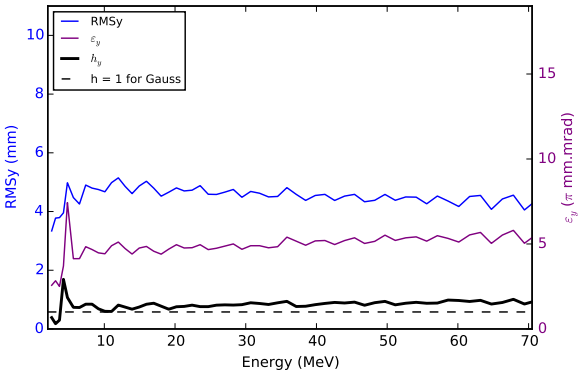

(d) Vertical RMS, Emit, h

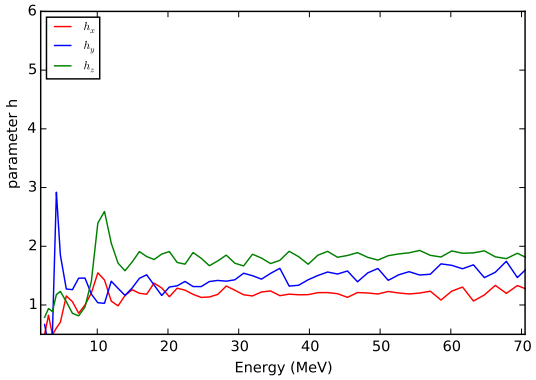

(e) Profile parameter h

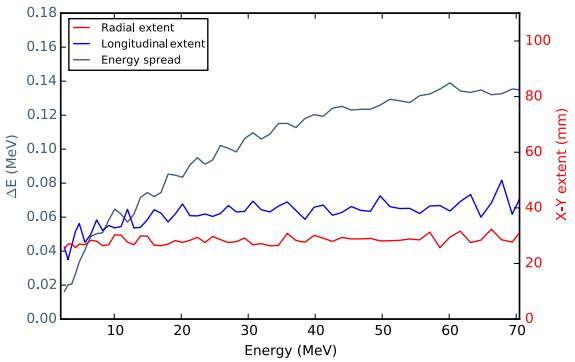

(f) Full extent of the bunch with energy spread

Figure 4.24: Upgraded set-up 5.8 mA case applied to 6-turn 4σ cut with injected 6 mA $5 \cdot 10^4$ particles.

4.4 Chapter summary

We have considered 3 models (out of which 2 are described in this chapter) of Injector II under production and upgraded configurations. For simplicity we have started from a very simple model cutting particles around 4σ continuously throughout the acceleration. This model is idealised as we clean the beam with collimators over the first few turns only. To better represent the central region, in the next model, we stop cutting after 6 turns. All models are based on parameters that are optimised to best match Injector II.

Under the production configuration, the continuous cut model limit is approximately 3.5 mA and the 6-turn model limit is a bit lower, of order of 3 mA, since we stop cutting after 6 turns and allow the space charge time to expand the bunch. If new cavities are installed extracting 5 mA should be still feasible. These are approximate models and the physical collimator model will be discussed in the following chapters. Being able to run Injector II at 3 mA with existing cavities would be an amazing achievement as this is the intensity planned after the upgrade. The upgrade would then bring even more advantages.

Chapter 5

Physical collimator model

In this Chapter we describe the final stage of the precise model of injector II, the physical collimator model. Full analysis with collimator currents and peak matching is focused on the production configuration. We also present initial modelling of the upgraded configuration.

5.1 Applying the physical collimation model to the production configuration

In recent years flat-top cavities have been running in accelerating mode. The presented model is based on the original flat-topping mode, and later in the Section 6.3.2 we show comparison of both modes showing negligible differences, which proves that not using flat-top cavities is possible since the beam width is small enough. There is an advantage from such changes, that can help to accelerate in fewer turns, as the slightly increased gradient of the final turn separation. The 2015 year operation parameters have been used in the collimation model. Below are the main parameters used in the production mode model:

- 83 turns ± 1 (81 ± 1 in the previous year),
- Injection energy: 868.5 keV,
- Energy: 72 MeV,
- Radius: 392.0 mm,
- Resonator gap voltage: 215.7 kV_{peak},

- 3rd harmonic: 31.0 kV_{peak},
- Added voltage offset: 87.919 kV_{peak},
- RF phase: 50°,
- Azimuth: 30°,
- Radial momentum: -5.50008 $\cdot 10^{-3}$ ($\beta\gamma$).

The collimation model simulation starts at 30° angle from the centre of the SM1 magnet. The central 90° injection is not included in the model. As mentioned before, Injector II central region beam is strongly correlated and generating bunches that would represent the real beam fairly in the machine is not trivial. This could be done by modelling the buncher and the transfer line, however it does not fit into the scope of this work. At the point where we start the simulation, 11 mA bunch is cut by KIS2 and KIP1 collimators, therefore 9.5 mA is believed to be a good approximation.

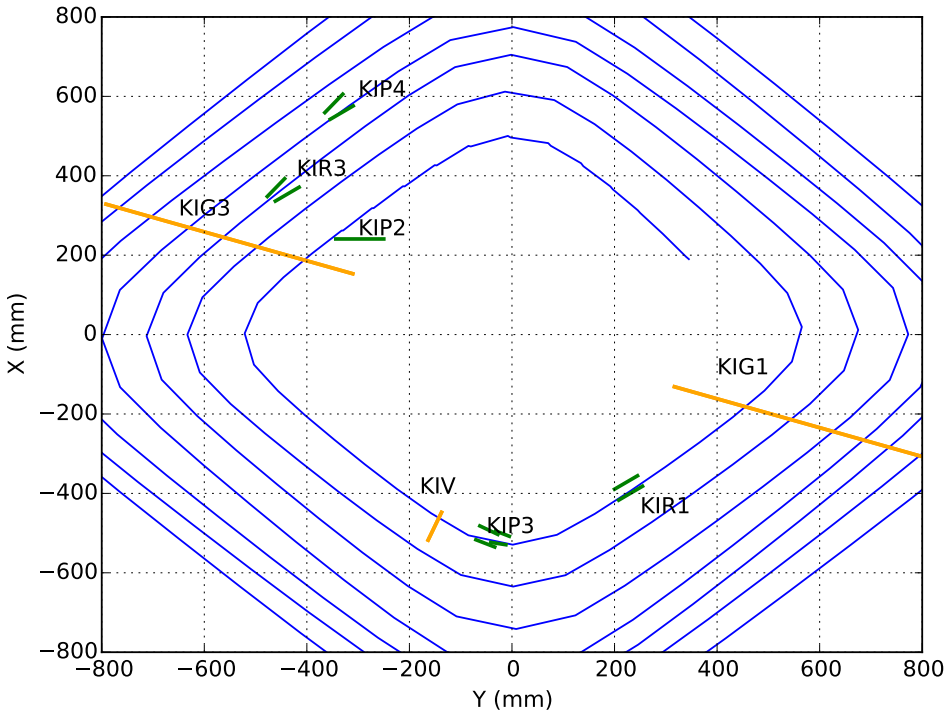

Figure 5.1: Top view on the modelled collimators in the central region. Green colour marks horizontal and yellow vertical collimators.

Figure 5.1 shows the modelled central region of Injector II with collimators included in the simulations. Several collimators that are used to protect the magnets or cavities have been excluded from the model e.g. KIP1 or KIS2. In Section 5.1.2 we take a closer look on the topic of collimators.

5.1.1 Probe environment

For more accurate data validation, several Injector II probes have been included in the model matching their locations in the cyclotron. A schematic of diagnostic instruments in the machine is shown in Figure 5.2. Radial probes save intensity information along its length. The probes of Injector II are as follow:
1. RIE1: extraction probe located 158° from SM1 sector magnet, covers all intensities over the last 7 turns, built up from a wire with a stopping block;
2. RIE2: vertical extraction probe, over the last 5 turns, made up of two plates approx 15 mm apart with beam going in between, measures how much the bunch deviates vertically from the centre;
3. RIL1: radial intensity probe, allows full machine scan but only to approx 2 μA as at higher intensities the probe saturates;
4. MXPO1: extraction probe, up to 1 mA, covers last 4 turns, located after the septum, shows the extraction radius;
5. RIZ1: time structure measuring probe, located 5° before RIE1;
6. MIF: phase probe located at 30° from SM1, measuring the RF phase.

As we aim at investigating all intensities from micro to milli Ampere, RIE1 and RIZ1 probes have been chosen for validation as they can measure full intensity range. The radial probe RIL1 measures across all turns, however at very small intensities. Matching to this data does not guarantee that our model would fit the data of higher intensities. Each of the sets of initial conditions we generate is only a small fraction of what Injector II is operating at. At any given time these initial conditions can change. Matching turn patterns for higher intensity measurements seems to be sufficient to investigate the upper end of this scale.

The final step of the 3D model is to introduce the collimation system. We have started with selecting collimators based on the current recorded on real machine collimators (more details in Section 5.1.3). A 9.5 mA[1] stationary distribution has been

[1] At KIP2, where we start to model collimators there is approx. 9.5 mA of the 11 mA beam left.

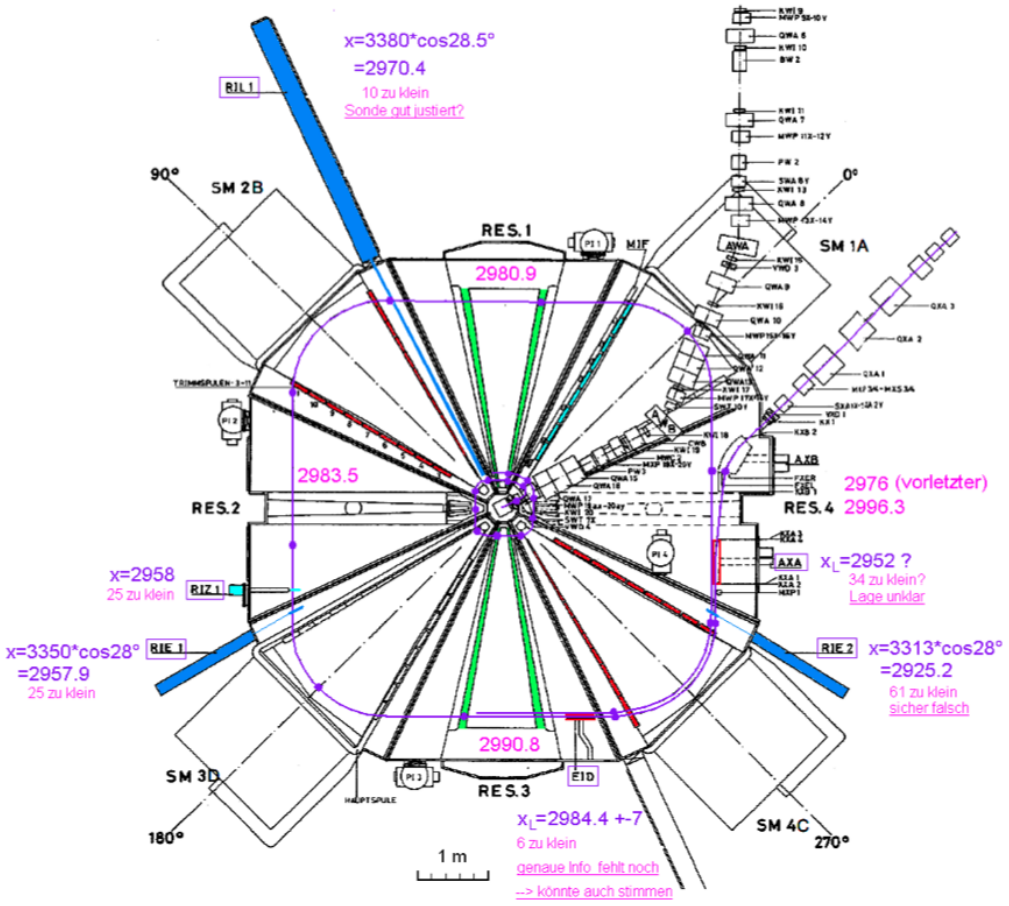

Figure 5.2: Diagnostic devices in Injector II with marked predicted last turn orbit and corresponding energies and radii [1].

used, as expected at 870 keV orbit after injection, to give us an overview of the operation of the collimators. However, an obvious step would be to model parts of the injection line with the buncher to develop an elongated distribution with time structure matching the one found in Injector II. Unfortunately this does not fit into the timescale of this project.

Initial analysis of the distribution passed through the collimators and accelerated to 72 MeV indicates that even though the bunch is significantly cut by collimators (KIP2 alone cuts around 50%), we observe the formation of a steady compact core with some halo around. This is due to the strong longitudinal-transverse coupling combined with space charge. In Figure 5.3 we can see a large and increasing h-parameter that is consistent with the configuration space density plots in Figure 5.4 in which we can clearly see the formation of compact core with large halo around it. This follows predictions as

described in [37], where we read that *"a non-matched non-circular bunch will match itself after a number of turns (...) and the generated halo will depend upon the initial mismatch"*, machine non-linearities and space charge.

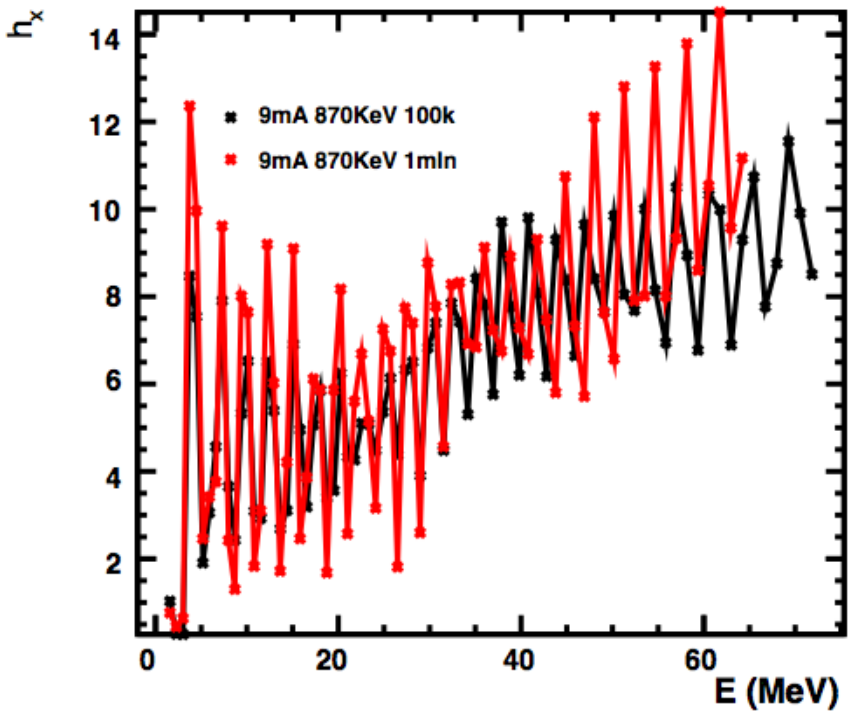

Figure 5.3: Horizontal halo parameter for 10^5 and 10^6 particle distributions. We observe steady growth of this parameter which is consistent with the configuration space plots.

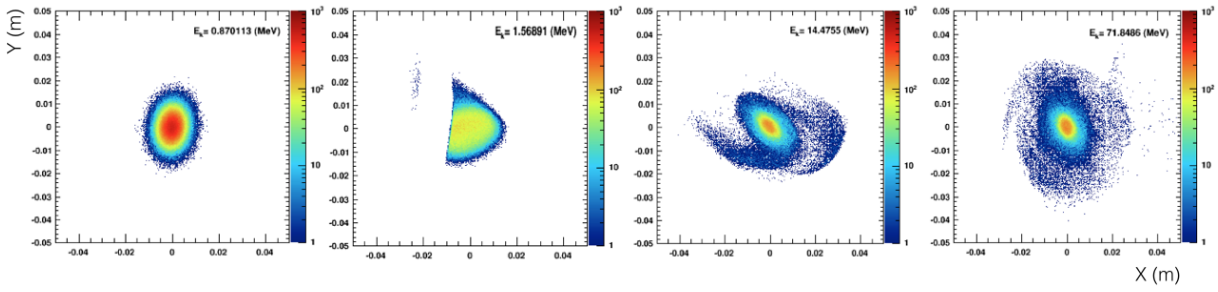

Figure 5.4: An example of progression of the distribution in the configuration space passed through collimators and accelerated to 72 MeV. Despite significant distribution deformations due to large cuts, the tails "wrap" around the spiralling centre of the distribution leading to formation of a stable core with halo around.

5.1.2 The collimators

11 mA beam entering the central region of Injector II is heavily collimated. Around 60% of the initial intensity is lost at the collimators in the first four turns at energies of 0.87 and 2.5 MeV leading to excellent beam properties. The successful operation of Injector II has been done by years of experience, however it is not known whether this is the best set-up. The provided collimator locations are based on 40 year old drawings and measurements of the exact positions is ongoing. There are 14 collimators in the central region of the cyclotron of which 8 are included in the model. Those cutting small currents or used as magnet protectors are omitted at this point, however they can be reconsidered as they may turn out to be crucial in halo cleaning. There are two horizontal single-leaf collimators: KIP1 and KIP2, four double-leaf collimators (KIL, KIP3-RIL2, KIR1, KIR3 and KIP4) and seven double-leaf vertical collimators (KIL, KIG2, KIG3, KIV, EIV2, KIG1 and KIV5) plus central region collimators. Those included in the model are KIP2, KIG3, KIG1, KIV, KIR1, KIR3, KIP4 and RIL2I4.

The modelled collimators are located at an angle with respect to the beam direction, and each leaf can move independently. In Figure 5.5 we see the top view of the central region with the collimators. Currents read on the collimators from the PSI EPICS control system that are used in this research have been measured over one hour and can be found in the Appendix A.27.

Additional readings of Injector II collimators were taken on a stable day, where no cyclotron trips where noted for 24 hours. Table 5.1 shows average, minimum and maximum currents read during that day on the collimators included in the model. The current read on the probe EWBRI before injection is on average 10.5 mA and current (MHC1) of nearly 2.2 mA had been extracted that day. The total current on selected collimators adds up to around 7.2 mA, as we are starting cutting at KIP2, the simulated distribution should be of around 9.3 mA. For simplicity 9.5 mA particle matched distributions have been generated for $5 \cdot 10^4$, 10^5 and 10^6 macroparticles with injected emittance of 3.8 mm$\times$mrad and energy of 870 keV. Injected bunch entering Injector II has mixed phases and it is through cutting with injection collimators (KIS, KIP1, KIP2) that the phase is established. Without modelling the injection line and the buncher, that is outside of the scope of this work, we cannot predict parameters of such distribution. The simulation starts after the 90° bend at azimuth of 30°. The analysis and statistical significance will be discussed in the following sections.

The method used to implement this data into the model has been based on calculating relative current on each simulation macroparticles. $5 \cdot 10^4$ particle distribution was

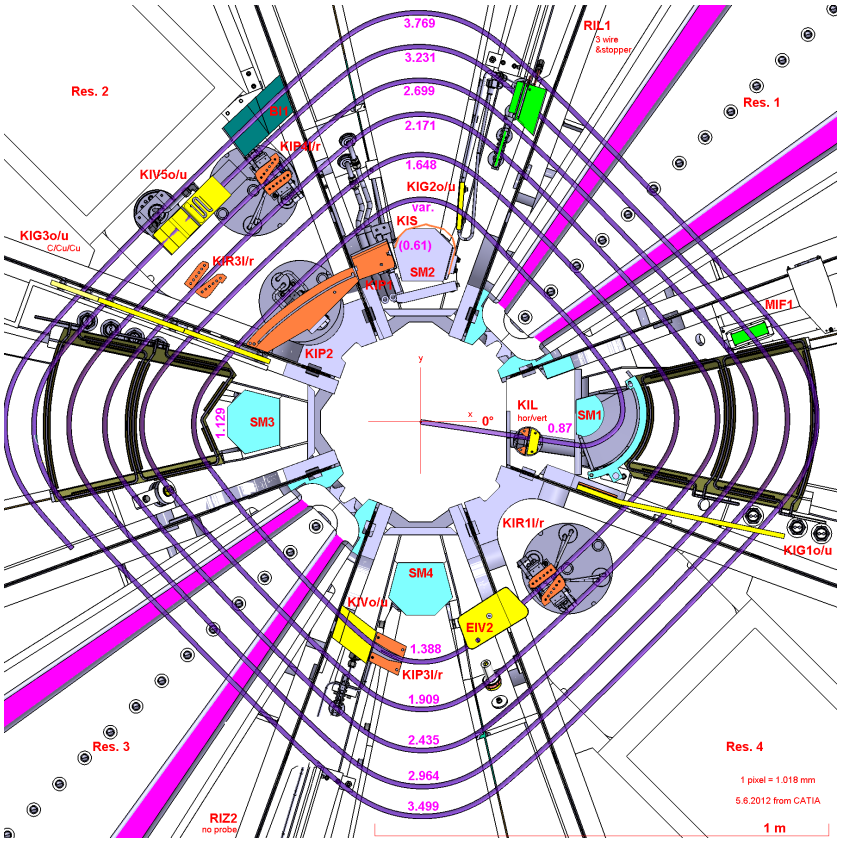

Figure 5.5: Central region of Injector II with highlighted collimators. Vertical ones are marked in yellow and horizontal in orange [1].

used for adjusting collimator positions, to speed up this lengthy process. These values were then used to calculate the number of (macro)particles that need to be removed by the collimators. Then the 10^5 and 10^6 particle distributions have been propagated throughout the accelerator. More collimator data can be found in the Appendix A.27.

5.1.3 Currents on collimators

In Figure 5.6 we see the currents read on each collimator pair in Injector II. The scan of intensities has been performed in 2014, while the black line shows the measurement for 2 mA after the last commissioning. These machine readings vary with each shutdown and retuning.

The positions of collimator leaves were set using $5 \cdot 10^4$ bunches purely for time-efficiency. This unfortunately limits the movement flexibility due to the macroparticle size and time-step. This adds to the discrepancy between measured and simulated currents on collimators (Figure 5.7). Nevertheless, it is still considered sufficient for this

Table 5.1: Currents read on the selected collimators from EPICS system (See Figure 5.6 for graphical representation. The currents are shown in μA.)

Stable day (26/7-07-15)	Mean	Minimum	Maximum
EWBRI mA	10.5931	10.4965	10.6047
MHC1μA	2189.99	2189.99	2195.7
KIP2	2981.32	2818.38	3090.3
KIVU	9.00E-06	9.00E-06	9.00E-06
KIVO	199.606	174.292	244.433
KIP3/RIL2I4	764.819	745.746	796.603
KIR1L	46.829	44.3923	54.1034
KIR1R	383.594	365.28	404.99
KIG1OI	26.5898	22.6464	31.6228
KIG1UI	0.803044	0.549541	1.08393
KIG3OI1	240.676	264.83	211.469
KIG3UI1	73.45	90.4946	53.1111
KIG3OI2	144.647	162.503	131.117
KIG3UI2	9.00E-06	9.00E-06	9.00E-06
KIR3L	536.25	536.25	536.25
KIR3R	564.5	564.5	564.5
KIP4L	605.498	605.498	605.495
KIP4R	615.024	615.328	614.946
Total I (μA)	7183.60586	7010.689859	7340.024248

study. Smaller time-step and bigger number of particles, will make the simulations and collimator set-up impractically long.

In Figure 5.8 we have a plot of currents cut by collimators for various simulated intensities. It is the final KIP4 collimator that varies significantly. In this model (and in operation) only KIP2 is moved to select the required intensities. In order to produce higher than operating 2 mA currents other collimators, and particularly KIP4, should be also adjusted.

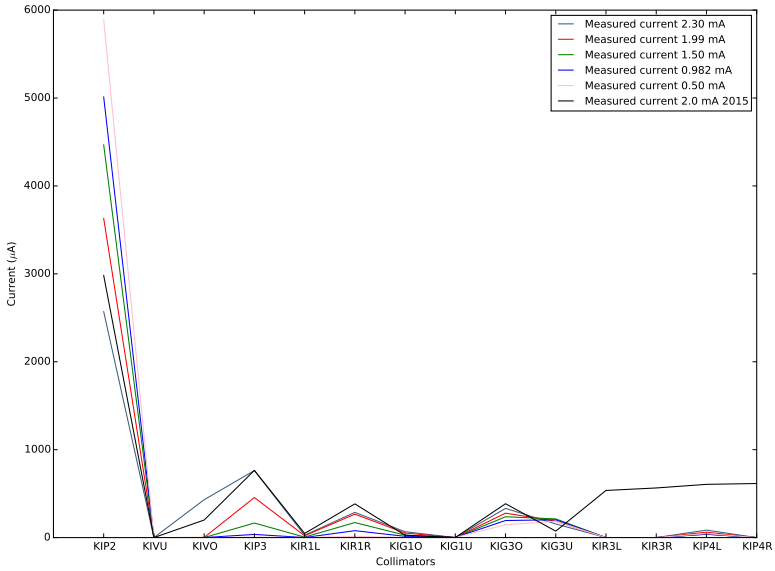

Figure 5.6: Current measured on the collimator leaves in Injector II. These readings vary with each commissioning. Up to 5% discrepancy in measurement can be observed due to equipment limitations and secondary electron emission (SEE).

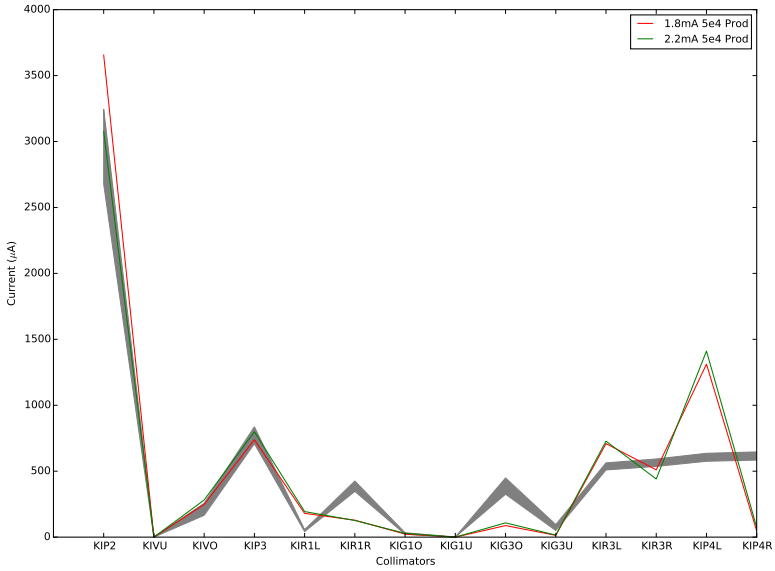

Figure 5.7: Current measured on the collimator leaves in Injector II compared to a simulated 2 mA current. Measured current (grey) shown with variation over a whole day with 5% discrepancy. Main limitation in better matching is the small number of macroparticles. Up to 5% discrepancy in measurement can be be observed, due to equipment limitations and secondary electron emission (SEE) [4].

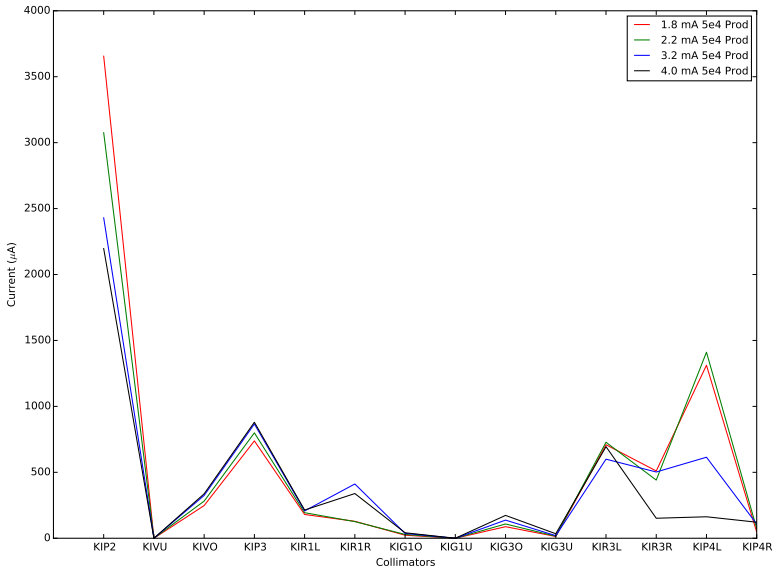

Figure 5.8: Simulated current scanned from 1.8 to 4 mA.

5.1.4 Peak matching

One of the ways to validate the model, apart from matching the number of turns and the extraction energy, is to match the final radii. A single particle optimisation has been used to search for initial conditions that will match the last 7 radial intensity peaks measured in Injector II (shown in Table 5.2). Successful matching will give confidence that modelled distribution is exposed to conditions that are closer to reality. Injector II turn pattern changes with intensity, thus there is no fixed radial peak positions but rather a range (marked in grey in Figure 5.9). This is due to both the trim coil adjustment and tune manipulation in the last turns.

The optimisation has been done matching to the 2.3 mA radial peak profile shown in Figure 5.9 (red) and to the lowest current of 1.7 μA (blue). As the operating current is around 2 mA, initial conditions found for the upper bound (2.3 mA) have been chosen to be used in the space charge runs. Radial intensity peaks of a space charge model, though run with exact same starting conditions are shifted (Figure 5.10 in green), within the measured range. This is simply because the peak-finding routine has to deal now with a distribution and not a single particle anymore.

Table 5.2: Last peak positions (mm) of the measured Injector II beam with the RIE1 probe for currents from 0.05 to 2.5 mA (Figure 5.9 in grey).

1.7 μA	0.5 mA	1.5 mA	2.0 mA	2.5 mA	Δ peaks (mm)
3210.71	3210.32	3208.76	3207.59	3206.42	4
3238.45	3236.49	3236.88	3237.66	3238.06	2
3255.63	3257.19	3257.97	3257.97	3257.19	2
3279.07	3278.29	3276.72	3275.94	3275.16	4
3306.02	3304.45	3305.24	3306.02	3306.02	2
3323.59	3325.16	3325.94	3325.55	3324.37	2
3347.42	3346.64	3345.08	3344.29	3343.51	4

The measurements were taken using the RIE1 radial probe located at 158° from the SM1 magnet. The RIE1 probe has been introduced in the model, detecting radial intensity peaks, then used for optimisation and matching with the measured data.

The fact that we have managed to find starting conditions matching radial intensity peak of Injector II is rather remarkable, as these positions are very sensitive, this proves that the field maps used and starting parameters are an appropriate representation of the Injector II.

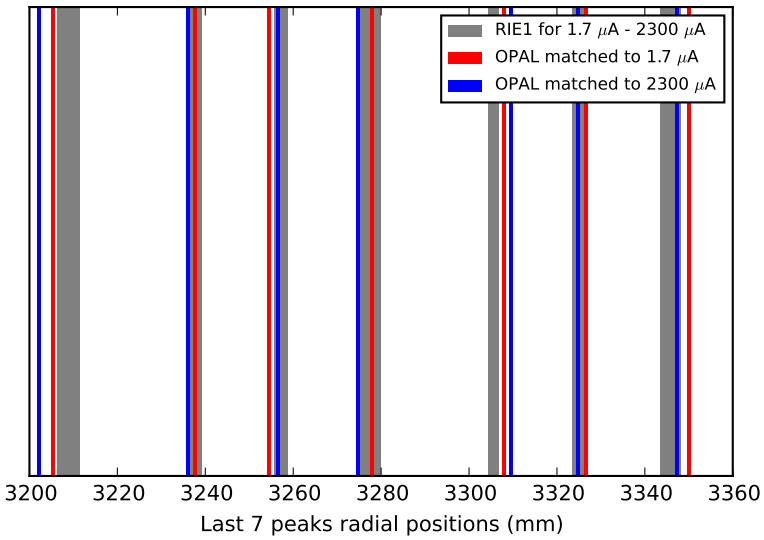

Figure 5.9: Positions of measured and simulated radial intensity peaks of Injector II. The range of measured peak locations is marked in grey, the simulated peaks matched to the lower bound are shown in red and those matched to the higher bound in blue.

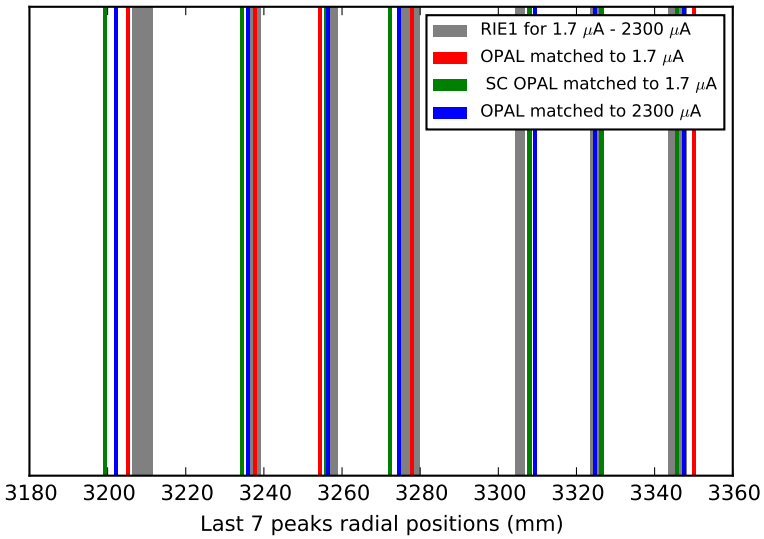

Figure 5.10: Positions of measured and simulated radial intensity peaks of Injector II in the production configuration. The range of measured peak locations is marked in grey, the simulated peaks matched to the lower bound are shown in red and those matched to the higher bound. The peak positions of multi particle space charge run are in green.

Since the peak matching is done using optimising script *opt.py*, we are dealing with large numbers of possible solutions. One of the ways to visualise optimised data is the parallel coordinate method, as shown in Figure 5.11. Each column represents a range of possible values of either a variable or an objective. Looking from left to right, we see parameters used to vary initial conditions in the first five columns. This includes start azimuth (*phi*0), radial momentum (*pr*), voltage off-set added to the RF voltage (*volt*), starting radius (*r*) and initial energy (*ekin*).

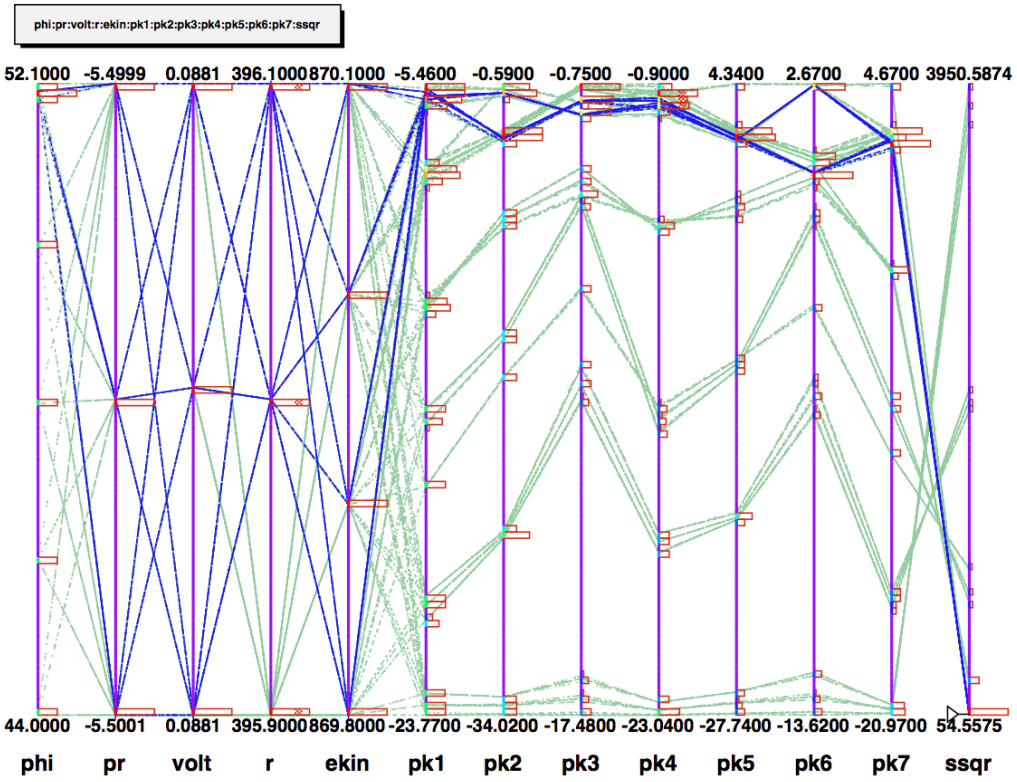

Figure 5.11: Visualisation of good solutions of the peak matching python script. *Phi*, *pr*, *volt*, *r* and *ekin* correspond respectively to RF phase, radial momentum, voltage offset, start radius and kinetic energy. $Pk1-7$ refer to deviation of peak positions from measured values and *ssqr* is the least squared value. Blue lines indicate possible good solutions with minimum *ssqr*, the remaining solutions are marked in green.

Each column shows a range of parameter values growing from the bottom. This is followed by pk1-7 columns that show the result of optimised peak position in respect to the ideal case. The last entry is the SSQR (Sum of the Square Root) of the ideal and optimised peak positions. This value is used as the main objective in the minimising function (see Section 3.2 for more details on the routine). This objective can be used

to display desired solutions by dragging an interactive bar to select the range of interest. Selected solutions with their corresponding parameters are shown in blue and the remaining solutions in green. These lines connect variables (input parameters) of optimised solutions and the sliding bar on the right allows selection of the SSQR value. One can follow the values of parameters and peak positions of selected solutions along parallel plane and if necessarily select more suitable values.

5.2 Applying the physical collimation model to the upgraded configuration

The physical collimator model can be also applied for the upgraded configuration. The positions of collimators will not change significantly as the new cavities start after several turns. In this new model only radius R and initial RF phase have changed to match collimator positions and the last turn radius. Below are listed selected initial conditions:

- Injection energy: 868.5 keV,
- 60 $\pm$1 turns,
- Energy: 71.6 MeV,
- Radius: 399.0 mm,
- Resonator gap voltages: 215.7 and 200.2 kV_{peak},
- Added voltage offset: 87.919 kV_{peak},
- New cavity: 424.0 kV_{peak},
- RF phase: 21.0°,
- Azimuth: 30.0°,
- Radial momentum: 5.50008 $\cdot 10^{-3}$ $\beta\gamma$.

Upgraded collimator model includes a new voltage profile for the resonators that will replace the 3rd harmonic cavities. The new cavity voltages differ from the approximated models, as the voltages are no longer "symmetric" and an offset value added to the double-gap resonators was used to find the best initial conditions. Voltages may appear elevated, however we accelerate in 60 turns and match the last turn, therefore the approximation is appropriate. In Figure 5.12 the last two radial peaks have been also matched to the measured ones, however in practice, only last turn should be matched to take the advantage of the large turn separation. Therefore the upgraded collimator model is taking that into the account. The expected turn separation is approximately 30-40 mm.

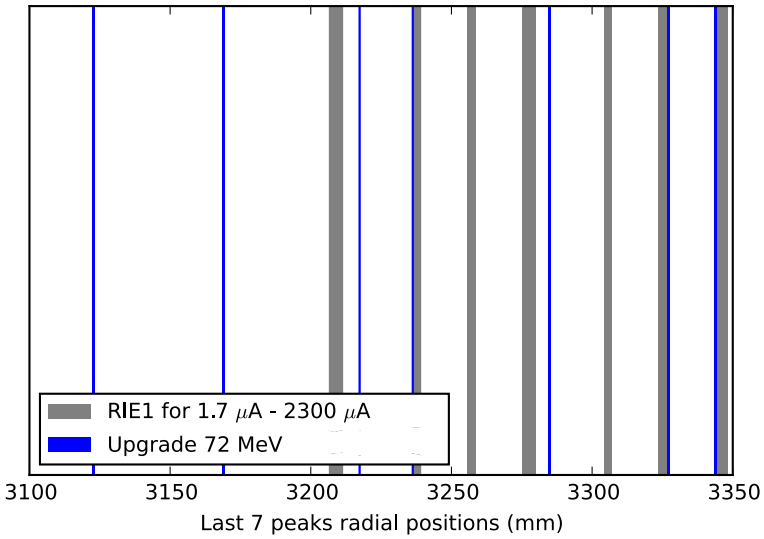

Figure 5.12: Positions of radial intensity peaks measured and simulated in Injector II in the upgraded configuration. The range of peak locations measured is marked in grey, the simulated peaks matched to the lower bound are shown in red and those matched to the higher bound in blue. This is more an exercise, the goal is to match only the last turn.

5.3 Chapter summary

We have discussed the physical collimator model, as those described in Chapter 4 are only approximate. We have expanded the 3D model with the actual collimators and probes and validated this set-up with measurements. Figure 5.6 shows the extracted current on the collimators. We observe that intensities on KIP2 vary inversely to the rest of the collimators. To ensure a scenario closest to reality, an optimisation has been used to match the measured radial intensity peaks over the last several turns. This is also demonstrated in the upgraded configuration, where we match the last two orbits . Although the optimisation have been done with single particles, even if the full bunch is used, the peaks still fall within the required ranges (Figure 5.10). This model is used for intensity scans and further analysis discussed in the following chapter.

Chapter 6

Comparison and validation of 3D models

In this chapter we present a comparison of numerical simulation data produced for various considered cases (continuous 4σ cut, 6-turn 4σ cut, physical collimation), intensity and statistics.

Additionally we verify the difference between the acceleration and flat-top modes of the RF phases. We also demonstrate how longitudinal halo tails can be removed with appropriate collimation. All the presented models are validated with measurements and the scaling of evolution of beam size with intensity is also discussed. To search for the real intensity limits of Injector II we extend it to higher intensities not yet achievable in the real machine.

6.1 Continuous and 6-turn cut 4σ models before and after the upgrade

In this section we make a comparison between production and upgraded configurations operating at 2 mA current for the continuous 4σ cut (Figure 6.1) and the 6-turn 4σ cut models (Figure 6.2).

With continuous 4σ cut, as expected, we do not gain much with additional acceleration, however, in the model mimicking collimators advantages become more apparent. As we can see in Figure 6.2 both RMSx and RMSy are significantly smaller (a), and for the upgraded configuration no major halo growth is observed. In the production set-up the halo is at a comparable level, however the physical bunch size is nearly twice as

big as in the upgraded case (d).

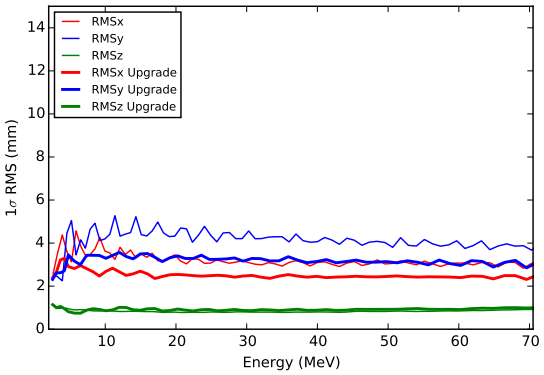

(a) RMS beam size

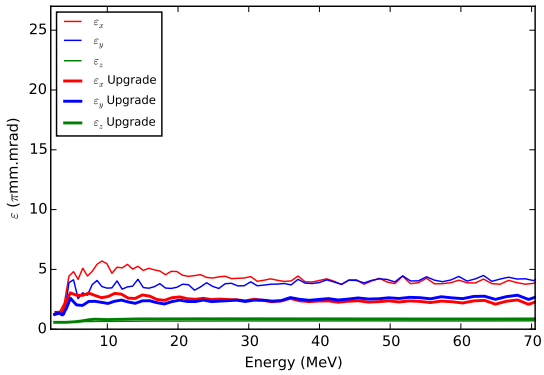

(b) Emittance

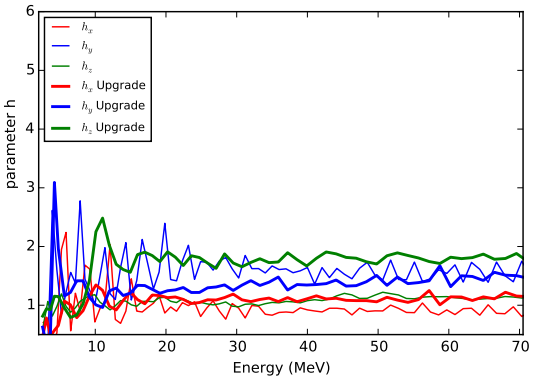

(c) Profile parameter x y z

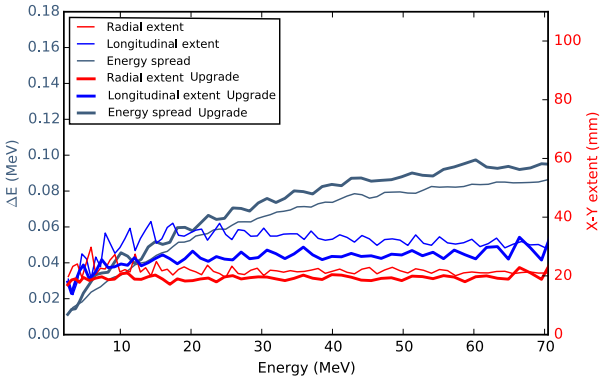

(d) Beam extent and energy spread

Figure 6.1: Upgraded set-up (bold) compared to production set-up at 2 mA current. Continuous 4σ cut model with 10^6 particles.

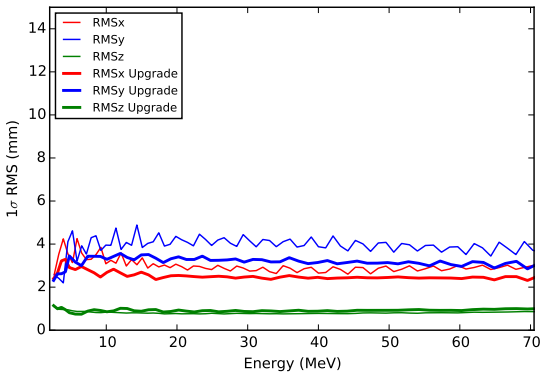

(a) RMS beam size

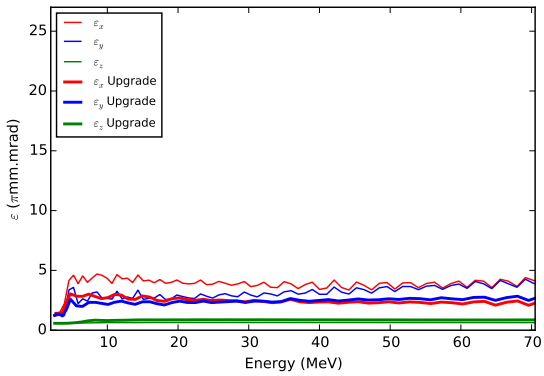

(b) Emittance

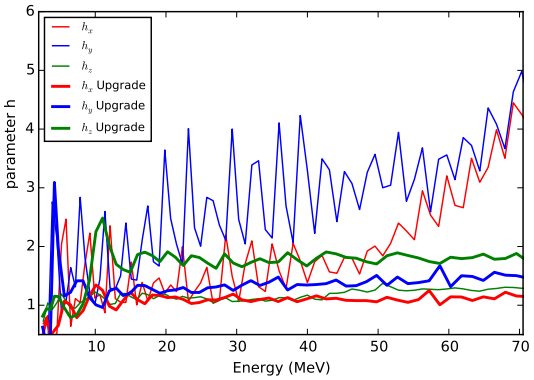

(c) Profile parameter x, y and z

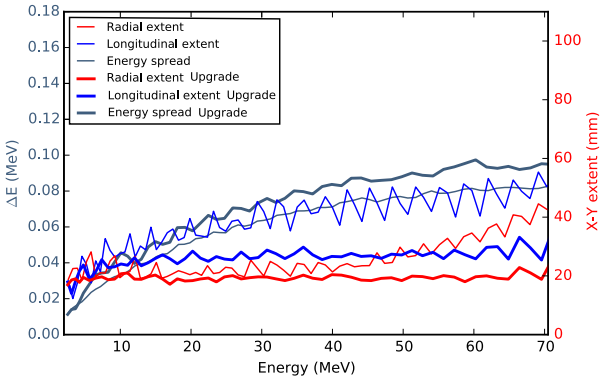

(d) Beam extent and energy spread

Figure 6.2: Upgraded set-up (bold) compared to production set-up at 2 mA case. 6-turn 4σ cut with $5 \cdot 10^4$ particles.

6.2 Physical collimator model comparison

In this section we compare the physical collimator model in the production configuration at various intensities. We also introduce an approach of quantifying halo by simply calculating current outside of the 5σ region. These particles already have a good chance of interacting with other bunches and the extraction septum, therefore keeping these numbers to a minimum is important. Additionally, we have tagged particles found in the final step halo and tracked them back to the start (marked red in all plots) in order to see the exact point where it has been generated. This will be further discussed in Section 6.3.1.

Just looking at $5 \cdot 10^4$ particle simulations of currents from 1.8 to 4.7 mA compared

in Figure 6.3, it is quite visible that radially no significant differences are observed. The beam extent is quite large reaching 55 mm x 90 mm at 2.2 mA, mainly due to the longitudinal tail of scattered particles (See Figure 6.4). RMSx is within 3.2 mm at lower intensities, for 4.7 mA it reaches 3.5 mm, however the halo will have the predominant effect here. A compact core can be formed also at higher intensities if the tail is not present.

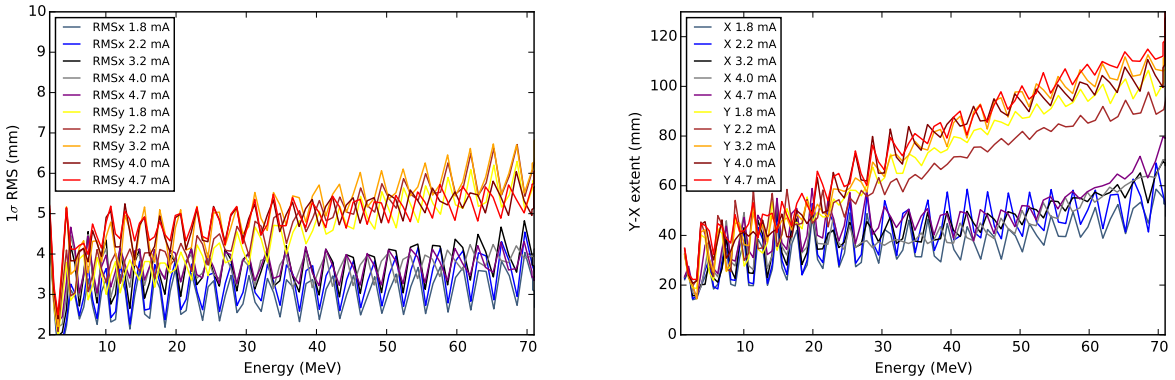

(a) RMS x and y

(b) Total beam extent

Figure 6.3: Production set-up with collimators at 1.8, 2.2, 3.2, 4.0 and 4.7 mA modelled with $5 \cdot 10^4$ macroparticles over 82 turns comparison.

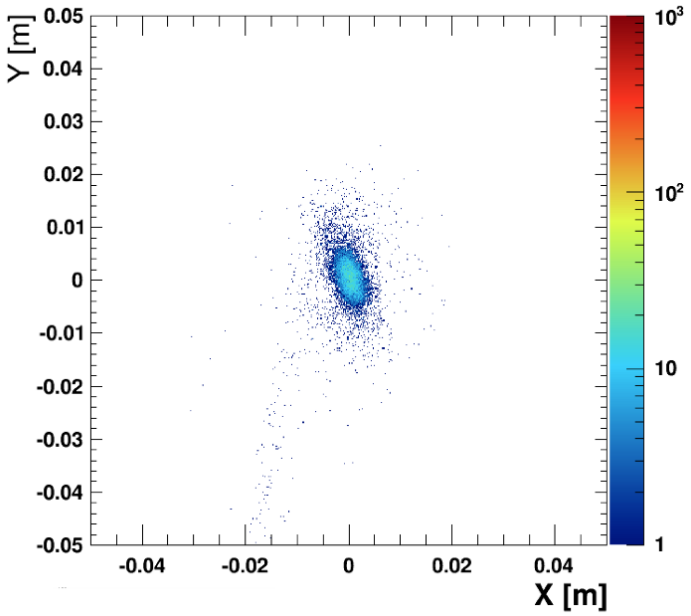

Figure 6.4: Mid-plane of 2.2 mA bunch at 71.9 MeV, showing a large tail.

Looking closer at the Injector II running at the production current of 2.2 mA (Figure 6.5), RMSx is within the measured data (6σ of 20 mm). The full beam extent, including all particles, reaches an extreme at 90 mm longitudinally and 60 mm horizontally (3 times turn separation). A substantial amount of halo outside of 5σ is carried up to 0.025 mA current which is not acceptable (Figure 6.6). It is mainly because of the large tail created due to mismatching and not precise enough collimator positions. We will look at it in more detail in Section 6.3.1.

3.2 mA beam with $5 \cdot 10^4$ macroparticles has RMSx of order of 3.2 mm as we can see in Figure 6.7, with 6σ falling close to 20 mm turn separation. We can estimate that with appropriate collimation a current of 3 mA could be delivered with the present configuration of Injector II.

When 2.3 mA is modelled with 10^5 macroparticles halo is less prominent, and RMSx and RMSy are closer to a round beam with 5 μA outside the 5σ region (Figures 6.8 and 6.9). Running 10^5 macroparticles increases the ratio between the stable core and halo of the accelerated charge distribution. Nonetheless, the core remains well matched with RMSx of 3 mm at production current giving the beam width of less than 18 mm (6σ).

This follows up to 3 mA currents with 5-10μA outside the 5σ even up to 3 mA currents (Figure 6.11), longitudinal tail is not so prominent here (Figure 6.10). The 10^5 macroparticle beam has a similar halo parameter values, however in real space the tail is less visible (See Appendix A.26). In Figure 6.12 we look at the halo a bit closer over the last turn. It is interesting that even though we look at particles outside of 5σ region, a fraction of the particles hide over the 180°region. Particles found in the final halo also are not fully outside this region over the last turn as one would expect. In Figure 6.13, on the other hand, we see how the beam parameters evolve over the 360°before the extraction RMS beam size and emittance steadily follow the lattice in (a) and (b). However, profile parameter h does not follow the lattice symmetry (as in Figure 6.12).

The 3.1 mA case is looking promising, apart from the long tail that, as we will see later, can be removed. Here RMSx is within the limits with 5 μA outside 5σ. Comparing the 10^5 macroparticle results at currents from 0.5-3.1 mA, we see in Figure 6.14 that RMSx and y is comparable for all cases with slightly elevated longitudinal parameters due to the tail.

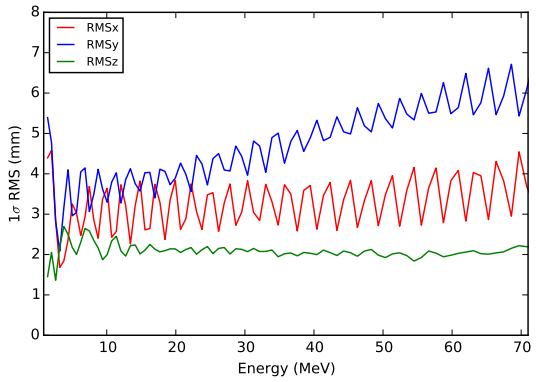

(a) RMS beam size

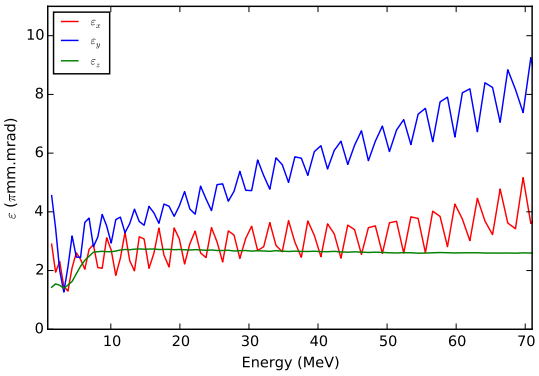

(b) Emittance

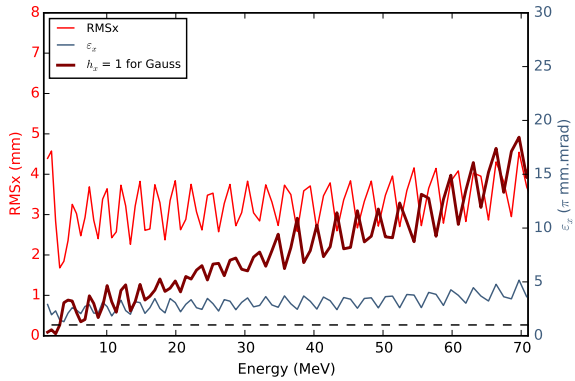

(c) Horizontal RMS, Emit, h

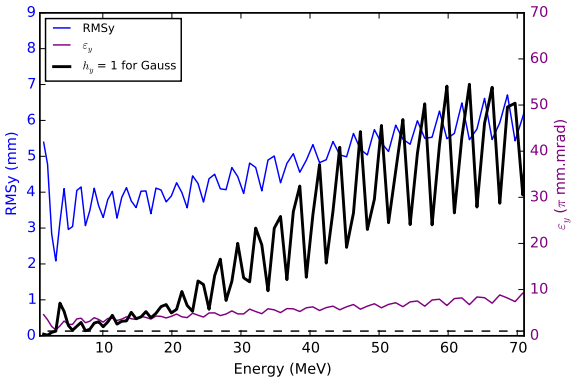

(d) Longitudinal RMS, Emit, h

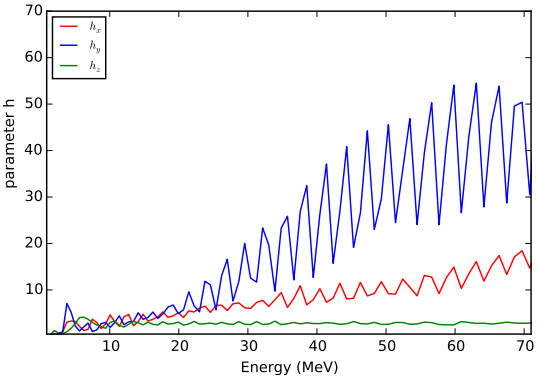

(e) Profile parameter h

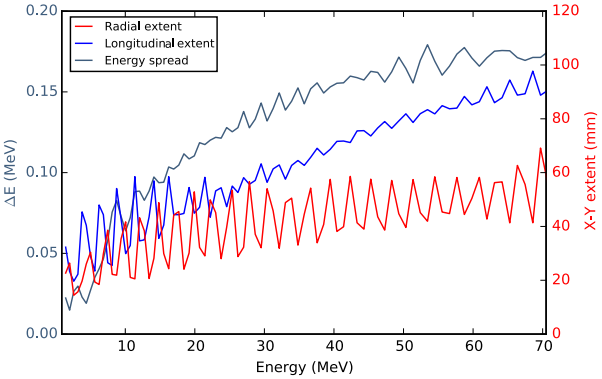

(f) Total beam extent

Figure 6.5: Production set-up with collimators at 2.2 mA modelled with $5 \cdot 10^4$ macroparticles over 82 turns.

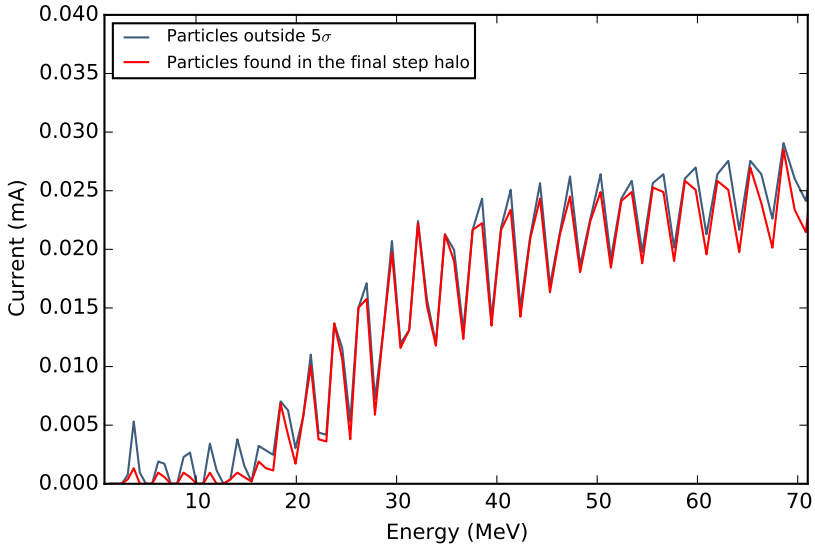

Figure 6.6: Halo particles outside 5σ 2.2 mA and $5 \cdot 10^4$ macroparticles. The current outside the region reaches 0.025 mA. Particles outside 5σ are tagged in the last step, traced back to the beginning (red) and then compared to the total halo outside the cut (grey).

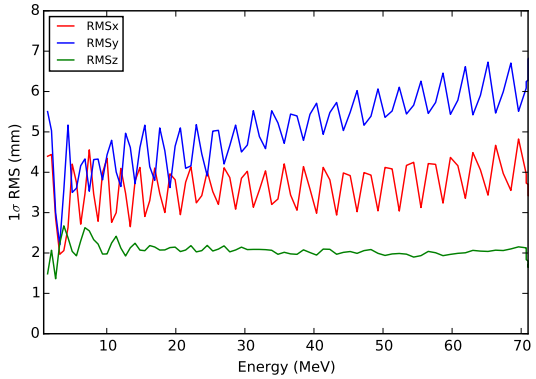

(a) RMS beam size

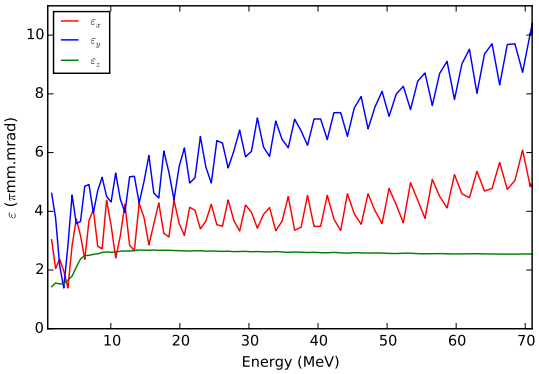

(b) Emittance

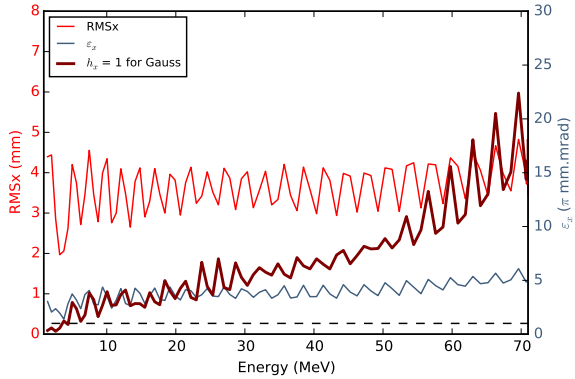

(c) Horizontal RMS, Emit, h

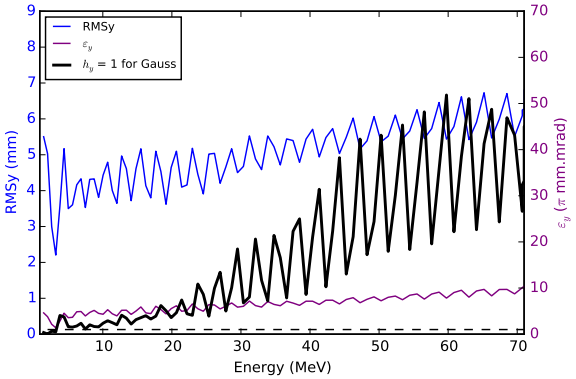

(d) Longitudinal RMS, Emit, h

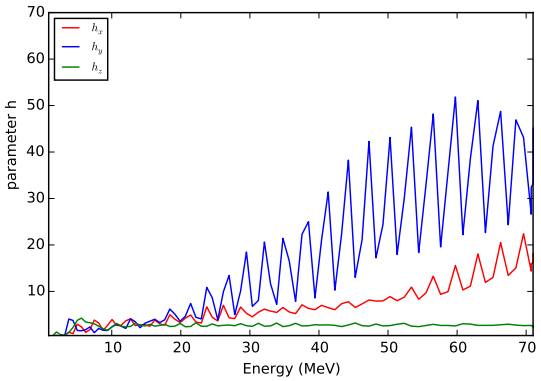

(e) Profile parameter h

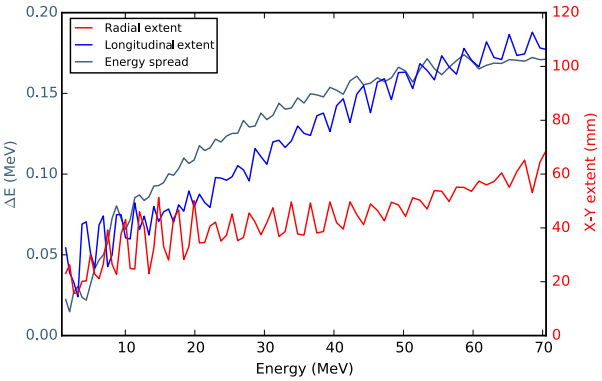

(f) Total beam extent

Figure 6.7: Production set-up with collimators at 3.2 mA and $5 \cdot 10^4$ macroparticles modelled over 82 turns. The longitudinal tail is specially visible in (e) in the last 20 turns where it eventually couples to the radial plane increasing the RMSx thus full beam extent (f).

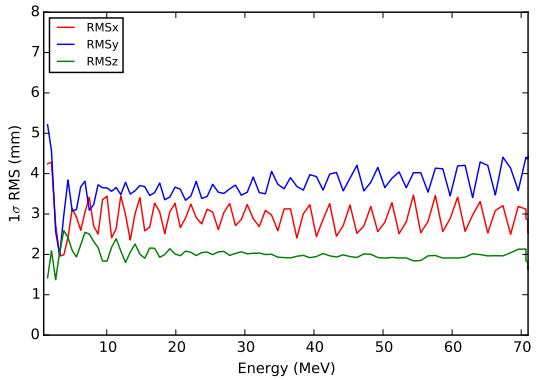

(a) RMS beam size

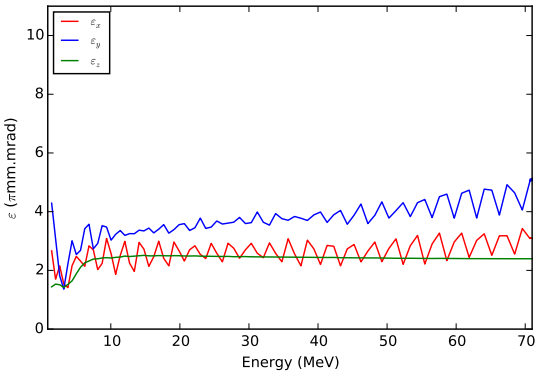

(b) Emittance

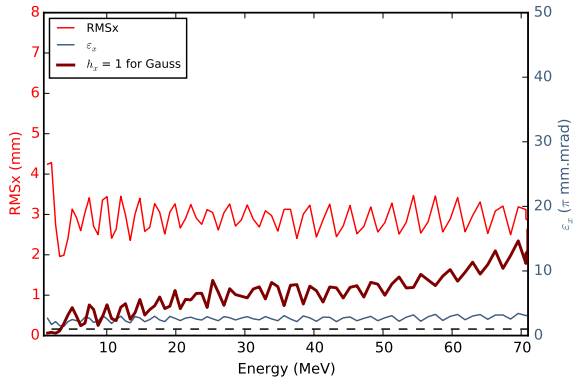

(c) Horizontal RMS, Emit, h

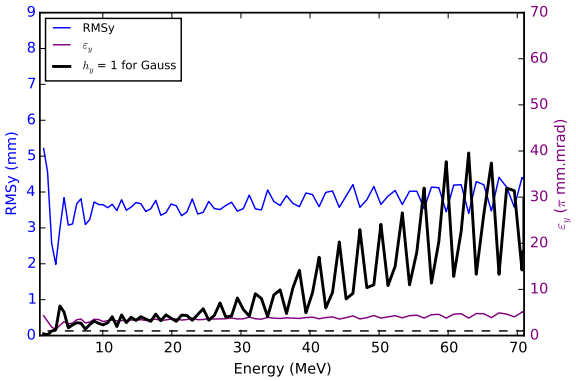

(d) Longitudinal RMS, Emit, h

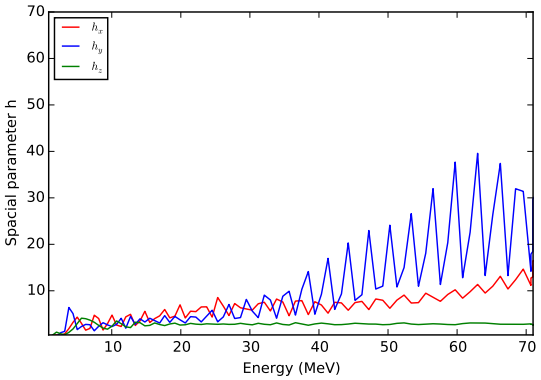

(e) Profile parameter h

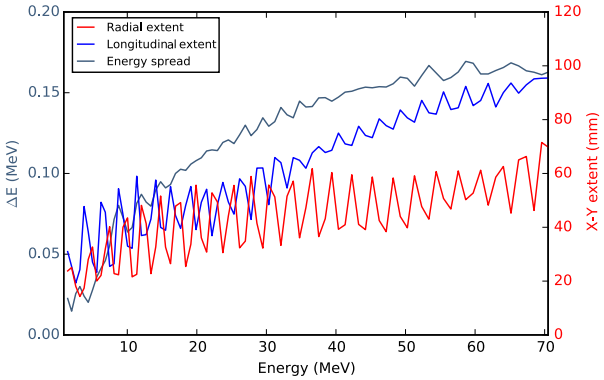

(f) Total beam extent

Figure 6.8: Production set-up with collimators at 2.3 mA and 10^5 macroparticles modelled over 82 turns. RMSx, y and z (a) remain steady despite the long tail.

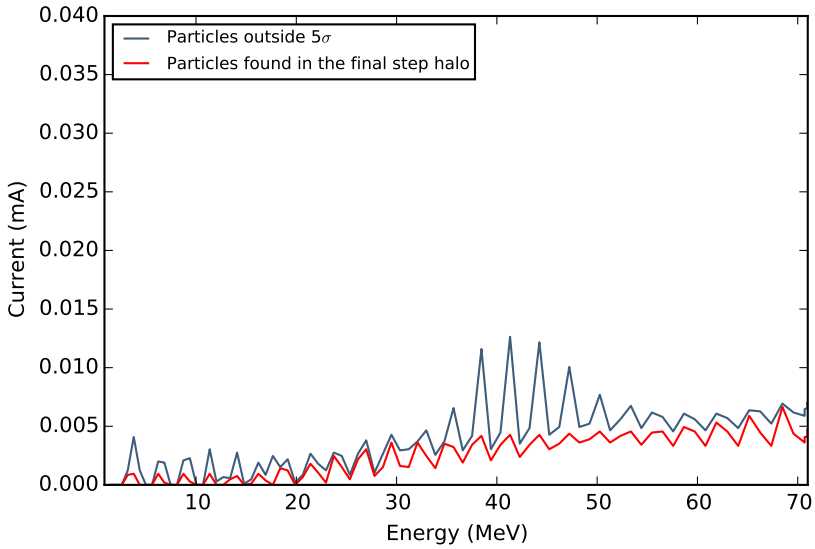

Figure 6.9: Halo particles outside 5σ at 2.3 mA current modelled with 10^5 macroparticles (physical collimator model). The amount of charge in this region is of order of 10^{-3}.

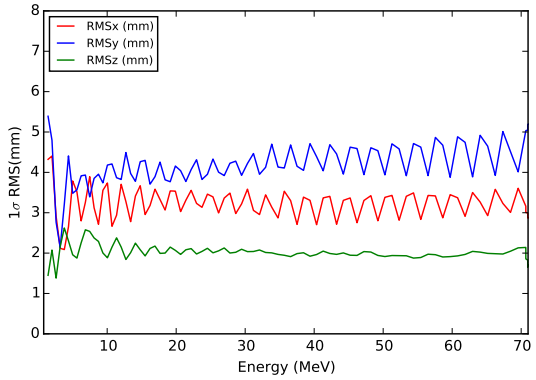

(a) RMS beam size

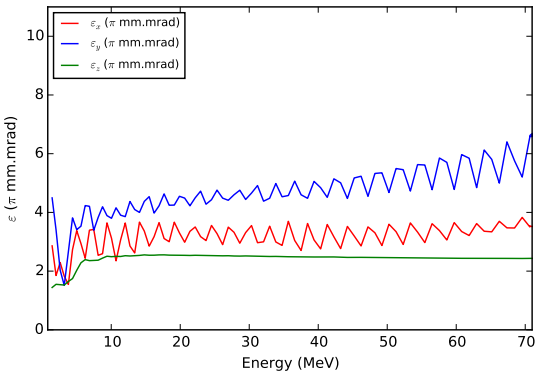

(b) Emittance

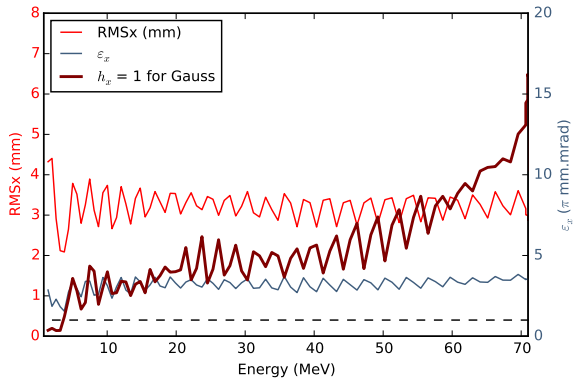

(c) Horizontal RMS, Emit, h

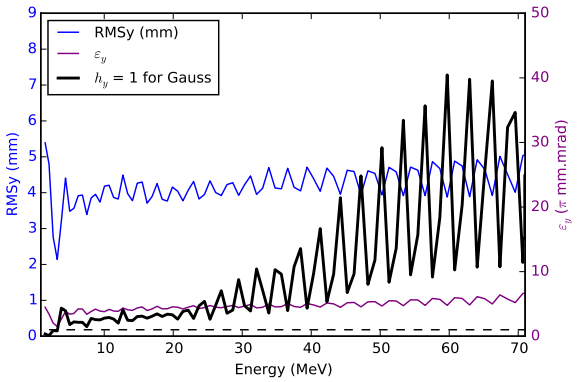

(d) Longitudinal RMS, Emit, h

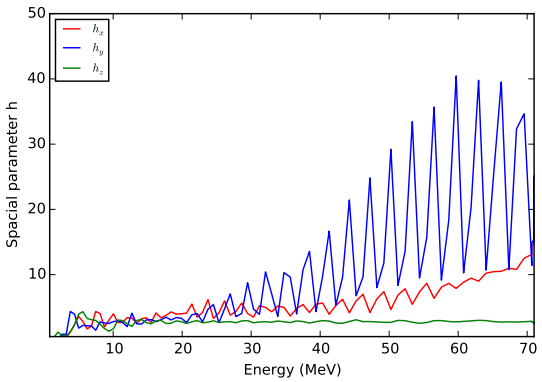

(e) Spatial parameter h

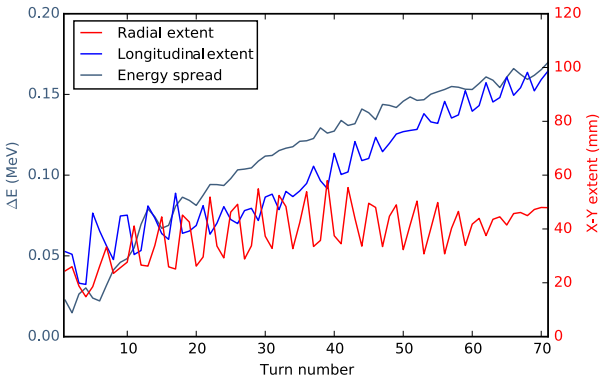

(f) Total beam extent

Figure 6.10: Production set-up with collimators at 3.1 mA modelled with 10^5 macroparticles over 82 turns. For all intensities RMSx and y remains comparable (a). Large longitudinal tail is formed in (d) and later coupled to form radial halo (e).

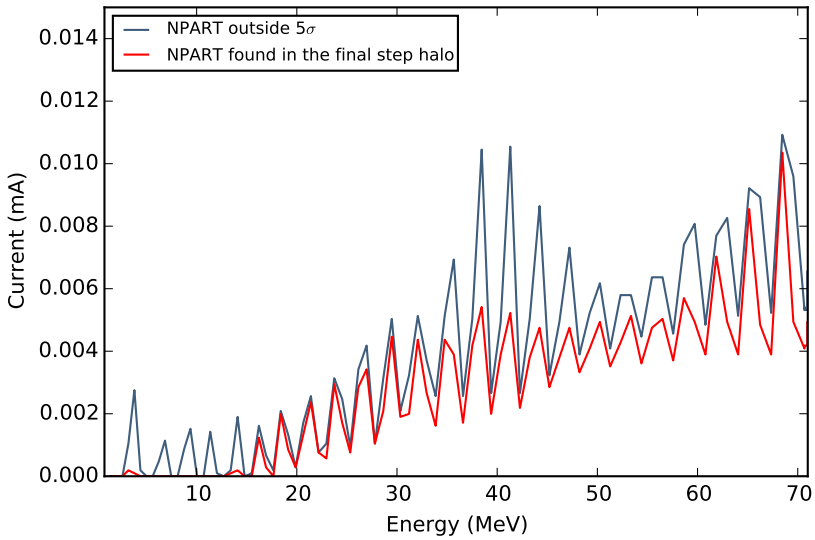

Figure 6.11: Halo particles outside 5σ region at 3.1 mA current modelled with 10^5 macroparticles.

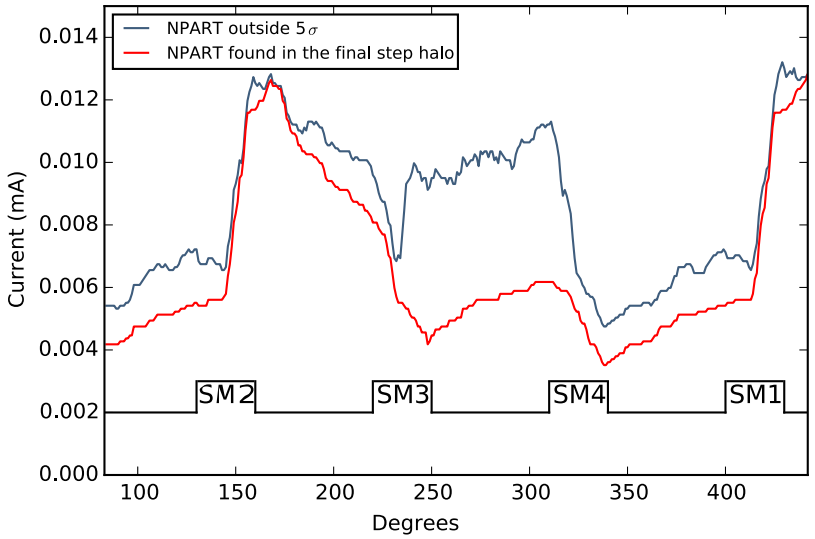

Figure 6.12: Production set-up with collimators. The current outside 5σ in x and y planes at 3.1 mA with 10^5 macroparticles over the last turn.

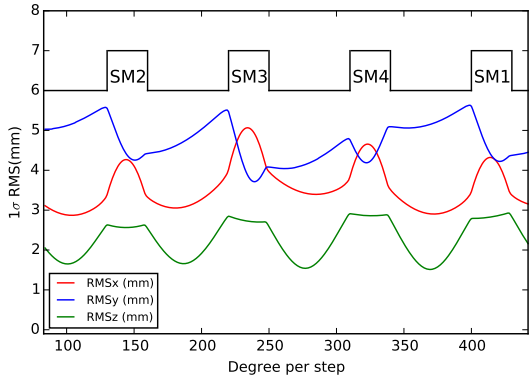

(a) RMS beam size

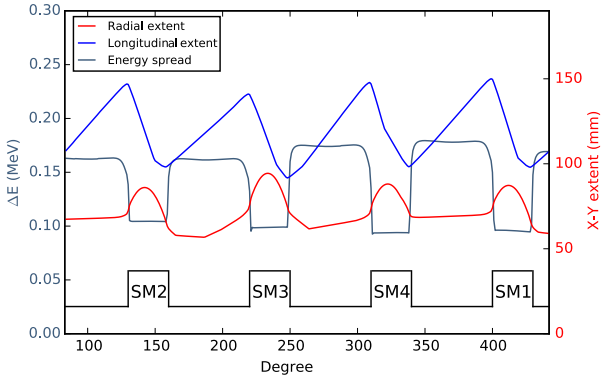

(b) Total beam extent

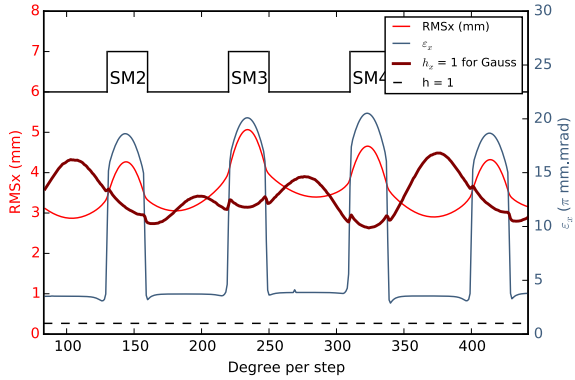

(c) Horizontal RMS, Emit, h

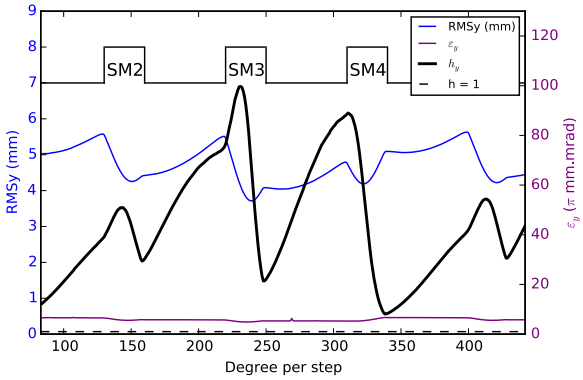

(d) Longitudinal RMS, Emit, h

Figure 6.13: Production set-up with collimators at 3.1 mA with 10^5 macroparticles over the last turn.

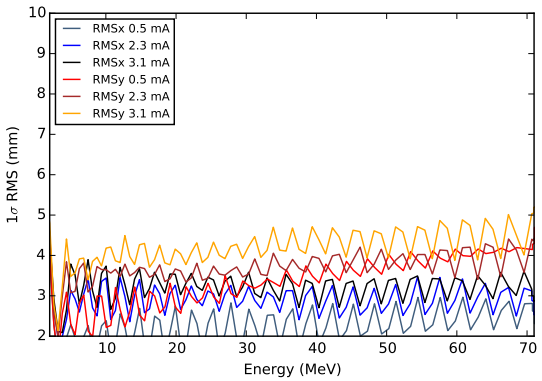

(a) RMS x, y

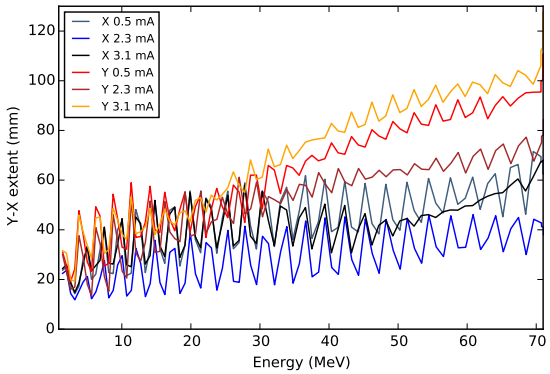

(b) Total beam extent

Figure 6.14: Beam size of the production set-up with collimators at 0.5, 2.3 and 3.1 mA modelled with 10^5 macroparticles over 82 turns.

6.3 Comparison of the physical collimator model based on statistics (particle number)

Numerical simulations of millions of particles can be very slow as they require large computing resources. For such iterative work this is too timely, therefore some shortcuts have to be used, e.g. a small number of macroparticles (collections of particles). For fast simulations this is sufficient, but for more detailed halo studies, the number of macroparticles should be kept as large as time-efficiency allows. This can contribute to the discrepancies between the data sets with only varied statistics (e.g. number of macroparticles in the distribution) as with collimator positions what will be discussed in the next subsection.

In Figures 6.15 to 6.17 we compare 2.2 mA simulations performed for $5 \cdot 10^4$, 10^5 and 10^6 number of macroparticles. We would like to see, how much the modelled beam varies or if at all, and what is the optimal number of particles. It is striking that the radial data is consistent across all the considered cases, however the longitudinal data is not. It is necessary to mention, that each time a number of particles is changed, collimator positions have to be adjusted. Since we model the same initial current (9.5 mA) with varied macroparticle number, their size (charge) will be changed. Mesh size cannot be exactly scaled, therefore discrepancies are expected. Finding the exact starting parameters in such way is not possible, hence we get slightly varying final currents. In Figure 6.15 we are looking at halo outside 5σ as shown in increasing number of macroparticles decreases the amount of halo detected from 0.015 mA for $5 \cdot 10^4$ to 0.005 mA for 1 million particles. This is mainly due to the long tail that is present in the physical collimator model at $5 \cdot 10^4$ and 10^6 driving the values up.

To get a better idea of halo formation 10^5 or even 10^6 macroparticle simulations are required. Comparing 2.2 mA case across the models (Figure 6.18) radial RMSx is again similar but longitudinal plane is not consistent. If one wanted to check radial width the approximated models are a good guess.

The approach of setting up collimators for $5 \cdot 10^4$ macroparticles and 3600 steps per turn has been chosen to be optimal, requiring only small adjustments of collimators when particle number is increased. However, this is not ideal if we would like to study halo in more detail.

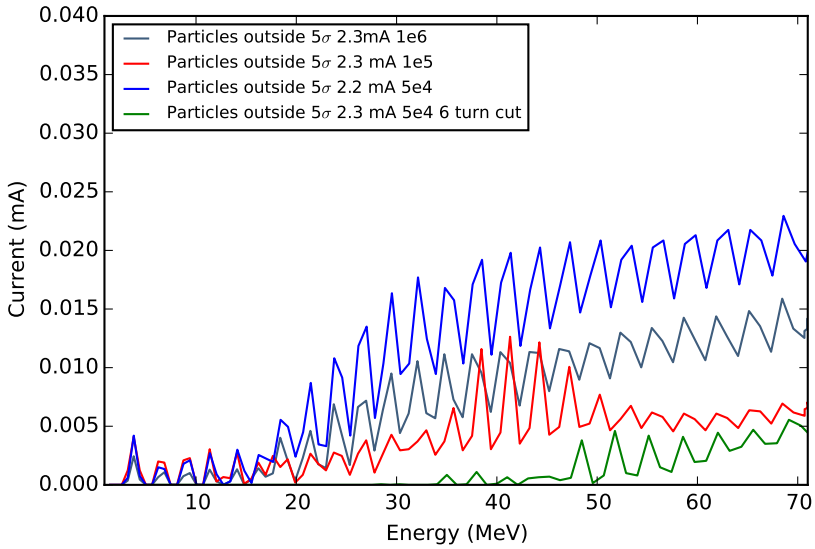

Figure 6.15: Comparison between the models with additional 6-turn cut simulation.

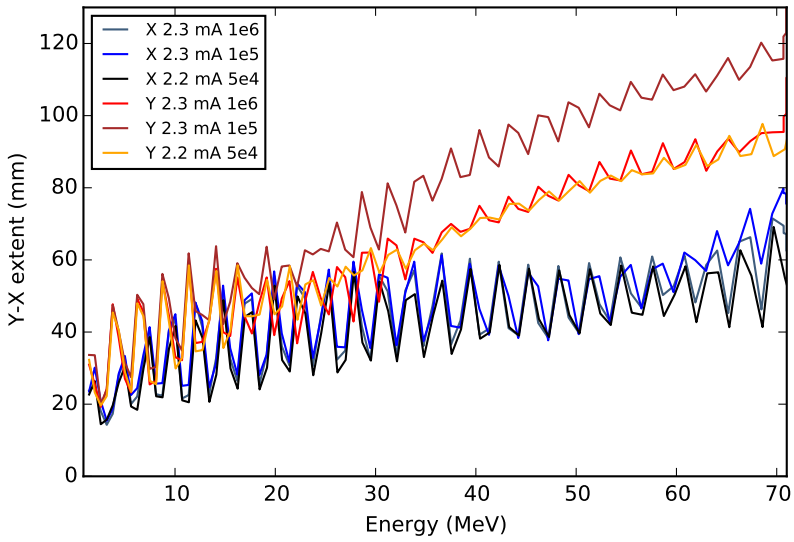

Figure 6.16: Beam extent horizontal x and longitudinal y. Collimator model comparison of the number of macroparticles for around 2 mA. This variation is due to the need to readjust collimators every time the number of macroparticles changes, here only KIP2 has been moved.

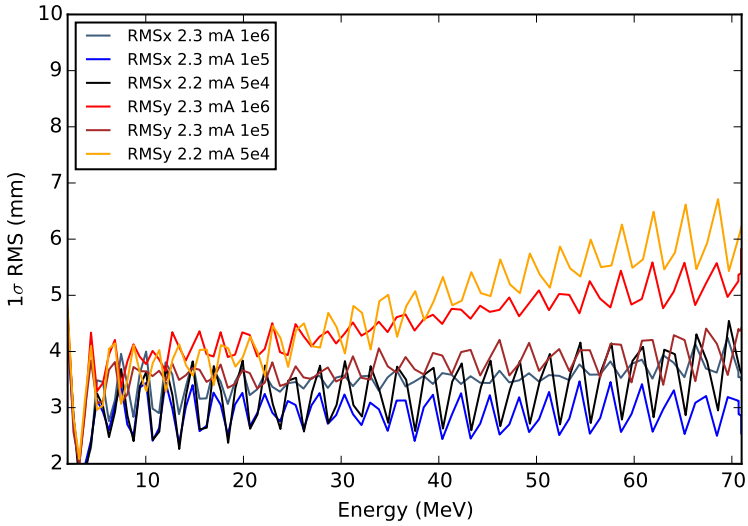

Figure 6.17: RMS x and y. Collimator model comparison of the number of macroparticles at 2 mA beam current. This variation is due to the need to readjust collimators every time the number of macroparticles changes. Here only KIP2 is moved.

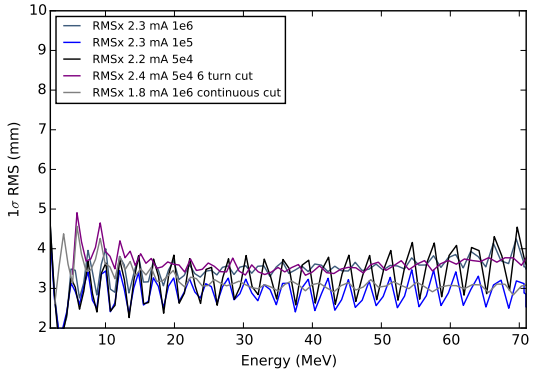

(a) RMSx beam size

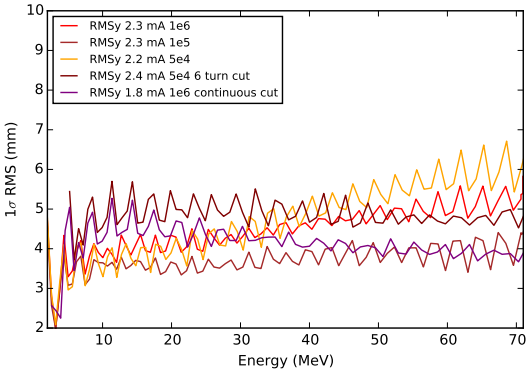

(b) RMSy beam size

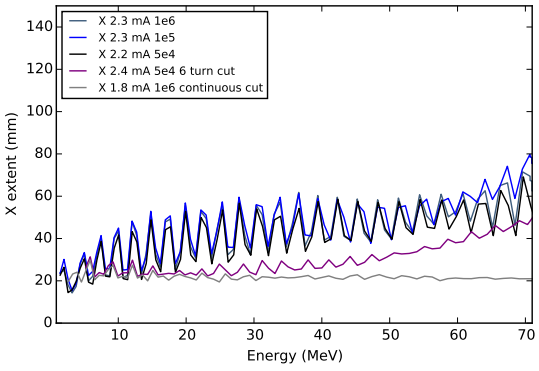

(c) Horizontal extent

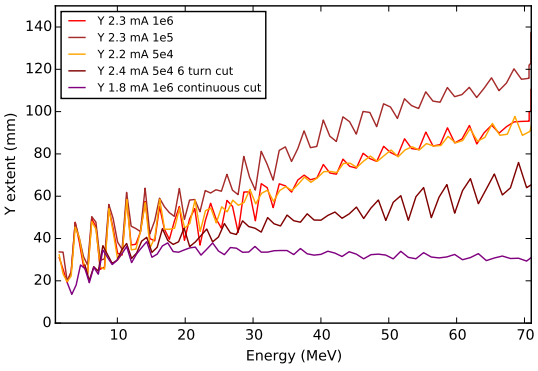

(d) Longitudinal extent

Figure 6.18: Comparison between approximated 6-turn 4σ cut models and the physical collimator model at 2 mA intensity.

6.3.1 Longitudinal tail correction with KIP4 collimator

The collimator model is not perfect as large tails are formed with full acceleration all intensities. To investigate in detail halo found in the final steps, particles outside 5σ are tagged in the last step, traced back to the beginning (marked in red) and then compared to the total halo outside the cut (grey in Figure 6.19). In this way we can trace the tails back to the point where they have been first created and clean it with the appropriate collimation.

Figure 6.19 shows all particles found outside 5σ over the first 7 turns where collimation occurs. Phase-space data has been saved every degree to allow easier location of the halo origins. We can see that particles found in the last step halo tail appear just after the first 3 turns. First occurrence of these tagged particles is at step 1140, with peak starting at 1175 until 1186 and it ends at step 1227, corresponding to one third of the 4th turn. Tagged halo outside of the 5σ is hidden and reappears again after approximately every 180°. That suggests that particles do not stay in the physical 5σ region but come in and out of the central bunch region. This is not typical for isochronous machines where the bunch does not turn because all particles are accelerated at the same time. This could have an explanation in particle core model and/or phase mixing due to space charge [48].

Knowing the point at which halo appears we attempt to move collimators and clean it efficiently. The region where the tagged halo first appears is near KIP4 location, however its original location misses the halo peak. The second peak appears on the 5th turn, starting with steps 1496-1500 corresponding to 86° from SM1. This happen to be located inside the sector magnet SM2, where it is not possible to collimate. Next peak (from step 1774 to 1805) is also at the end of the 5th turn corresponding to 4-35° from SM1 sector magnet, which is just at the entrance to the double-gap resonator and peak at 2065-2100 steps corresponds to the vertical collimators positions. The only reasonable solution with present collimator set-up is to shift KIP4 longitudinally.

We have rerun the physical collimator model at 2.2 mA to test the improvements. The results are presented in Figure 6.20. Shifting the position of KIP4 by 16.41° back in respect to SM1 significantly removes the tagged halo with the total halo outside of 5σ nearly halved in the central region. Looking at the full acceleration, now with data saved after each turn, we also observe dramatic decrease in total halo as shown in Figure 6.21. KIP4 is positioned at the point where the future longitudinal tails are cleaned. Shifting KIP4 back successfully removes the halo from the final steps.

We have achieved a decent agreement with initial conditions and transverse real-space information. Moving the collimator longitudinally already makes a tremendous difference, the longitudinal profile parameter goes down significantly as the long tail is removed. Radial beam data stays consistent across all the models, however, full beam extent remains unchanged as several scattered particles drive this parameter up. Nonetheless, with more optimisation this could be completely removed.

Figure 6.22 and Figure 6.23 show a comparison of the original and corrected KIP4 models. Comparing the beam evolution in the real space in Figure 6.24 we can see how the longitudinal tail does not appear in (f,g) when KIP4 is shifted. For benchmarking and estimation of intensity limits the horizontal data is sufficient. However, exaggerated longitudinal tails will underestimate the limits. This is because the long tail eventually couples to the radial plane due to the vortex motion increasing its radial size.

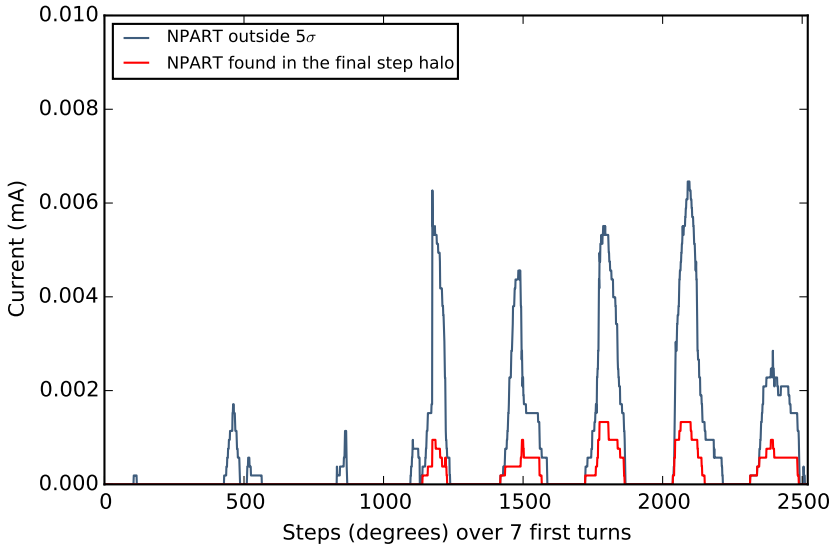

Figure 6.19: Current outside 5σ per degree over first 7 turns where the collimators are present. Each step is a degree. We can see that final halo is never fully visible as these are phase tails.

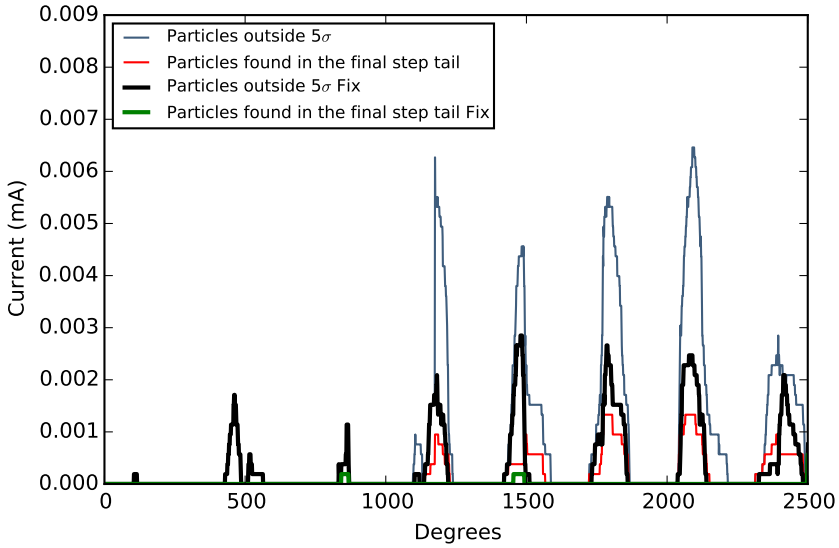

Figure 6.20: Current outside 5σ in x and y. First 7 turns where the collimators cut. Significantly improved results of simulations with shifted KIP4 are shown in bold.

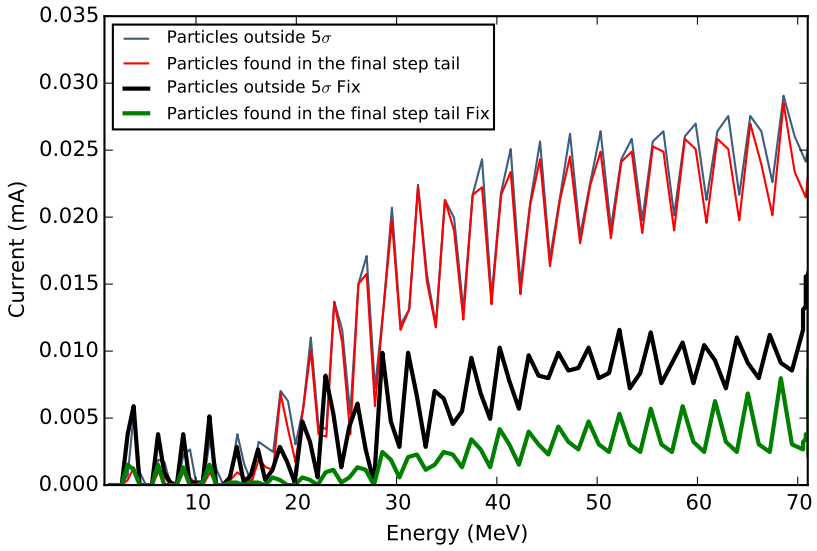

Figure 6.21: Comparison of halo outside 5σ over the full acceleration with halo after the KIP4 shift. The halo is 5 times smaller. Modelled with $5 \cdot 10^4$ macroparticles.

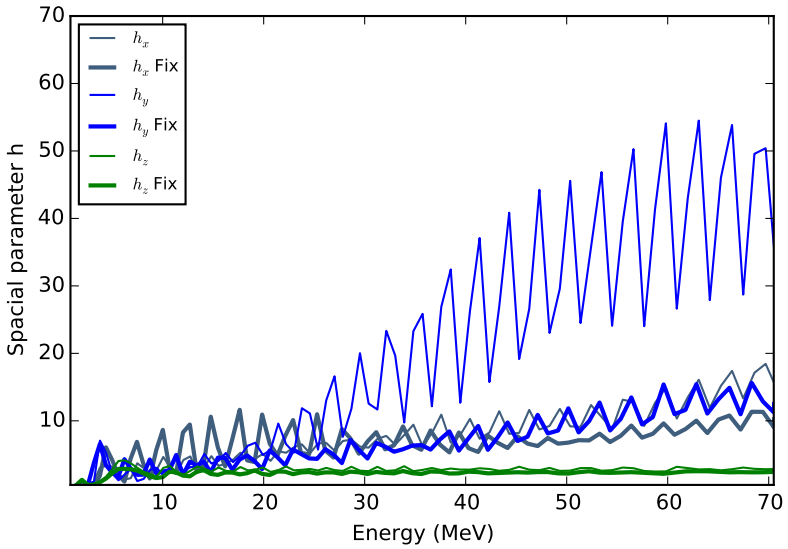

Figure 6.22: Profile parameter h for original set-up and after shifting KIP4 (bold).

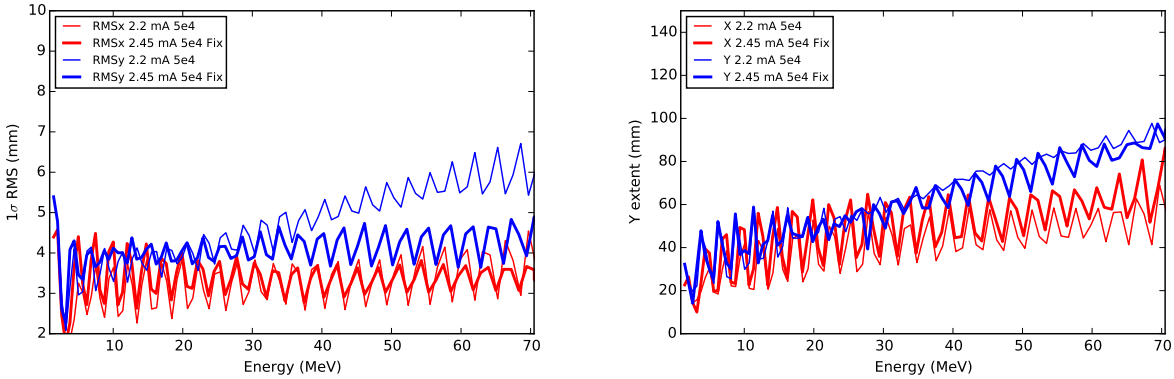

(a) RMS beam size

(b) Emittance

Figure 6.23: Parameters after fixing the KIP4 collimator (in bold) compared to original KIP4 position. Improved model is marked in bold. The major change is observed in the longitudinal direction with significantly decreased RMSy, the extent remains similar, due to a few particles that were not cleaned.

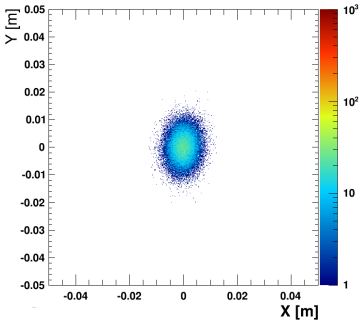

(a) 0.87 MeV

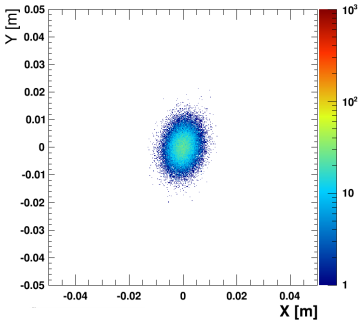

(b) 0.87 MeV fixed KIP4

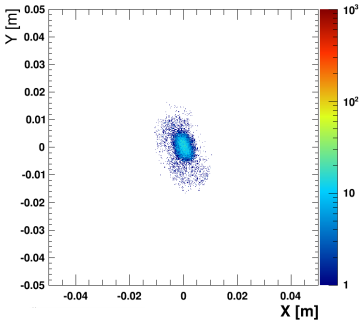

(c) 10.7 MeV

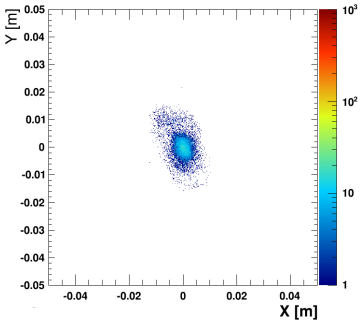

(d) 10.7 MeV fixed KIP4

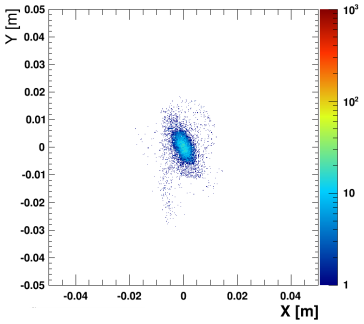

(e) 20.7 MeV

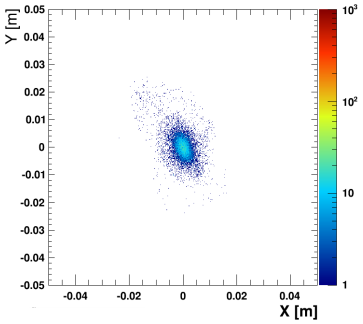

(f) 20.6 MeV fixed KIP4

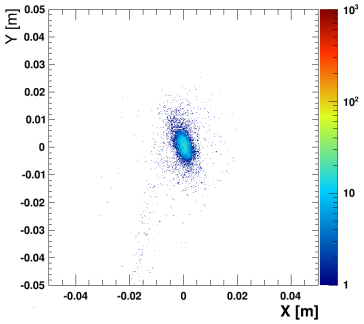

(g) 71.9 MeV

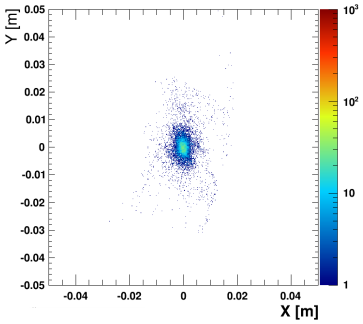

(h) 71.8 MeV fixed KIP4

Figure 6.24: Mid-plane of the distribution at different energies simulated with $5 \cdot 10^4$ (first two columns). The tail that is seen in (e) and after removing (f). In the first case it remains stationary.

6.3.2 Flat-top mode check

Currently, Injector II operates its 3rd harmonic flat-top RF cavities in an accelerating mode. The bunch size is so small that there is no apparent advantage of running it with the flat-topping on (longer bunch acceptance). However, since Injector II bunches are so small, the cavities are switched to slightly accelerating mode with the small advantage of decreased turn number (accounting for a 10 % improvement).

The analysis of the production configuration presented in this research is based on the original RF settings of the machine. We use the same number of turns as currently used but with elevated accelerated voltage to compensate for the deceleration. We cross-check whether flat-topping phase really has no significant effect on beam quality. As we can see in Figures 6.25 and 6.26 where the accelerating mode on is shown in bold, the picture looks very much the same at the level of RMS beam size and emittance confirming predictions. Halo looks a bit worse with the decelerating mode having larger h parameter due to the long tail we have discussed before as shown in Figure 6.27, however that does change the full beam extent much (6.28). As we can see in Figure 6.29, the tail is still present but shifted in the mid plane, accounting for lower kurtosis.

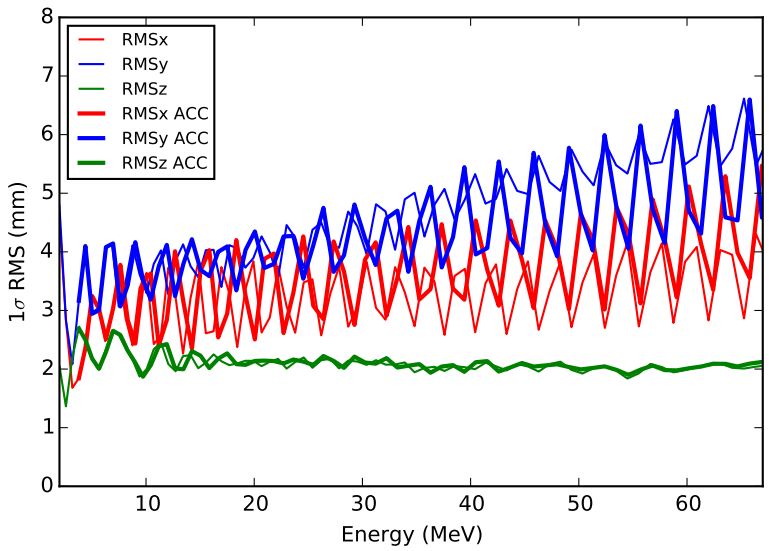

Figure 6.25: Comparison of RMS beam size in 3 planes in accelerating (bold) and decelerating operation.

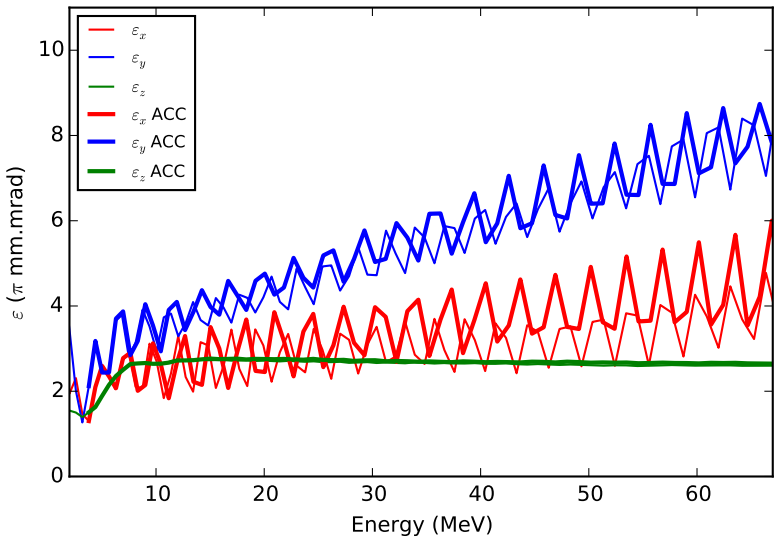

Figure 6.26: Comparison of emittance in 3 planes in accelerating (bold) and decelerating operation.

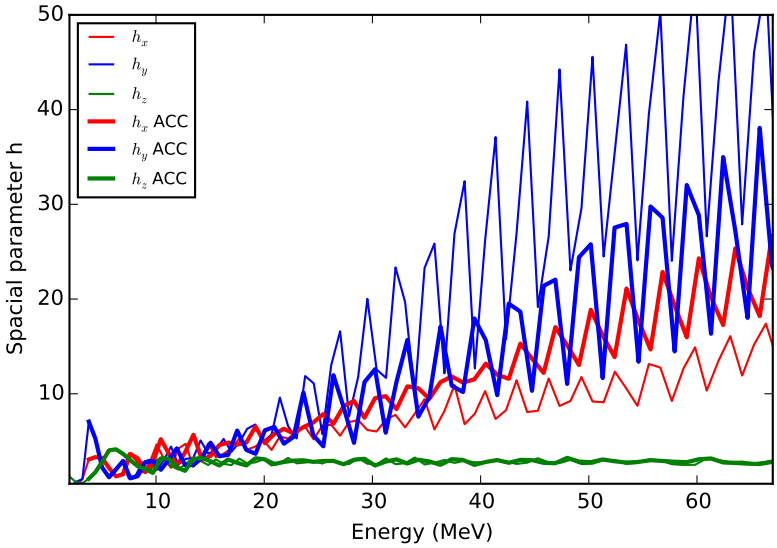

Figure 6.27: Comparison of profile parameter h in 3 planes in accelerating (bold) and decelerating operation.

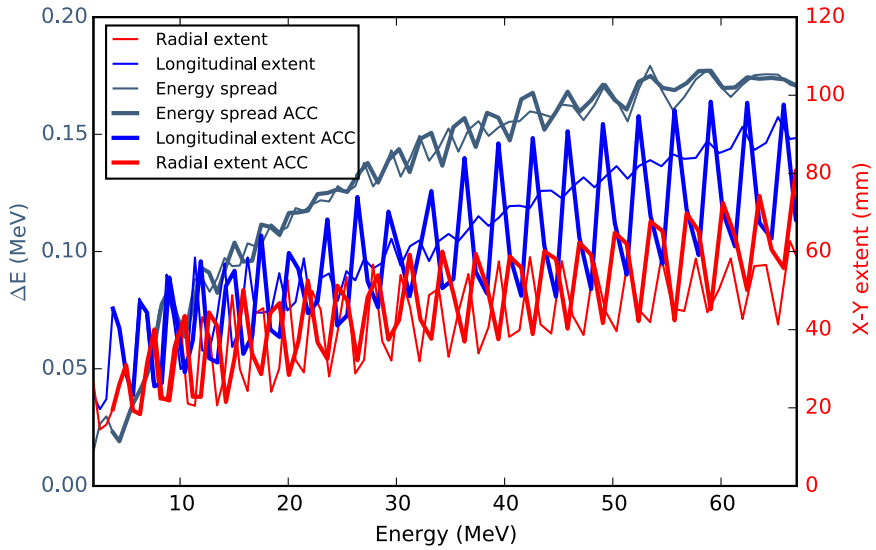

Figure 6.28: Comparison of radial and longitudinal full beam extent with energy spread of accelerating (bold) and decelerating operation.

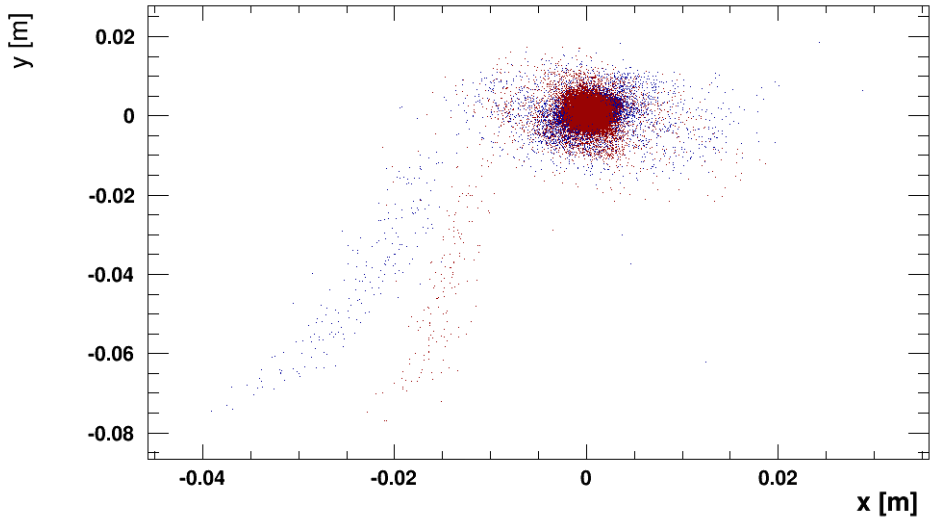

Figure 6.29: Bunch mid-plane after 61 turns. Blue colour marks 3rd harmonic cavity set to accelerating mode, red is the original decelerating operation.

The bottom line of this study is that, in the end, there is not much difference in bunch quality when flat-topping is used. We have demonstrated that the decision to switch off flat-tops at PSI was valid taking the advantage of fewer turns and wider turn separation.

6.4 Validation with measurements

Validation of the models has been approached from many different aspects. Collimator and probe positions are based on those measured in Injector II. Additionally currents extracted on collimator leaves have been used to optimise the physical collimator model under the production configuration (Section 5.1). Another benchmark with measurements considers the turn pattern as in Injector II turn pattern changes with the intensity (See Figure 6.30). This is partially due to the trim coils that are used to manipulate the orbits in such way that the extraction orbit valley is kept fixed. Optimisation of initial conditions needed to match the orbit pattern is discussed in Subsection 5.1.4.

In the next Subsections we further validate the complete models based on the beam size of the bunches extracted from RIZ1 probe and attempt to find scaling laws fitting the data.

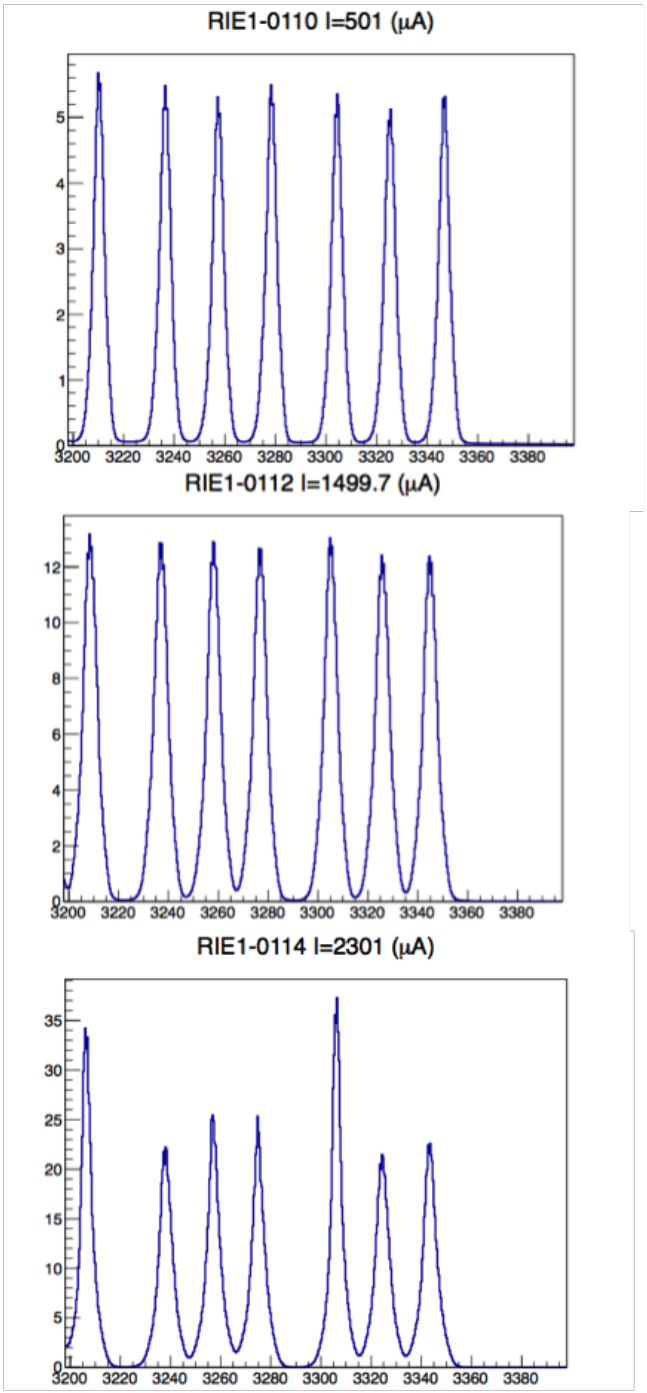

Figure 6.30: Orbit patterns of Injector II at various intensities. We observe ”clustering” of orbits at higher intensities, where trim coils are used to manipulate final orbits.

6.4.1 Scaling laws

In this subsection we discuss scaling based on measured and numerically simulated data. The current limit predicted for isochronous machines such as the Ring cyclotron is not sufficient for Injector II as space charge and strong transverse-longitudinal coupling play a dominant role here in beam size formation. However, being able to simulate higher intensities, we can focus in more detail on how the beam size changes with increasing intensity. We consider all models and configurations starting with the 6-turn 4σ models for production and upgraded configurations, followed by the physical collimator model in its production mode. The presented data is based on RIZ1 probe measurements of beam widths located on the extraction orbit. Figure 6.31 shows the real-space of the bunch captured by the probe. From this measurement RMS beam size data is extracted. We have implemented it also in our model for selected intensities as shown in Figure 6.32.

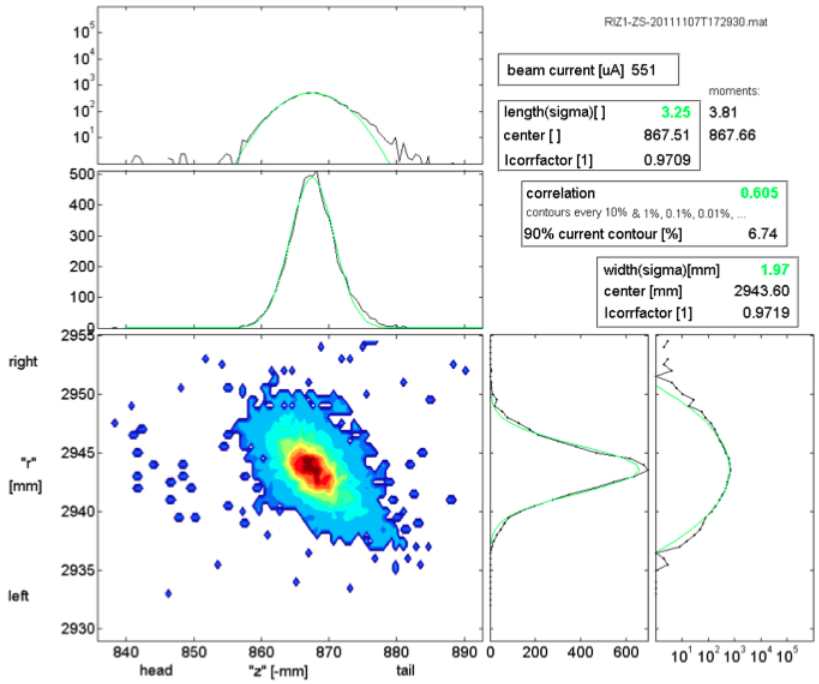

Figure 6.31: RIZ1 probe real-space measurement for 0.5 mA current. The top histogram shows 1D longitudinal projection and bottom right plot, the 1D radial projection of the bunch. Halo is large, however the measuring equipment is not sensitive enough to adequately quantify it.

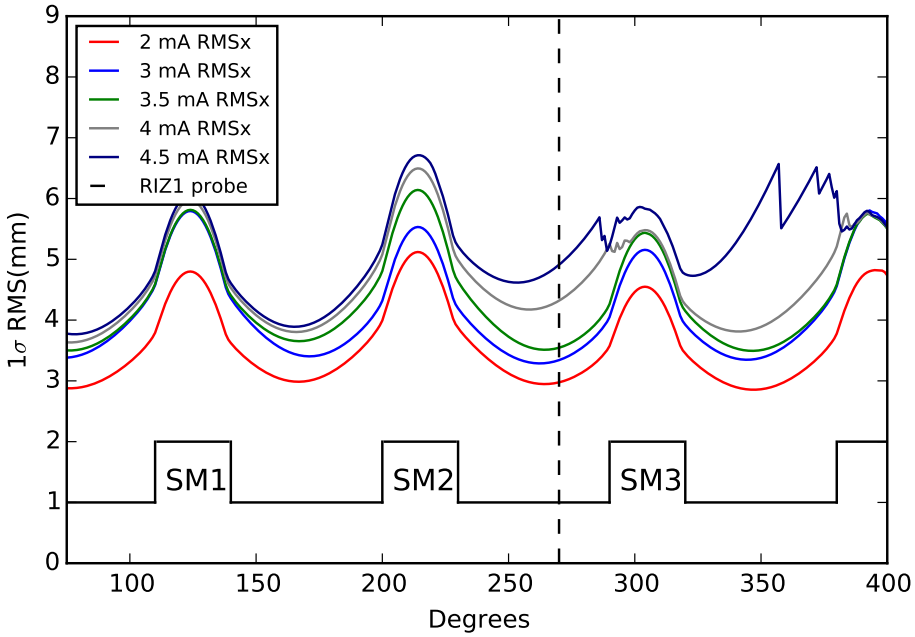

Figure 6.32: Variation of 1σ RMS beam size in the last turn for simulated 2-4.5 mA measured by RIZ1 probe (dash line). Beam is extracted after SM3. Spikes in 4.5 mA beam size indicate the field fringe having an imbalancing effect at higher intensities.

We begin with taking a close look at measured data. One would follow up on Joho's power law of intensity limits scaling to the power of three with the voltage also for space charge in Injector II. It can be expressed as $I \propto V^3$, where I is the current and V is the RF cavity voltage [6]. We can find 3rd power fit where the beam size scales with the intensity as cubed root, nevertheless, 4th power scaling seems to be a better fit. In Figure 6.33 (log-log plot Figure 6.34) in purple we have scaling of intensity with available voltage, where the beam size scales with current to the power of 3:

$$\sigma \propto \sqrt[3]{I}. \tag{6.1}$$

Although the χ^2 of 1.32 with 6 degrees of freedom is acceptable for the 3rd root scaling, a better fit, particularity for higher currents, is found with the beam size depending on the current with the 4th root (blue). χ^2 in this case is 0.83. Following the cubed root as shown in Figure 6.33, 1σ RMS beam size depends on the current as follows:

$$\sigma \propto 0.2\sqrt[3]{I} + 0.4, \tag{6.2}$$

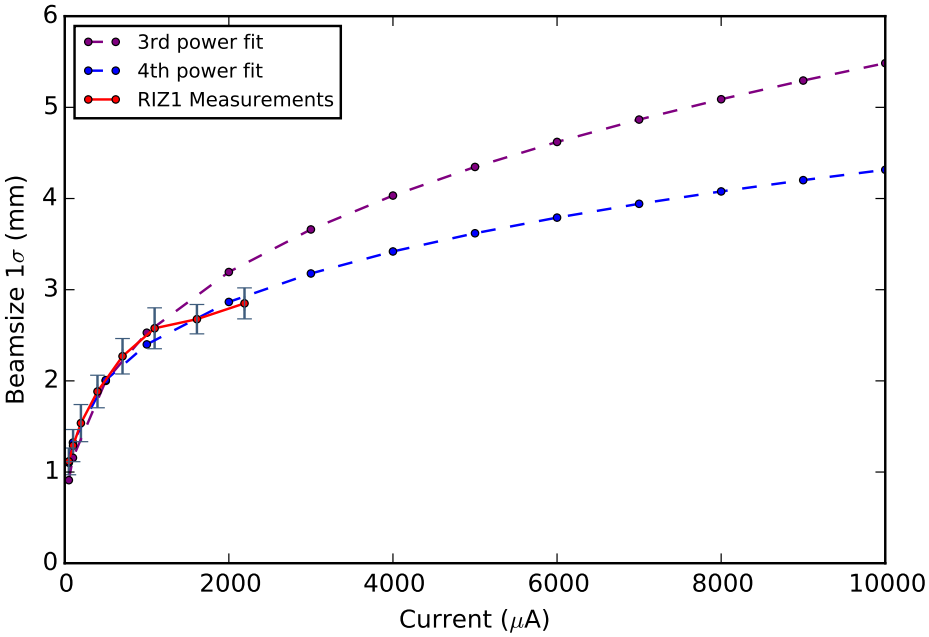

Figure 6.33: Measurements compared to 3rd and 4th power scaling.

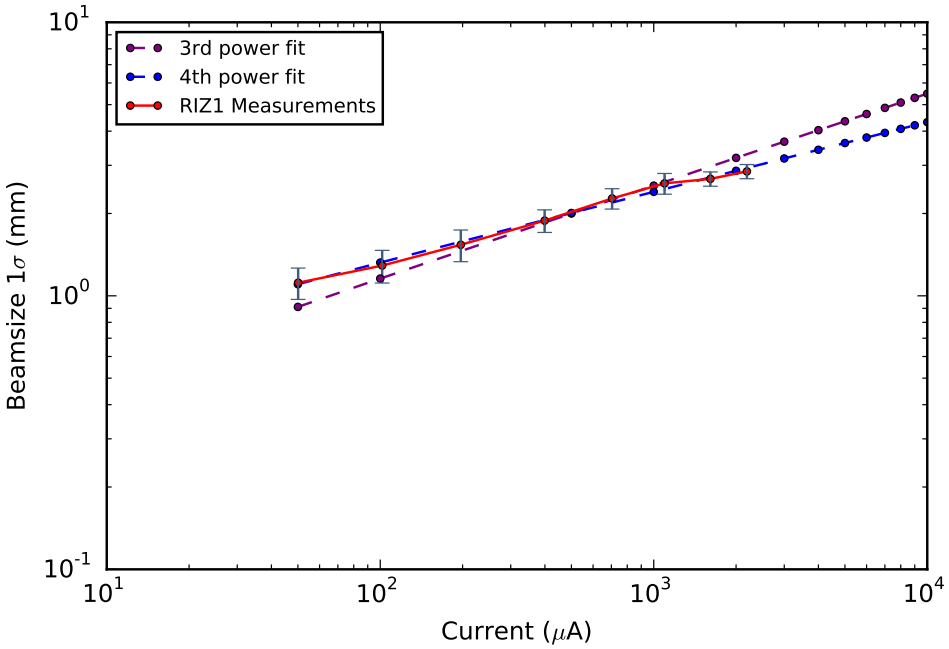

Figure 6.34: Log plot of measurements compared to 3rd power scaling law and new suggested scaling.

And the new scaling then is:

$$\sigma \propto 0.44\sqrt[4]{I} - 0.06. \tag{6.3}$$

The limits are dictated by the extraction septum and turn separation. The real machine currently operates at 20 mm turn separation (centre to centre) at the extraction radii. Simulations suggest this could be increased with appropriate parameter manipulation such as off-set injection.That is already used in Injector II with the help of trim coils to keep the 20 mm turn separation fixed. This 20 mm corresponds to about 6σ of the measured bunch and simulations have been matched to that (Figure 5.9). In Figure 6.35 we combine selected simulations with measurements. The beam size of the 6-turn mode matches the measurements well up to 2 mA. Higher intensity σ beam size goes over the predicted 4th power fit. If, indeed, the current scales with the power of 4, its advantage over the 3rd power would be seen only at currents above 2mA, where it implies that higher intensities of order of 3 mA could be achieved.

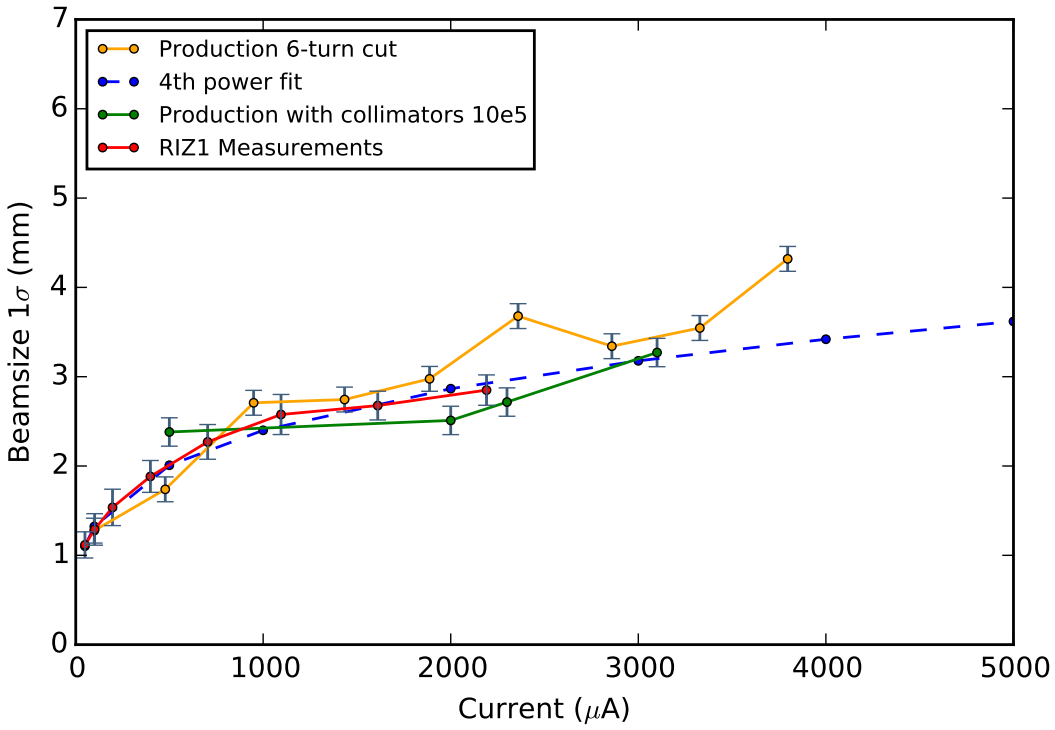

Figure 6.35: 6-turn sigma and physical collimator model simulation results compared to measurements and new suggested scaling.

In Figure 6.36 we fit the 6-turn 4σ model of the production configuration, where the beam size scales as

$$\sigma \propto 0.6\sqrt[4]{I} - 0.8 \tag{6.4}$$

with χ^2 of 28.4. If we perform cubed root fit:

$$\sigma \propto 0.26\sqrt[3]{I} + 0.03 \tag{6.5}$$

is now with slightly better $\chi^2 = 25.9$.

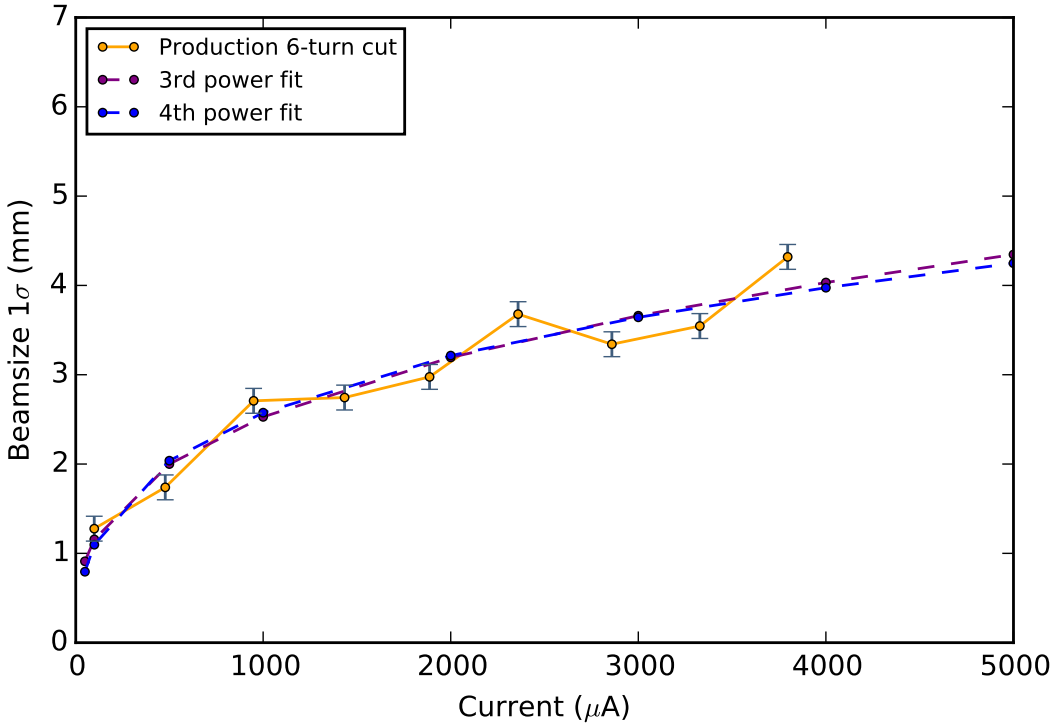

Figure 6.36: 6-turn 4σ beamsize and both 3rd and 4th power fits that appear to be equivalent.

Comparing the models in Figure 6.37, we can see in the physical collimator model (at $5 \cdot 10^4$, 10^5 and 10^6 macroparticles) overestimates the beam size when the lowest and highest statistics are used. One of the main contributors is the prominent longitudinal tail that couples to the radial plane. The tail is smaller for 10^5 case, hence these results are closer to the measured values. Each time a larger particle number is chosen in simulations, KIP2 (the collimator responsible for intensity selection) has to be adjusted to achieve the target current. This just proves how sensitive the model is and

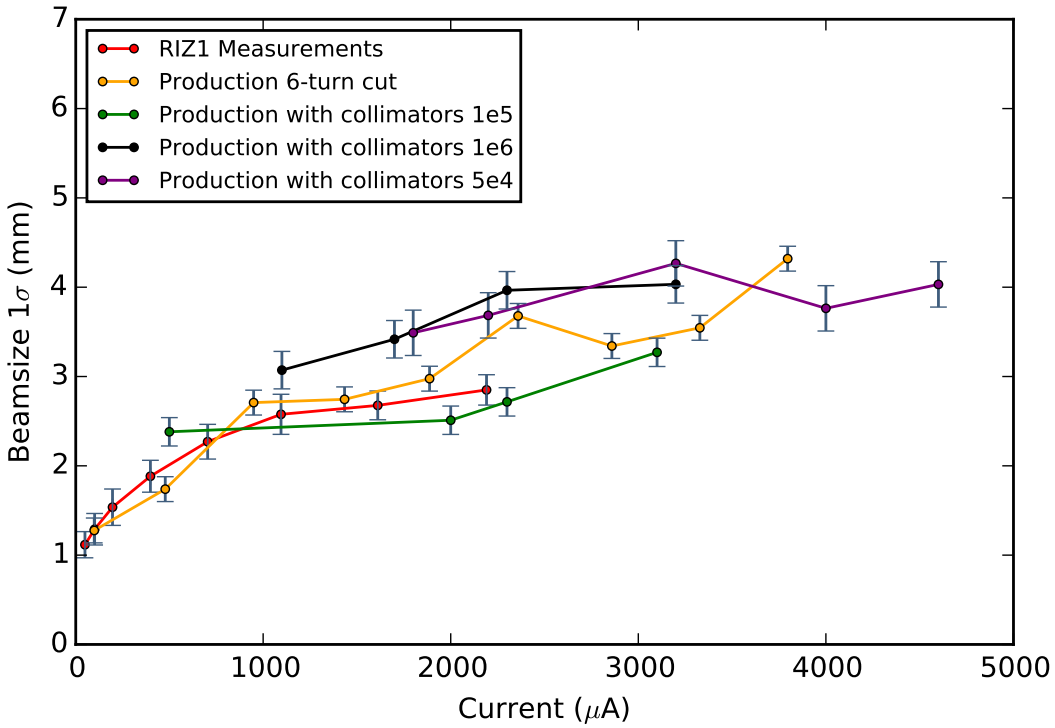

Figure 6.37: Beam size evolution with intensity of production configuration of 6-turn 4σ and physical collimator models compared to measurements. Added uncertainties on the simulated beam size based statistical fluctuations of multivariate random distribution.

such a change is sufficient to contribute to tail generation.

Further, we explore the 6-turn 4σ cut model under upgraded configuration. Fitting simulated data, we see in Figure 6.38 that 1σ RMS beam size is related to the current as follow:

$$\sigma \propto 0.44\sqrt[4]{I} - 0.5. \tag{6.6}$$

And cubed root scaling becomes:

$$\sigma \propto 0.17\sqrt[3]{I} + 0.3. \tag{6.7}$$

χ^2 is 0.11 and 0.079 respectively, but not a significant enough difference and they both indicate that 5 mA could be reached with RMS beam size of 3.2 mm.

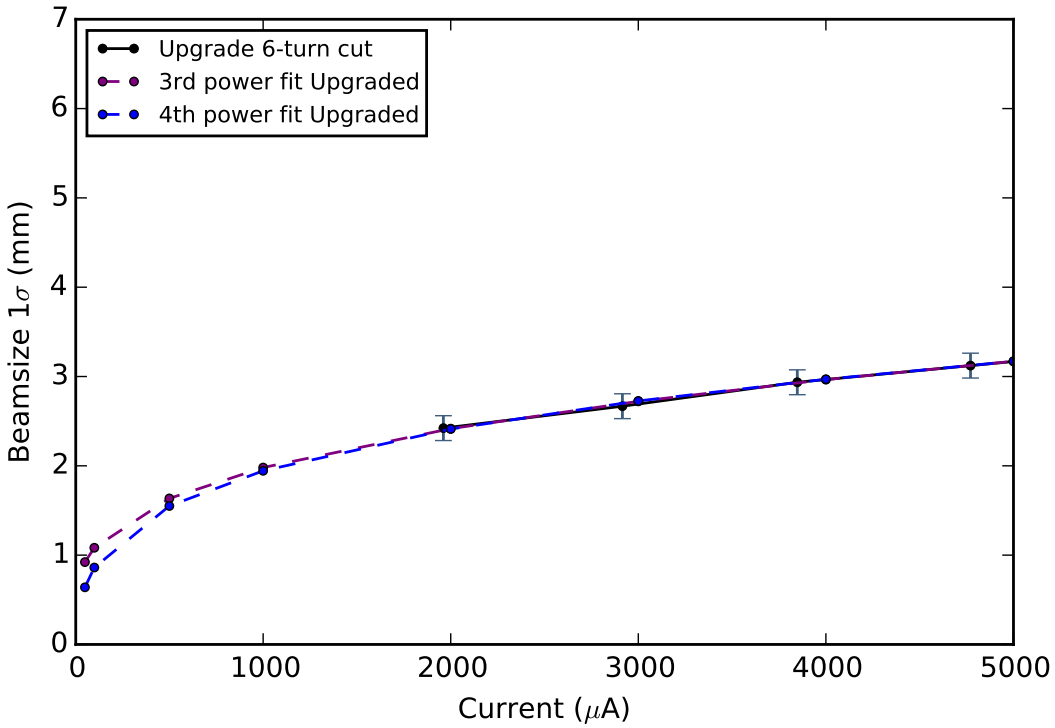

Figure 6.38: Plot of beam size evolution with intensity of the upgraded 6-turn 4σ model with its fits.

To summarise findings in a more general form we set the final beam size to σ (1σ RMS beam size). The σ_{sc} is the beam size with blow up (or hopefully shrinking) due to space charge, strong longitudinal-transverse coupling and lattice nonlinearities. The initial beam size σ_0 comes with the bunch if no space charge is acting on it. Therefore, the final beam size can be expressed as:

$$\sigma^2 = (\sigma_0 + \sigma_{sc})^2, \tag{6.8}$$

thus

$$\sigma_{sc} \propto \sqrt[3]{I} \tag{6.9}$$

or

$$\sigma_{sc} \propto \sqrt[4]{I}. \tag{6.10}$$

The general form of the beam size scaling can be written as:

$$\sigma \propto a\sqrt[n]{I} - b, \tag{6.11}$$

where a, b and $n \in \mathbb{R}$.

The trends in simulated and measured data suggests that 3 mA beam can be extracted in the production configuration. Fast acceleration contributes to even more compact bunches and with increased acceleration up to 5 mA could be extracted provided halo is kept at its minimum. Nonetheless, the best test of whether the 4th power fit to measurements is closer to the limits of Injector II would be to perform tests on Injector II.

6.4.2 Uncertainties on the Injector II parameters and our predictions

It is important to answer the question of how close to the real machine set-up we actually are. Injector II operates at different modes at any specific time, where either voltage on the resonators, trim coils or collimator positions are adjusted to decrease the losses or simply centre the beam. It is practically impossible to reproduce the exact same state in the model, however knowing the main characteristics we should be able to fit our solution closer to the Injector II operation. There are 12 trim coils fixing isochronicity due to field variation. Trim coils T1A and T1B located in the central region are also used to shift the beam in the radial direction. To address that in our models, changing the radius (R) and the radial momentum (PR) in our model has an equivalent effect.

It is indeed difficult to establish the level of uncertainties as the positions of the instruments and collimators are not well known and the drawings date back to the 1970s and may no longer be accurate. The transversal absolute position of the beam centre and the radial probe environment are not well known. Relative reading accuracy of short probes is of order of 0.3 mm, this becomes 2 mm for long ones [4]. In such case the probe measurement position accuracy may vary from few to even 15 mm. Another questionable parameter is the energy of the machine, as the energy analytically calculated from probe measurements is lower than the one that is believed to be in the machine and the absolute value may vary even up to ± 0.5 MeV. This would change the nominal values of the modelled beam size but not the trend of the data with intensity.

Not even mentioning the starting parameters, there is of course also a large uncertainty on the simulations. Attempting to put an error bar on simulations in a ”classical” sense is not a right approach. Nonetheless, we could look, for instance, on the statistical uncertainty on the multivariate distribution and estimate how it will affect the

beam size data. A simple simulation set-up will bring uncertainty with the selection of the number of macroparticles or mesh for calculating space charge. Additionally uncertainty carried with the generation of multivariate distributions will have an influence on the results. To address that a 9.5 mA 10^5 macroparticle distribution input file has been split into four 25000-particle parts and run in separate simulations. Standard deviation of RMS beam sizes measured by RIZ1 has been calculated for all cases and added as an error to the modelled data. The mesh had to be adjusted from 16 to 8 as the number of particles significantly decreased. The same approach has been applied for the remaining macroparticle distributions. In Figure 6.37 we can see how the results with error bars compare to the measured data. As one would expect, this improves how the physical collimator model fits the measured RIZ1 data. However, the errors are an estimate because they have been calculated in each case only for one intensity as each data point error analysis would require 4 full simulations.

Our models represent only a small fraction of the many operating and constantly changing states of the real machine, but if we ensure correct:

- Turn number: 83 $\pm$1,
- Radial turn pattern,
- Extraction radius: 3-3.7 m,
- Cyclotron frequency: 5.063 MHz,
- Acceleration system frequency: 50.63 MHz,

then the energy should be correct thus the model solutions are believed to fit into the operating range of solutions.

6.5 Chapter summary

We have analysed and compared all the considered models under the production and upgraded configurations. Just by looking at the approximated models, the upgrade brings tremendous advantages, nearly doubling the turn separation and current limit. The 6-turn 4σ cut model comparison of both configurations shows how in the upgraded case halo is not generated after we stop cutting. The beam is well matched with fast acceleration and good starting conditions.

Looking at the physical collimator model in more detail, we see a generated long longitudinal tail that eventually couples to the radial plane leading to a large RMS beam size. However, adjustment of KIP4 collimator seem to clean the tail sufficiently, decreasing the beam parameters significantly. The halo outside 5σ carries a significant amount of current, particularly for lower statistics runs. Unfortunately, we are not in the place to do one-to-one simulations as yet due to time constraints and insufficient computing resources.

For benchmarking and the estimation of intensity limits, horizontal data is sufficient as it is the width of the septum that is the main physical constraint, however exaggerated longitudinal tails will decrease the limits. Based on the measurements and simulations we have attempted to find scaling laws that govern the beam size variation with intensity thus intensity limits. We have found that the production configuration current scales to the power of four with the beam size, setting the limit to approximately 3 mA. Further analysis of an upgraded configuration suggests that intensities of over 5 mA could be produced with an adjusted collimation scheme.

Chapter 7

Summary

7.1 Summary

The Injector II separate-sector isochronous cyclotron has been in operation for over 40 years, initially designed to operate at pA level, it has beaten the predicted limits on multiple occasions. This research is aimed at showing that this machine can do even better, and that space charge induced vortex motion and phase mixing can aid in achieving this. Measured and simulated data suggests that the beam size scales with 3rd power with intensity. However, measurements of higher currents fit better the 4th order. If this is the case, Injector II could operate at 3 mA with its current resonators and flat-top cavities. This limit nearly doubles for the planned upgrade, where the currents could reach over 5 mA.

In order to investigate the limits, three models of Injector II have been developed for both the production and upgraded configuration. The models are: continuous 4σ cut, 6-turn 4σ cut, and physical collimation. The numerical models have been validated and analysed based on various intensities, statistics and Injector II measurements.

A matched distribution generator, even though not perfectly matched for the Injector II lattice, works well for the models considered. The upgraded set-up looks very promising with nearly doubled turn separation and intensity. All models have been validated with data from radial profile measurements (RIZ1) and loss rates read from the collimators in Injector II. At this level the 6-turn 4σ cut, and physical collimation model with 10^5 particles, fits very well. In the case of $5 \cdot 10^4$ and 10^6, a large tail is generated that couples to the radial plane leading to overestimation of the RMSx beam size. This is not the case in the two other cases. A successful attempt has been made to remove this tail by tracing the particles found outside the 5σ region back to where

they first appeared and adjusting the collimator. However, due to time limitations these adjustments have not been used in other simulations. If one is to look at the halo, 10^5 or 10^6 macroparticle simulations are required.

The model could be still improved, however we have achieved a good agreement with initial conditions and transverse real-space information. Moving a collimator longitudinally makes a tremendous difference. The longitudinal profile parameter goes significantly down, as the long tail is removed with KIP4. Radial beam data is consistent across all the models. The full beam extent remains unchanged as scattered particles remain, but it is apparent that with more optimisation this could be completely removed. Figure 6.23 show comparisons of original and fixed models. Comparing beam evolution of both models looking at Figure 6.24 (e) and (f) we can see how the longitudinal tail is removed.

The physical collimator model requires careful adjusting of the collimator leaves and for time-efficiency $5 \cdot 10^4$ macroparticle bunches have been used. Once the collimators have been set-up and distributions of $5 \cdot 10^4$, 10^5 and 10^6 macroparticles run through, the final currents differed in each case. This is partially due to step size versus macroparticle size. Each time the macroparticle size is changed and step size kept, different amount of particles will be captured by the collimators. There is a bottom limit of modelled current of 1.8 mA for $5 \cdot 10^4$ particles due to that fact. There is a point at which a large amount of particles is stopped by collimators at less than μm range movement thus making it impossible to select specific currents. Unfortunately, increasing either the time step or number of particles will increase the simulation time and setting up collimators (which requires moving collimators at submillimeter level, with no prior knowledge of where they should be). For 14 collimator leaves, this is just not feasible. Therefore the approach of setting up collimators for $5 \cdot 10^4$ particles and 3600 steps per turn was chosen to be optimal, requiring only small adjustments of collimators when the macroparticle number is increased.

We have found that the production configuration current scales to the power of four with the beam size, setting the limit to approximately 3 mA. Further analysis of an upgraded configuration suggests that intensities of over 5 mA could be produced with an adjusted collimation scheme.

For benchmarking and estimation of intensity limits, horizontal data is sufficient as it is the width of the septum that is the main physical constraint, however exaggerated longitudinal tails will decrease the limits. Radially all models are relatively close, it is the longitudinal plane data that varies the most. The results are promising, however

there is field for improvement that could change the presented picture. The best validation of the predictions would be to perform experiments on Injector II, testing whether 3 mA is indeed possible with this configuration.

7.2 Possible improvements

We have answered the question of intensity limits based on the developed models and data fitting, however there is always a place for improvement as no model is flawless. During the research we have identified fields for improvement. First of all, generating a matched distribution is limited as it is based on linear space charge. The PSI Accelerator Modelling and Advanced Simulations (AMAS) group is currently working on a non-linear matched distribution generator, which could be interesting to investigate [49]. However, in order to precisely model strongly coupled particle distributions as found in Injector II one should model the transfer line, together with the buncher and 90° injection. Also the model itself could be improved by adding a more realistic RF gap profile. Multi-objective Optimisation has been considered, in order to efficiently select collimator positions yielding minimal halo and thus losses, but this would require more computing power than was available.

Another important improvement would be to implement the remaining collimators to check whether this indeed would limit the modelled halo. However from looking at the positions where the halo has been generated, there is no obvious indication that this would improve the simulations. And if that is the case, one could consider removing unnecessary collimators from the central region.

Since simulated data suggests that the beam size scales to the 4th power with intensity, a theory behind this result could be developed.

And finally, with the arising opportunity, an experimental investigation could confirm or disprove suggested limits for the present configuration. Some of the experimental steps would include minimising turn number, increasing last turn separation with trim coils, allowing more current through with KIP2 collimator while moving KIP4 collimator and possibly other collimators. Simulations suggest that is where the beam is stopped when current is increased.

Bibliography

[1] PSI facility technical data.

[2] https://www.psi.ch/abe/facilities.

[3] M. Seidel et al. Production of a 1.3 MW Proton Beam at PSI. In *International Particle Acceleraotor Conference*, pages 1309–1313, Kyoto, Japan, 2010.

[4] Private conversation.

[5] A. Adelmann et al. The OPAL Framework (Object Oriented Parallel Accelerator Library) Version 1.4.0 User's Reference Manual. Technical report, Paul Scherrer Institut, 2016.

[6] W. Joho. High Intensity Problems in Cyclotrons. In *Proceedings of the 9th International Conference on Cyclotrons and their Applications , Caen, France*, pages 337–347, Caen, France, 1981.

[7] S. Adam. Space Charge Effects in Cyclotrons - from Simulations to Insights. In *Proceedings of the 14th Inernational Conference on Cyclotrons and their Applications*, pages 446–449, Cape Town, SA, 1995.

[8] M. Humbel. Comissioning and tuning of the new buncher system. In *Proceedings of the 18th Inernational Conference on Cyclotrons and their Applications*, page 464, Giardini Naxos, Italy, 2007.

[9] Th. Stammbach et al. The PSI 2 mA Beam and Future Applications. In *16th International Conference on Cyclotrons and Their Applications*, pages 423–428, East Lansing, Michigan, 2001.

[10] Th. Stammbach et al. The Feasibility of High Power Cyclotrons. *Nuclear Instruments and Methods in Physics Research Section B: Beam Interactions with Materials and Atoms*, (113), 1996.

[11] M. Bopp, H. Fitze, P. Sigg, and L. Stingelin. Upgrade Concepts of the PSI Accelerator RF Systems for a Projected 3 mA Operation. In *16th International Conference on Cyclotrons and Their Applications*, page 300, East Lansing, Michigan, 2001.

[12] M. M. Gordon. The Longitudinal Space Charge Effect and Energy Resolution. In *5th International Cyclotron Conference*, pages 305–317, Oxford, United Kingdom, 1969.

[13] A.J. Baltz C. Chasman. Space charge effects in a heavy ion cyclotron. *Nuclear Instruments and Methods in Physics Research*, 219:279–283, 1984.

[14] S. Adam. Calculations of Space Charge Effects in Isochronous Cyclotrons. *IEEE Transactions on Nuclear Science*, NS-32(5), 1985.

[15] S. Adam and W. Joho. Longitudinal space charge effects in the sin injector ii and in the sin ring cyclotron. In *Proceedings of the 9th International Conference on Cyclotrons and their Applications*, page 337, Caen, France, 1981.

[16] W. J. G. M. Kleeven. *Theory of Accelerated Orbits and Space-charge Effects in an AVF Cyclotron*. PhD thesis, Technical University of Eindhoven, 1988.

[17] E. Pozdeyev. *CYCO and SIR: New Tools for Numerical and Experimental Studies of Space Charge Effects in The Isochrnous Regime*. PhD thesis, Michigan State University, 2003.

[18] A. J Cerfon et al. Vlasov equation approach to space charge effects in isochronous machines. In *Proceedings of the 21st Inernational Conference on Cyclotrons and their Applications*, pages 310–14, Vancouver, Canada, 2013.

[19] Y.J. Bi, A. Adelmann, et al. Towards quantitive simulations of high power proton cyclotorns. *Physical Review Special Topics - Accelerators and Beams*, 14(054402), 2011.

[20] J. J. Yang, A. Adelmann, M. Humbel, M. Seidel, and T. J. Zhang. Beam Dynamics in High Intensity Cyclotrons Including Neighboring Bunch Effects: Model, Implementation and Application. *Nuclear Instruments and Methods in Physics Research Section A: Accelerators, Spectrometers, Detectors and Associated Equipment*, 704:84–91, 2013.

[21] C. Aberle et al. Whitepaper on the DAEδALUS Program. Technical Report arXiv:1307.2949v1.

[22] Y. Ineichen. *Toward Massively Parallel Multi-objective Optimization with Application to Particle Accelerators*. PhD thesis, ETH Zürich No. 21114, 2012.

[23] P. Bertrand and Ch. Ricaud. Specific cyclotron correlations under space charge effects in the case of a spherical beam. In *Proceedings of the 16th International Conference on Cyclotrons and Their Applications*, page 379, East Lansing, Michigan, 2001.

[24] F. Sacherer. RMS Envelope Equations with Space Charge. In *Particle Accelerator Conference*, page 1105, Chicago, United States, 1971.

[25] C Baumgarten. A Symplectic Method to Generate Multivariate Normal Distributions. (arXiv:1205.3601v1), 2012.

[26] C. Baumgarten. A New Look at Linear (non-?) Symplectic Ion Beam Optics in Magnets. *Nuclear Instruments and Methods in Physics Research Section A: Accelerators, Spectrometers, Detectors and Associated Equipment*, 735:546–551, Jan 2014.

[27] K.R. Cardinall T.P. Wangler. Relation between field energy and rms emittance in intense particle beams. *IEEE Transactions on Nuclear Science*, 32(2196), 1985.

[28] C. K. Allen, T. P. Wangler, et al. Beam-Halo Measurements in High-Current Proton Beams. *Physical Review Letters*, 89(21):18–21, 2002.

[29] C.K. Allen and T.P. Wangler. Parameters for quantifying beam halo. *Proceedings of Particle Accelerator Conference*, 3:1732–1734, 2001.

[30] The large hadron collider conceptual design. Technical Report CERN/AC/95-05(LHC), CERN, 1995.

[31] A. Wu Chao and M. Tigner. *Handbook of Accelerator Physics and Engineering*. World Scientific Publishing, 1998.

[32] S. Y. Lee. *Accelerator physics*. World Scientific Publishing Co. Pte. Ltd, 2nd edition, 2004.

[33] K. Strijckmans. The Isochronous Cyclotron: Principles and Recent Developments. *Computerized medical imaging and graphics: the official journal of the Computerized Medical Imaging Society*, 25(2):69–78, 2001.

[34] W. Joho. Cyclotron specials talk at PSI. Paul Scherrer Institut Indico (https://indico.psi.ch/getFile.py/access?resId=41&materialId=slides&confId=3484), 2011.

[35] M. Seidel. Cyclotrons for high-intensity beams. (arXiv:1302.1001), 2013.

[36] K. Schindl. Space Charge. In *Space charge*, pages 127–151, Joint US-CERN-Japan-Russia School on Particle Accelerators, Beam Measurements, Montreux, 1998.

[37] R. Baartman. Space charge limit in separated turn cyclotrons. In *Proceedings of the 21st Inernational Conference on Cyclotrons and their Applications*, Vancouver, Canada, 2013.

[38] A. Wolski. Alternative approach to general coupled linear optics. *Physical Review Special Topics - Accelerators and Beams*, 9, 2006.

[39] C. Baumgarten. A geometrical method of decoupling. *Physical Review Special Topics - Accelerators and Beams*, 15, 2012.

[40] A. A. Vlasov. The vibrational properties of an electron gas. *Soviet Physics Uspekhi*, 10(6), 1968.

[41] F.C. Iselin et al. Mad version 9. In *7th European Particle Accelerator Conference*, Vienna, Austria, 2000.

[42] F. C. Grote, H. Iselin. The MAD Program (Methodical Accelerator Design). Technical report, Users Reference Manual, 1994.

[43] A. Adelmann et al. The Object Oriented Parallel Accelerator Library (OPAL), Design, Implementation and Application. In *Proceedings of 10th Inernational Computational Accelerator Physics Conference*, pages 107–110, San Francisco, US, 2009.

[44] PSI intranet.

[45] Gnuplot (http://gnuplot.sourceforge.net).

[46] Rene Brun and Fons Rademakers. ROOT–An Object Oriented Data Analysis Framework. *Nuclear Instruments and Methods in Physics Research Section A: Accelerators, Spectrometers, Detectors and Associated Equipment*, 389(1):81 – 86, 1997.

[47] Python (https://www.python.org).

[48] T. P. Wangler, K. R. Crandall, R. Ryne, and T. S. Wang. Particle-core model for transverse dynamics of beam halo. *Physical Review Special Topics - Accelerators and Beams*, 1(084201), 1998.

[49] M. Frey. Matched Distributions in Cyclotrons with Higher Order Moments of the Charge Distribution. Mester Thesis ETH Zurich, 2016.

Appendix A

Additional data

The Appendix collects additional results of intensity scans varied from 0.5 mA to 6.0 mA. The data includes both production and upgraded configurations concerning continuous 4σ cut, 6-turn 4σ cut and the physical collimator models. Number of macroparticles shown include $5 \cdot 10^4$, 10^5 and 10^6. Analysis data includes beam properties (such as RMS beam size, emittance and profile parameter with full beam extent), current outside 5σ region (with additional halo particles tagged at the last step and tracked back to the start). That is followed by real space plots comparison of simulated data before and after shifting KIP4 collimator for $5 \cdot 10^4$ and 10^5 macroparticles at various energies. The last section of the Appendix collects additional analysis of simulated currents on collimators in terms of macro particle size and intensity.

A.1 Production configuration models

A.1.1 Continuous 4σ cut

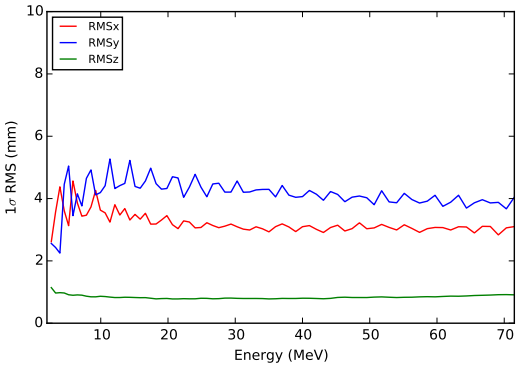

(a) RMS beam size

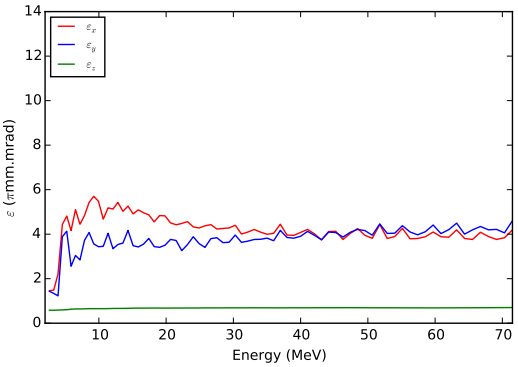

(b) Emittance

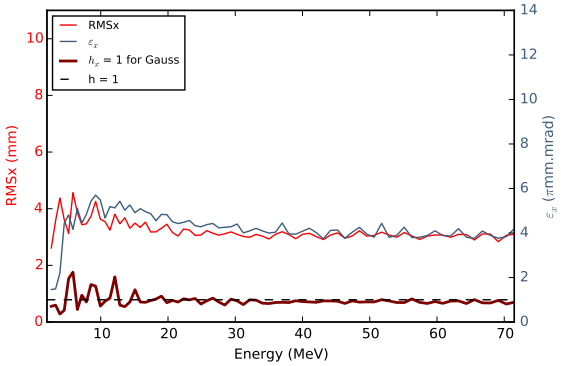

(c) Horizontal RMS, Emit, h

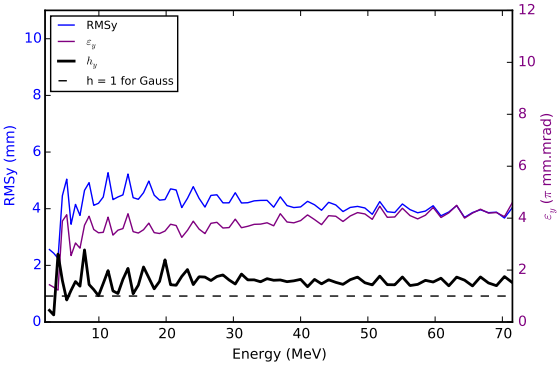

(d) Vertical RMS, Emit, h

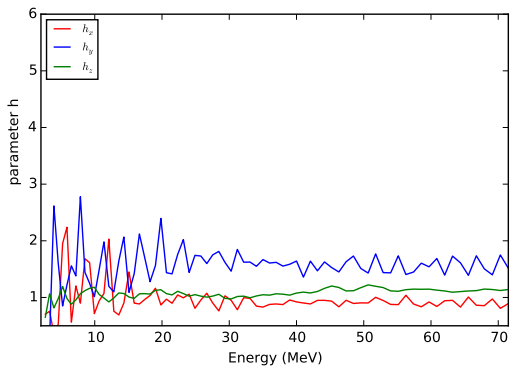

(e) Profile parameter x, y and z

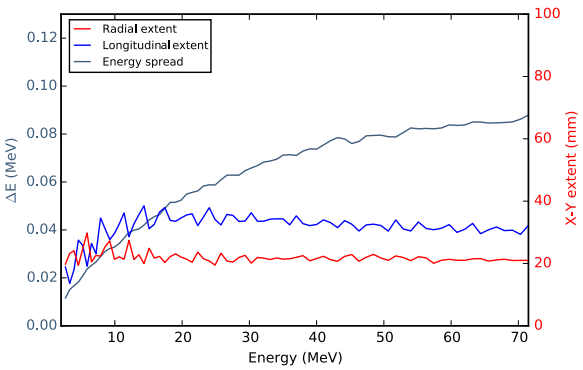

(f) Full extent of the beam and energy spread

Figure A.1: Production set-up 2 mA case. Continuous 4σ cut with 10^6 macro-particles.

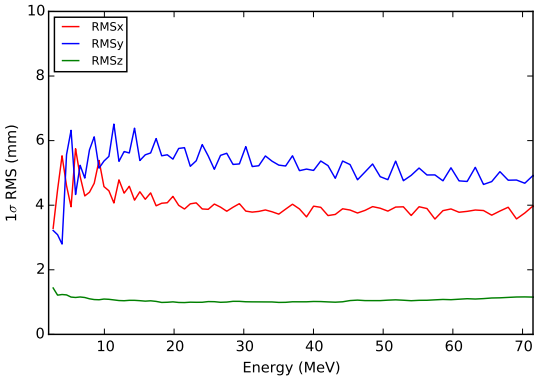

(a) RMS beam size

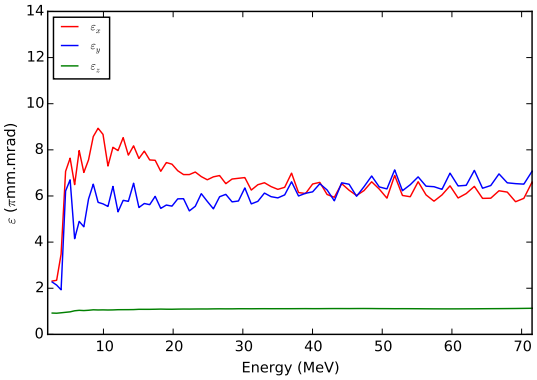

(b) Emittance

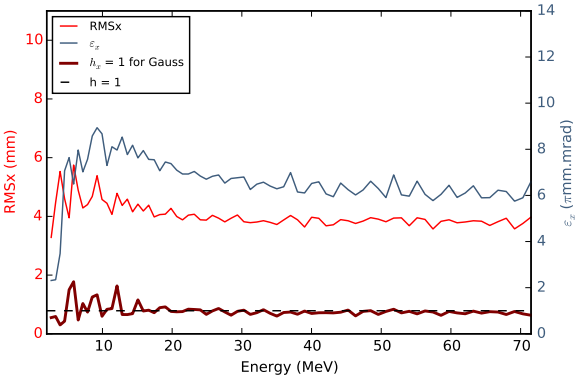

(c) Horizontal RMS, Emit, h

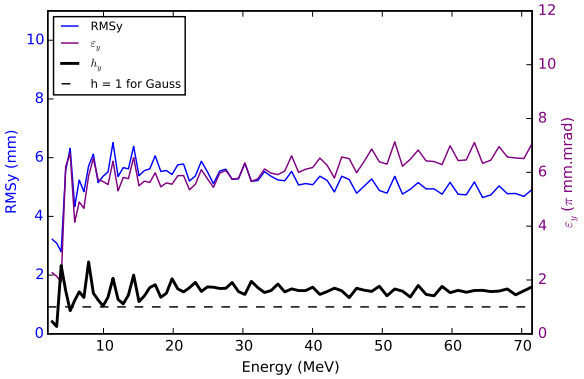

(d) Vertical RMS, Emit, h

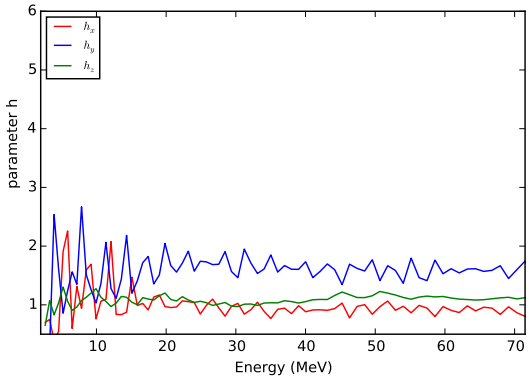

(e) Profile parameter x, y and z

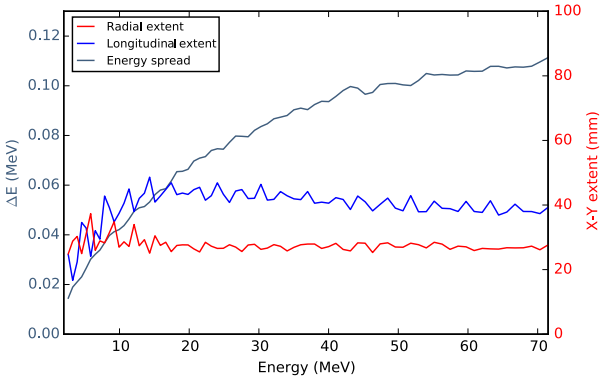

(f) Full extent of the beam with marked energy spread

Figure A.2: Production set-up 4 mA case. Continuous 4σ with 10^6 macro-particles.

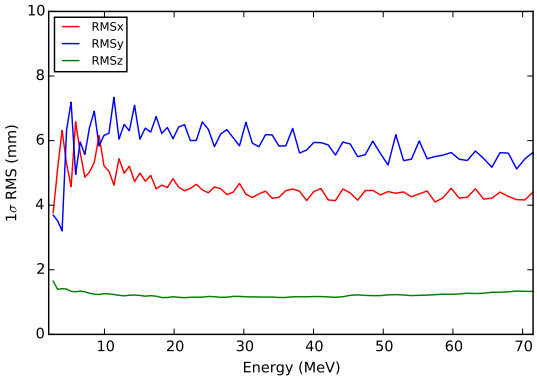

(a) RMS beam size

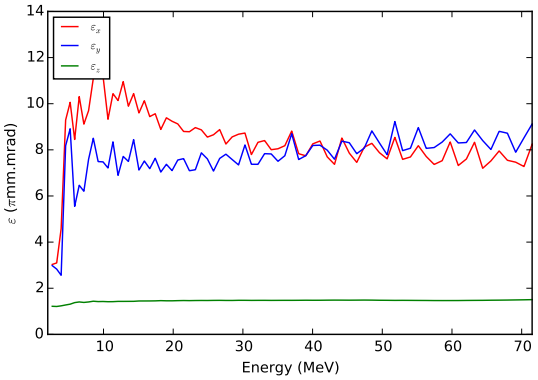

(b) Emittance

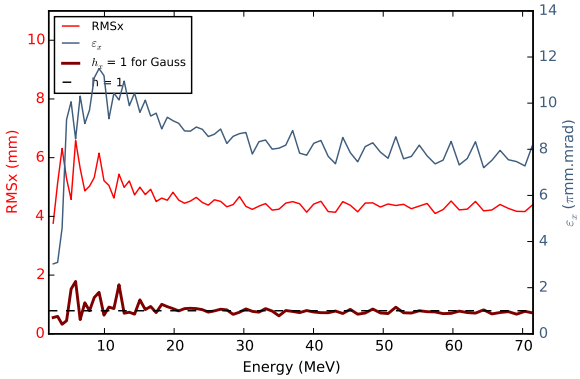

(c) Horizontal RMS, Emit, h

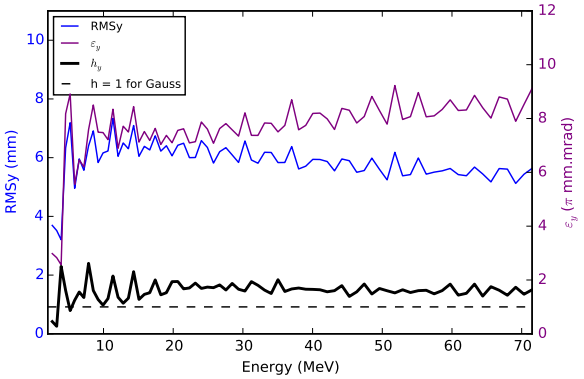

(d) Vertical RMS, Emit, h

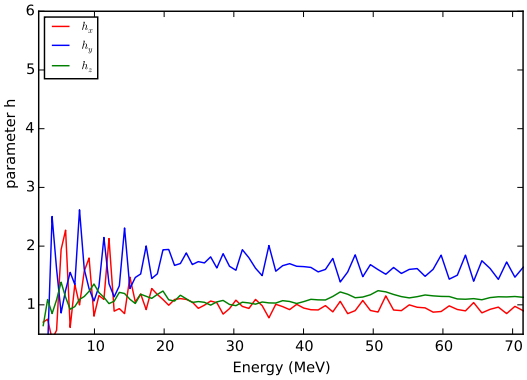

(e) Profile parameter x, y and z

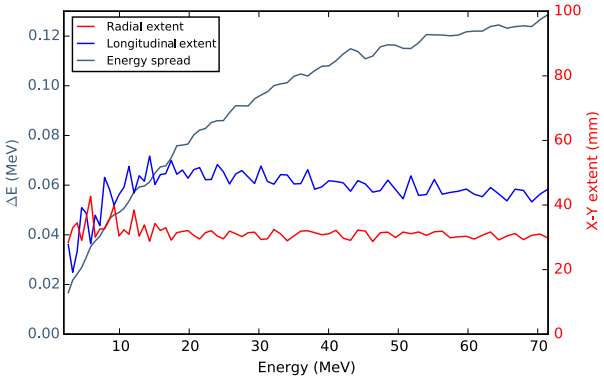

(f) Full extent of the beam with marked energy spread

Figure A.3: Production set-up 6mA case. Continuous 4σ with 10^6 macro-particles.

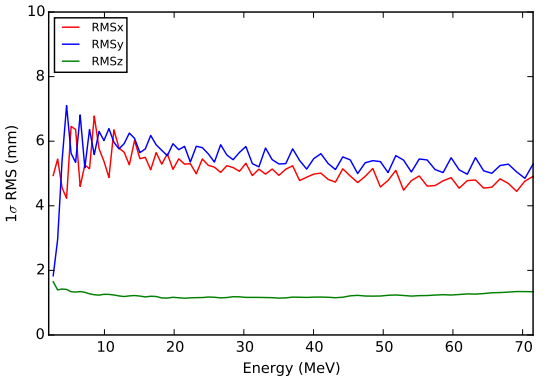

(a) RMS beam size

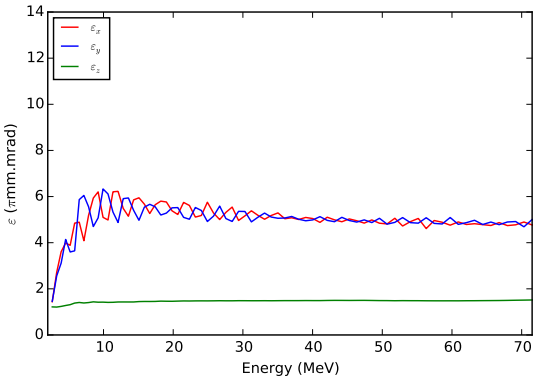

(b) Emittance

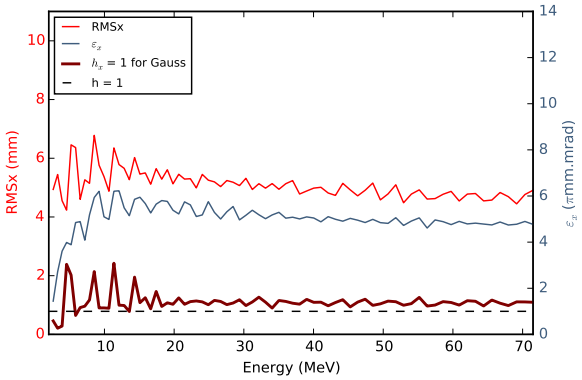

(c) Horizontal RMS, Emit, h

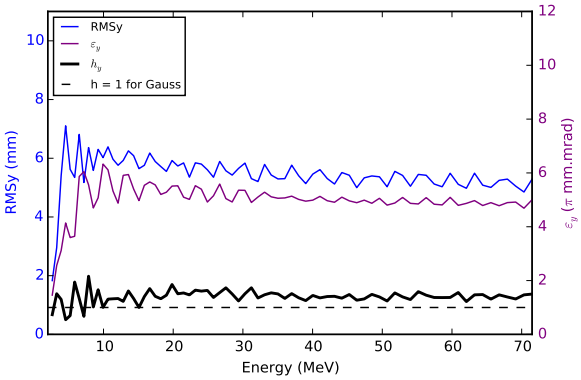

(d) Vertical RMS, Emit, h

Figure A.4: Production set-up 6 mA case. Continuous 4σ cut with $5 \cdot 10^4$ macro-particles.

A.1.2 6-turn 4σ cut

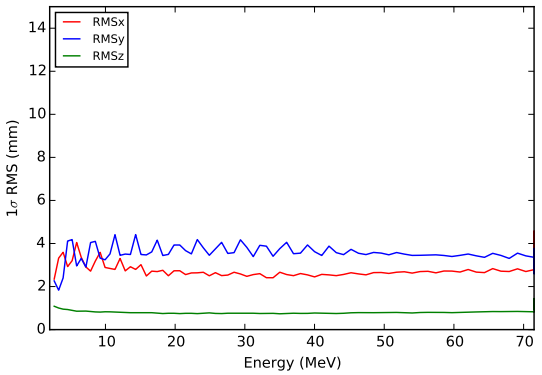

(a) RMS beam size

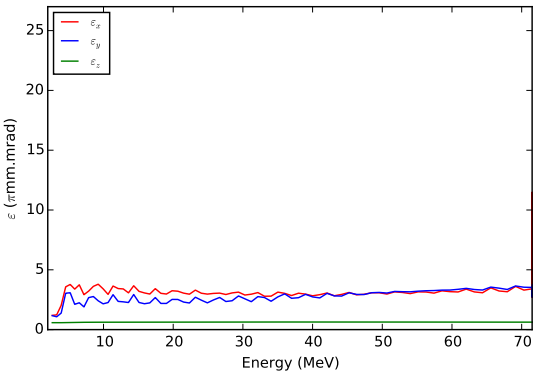

(b) Emittance

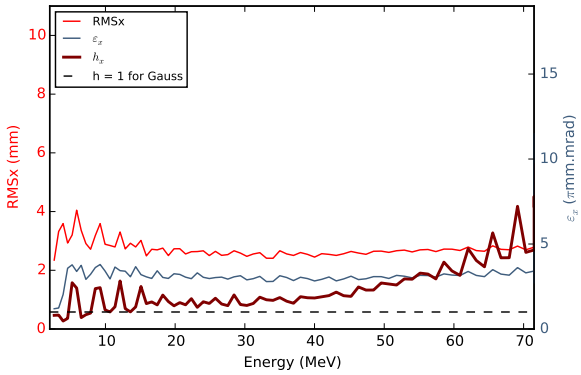

(c) Horizontal RMS, Emit, h

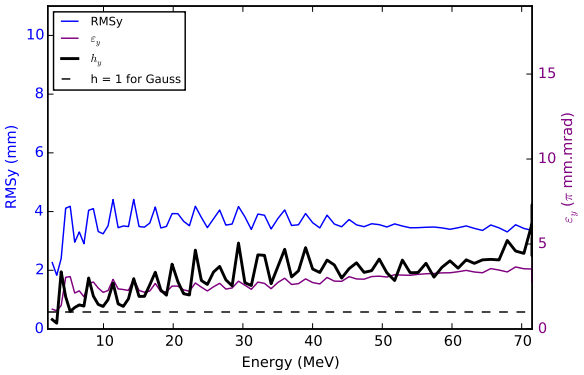

(d) Vertical RMS, Emit, h

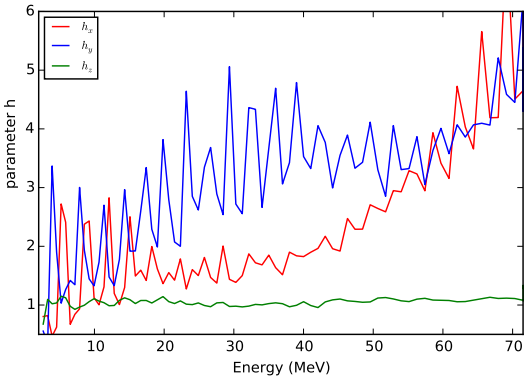

(e) Profile parameter h

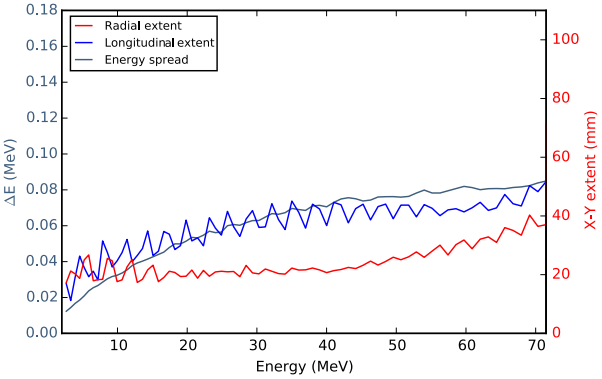

(f) Total beam extent

Figure A.5: Production set-up 1.0 mA case. 6-turn 4σ cut with $5 \cdot 10^4$ macro-particles.

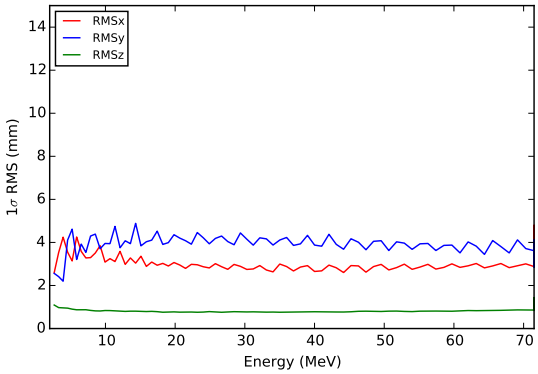

(a) RMS beam size

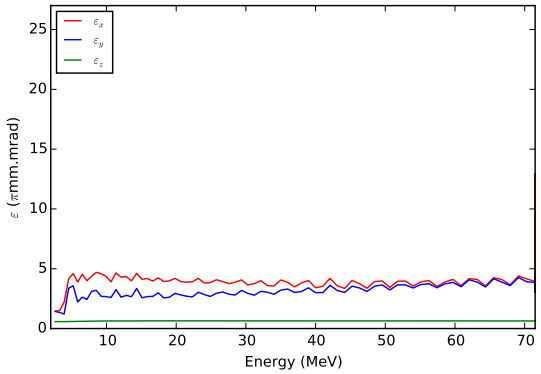

(b) Emittance

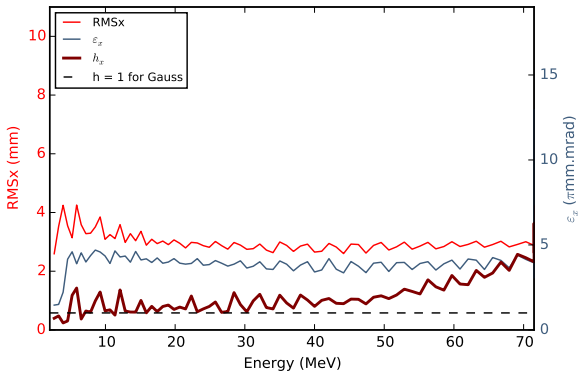

(c) Horizontal RMS, Emit, h

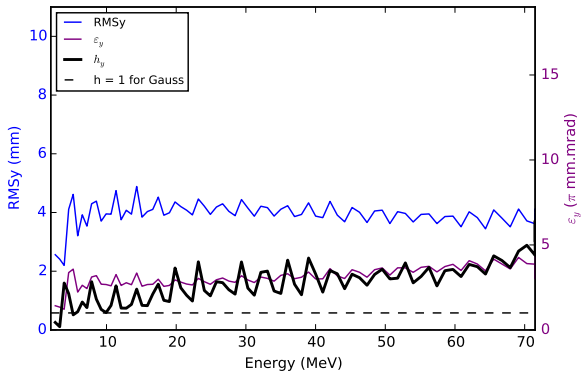

(d) Vertical RMS, Emit, h

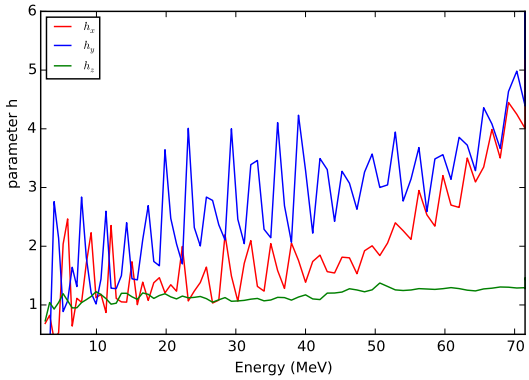

(e) Profile parameter h

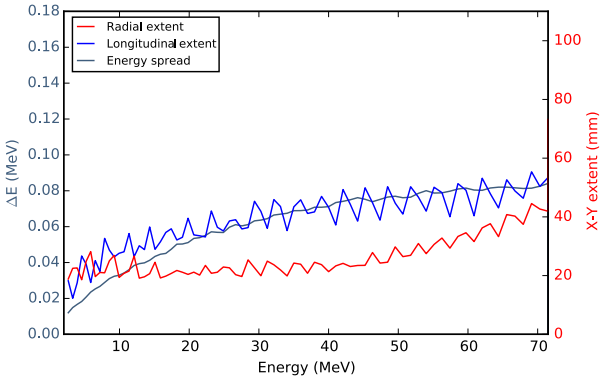

(f) Total beam extent

Figure A.6: Production set-up 2.0 mA case. 6-turn 4σ cut with $5 \cdot 10^4$ macro-particles.

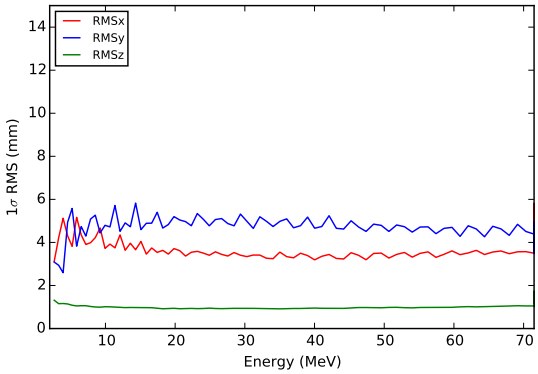

(a) RMS beam size

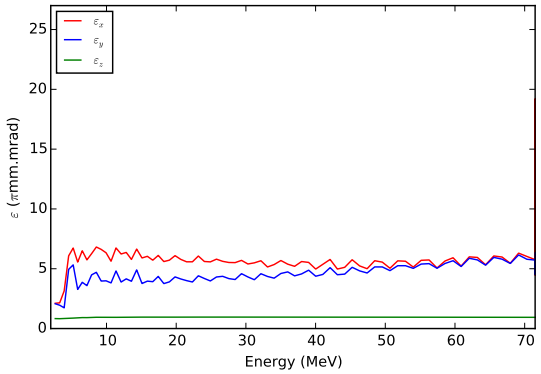

(b) Emittance

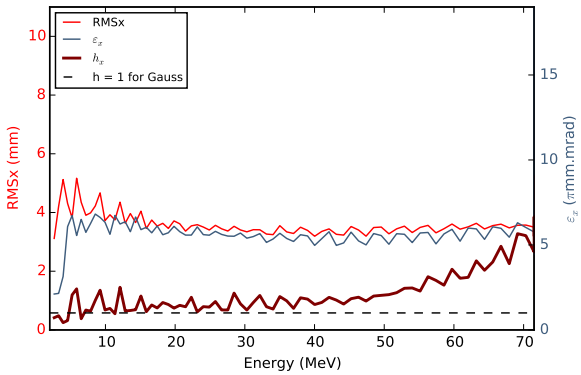

(c) Horizontal RMS, Emit, h

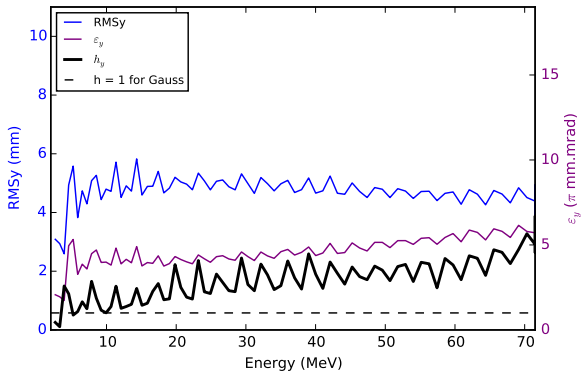

(d) Vertical RMS, Emit, h

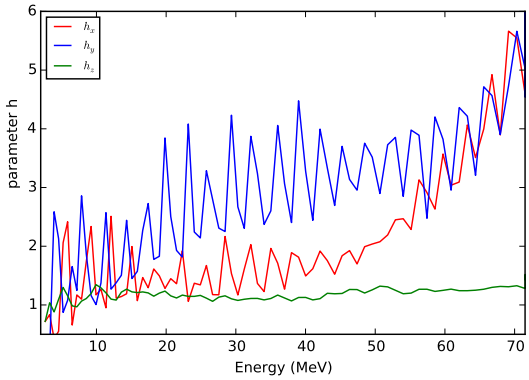

(e) Profile parameter h

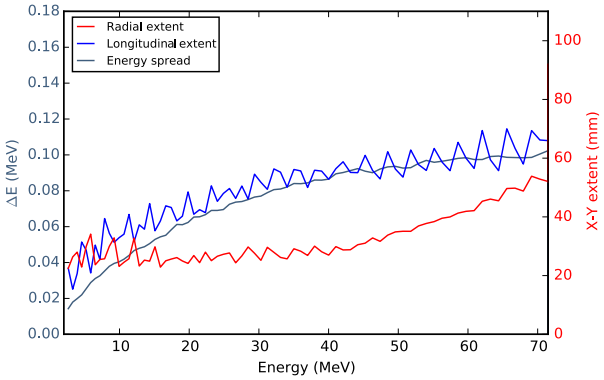

(f) Total beam extent

Figure A.7: Production set-up 3.5 mA case. 6-turn 4σ cut with $5 \cdot 10^4$ macro-particles.

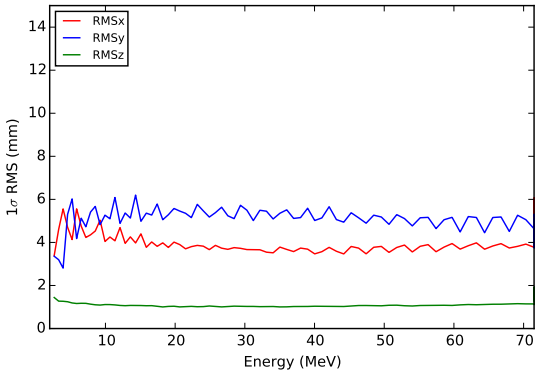

(a) RMS beam size

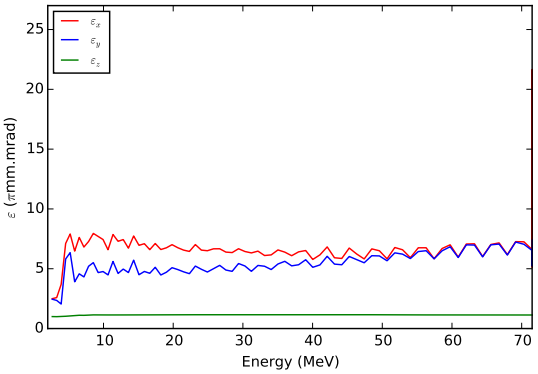

(b) Emittance

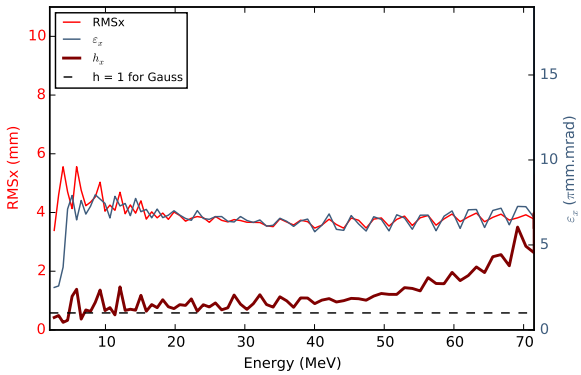

(c) Horizontal RMS, Emit, h

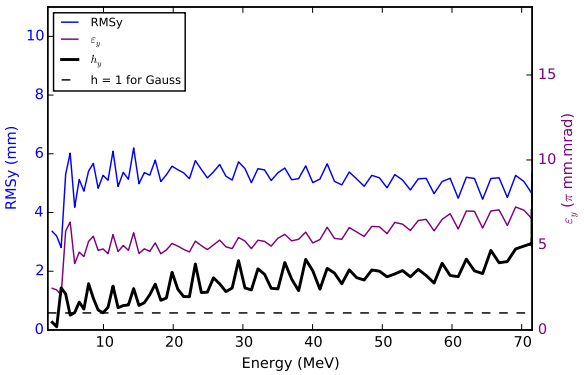

(d) Vertical RMS, Emit, h

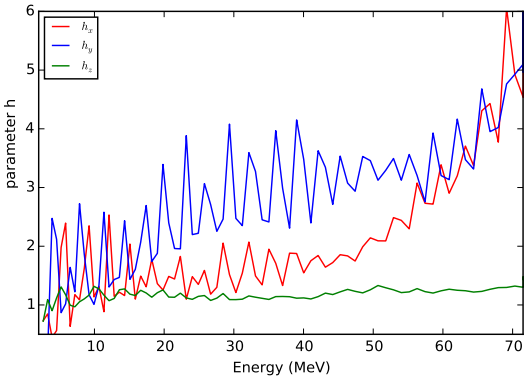

(e) Profile parameter h

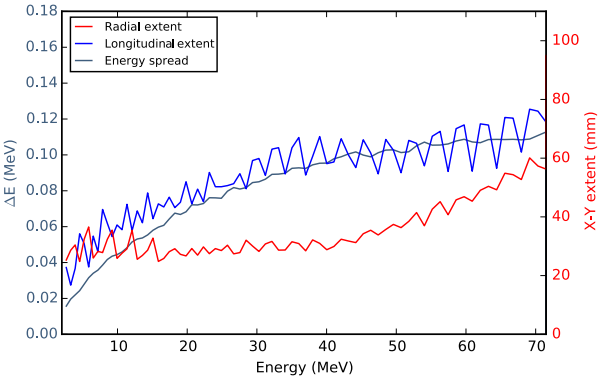

(f) Total beam extent

Figure A.8: Production set-up 4.5 mA case. 6-turn 4σ cut with $5 \cdot 10^4$ macro-particles.

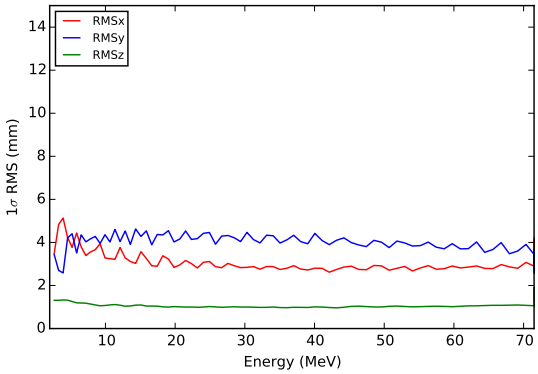

(a) RMS beam size

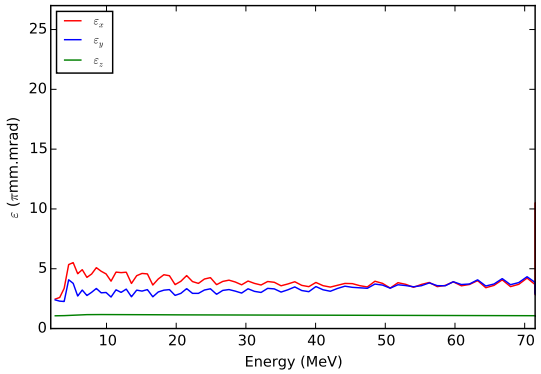

(b) Emittance

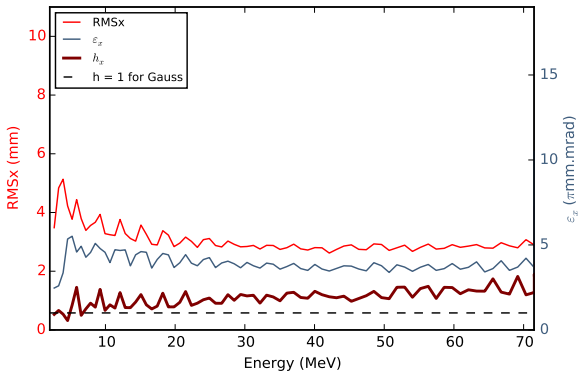

(c) Horizontal RMS, Emit, h

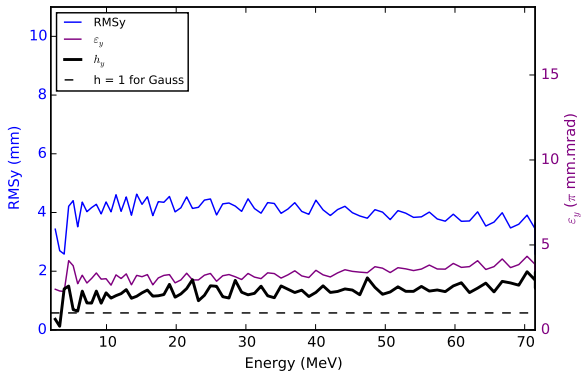

(d) Vertical RMS, Emit, h

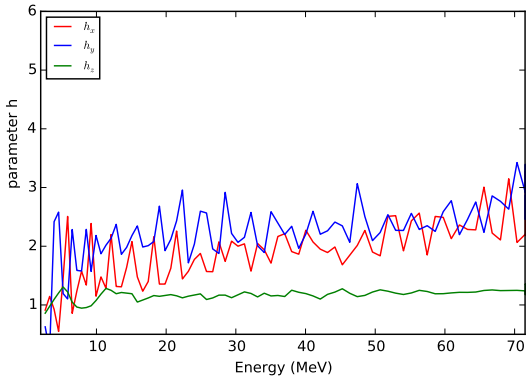

(e) Profile parameter h

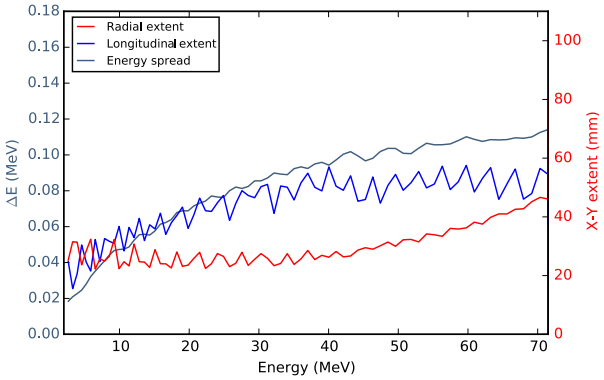

(f) Total beam extent

Figure A.9: Production set-up 5.0 mA case. 6-turn 4σ cut with $5 \cdot 10^4$ macro-particles.

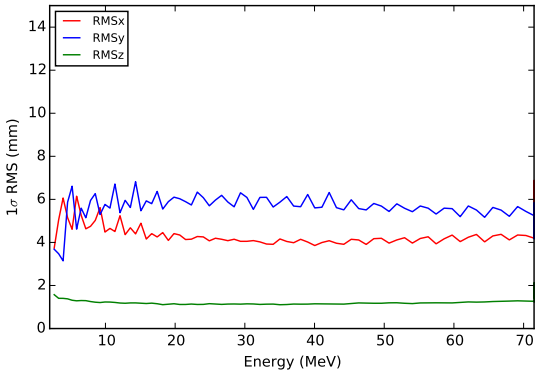

(a) RMS beam size

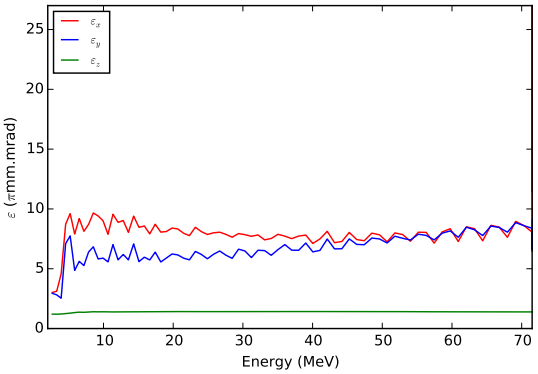

(b) Emittance

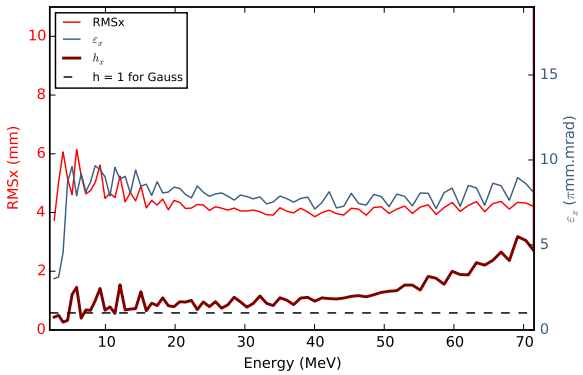

(c) Horizontal RMS, Emit, h

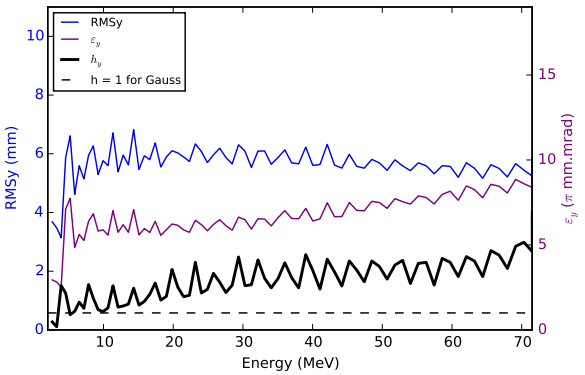

(d) Vertical RMS, Emit, h

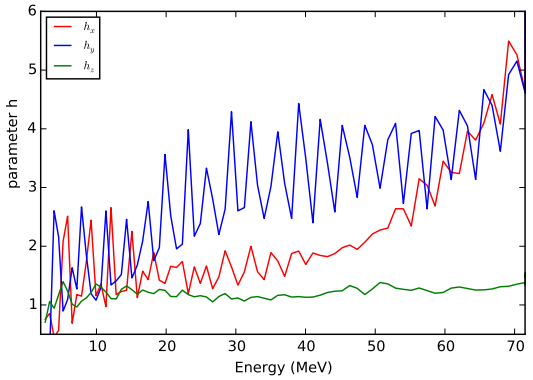

(e) Profile parameter h

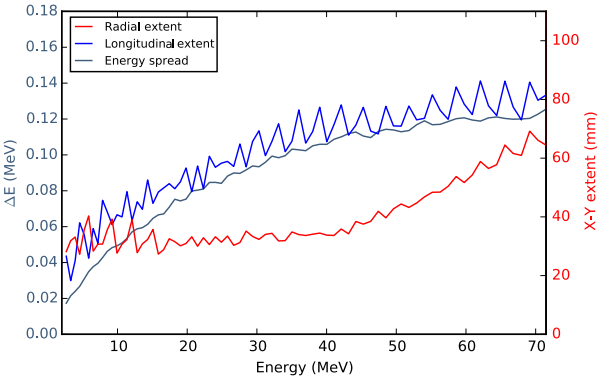

(f) Total beam extent

Figure A.10: Production set-up 6.0 mA case. 6-turn 4σ cut with $5 \cdot 10^4$ macro-particles.

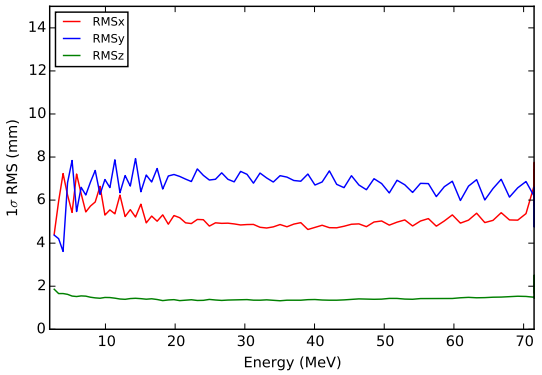

(a) RMS beam size

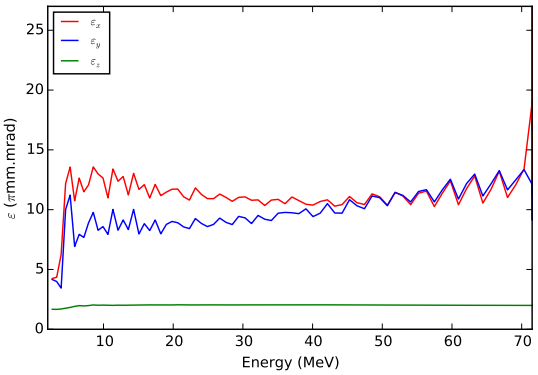

(b) Emittance

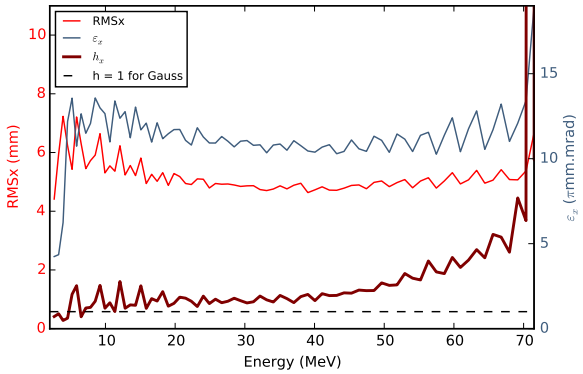

(c) Horizontal RMS, Emit, h

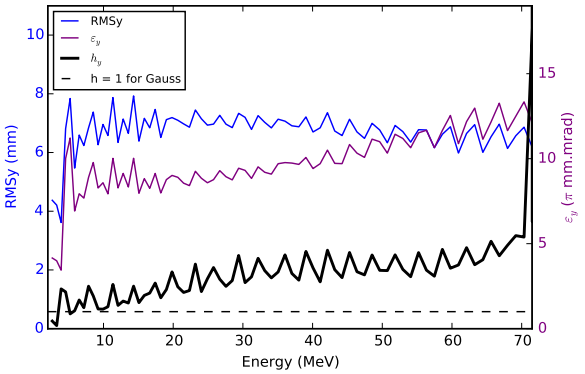

(d) Vertical RMS, Emit, h

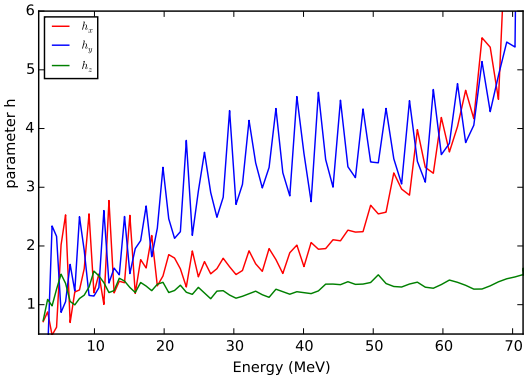

(e) Profile parameter h

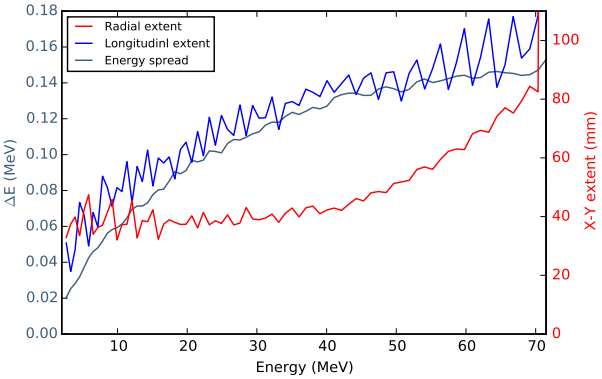

(f) Total beam extent

Figure A.11: Production set-up 10.0 mA case. 6-turn 4σ cut with $5 \cdot 10^4$ macro-particles.

A.2 Physical collimator model

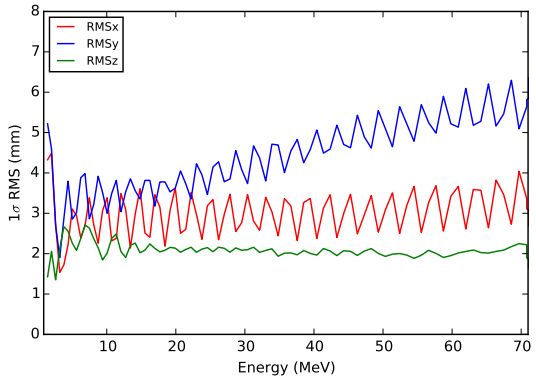

(a) RMS beam size

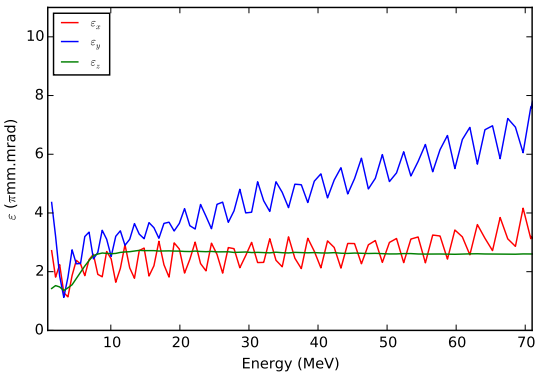

(b) Emittance

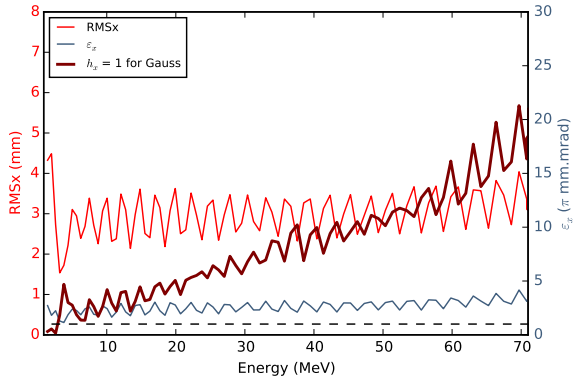

(c) Horizontal RMS, Emit, h

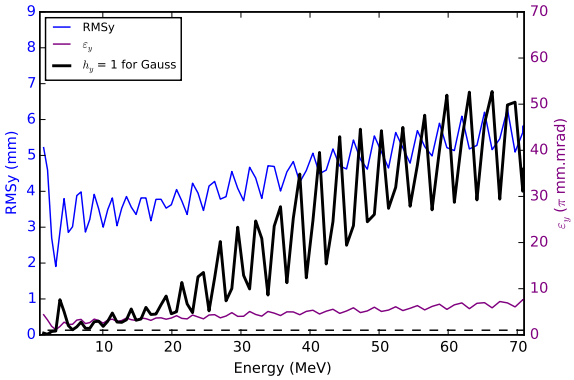

(d) Vertical RMS, Emit, h

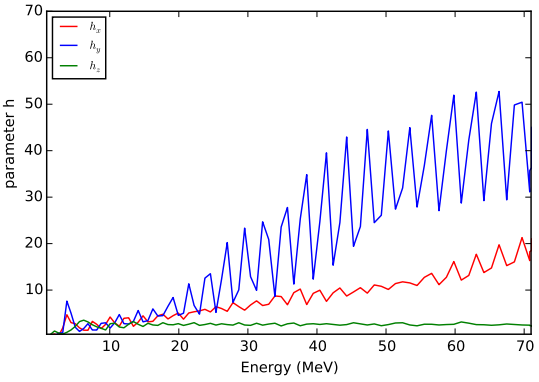

(e) Profile parameter h

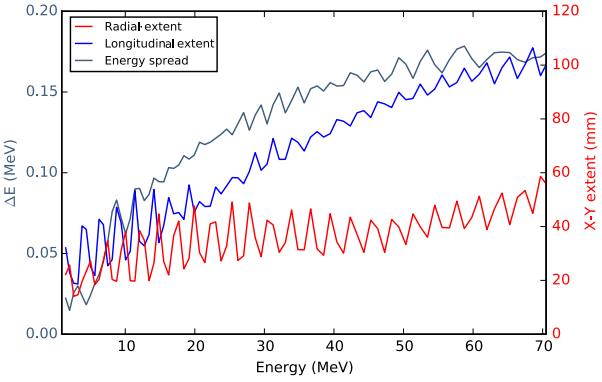

(f) Total beam extent

Figure A.12: Production set-up with collimators 1.8 mA and $5 \cdot 10^4$ macro particles over 82 turns.

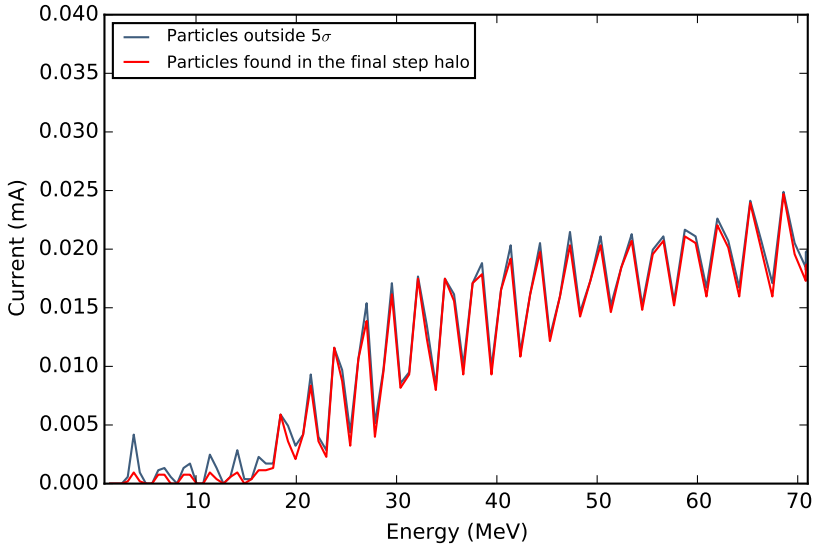

Figure A.13: Halo particles outside 5σ at 1.8 mA modelled with $5 \cdot 10^4$ macroparticles.

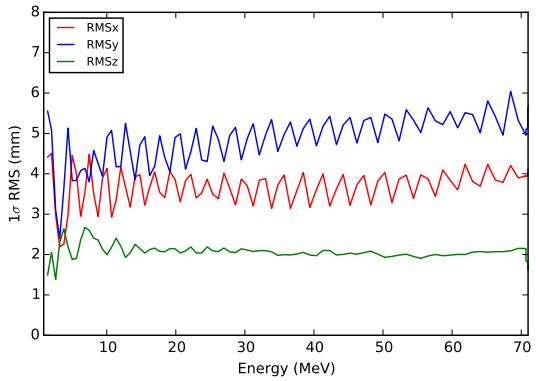

(a) RMS beam size

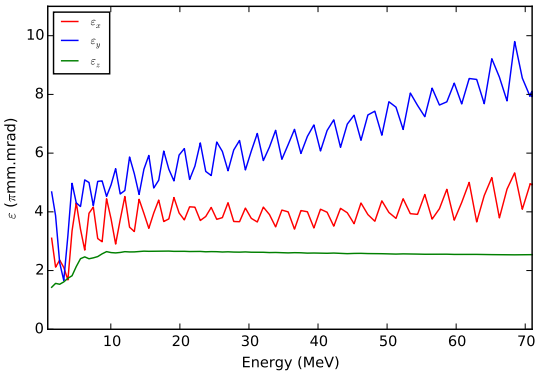

(b) Emittance

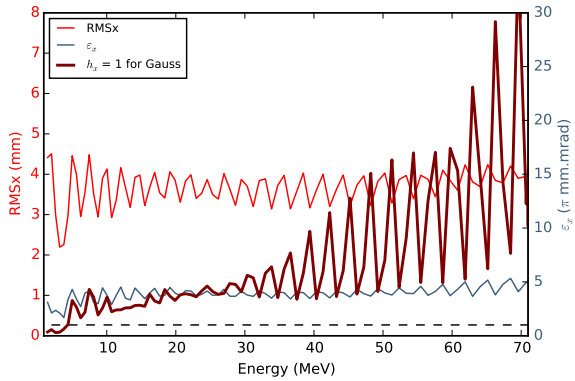

(c) Horizontal RMS, Emit, h

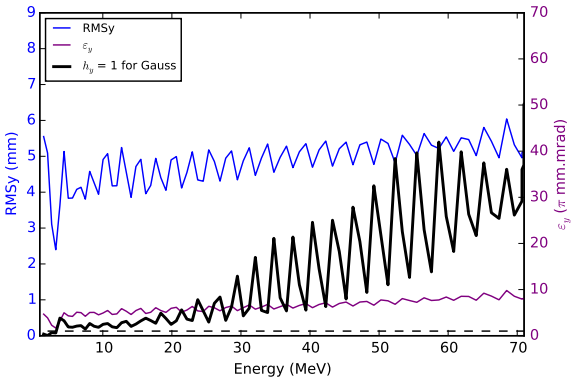

(d) Vertical RMS, Emit, h

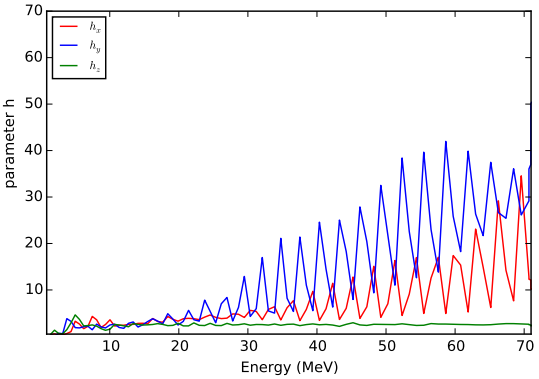

(e) Profile parameter h

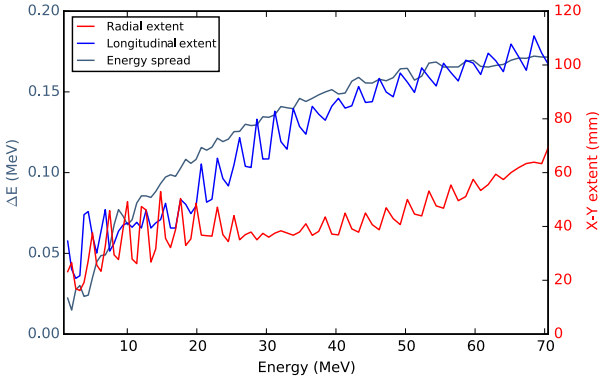

(f) Total beam extent

Figure A.14: Production set-up with collimators 4.0 mA and $5 \cdot 10^4$ macro particles over 82 turns.

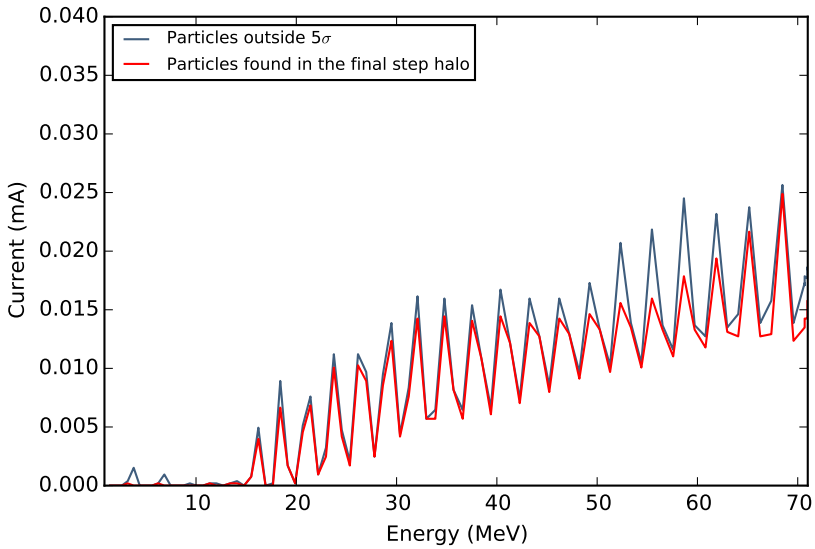

Figure A.15: Halo particles outside 5σ at 4.0 mA modelled with $5 \cdot 10^4$ macroparticles.

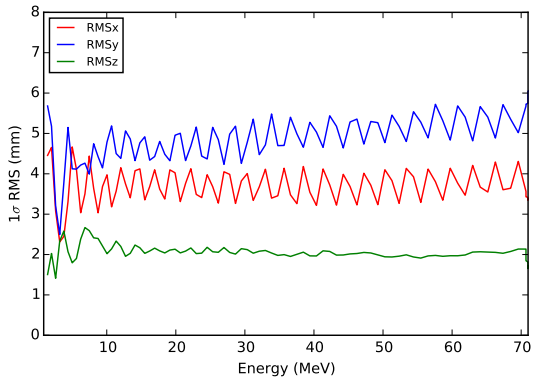

(a) RMS beam size

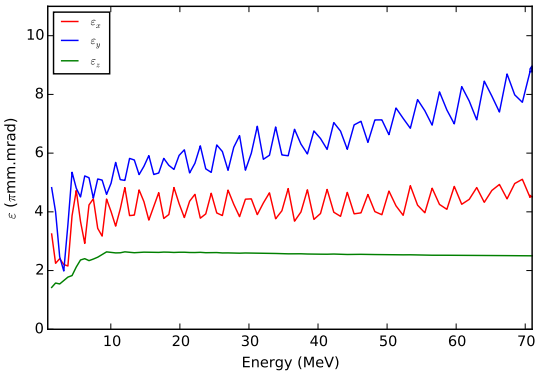

(b) Emittance

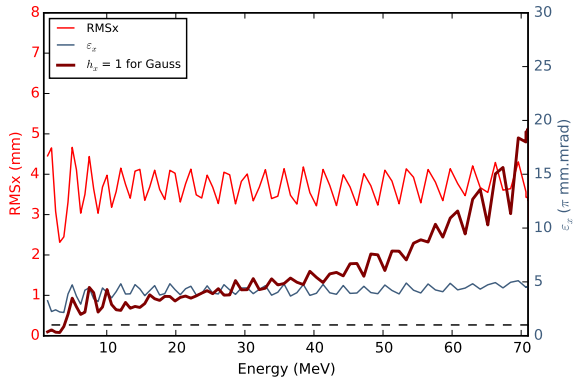

(c) Horizontal RMS, Emit, h

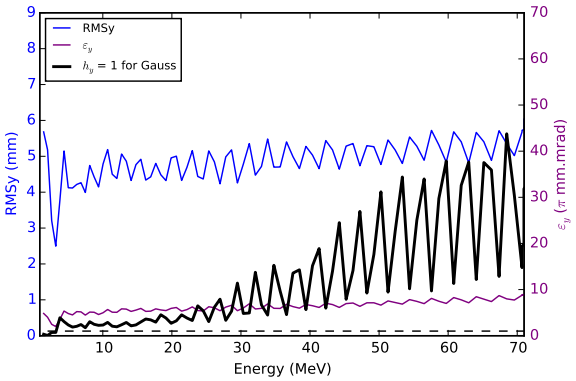

(d) Vertical RMS, Emit, h

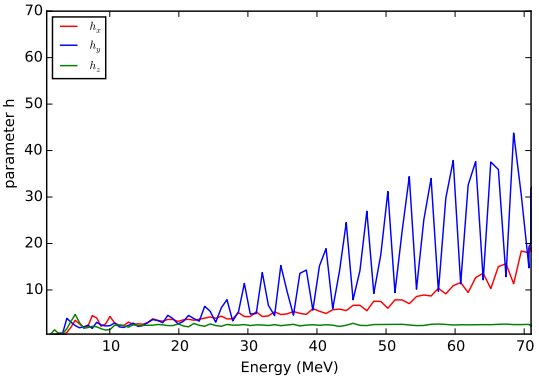

(e) Profile parameter h

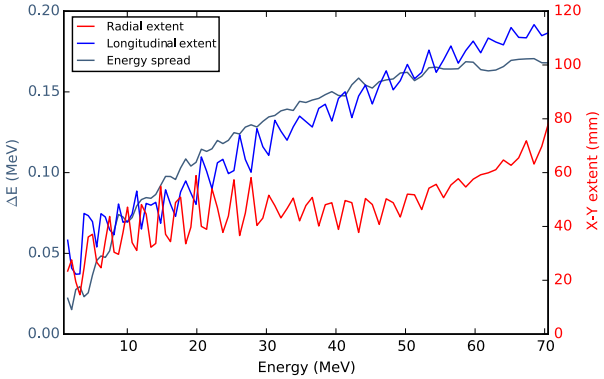

(f) Total beam extent

Figure A.16: Production set-up with collimators 4.66 mA and $5 \cdot 10^4$ macro particles over 82 turns.

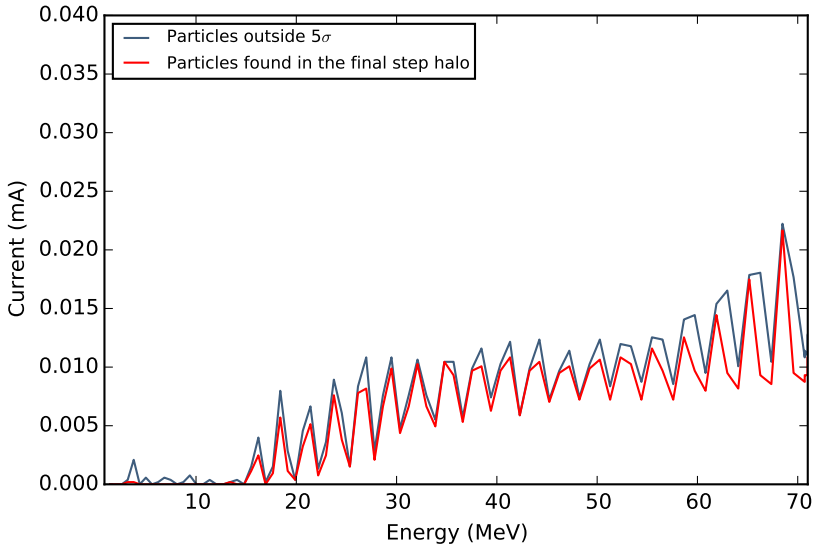

Figure A.17: Halo particles outside 5σ at 4.66 mA modelled with $5 \cdot 10^4$ macroparticles.

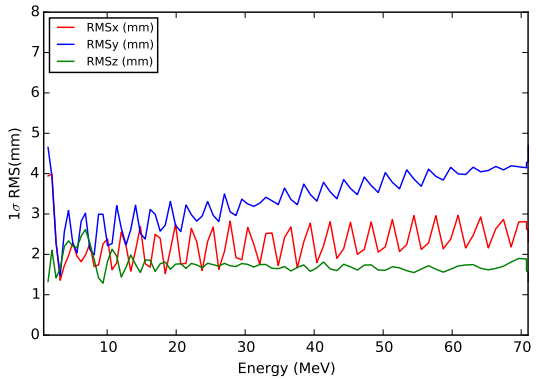

(a) RMS beam size

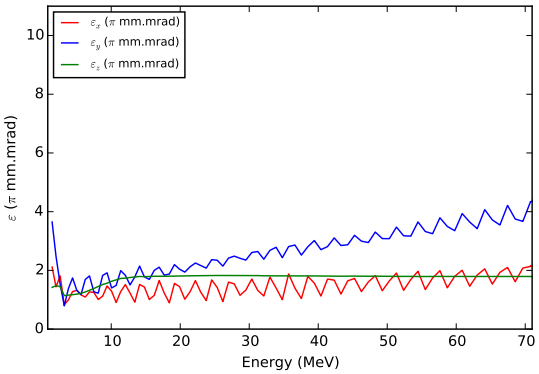

(b) Emittance

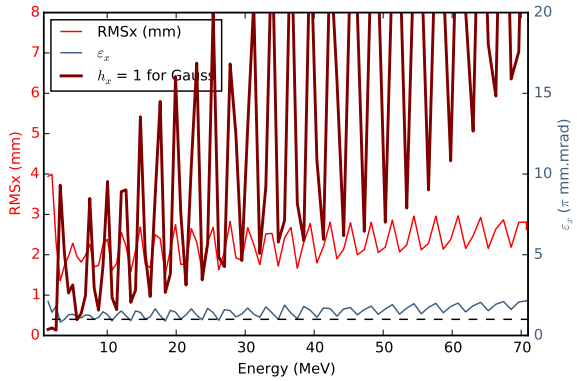

(c) Horizontal RMS, Emit, h

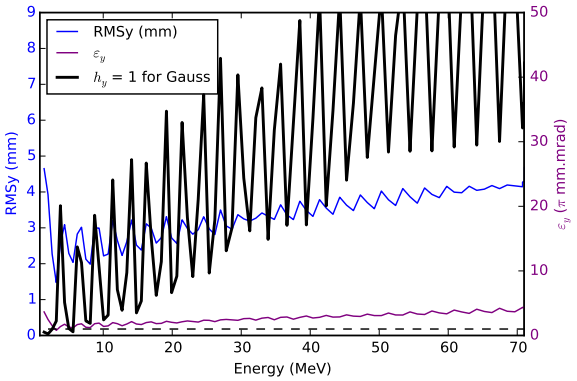

(d) Vertical RMS, Emit, h

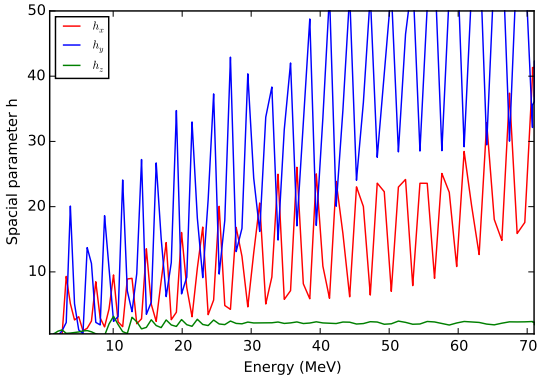

(e) Profile parameter h

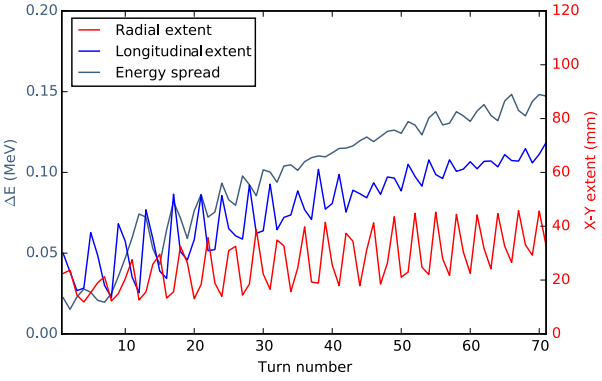

(f) Total beam extent

Figure A.18: Production set-up with physical collimators 0.5 mA case with and 10^5 macro-particles

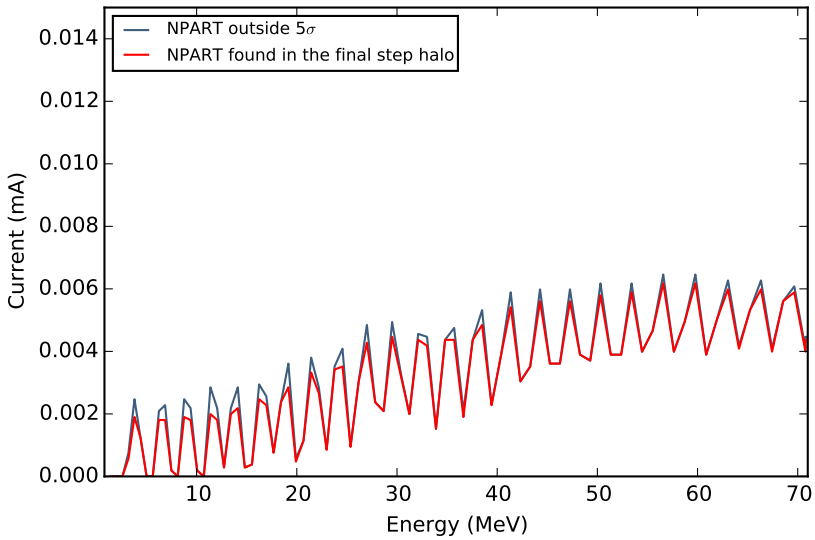

Figure A.19: Current outside 5σ in x and y for 0.5 mA with 10^5 macro-particles.

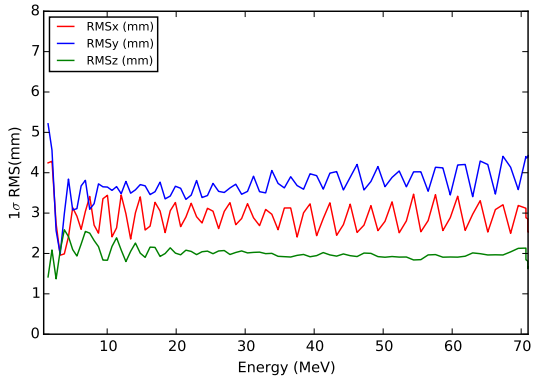

(a) RMS beam size

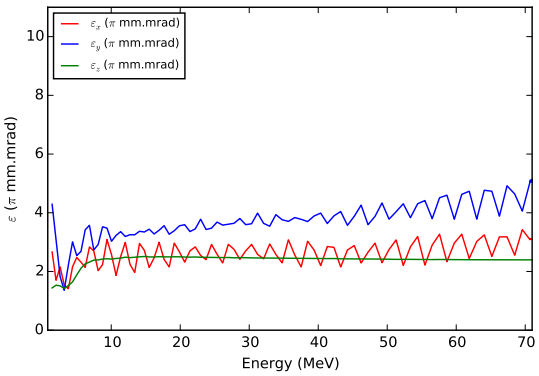

(b) Emittance

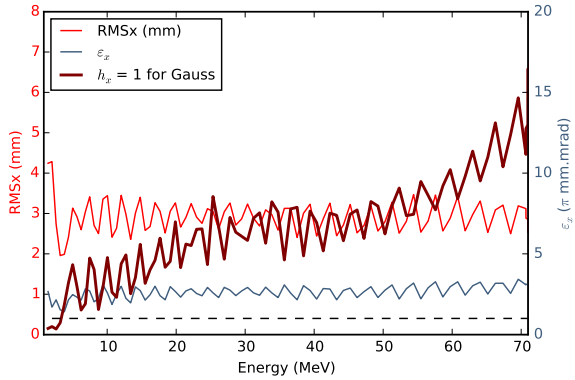

(c) Horizontal RMS, Emit, h

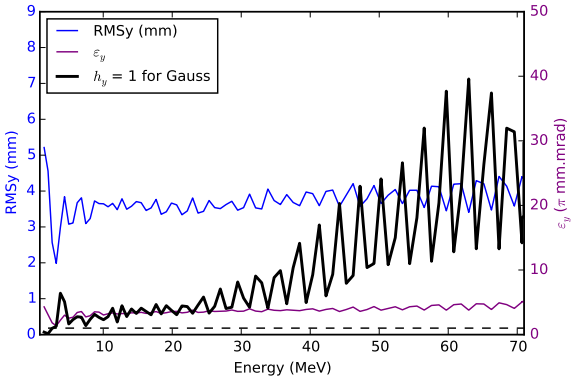

(d) Vertical RMS, Emit, h

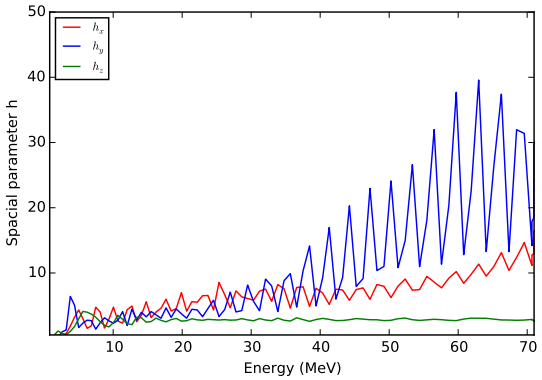

(e) Profile parameter h

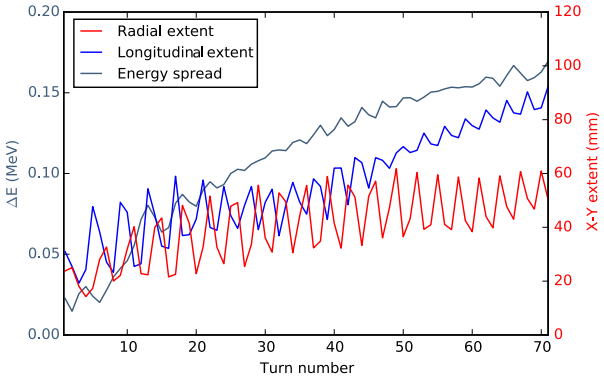

(f) Total beam extent

Figure A.20: Production set-up with collimators 2.3 mA with 10^5 macro-particles.

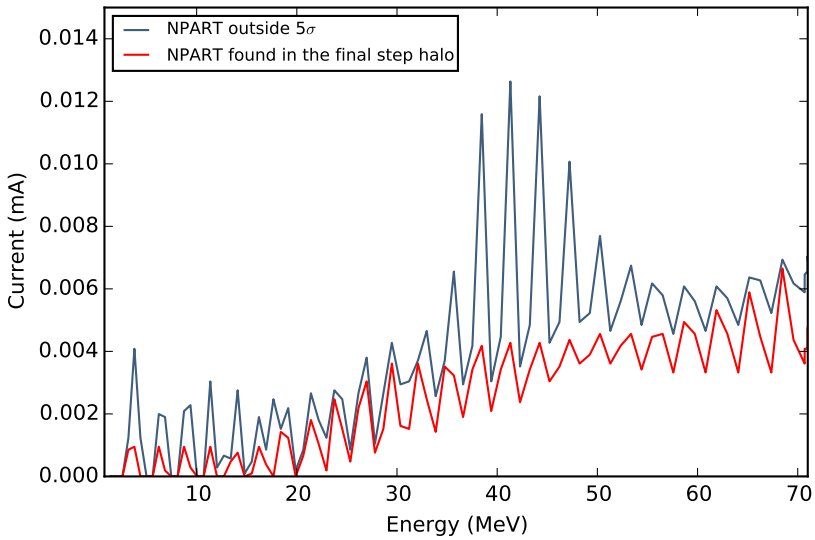

Figure A.21: Current outside 5σ in x and y at 2.3 mA with 10^5 macro-particles.

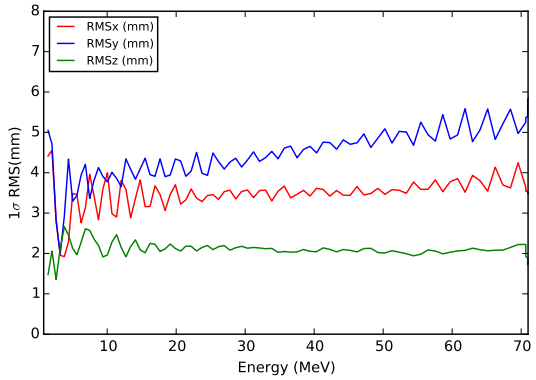

(a) RMS beam size

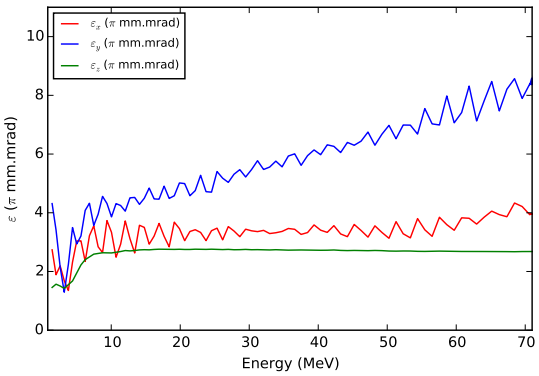

(b) Emittance

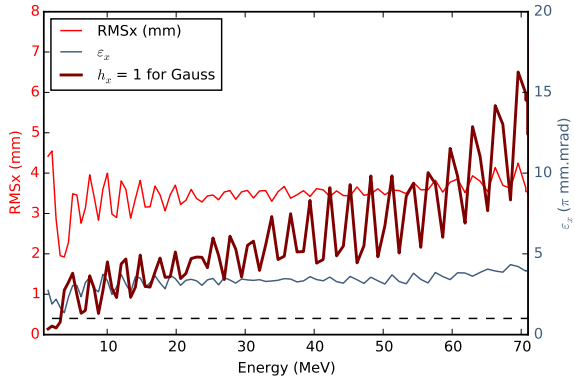

(c) Horizontal RMS, Emit, h

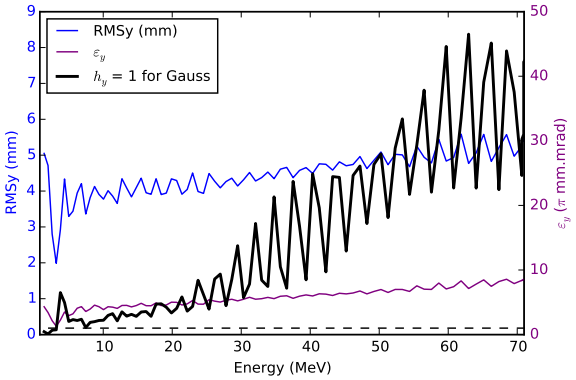

(d) Vertical RMS, Emit, h

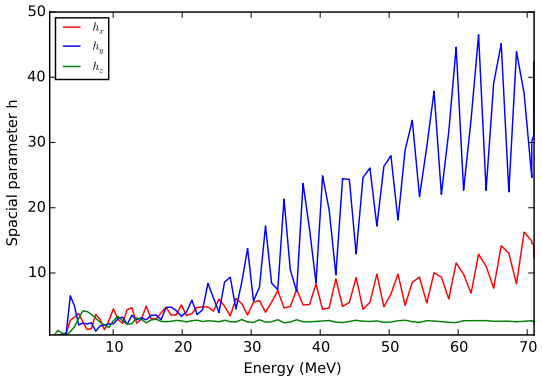

(e) Profile parameter h

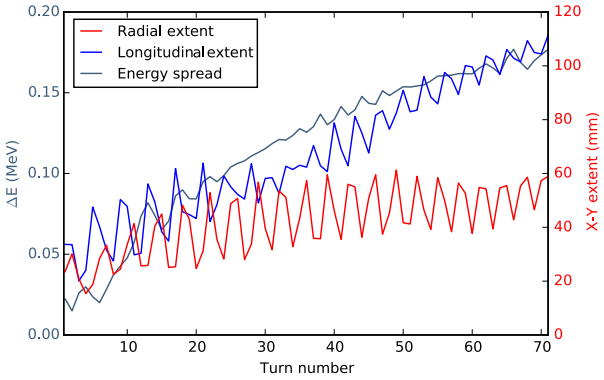

(f) Total beam extent

Figure A.22: Production set-up with collimators at 2.3 mA with 10^6 macro-particles.

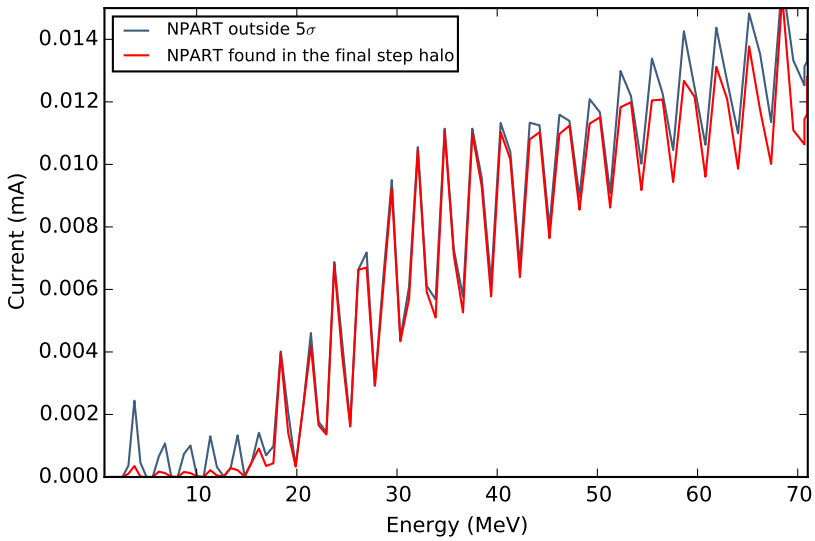

Figure A.23: Current outside 5σ in x and y at 2.3 mA with 10^6 macro-particles.

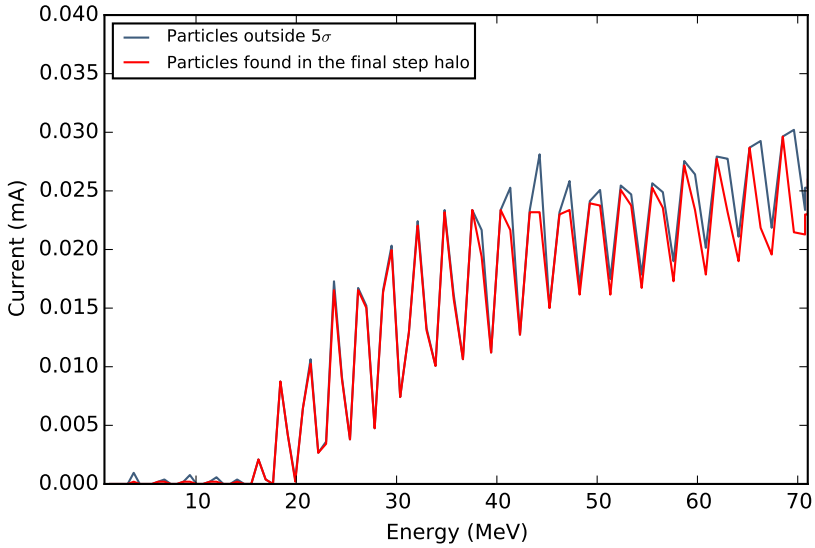

Figure A.24: Halo particles outside 5σ at 3.2 mA modelled with $5 \cdot 10^4$. The amount of halo found in the last step traced back through turns remains unchanged.

A.2.1 KIP4 collimator adjustment

A.2.2 Current on collimators

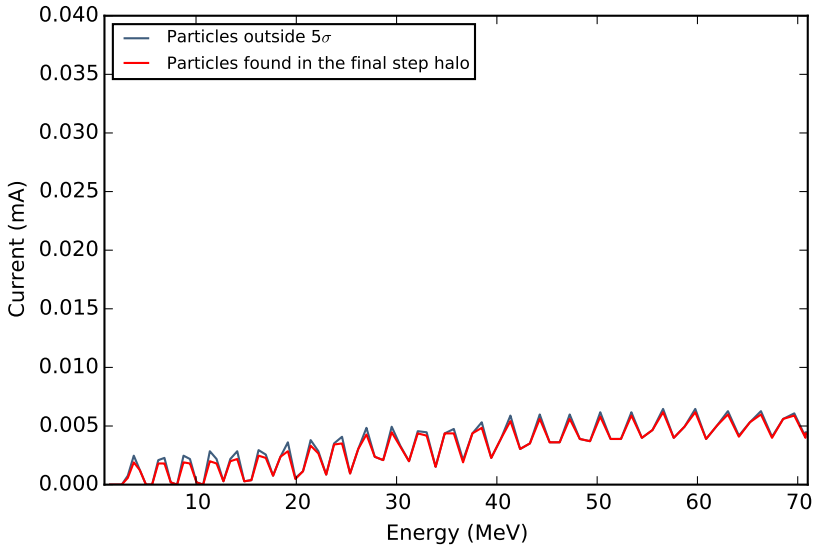

Figure A.25: Halo particles outside 5σ at 0.5 mA with minimal 0.005 mA outside 5σ region modelled with 10^5 macroparticles.

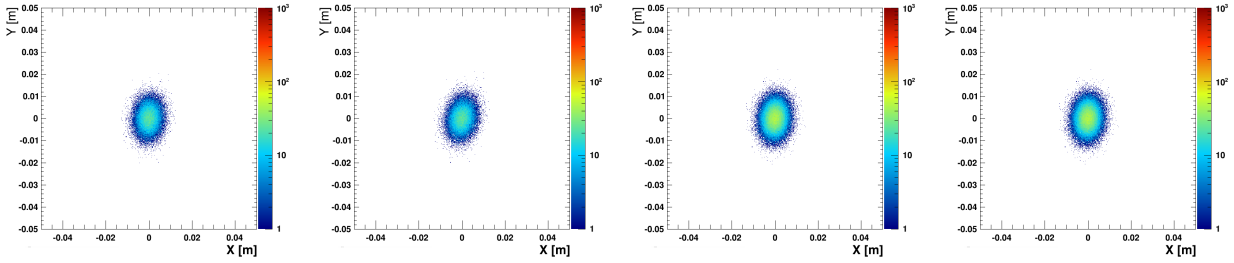

(a) 0.87 MeV (b) 0.87 MeV Fixed (c) 0.87 MeV (d) 0.87 MeV Fixed

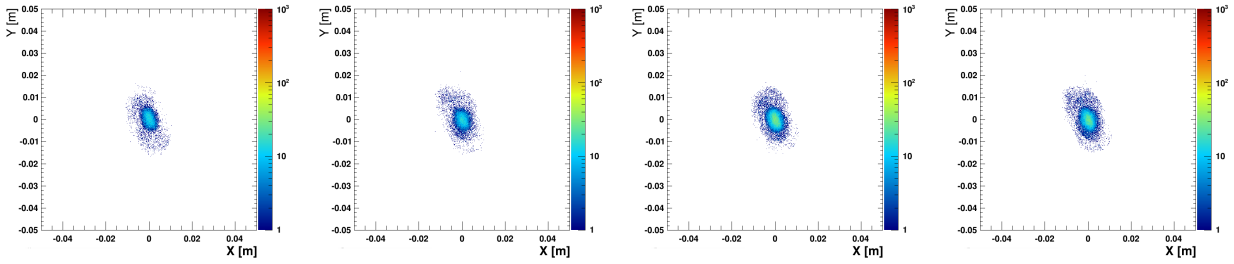

(e) 10.7 MeV (f) 10.7 MeV Fixed (g) 10.6 MeV (h) 10.7 MeV Fixed

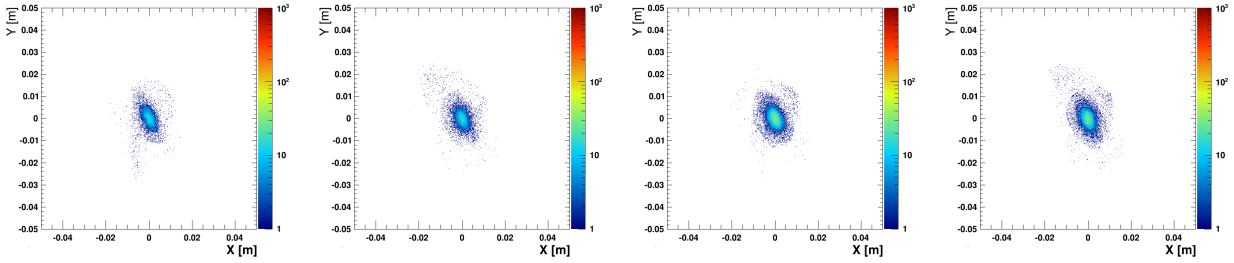

(i) 20.7 MeV (j) 20.6 MeV Fixed (k) 20.7 MeV (l) 20.6 MeV Fixed

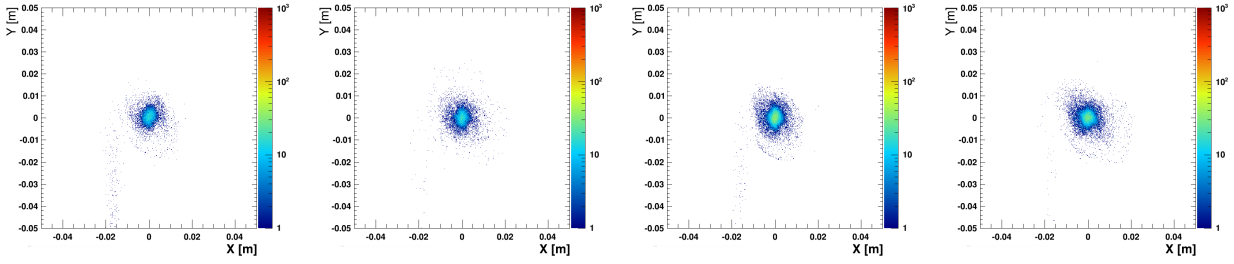

(m) 50.0 MeV. (n) 50.0 MeV Fixed (o) 50.0 MeV. (p) 50.0 MeV Fixed

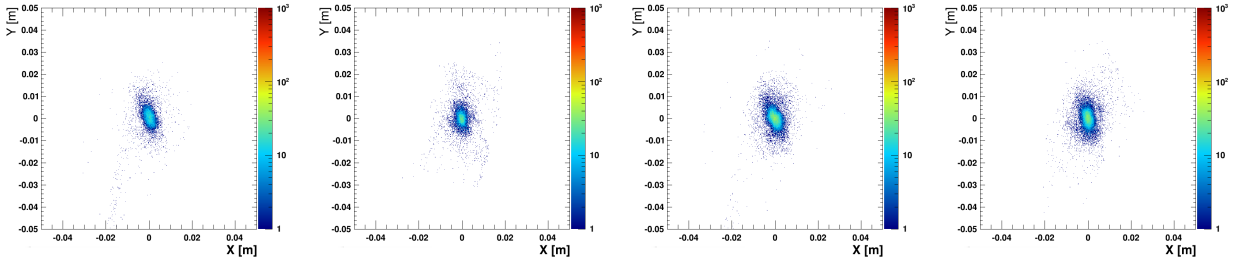

(q) 71.9 MeV (r) 71.8 MeV Fixed (s) 71.8 MeV (t) 71.7MeV Fixed

Figure A.26: Mid-plane of the distribution at different energies of the KIP4 collimator correction (FIX) simulated with $5 \cdot 10^4$ (first two columns) and 10^5particles (last two columns). The tail that appears at (i) and after removing (j). In the first case it remains stationary.

FROM EPICS:	26-27 Jul2015	min	Max
EWBRI	10.5931	10.4965	10.6047
MHC1	2189.99	2189.99	2195.7
	mean over a stable day		
KIP2	2981.32	2818.38	3090.3
KIVU	9.00E-06	9.00E-06	9.00E-06
KIVO	199.606	174.292	244.433
KIP3/RIL2I4	764.819	745.746	796.603
KIR1L	46.829	44.3923	54.1034
KIR1R	383.594	365.28	404.99
KIG1OI	26.5898	22.6464	31.6228
KIG1UI	0.803044	0.549541	1.08393
KIG3OI1	240.676	264.83	211.469
KIG3UI1	73.45	90.4946	53.1111
KIG3OI2	144.647	162.503	131.117
KIG3UI2	9.00E-06	9.00E-06	9.00E-06
KIR3L	**536.25**	**536.25**	**536.25**
KIR3R	**564.5**	**564.5**	**564.5**
KIP4L	605.498	605.498	605.495
KIP4R	615.024	615.328	614.946
SUM (Model)	7183.60586	7010.68986	7340.02425
LEFT	3.40949414	mA	

Figure A.27: Selection of extracted collimator currents in Injector II.

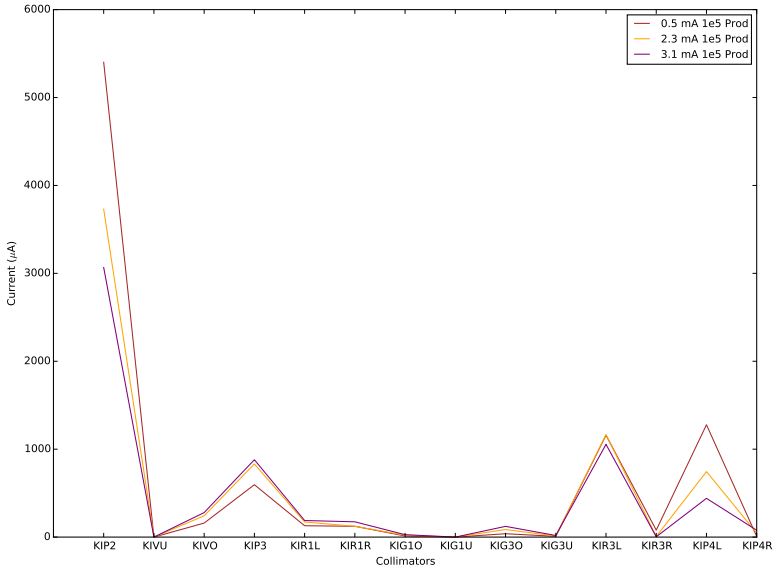

Figure A.28: Simulated current read on collimators for 10^5 macro-particles.

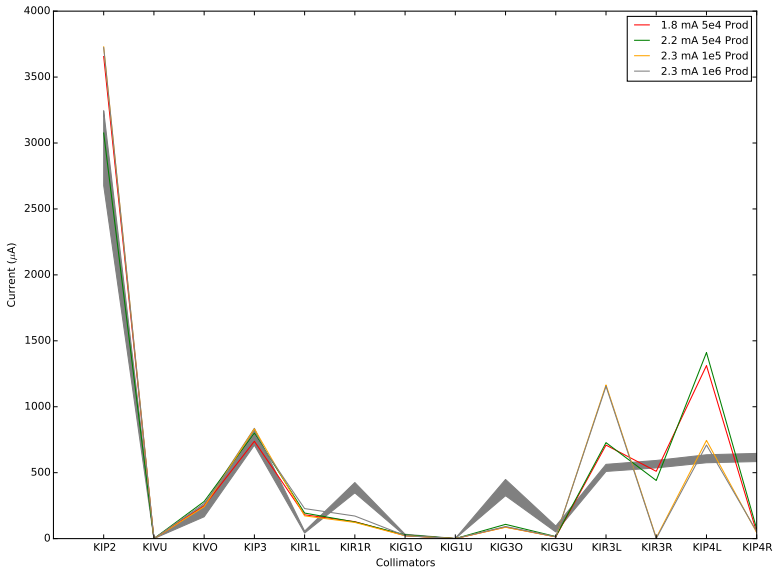

Figure A.29: Simulated current read on collimators for $5 \cdot 10^4$, 10^5 and 10^6macro-particles at 2mA. Only KIP2 has been moved, discrepancies noticeable in the last collimators.

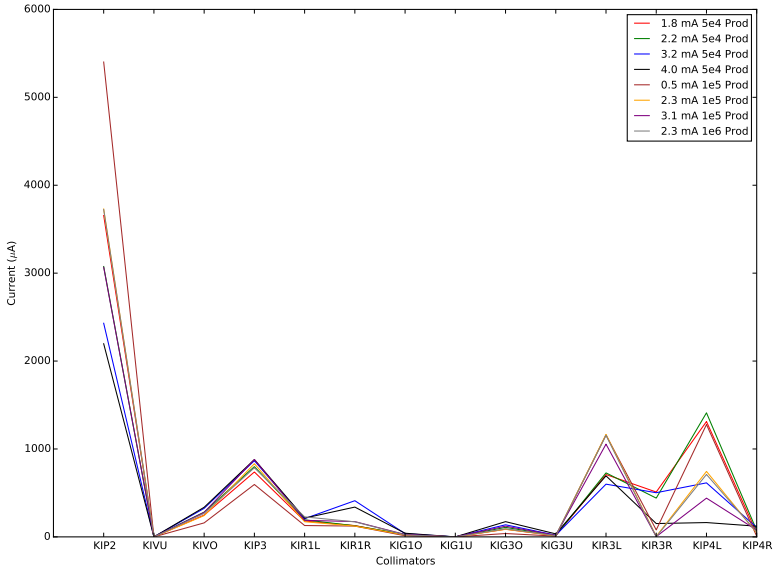

Figure A.30: Simulated current on collimators for selected intensities.